THE BIOGEOCHEMISTRY OF TRACE METALS AND THEIR ISOTOPES IN THE MEDITERRANEAN AND BLACK SEAS

John Michael Rolison

A thesis submitted for the degree of
Doctor of Philosophy
University of Otago, Dunedin, New Zealand

February, 2016

ABSTRACT

The marine biogeochemistry of trace metals and their isotopes is a burgeoning field in Earth sciences. The primary interest in trace metals stems from the fact that many metals are utilized in biochemical functions of marine phytoplankton which form the base of the marine food web. Low concentrations of bioessential elements may limit primary productivity in large swaths of the global ocean, while elevated concentrations around anthropogenic sources can prove toxic to marine phytoplankton. Thus, it is important to understand the sources and sinks of metals to the ocean and the biogeochemical processes that influence their distributions. Furthermore, sedimentary records of trace metals provide important constraints on environmental change, such as the redox evolution of the ocean-atmosphere system throughout Earth's history.

In this study, the biogeochemistry of trace elements and their isotopes was investigated as part of the 2013 GEOTRACES expeditions in the Mediterranean and Black Seas. The unique oceanographic properties of these marine basins were exploited to better understand how specific processes influence the distributions of trace metals and their isotopes. The Mediterranean Sea receives the largest flux of atmospheric deposition of any modern marine basin, is strongly impacted by anthropogenic activity, and experiences overturning circulation analogous to the global ocean. The distribution of dissolved aluminum displayed high concentrations (up to 175 nM) in the Mediterranean Sea that are likely a result of the intense dust deposition. Strong correlations between dissolved aluminum and silica with salinity indicate that the general distribution of dissolved aluminum is controlled by conservative mixing, including the long recognized covariation between aluminum and silica. The distributions of dissolved iron, zinc, cadmium and lead in the Mediterranean Sea were also investigated, which reveal striking concentration gradients between the eastern and western Mediterranean basins. Atmospheric deposition of lithogenic material results in elevated concentrations of dissolved iron in Mediterranean surface waters, while anthropogenic sources of zinc, cadmium and lead within the western Mediterranean basin may support the observed concentration gradients.

The Black Sea is the world's largest anoxic marine basin and is an ideal natural laboratory for investigating the behavior of trace metals and their isotopes under variable redox conditions. The distributions of a suite of dissolved trace metals including aluminum, titanium, manganese, iron, copper, zinc, gallium, yttrium, zirconium, cadmium, lanthanum, and uranium in the Black Sea water column are reported. The distributions of trace metals in the Black Sea are primarily controlled by redox reactions that induce changes in solubility of the metals, the formation of insoluble metal-sulfides in the deep sulfidic basin, and the scavenging/regeneration of metals associated with the remineralization of sinking particles. Additionally, the iron and uranium isotope systems are investigated in the water column and sediments of the Black Sea. Iron isotope fractionation factors associated with pyrite formation, $\varepsilon_{\mathrm{Fe(II)-pyrite}}$ = +2.75 ± 0.22‰ (2SE), and oxidation reactions, $\varepsilon_{\mathrm{Fe(II)-Fe(III)}}$ = -0.19 ± 0.07‰ to -0.40 ± 0.12‰ (2SE), are calculated from the isotopic composition and concentration of iron in the water column. Similarly, the isotopic composition and concentration of U in the water column is used to calculate the uranium isotope fractionation factor associated with reduction of U(VI) to U(IV), $\varepsilon_{\mathrm{U(VI)-U(VI)}}$ = -0.61 ± 0.08‰ to -0.84 ± 0.11‰ (2SE). Implications for the application of the iron and uranium isotope paleoredox proxies to the sedimentary record are discussed.

ACKNOWLEDGMENTS

The successful completion of this thesis was in no small part the result of the excellent guidance and advice provided by of my two supervisors, Drs. Claudine Stirling and Rob Middag. Thank you for your inspiration and unwavering support during the past three years. I am grateful for the productive relationships we have developed.

Prof. Hein de Baar and Dr. Micha Rijkenberg were instrumental in securing funding for the Dutch GEOTRACES expeditions to the Mediterranean and Black Seas in 2013. Thank you for inviting me to join the expeditions and for the resultant fruitful collaborations. The captain and crew of the R/V *Pelagia* are also thanked for their excellent professional support during the expeditions (cruises 64PE370, 64PE373, and 64PE374). The expedition participants are acknowledged for their tireless efforts sampling seawater sample at all hours of the day and night for over two months of cruising.

The members of the Centre for Trace Element Analysis, Melanie Gault-Ringold, Ejin George, Matt Clarkson, and Phil Nasemann are thanked for their scientific insights and friendship over the years. Dave Barr is thanked for being super reliable at producing high quality trace element data on the Q-ICP-MS at short notice.

I thank the Department of Chemistry administrators, Pip Jack and Theresa Mendoza, for their assistance in navigating through the PhD program. Nigel Alefosio in the chemistry store is thanked for tracking down all of the deliveries that are inevitably lost in transit down to the South Island of New Zealand. Mat Rooney is acknowledged for providing excellent computer support.

Ken Bruland and Rob Franks are thanked for providing access to the ICP-MS facilities at the University of California Santa Cruz. The high quality of the data collected in this study was made possible by the excellent maintenance and operation of the instrumentation at UCSC.

I thank my family for their love and support through the last three years of my PhD and over the previous years leading up to my time here in New Zealand. Their positivity and encouragement have made the entire journey much more manageable. I am eternally grateful for having such a kind and loving family.

Finally, I thank my amazing fiancée Kristina. None of this would have been possible without your unwavering support. Thank you for staying positive during all of my long nights in the lab and all of my trips to sea. You are an amazing person and I am happy to call you my best friend. It has been an incredible experience exploring New Zealand with you and I look forward to many more wonderful years of adventure to come.

TABLE OF CONTENTS

LIST OF TABLES

LIST OF FIGURES

CHAPTER 1

INTRODUCTION

1.1 Marine biogeochemistry of trace metals

The biogeochemical cycles of trace metals in the world's oceans have been intensely investigated since the 1970s (trace elements are generally defined as having concentrations less than 10 µmol/kg). Advances in instrumental analysis have been paramount in the progression of our understanding of the role trace metals play in the biogeochemistry of the oceans. For instance, improvements in instrumental detection limits highlighted the requirement of clean sampling and analytical techniques for acquiring reliable and 'oceanographic consistent' data due to the vanishingly low concentrations of trace metals in seawater and the ubiquity of metals in ships and in laboratories (Boyle and Edmond, 1975; Patterson, 1974). Current shore based techniques, particularly inductively coupled plasma mass spectrometry (ICP-MS), now allow for the rapid analysis of samples with even the lowest concentrations of trace metals and the development of sensitive shipboard methods, such as flow injection analysis (FIA) with spectrophotometric detection, enable near real-time data collection during oceanic expeditions. Moreover, the recent application of multiple-collector ICP-MS to oceanography has facilitated the high-precision stable isotope analysis of a variety of trace elements, providing a wealth of new information on the sources, sinks, and cycling of trace metals in the oceans. For example, Conway and John (2014) used the isotope composition of dissolved iron in seawater to provide the first quantitative estimate of the relative importance of different sources of iron to the North Atlantic Ocean, which include dust deposition, hydrothermal venting, rivers and marine sediments. These authors concluded that Saharan dust is the largest source of iron to the modern North Atlantic Ocean. Furthermore, the sources of iron to the deep Pacific Ocean over the past 76 My were investigated by Horner *et al.* (2015) using the iron isotope composition of seawater recorded in iron-manganese crusts leading to the conclusion that deeply sourced iron from hydrothermalism and sediment dissolution was the dominant source of iron to the Pacific over this time period.

The interest in the biogeochemical cycle of trace metals in the oceans stems from observations of nutrient-like vertical profiles (low concentrations at the surface and increasing concentrations with depth) for many of the trace metals of interest. Due to biological utilization, the concentrations of macronutrients such as phosphorus (P), nitrogen (N), and silica (Si) are depleted in surface waters. Remineralisation of sinking organic matter releases the nutrients back to the water column, thereby enriching the deep waters in N, P, and Si. Trace metals with nutrient-like vertical profiles were the first clue that certain trace metals are biologically sequestered (Boyle *et al.*, 1976; Bruland *et al.*, 1978; Bruland, 1980). Subsequent culturing experiments have proven that transition metals are essential micronutrients for many marine photosynthetic organisms (Brand *et al.*, 1983). These observations form the basis of the theory that certain trace metals (*e.g.* iron) are capable of limiting the growth of primary producers in some areas of the world's oceans, particularly in high-nutrient low-chlorophyll (HNLC) waters (Martin, 1990). Indeed, iron-enrichment experiments ranging in scale from bottle incubations to large-scale open-ocean amendment studies have convincingly demonstrated that iron supply stimulates phytoplankton growth in HNLC waters (Martin and Fitzwater, 1988; de Baar *et al.*, 2005; Boyd *et al.*, 2007). Importantly, HNLC waters represent ~30% of the world's ocean (Moore *et al.*, 2013).

In addition to iron, other biologically essential trace metals (*e.g.* zinc and cobalt) have the potential to limit or co-limit phytoplankton growth due to their exceedingly low concentrations in surface waters (Saito *et al.*, 2008). By significantly limiting the growth of primary producers, trace metals in the ocean are intimately linked to global climate through the 'biological pump' (Fig. 1.1). In the photic zone of the oceans, phytoplankton convert sunlight and carbon dioxide into organic carbon. This process lowers pCO_2 in the surface water and enhances CO_2 flux across the air-sea interface. Much of the organic carbon is recycled in the surface ocean but a small amount sinks and is subsequently sequestered into the interior of the ocean. This process is termed the 'biological pump'. The strength and efficiency of the biological pump influences the rate of carbon sequestration in the deep ocean, thereby exerting an influence on the pCO_2 in the atmosphere and therefore global climate due to the fact that CO_2 is a 'greenhouse gas'. Most sinking organic carbon is remineralized before reaching the sediments and therefore the CO_2 is only sequestered on time scales similar to the mixing time of the global ocean (~1 ky). However, some organic carbon and inorganic carbon of biogenic origin (*e.g.* calcite) reach the seafloor and becomes buried in marine

sediments. Marine sediments represent the ultimate sink of carbon from the ocean-atmosphere system. Sequestration of CO_2 in the deep ocean, and in marine sediments, is the primary mechanism by which the biological pump influences atmospheric pCO_2 and therefore global climate on intermediate and geologic timescales.

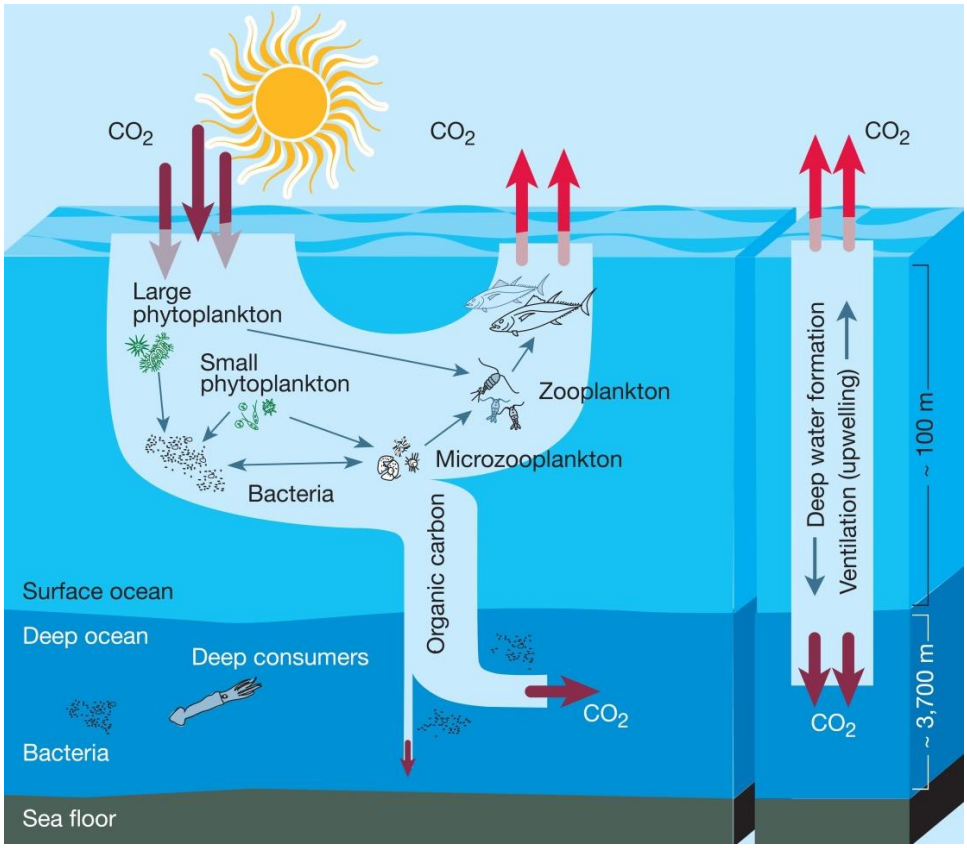

Fig. 1.1. Schematic representation of the marine 'biological pump'. Phytoplankton growing in sunlight surface waters consume CO_2 and nutrients, producing organic carbon and forming the base of the marine food web. Sinking organic carbon that escapes remineralization by bacteria in surface waters is transported to deep water, resulting in the net transport of CO_2 from the atmosphere to the deep ocean and sediments. The availability of biologically essential trace metals in surface waters influence the growth of phytoplankton and therefore the global CO_2 cycle and climate. Figure from Chisholm (2000).

In addition to biological activity, many important processes act in combination to control the dissolved concentrations and distributions of trace metals in the oceans. These processes include the external supply of trace metals to the ocean, internal recycling, complexation with organic ligands, and removal processes from the water column (Bruland and Lohan, 2003). Removal processes include biological uptake, passive scavenging on sinking particles, and formation of insoluble minerals. Ocean

circulation is a second-order process influencing trace metal patterns. Understanding how the combinations of these processes control the oceanic distributions of trace metals is of prime importance for interpreting the vertical profiles of trace metals and trace metal concentration and isotopic patterns in marine sediment cores. This point is emphasized by the fact that much of what is known about paleoceanographic conditions, such as temperature, salinity, pH, redox state, and carbon chemistry, is derived from trace element and isotopic patterns recorded in marine sediments. These records provide vital information about how the ocean operates under different climate scenarios which can be used to test models of how current and future global climate change may reshape the oceans.

The Mediterranean and Black Seas possess unique oceanographic characteristics (as discussed below) which make them ideal natural laboratories for investigating the biogeochemical processes that govern the distributions of trace metals in the marine environment. The aim of this study is to take advantage of these unique conditions to improve our understanding of the sources and sinks of trace metals to the oceans and how physicochemical processes within the oceans redistribute trace metals. Understanding the controls on the distribution of trace metals in the oceans will also provide a better understanding of the interplay between trace metal availability and primary productivity.

1.2 Trace metal and isotope paleoredox proxies

Earth's O_2-rich atmosphere has allowed for the existence and evolution of abundant complex life for hundreds of millions of years. As a result, different organisms now fill practically every available ecological niche on the surface of the planet. Yet, free O_2 was nearly absent from the atmosphere during the first half of Earth's 4.5 billion year history (Fig. 1.2.; Lyons *et al.*, 2014). The disappearance of non-mass dependent sulfur isotope anomalies from the geologic record constrains the first permanent rise in atmospheric O_2, known as the Great Oxidation Event (GOE), during the early Proterozoic around 2.3 billion years (Ga) ago (Bekker *et al.*, 2004; Farquhar *et al.*, 2000; Holland, 2002). Before the GOE, free O_2 produced through oxygenic photosynthesis would have been consumed by reactions with reduced compounds and minerals at Earth's surface, until the balance of reduced and oxidized species favored the accumulation of free O_2 in the atmosphere. The oxygenation of the

deep ocean lagged behind the oxygenation of the atmospheric, potentially for billions of years, with anoxic and ferruginous conditions likely dominating the marine environment with local to regional euxinic conditions (Canfield, 1998; Poulton et al., 2010). A second rise in atmospheric O_2 during the late Proterozoic around 600 million years (My) ago ushered in an age of rapid developments in eukaryotic evolution and the emergence of the first animals known from the fossil record (Lyons *et al.*, 2014 and references therein). This scenario leads to intriguing questions about how the prevailing redox chemistry of the Precambrian ocean evolved through time, how these changing conditions influenced the concentrations of redox sensitive trace metals in seawater, and in turn, how was the evolution of marine life dictated by the availability of bioessential trace metals.

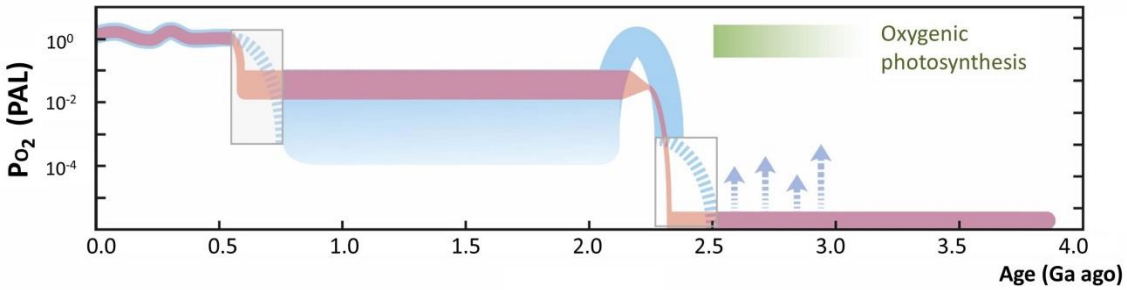

Fig. 1.2. Concentration of atmospheric O_2 throughout Earth's history. The traditional view of unidirectional two-step rise in O_2 through Earth's history (orange trace) is giving way to a modern understanding (blue trace) which suggests more protracted increases in atmospheric O2 at the beginning and end of the Proterozoic (boxes). Although oxygenic photosynthesis developed some 3 Ga ago, the initial rise in atmospheric O_2, i.e. the Great Oxidation Event, was delayed until around 2.3 Ga ago due to the reactions between free O_2 and reduced minerals and compounds at Earth's surface. There is evidence in the geologic record of localized production of O_2 resulting in spatially limited regions of oxidizing conditions before the GOE (blue arrows). PAL – present atmospheric level. Figure modified from Lyons *et al*. (2014).

Many bioessential trace metals are redox sensitive and their abundances in the ocean are directly related to the prevailing redox state of the ocean-atmosphere system. Under sulfidic conditions, many bioessential trace metals (*e.g.* Fe, Co, Zn, Mo) form insoluble metal-sulfides which may precipitate or are scavenged from the water column and deposited in sediments. If sulfidic conditions prevailed in the oceans during the middle Proterozoic, then the concentrations of bioessential trace metals may have been low enough to restrict primary productivity and challenge the evolution of marine life

(Anbar and Knoll, 2002). The abundance of redox sensitive trace metals in organic-rich marine sediments are commonly used to investigate paleoredox conditions during the Precambrian with many trace element records providing evidence of significant shifts in their marine inventories due to changes in the redox state of the ocean-atmosphere system (*e.g.* Lyons *et al.*, 2014). Furthermore, the investigation of redox sensitive metal isotope systems in marine sedimentary records is rapidly advancing, providing new insights into the marine cycling of metals in ancient oceans. For instance, the iron isotope composition of Precambrian pyrites displays a pronounced shift around the time of the GOE, possibly indicating a major shift in the marine cycle of iron in response to the initial oxidation of the Precambrian ocean (Fig. 1.3; Rouxel *et al.*, 2005). In their interpretation, Rouxel *et al.* (2005) assume that pyrite passively records the iron isotope composition of ambient seawater, necessitating the need for a major shift in the iron isotope composition of the seawater iron reservoir itself to explain the pyrite data. However, Guilbaud et al. (2011) challenged this interpretation through laboratory experiments which demonstrated large iron isotope fractionation associated with pyrite formation suggesting that the pyrite iron isotope record indicates a shift to a more sulfidic ocean after the GOE, rather than a shift to more oxidizing conditions. Successfully interpreting the true significance of variations in the abundance and isotope composition of redox sensitive trace metals in ancient marine sediments relies on accurate calibrations of the behavior of trace metals in modern anoxic marine basins, such as the Black Sea, that are analogous to the widespread anoxic and sulfidic conditions in the Precambrian ocean. Indeed, much of the current knowledge concerning the dominant processes controlling trace metal abundances in marine sediments is derived from studies of modern anoxic basins (*e.g.* Little *et al.*, 2015), while research on the processes and mechanisms which control the isotope compositions of trace metals in marine sediments is still in its infancy.

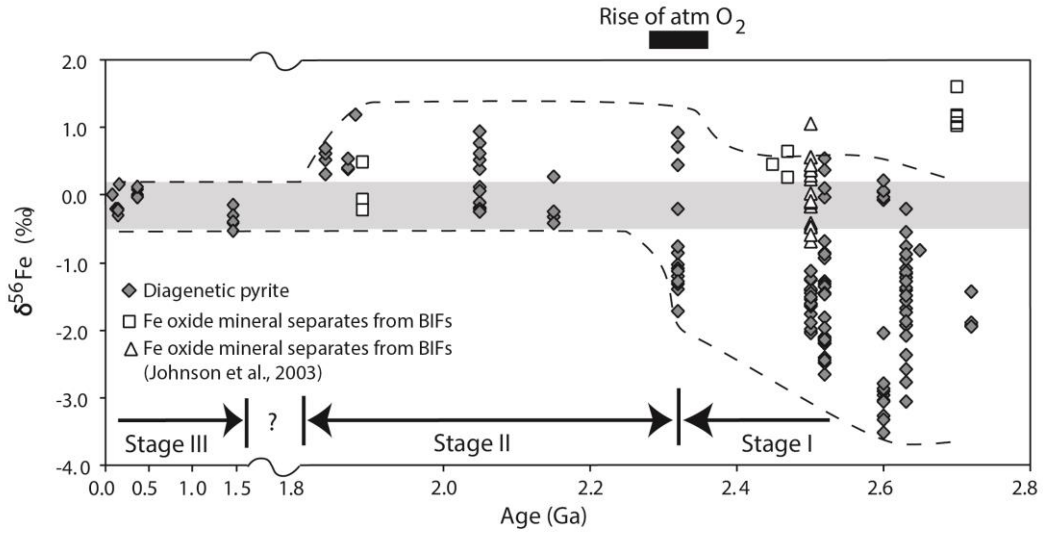

Fig. 1.3. Iron isotope composition of sedimentary pyrites from throughout Earth's history. The shift from predominantly negative δ^{56}Fe values to near zero values around 2.3 Ga occurs at roughly the same time as the Great Oxidation event, indicating a major shift in the depositional environment and redox state of the oceans. Figure from Rouxel *et al.* (2005).

Many other redox sensitive trace metal isotope systems (*e.g.* Cr, Mo, U) are being investigated in marine sediments in an effort to elucidate the redox evolution of the atmosphere and ocean through Earth's 4.5 Ga history. Each redox sensitive trace metal isotope system responds differently to evolving redox conditions due to their different chemistries. Therefore each isotope system requires a thorough understanding of the mechanisms that generate isotope fractionation and how these signals are transmitted to sedimentary archives. For the case of the uranium isotope system, observations of uranium isotope fractionation in the Black Sea has been exclusively used to calibrate the uranium isotope paleoredox proxy which has been applied to a wide range of time periods throughout Earth's history (Brennecka et al., 2011a; Montoya-Pino et al., 2010). However, the current calibration is based on a limited number of observations and do not include detailed observations within the water column. The aim of this study is to provide the first comprehensive investigation of iron and uranium isotope fractionation in the Black Sea water column and sediments which will inform the application of the uranium and iron isotope paleo redox proxies. Furthermore, as the analysis of seawater iron isotope composition is very analytically challenging with only a handful of capable laboratories around the world, method

development was an essential prerequisite to collecting the iron isotope data presented in this thesis.

1.3 Basic oceanographic properties of the Mediterranean and Black Seas

1.3.1 Mediterranean Sea

The Mediterranean Sea is a semi-enclosed concentration basin (i.e. evaporation exceeds precipitation and river runoff) connected to the Atlantic Ocean by the Strait of Gibraltar and to the Black Sea via the Dardanelles/Marmara Sea/Bosphorus system. It is one of the most heavily impacted marine basins in the world in terms of atmospheric deposition from natural and anthropogenic sources due to its proximity to the Sahara Desert and Europe, respectively (Guerzoni *et al.*, 1999). Thus, the Mediterranean Sea is an important marine system for investigating the effects of atmospheric deposition and anthropogenic contamination on the marine biogeochemistry of trace metals. Additionally, the Mediterranean Sea has active deep overturning circulation cells that are analogous to polar Atlantic deep convection cells and this overturning may be sensitive to climatic changes (Font *et al.*, 2013). For these reasons, and because of its relatively small size and ease of accessibility to all areas of the basin, the Mediterranean Sea is considered to be an ideal natural laboratory for oceanographic research that is applicable on both a regional and global scale (Bergamasco and Malanotte-Rizzoli, 2010).

1.3.2 Black Sea

The Black Sea is a large inland marine basin in Eastern Europe. Seawater exchange is limited to the Bosporus Strait and freshwater enters the basin primary in the form of rivers, such as the Danube. The hydrologic balance results a classic 2-layer density stratified system with relatively fresh surface water (salinity ~18-18.5) overlying more saline (salinity ~22-22.5) deep water (Murray *et al.*, 1991). Consequentially, vertical mixing is extremely limited which allows for the development of anoxic conditions in deep waters, making the Black Sea the world's largest anoxic basin. As such, the Black Sea represents the reducing end member of the spectrum of oceanic redox environments. The classic progression of redox reactions associated with the microbial oxidation of organic matter occurring in marine sediments worldwide

(Froelich *et al.*, 1979), is persevered in the water column of the Black Sea across a depth range of tens of meters thick (Murray *et al.*, 1991). This makes it possible to collect high resolution samples across the redox gradients, which is not feasible in sediments because the entire redox sequence occurs over distances of centimeters. Thus, the Black Sea is an ideal natural laboratory to investigate the effects of biotic and abiotic reduction and oxidation reactions and redox cycling of sulfur on the behavior and distributions of trace metals and their isotopes.

1.4 Objectives

1.4.1 GEOTRACES

The research presented in this thesis was conducted in the context of the GEOTRACES program (www.geotraces.org). The GEOTRACES program is "An International Study of the Marine Biogeochemical Cycles of Trace Elements and Their Isotopes". The goal of the program is conduct coordinated research that utilizes recent advances in clean sampling techniques and analytical methods to map the distributions of trace elements and their isotopes in the world's oceans. The program was initiated in the mid-2000s as the international community of marine biogeochemists agreed global coverage of trace metal distributions were needed to better understand how trace metal concentrations influence marine ecosystems, to constrain global climate models that include marine biogeochemistry, to better develop paleoceanographic proxies, and to characterize the baseline distributions of trace elements and their isotopes before anthropogenic contamination perturbs their natural distributions (GEOTRACES, 2007). In the Mediterranean and Black Seas there is an incomplete understanding of the biogeochemistry of trace metals and their isotopes because high quality data sets are generally very spatially limited in their scope. Thus, the objective of the GEOTRACES expedition in the Mediterranean and Black Seas was to provide unprecedented spatial coverage of the distributions of trace elements and their isotopes in these oceanographically unique marine basins.

1.4.2 Biogeochemical cycling of trace metals in the Mediterranean Sea

Distributions of trace metals in the Mediterranean Sea have been investigated intensely in previous decades primarily due to the recognition of the potential for trace

metal contamination due to anthropogenic activities in the region. Elevated concentrations of trace metals with known anthropogenic sources to the environment, such as lead (Pb), cadmium (Cd) and zinc (Zn), have been observed in the water column (*e.g.* Boyle *et al.*, 1985; Migon and Nicolas, 1998; Morley *et al.*, 1997; Statham *et al.*, 1985; van Geen *et al.*, 1988, 1991), marine sediments (*e.g.* Azoury *et al.*, 2013; Castillo *et al.*, 2013; Cossa *et al.*, 2014; Elbaz-Poulichet *et al.*, 2011; Martin *et al.*, 2009; Miralles *et al.*, 2006) and marine organisms (*e.g.* Benedicto *et al.*, 2011; Copat *et al.*, 2012; Yilmaz, 2003) at different locations in the Mediterranean Sea. These observations indicate that anthropogenic activities significantly impact the trace metal fluxes to coastal zones of the Mediterranean Sea. To date, there is a paucity of high-quality data available covering the full basin-scale distribution of dissolved trace metals in the Mediterranean Sea, which hinders our ability to understand the true scale of pollution in this vital marine basin. An objective of this study is to examine the basin-scale distribution of dissolved Cd, Zn and Pb to better understand how the distributions of these metals are influenced by anthropogenic activities on a large scale.

The concentration of dissolved aluminum (Al) in the Mediterranean Sea is the highest of any marine basin (up to ~175 nM in the deep basin) and strong correlations between dissolved Al and silicic acid (Si) have been observed (Caschetto and Wollast, 1979; Chou and Wollast, 1997; Hydes et al, 1988; Mackenzie *et al.*, 1978). The coupled relationship between dissolved Al and Si in the Mediterranean Sea is not fully understood. Given that Si is biologically essential to diatoms, the covariation between these two elements suggests a biological control on the distribution of dissolved Al, although Al has no known biological function (Mackenzie *et al.*, 1978). An objective of this study is to investigate the distribution of dissolved Al in the Mediterranean Sea to better understand the processes controlling its high concentration and its enigmatic relationship with Si.

1.4.3 Redox controls on trace metals and their isotopes in the Black Sea

Redox chemistry is an especially crucial component of the biogeochemical cycles of many elements. As such, the abundance and isotopic composition of redox sensitive trace metals recorded in marine sediments provide information about the redox conditions of the oceans during the time of sediment deposition. The records of redox sensitive trace metals in marine sediments indicate that the Earth's ocean-atmosphere system has undergone significant changes its prevailing redox state

throughout Earth's history. The evolution of ocean redox chemistry through Earth's history is important for understanding how the evolution of Earth's early atmosphere influenced the evolution of complex life (Anbar and Knoll, 2002). The Black Sea is an important natural laboratory for understanding how variable redox conditions in the oceans affect the behavior of trace metals and their isotopes.

An objective of this thesis is to obtain high quality and high resolution data on the distributions of trace elements and their isotopes across the vertical redox zonation present in the water column of the Black Sea. The isotope systems of iron and uranium are specifically targeted. Iron isotope fractionation associated with oxidation reactions and pyrite formation in the water column of the Black Sea is investigated with the aim to provide a framework for which the iron isotope composition of Precambrian pyrites can be interpreted. Similarly, uranium isotope fractionation is investigated in the Black Sea water column and sediments with the aim of providing a modern calibration of the magnitude of the uranium isotope fractionation factor associated with the reduction of U(VI) to U(IV) in anoxic marine environments.

1.5 Chapter outline

This thesis organized into seven chapters. Chapters 2, 3, 4, 5, and 6 are organized in a format which is suitable for publication. Therefore, there may be slight repetition between some of the chapters. Notably, the description of the methods used for collecting seawater samples are similar in all chapters, the maps illustrating the sampling locations in the Mediterranean Sea are similar between Chapters 2 and 3 and the maps illustrating the sampling locations are similar between Chapters 4, 5 and 6.

Chapter 2 reports the zonal distribution of dissolved Al in the Mediterranean Sea. The impacts of atmospheric deposition and water circulation on the dissolved Al distribution are discussed in detail and an explanation is provided for the enigmatic relationship between dissolved Al and Si in the Mediterranean Sea. This chapter is based on the publication "J.M. Rolison, R. Middag, C.H. Stirling, M.J.A. Rijkenberg, and H.J.W. de Baar, 2015, Zonal distribution of dissolved aluminium in the Mediterranean Sea, *Marine Chemistry* 177, 87-100." My contribution to this publication includes participation in cruises 64PE370 and 64PE374, sample analysis, data interpretation and writing of the manuscript. R. Middag participated in cruise

64PE370, provided the analytical methods used and helped with the data collection. R. Middag, C.H. Stirling, M.J.A. Rijkenberg and H.J.W. de Baar provided financial support, assisted with the interpretation of the data and commented on the manuscript.

Chapter 3 describes the zonal distributions of dissolved Fe, Zn, Cd, and Pb in the Mediterranean Sea. The distributions of dissolved Zn, Cd, and Pb are discussed in terms of the potential effects of anthropogenic contamination, while Fe serves as an example of an element whose distribution is dominated by natural processes. This chapter is to be submitted for publication as "J.M. Rolison, R. Middag, C.H. Stirling, and M.J.A. Rijkenberg, Basin-scale distributions of anthropogenic dissolved trace metals in the Mediterranean Sea, *Marine Chemistry*." My contribution to this chapter includes participation in cruises 64PE370 and 64PE374, leading the data collection on cruise 64PE374, analysis, data interpretation and writing of the manuscript. R. Middag provided the analytical methods used, participated in cruise 64PE370, led the data collection on cruise 64PE370, and assisted in the sample analysis. R. Middag, C.H. Stirling, and M.J.A. Rijkenberg provided financial support, assisted with the interpretation of the data and commented on the manuscript.

Chapter 4 provides a description of the vertical profiles of dissolved Al, Ti, Mn, Fe, Cu, Zn, Ga, Y, Zr, Cd, and La in the water column of the Black Sea. The distributions of Mn, Fe, Cu, Zn, Cd and La are compared to previous reports on these elements in the Black Sea, while this represents the first data generated for the distributions of dissolved Al, Ti, Ga, Zr, and Y in the water column of the Black Sea. The effects of processing including redox cycling, metal sulfide formation, and scavenging on the distributions of the elements are discussed. This chapter is to be submitted for publication as "J.M. Rolison, R. Middag, C.H. Stirling, and M.J.A. Rijkenberg, Behavior of lithogenic and redox sensitive trace metals across the redox gradient in the Black Sea water column, *Deep-Sea Research*." My contribution to this chapter includes participation in cruise 64PE373, leading the data collection on cruise 64PE373, analysis, data interpretation and writing of the manuscript. R. Middag provided the analytical methods used and assisted in the sample analysis. R. Middag, C.H. Stirling, and M.J.A. Rijkenberg provided financial support, assisted with the interpretation of the data and commented on the manuscript.

Chapter 5 presents a new method for the analysis of Fe isotopes in seawater and the application of the method to the water column of the Black Sea. Iron isotope fractionation factors are modelled for water column pyrite formation in the deep basin and for oxidation reactions occurring in the upper water column. The implications of these isotope fractionation factors are discussed in terms of how the Fe isotope paleoredox proxy is applied. This chapter is to be submitted for publication as "J.M. Rolison, C.H. Stirling, R. Middag, M. Gault-Ringold, E. George, and M.J.A. Rijkenberg, Iron isotope fractionation during pyrite formation in a sulfidic Precambrian ocean, *Science*." My contribution to this chapter includes participation in cruise 64PE373, sample collection, method development, sample analysis, data interpretation and writing of the manuscript. C.H. Stirling helped design the research. M. Gault-Ringold and E. George assisted in method development and sample processing. C.H. Stirling, R. Middag, and M.J.A. Rijkenberg provided financial support, and all co-authors assisted with the interpretation of the data and commented on the manuscript.

Chapter 6 examines the behavior of U isotopes in the water column and sediments of the Black Sea. The U isotope fractionation factor during reduction of U(VI) to U(IV) is modelled from the water column data. The implications of these finding in terms of using U isotopes as paleoredox tracer are discussed. This chapter is to be submitted for publication as "J.M. Rolison, C.H. Stirling, R. Middag, and M.J.A. Rijkenberg, Uranium stable isotope fractionation in the Black Sea: Modern calibration of the $^{238}U/^{235}U$ paleo-redox proxy, *Geochimica et Cosmochimica Acta*." My contribution to this chapter includes participation in cruise 64PE373, sample collection, sample analysis, data interpretation and writing of the manuscript. C.H. Stirling helped design the research. C.H. Stirling, R. Middag, and M.J.A. Rijkenberg provided financial support, assisted with interpretation of the data and commented on the manuscript.

Chapter 7 summarizes the major findings from this research and discusses how the initial objectives were achieved. Recommendations for future work are also discussed.

CHAPTER 2

ZONAL DISTRIBUTION OF DISSOLVED ALUMINIUM IN THE MEDITERRANEAN SEA

2.1 Abstract

Dissolved aluminium (Al) is an important tracer of atmospheric dust input to the oceans. The GEOTRACES expedition to the highly dust impacted Mediterranean Sea afforded the opportunity to study the distribution of dissolved Al in the Mediterranean Sea in detail. Interestingly, the elevated concentration of dissolved Al observed in Mediterranean surface waters (up to 80 nmol kg^{-1}) is strongly correlated with salinity, both showing an increase from west to east due to mixing of low Al, low salinity Atlantic surface waters with high Al, high salinity Mediterranean surface and intermediate waters. At intermediate depths (100 to 1250 m), a strong correlation between dissolved Al and silicic acid (Si) was observed. Vertical mixing between surface, intermediate and old uplifted deep water between depths of 0 to 1300 m is primarily responsible for the long recognized Al:Si relationship at intermediate depths. However, since the subsurface waters have a surface water origin, vertical transport of Al and Si is required to maintain the high concentrations of dissolved Al and Si in Mediterranean deep waters relative to surface waters. The most likely vertical transport mechanism is suggested to be biogenic particles which would thus be ultimately responsible for the Al:Si relationship at intermediate depths. Elevated concentrations of dissolved Al relative to Si were observed in some Mediterranean deep waters with sediment resuspension during episodes of deep water formation as the most likely source of the additional dissolved aluminium.

2.2 Introduction

Atmospheric dust deposition is an important source of biologically essential trace nutrients (*e.g.* iron) and major nutrients (*e.g.* nitrate, phosphate, silicate) to the surface ocean and may therefore strongly impact biologically driven processes in the open ocean (Baker *et al.*, 2010; Rijkenberg *et al.*, 2012). For instance, primary

productivity in high-nutrient low-chlorophyll (HNLC) regions, which account for ~30% of the world's ocean, is limited by the availability of dissolved iron (de Baar *et al.*, 1990; Martin and Fitzwater, 1988; Moore *et al.*, 2013). The global pattern of atmospheric dust deposition is therefore a crucial component in models of global biogeochemical cycles (*e.g.* global carbon cycle), which in turn, has a direct bearing on constraining future climate scenarios. Due to logistical challenges associated with monitoring long term open ocean atmospheric deposition, direct measurements of atmospheric deposition to the open ocean are very limited (Duce *et al.*, 1991; Luo *et al.*, 2003). More efficient methods are required for constraining atmospheric deposition in the open ocean, and as a result the concentration of dissolved aluminium in surface waters has been developed as a tracer of atmospheric deposition to the surface of the open ocean (Gehlen *et al.*, 2003; Han *et al.*, 2008; Measures and Vink, 2000).

Dissolved aluminium (hereafter referred to as dAl) occurs at low nanomolar (nM) concentrations in the world oceans, yet it is the third most abundant element in Earth's upper continental crust (~8.2% by weight) (Taylor, 1964). The low concentration of dAl in the oceans is the result of multiple biogeochemical processes. Specifically, although rivers contain high concentrations of dAl and were therefore initially suggested to be an important source of dAl, it is now understood that riverine inputs of dAl to the open ocean are negligible due to estuarine removal processes (Mackin and Aller, 1984; Maring and Duce, 1987; Tria *et al.*, 2007 and references therein). Likewise, only relatively minor fluxes of dAl from hydrothermal vents have been observed (Hydes *et al.*, 1986; Middag et al, 2011) although from recent observations by Measures *et al.* (2014) it has been suggested that the Trans-Atlantic Geotraverse hydrothermal field on the Mid Atlantic Ridge might, or might not, be a source of dAl to local deep waters in the North Atlantic (also see Middag *et al.*, 2015). Furthermore, sediment resuspension has recently been documented as an important source of dAl to North Atlantic Deep Water (NADW) near its formation site (Middag *et al.*, 2015; van Hulten *et al.*, 2014). However, it has been demonstrated that atmospheric deposition is by far the primary source of dAl to the surface of the open ocean (*e.g.* Kramer *et al.*, 2004; Maring and Duce, 1987; Measures *et al.*, 2005; Orians and Bruland; 1986).

Atmospheric dust is predominantly sourced from arid regions around the world and therefore atmospheric dust deposition is expected to be strongest down-wind from these

regions. Small dust particles (ca. <5 μm) are most susceptible to long-range transport and thus account for the majority of dust deposition to the surface of the open ocean (Mahowald *et al.*, 2005). The dissolution of Al from dust particles in the surface ocean is not complete, with only 1 to 15% of the Al dissolving, while the rest remains in the particulate phase with perhaps an additional small fraction dissolving deeper in the water column as it sinks (Maring and Duce, 1987; Measures *et al.*, 2010). Elevated concentrations of dAl (>30 nM) in surface waters of the subtropical North Atlantic Ocean are attributed to the accumulative effect of atmospheric dust deposition (Bruland and Lohan, 2003; Hydes, 1983; Measures et al; 2014; Orians and Bruland; 1985; Rijkenberg *et al.*, 2012). In contrast, surface waters in regions with low atmospheric dust deposition, such as the Arctic and Southern Oceans, are characterized by low sub-nanomolar concentrations of dAl (*e.g.* Middag *et al.*, 2009, 2011).

The speciation of dAl in seawater is dominated by highly particle-reactive hydrolysed species (Turner *et al.*, 1981; Yuan-Hui, 1991) which can result in the rapid removal of dAl from surface waters via inorganic adsorption of dAl to the surfaces of sinking particles (*i.e.* scavenging) (Hydes, 1983; Moran and Mooore, 1988; Orians and Bruland, 1985). Removal of dAl from surface waters may also occur via biological uptake which has been inferred from nutrient-like vertical profiles of dAl in the Mediterranean Sea (Caschetto and Wollast, 1979; Chou and Wollast, 1997; Hydes et al, 1988; Mackenzie *et al.*, 1978) and recently in the Arctic Ocean (Middag *et al.*, 2009). Furthermore, Li *et al.* (2013) observed a high proportion of intracellular Al relative to extracellular Al in diatom cells, which led the authors to conclude that biological uptake was the dominant pathway for removing dAl from surface waters during a phytoplankton bloom in the southern Yellow Sea. Interestingly, aluminium is structurally incorporated in diatomaceous biogenic silica (Gehlen *et al.*, 2002), yet aluminium is not considered to be a biologically essential nutrient.

The first vertical profiles of dAl produced for the open ocean displayed a surface maximum, a mid-depth minimum and increasing concentrations with depth below 1000 m, thus suggesting that the distribution of dAl in the open ocean is controlled by atmospheric deposition at the surface, scavenging at mid-depths and dissolution of biogenic particles or a pore water source at depth (Hydes, 1979; Orians and Bruland, 1985). However, it is well documented that the distribution of dAl in the Mediterranean Sea, a confined marine basin, is remarkably different from that in the open ocean. Specifically, the highest dAl concentrations of any marine basin (up to 174

nM in deep waters) and strong correlations between dAl and silicic acid (Si) have been observed in the Mediterranean Sea (Caschetto and Wollast, 1979; Chou and Wollast, 1997; Hydes et al, 1988; Mackenzie *et al.*, 1978). Chou and Wollast (1997) thoroughly examined the sources of dAl to the western Mediterranean basin and concluded that atmospheric deposition is the largest external source of dAl and is responsible for maintaining such high concentrations of dAl. The coupled relationship between dAl and Si in the Mediterranean Sea is not fully understood. Given that Si is biologically essential to diatoms, the covariation between these two elements suggests a biological control on the distribution of dAl (Chou and Wollast, 1997; Mackenzie *et al.*, 1978).

The Mediterranean Sea is heavily impacted by atmospheric deposition from natural and anthropogenic sources due to its proximity to the Sahara Desert and Europe, respectively, and it is thus an important region for studying the effects of atmospheric deposition on the marine biogeochemical cycles of the elements. Additionally, the Mediterranean Sea has active deep overturning circulation cells that are analogous to polar Atlantic deep convection cells and this overturning may be sensitive to climatic changes (Font *et al.*, 2013). For these reasons, and because of its relatively small size and ease of accessibility to all areas of the basin, the Mediterranean Sea is considered to be an ideal natural laboratory for oceanographic research relevant on both a regional and global scale (Bergamasco and Malanotte-Rizzoli, 2010).

Here we present the distribution of dAl over the full water column during an uninterrupted zonal transect of the Mediterranean Sea. We demonstrate how mixing of different water masses is the primary control on many of the features in the distribution of dAl, while dust deposition is ultimately responsible for the high concentration of dAl. The roles of other processes, such as sediment resuspension and biology, in controlling the distribution of dAl are also discussed.

2.3 Methods

2.3.1 Study area

Samples were collected during GEOTRACES cruises 64PE370 (Lisbon-Istanbul; hereafter referred to as Leg 1) and 64PE374 (Istanbul-Lisbon; hereafter referred to as Leg 2) in the Mediterranean Sea aboard RV Pelagia during May-June 2013 and July-August 2013, respectively. In total, 56 stations were occupied (Fig. 2.1).

All stations were sampled for dAl with the exception of stations 1.25 and 1.37 during Leg 1 and station 2.16 during Leg 2. Leg 1 followed a west to east transect from the Atlantic Ocean to the eastern Mediterranean basin before turning north, and passing through the Aegean Sea (Fig. 2.1). Specifically, stations 1.1-1.4 were in the Atlantic Ocean, stations 1.5-1.12 were in the western Mediterranean basin, stations 1.13-1.15 were across the relatively shallow Channel of Sicily with bottom depths shallower than 1000 m (sill depth ~300 m), and stations 1.16-1.28 were in the eastern Mediterranean basin with station 1.23 being the most eastward. Stations 1.29-1.37 were in the Aegean Sea and the Sea of Marmara. Leg 2 generally followed an east to west transect beginning in the southern Aegean Sea and ending in the western Mediterranean basin. Specifically, station 2.1 was located in the southernmost region of the Aegean Sea, just to the north of the isle of Crete. Stations 2.2-2.11 were in the eastern Mediterranean basin and southern Adriatic Sea, stations 2.12-2.15 were in the Tyrrhenian basin, and stations 2.16-2.19 were in the western Mediterranean basin.

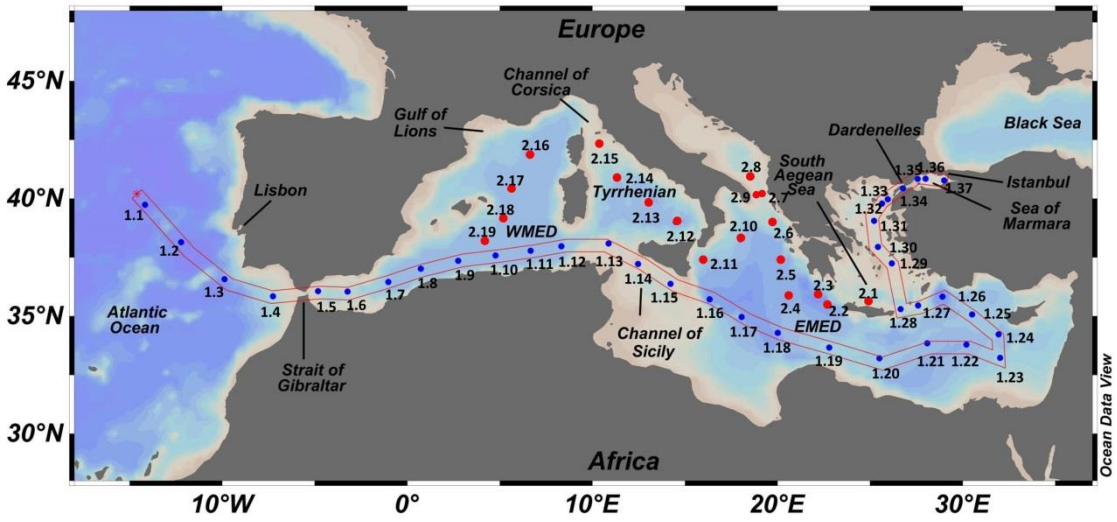

Fig. 2.1. Map of the sampling stations occupied during the GEOTRACES Mediterranean cruises 64PE370 (blue circles) in May-June 2013 and 64PE374 (red circles) in July-August 2013. The red outline indicates the cruise track followed during 64PE370. The remaining stations were occupied during 64PE374 and were sampled following an east to west cruise track. The acronyms WMED and EMED imply the western Mediterranean basin and eastern Mediterranean basin, respectively. This figure was made using Ocean Data View (Schlitzer, 2013).

2.3.2 Sample collection

Samples were collected using an ultraclean all-titanium framed TITAN CTD sampling system (de Baar *et al.*, 2008) outfitted with 24x24 L novel PRISTINE sample bottles constructed from ultrapure polyvinylidene fluoride (PVDF) and titanium (Rijkenberg *et al.*, 2015). Immediately upon recovery, the TITAN system was placed inside a purpose-built class 100 clean room container (de Baar et al, 2008). Inside the clean room container, seawater was filtered directly from the PRISTINE samplers using 0.2 µm filter cartridges (Sartobran-300, Sartorius) under nitrogen pressure (1.5 atm) and collected in acid-cleaned 60 mL low density polyethylene (LDPE) bottles with polypropylene (PP) caps (Nalgene^{TM}, Fisher Scientific). All LDPE sample bottles were cleaned following procedures outlined in Middag *et al.* (2009). Sample bottles were rinsed 5 times with sample seawater prior to sample collection. As a precaution against potential contamination from the PP caps, seawater samples were acidified to 0.024 M HCl using ultra-high purity 12 M HCl (Seastar^{TM} Baseline®) approximately 1-2 hours before analysis and kept in an upright position to minimize contact between the samples and PP caps (Sampling and Sample-Handling Protocols for GEOTRACES Cruises, www.geotraces.org).

Unfiltered seawater samples were collected for analysis of major nutrients in high density polyethylene (HDPE) bottles that were rinsed three times with sample water and then stored in the dark at 4 ˚C until analyzed within 8-12 hours.

2.3.3 Analytical reagents

All reagents were prepared with high-purity de-ionized water (R > 18.2 MΩ cm; Millipore Milli-Q, MQ water). A 0.10 M HCl solution was prepared using Suprapure® HCl (Merck). High-purity sub-boiled quartz distilled glacial acetic acid (Q-HAc) was produced by a single distillation of reagent grade glacial acetic acid. Ultraclean ammonium hydroxide (NH_4OH) was prepared by bubbling filtered anhydrous ammonia gas into MQ water. Ammonium acetate (NH_4Ac) crystals were prepared by bubbling filtered anhydrous ammonium gas in to Q-HAc and then slowly cooling the solution. A saturated NH_4Ac solution was prepared by adding MQ water to the NH_4Ac crystals. A 2 M NH_4Ac sample buffer and a 4 M NH_4Ac reaction buffer were prepared by dilution of the saturated NH_4Ac solution with MQ water. The sample buffer and reaction buffer were adjusted to a pH of 8.85 ± 0.05 and 6.45 ± 0.05, respectively, with NH_4OH. Prior

to each run, the fluorimetric compound lumogallion was added to a fresh aliquot of reaction buffer to obtain a 4.8 mM lumogallion solution. A 5% (v/v) detergent (Brij-35; Merck) solution was prepared by diluting concentrated Brij-35 with MQ water.

2.3.4 Analysis of dissolved Al

Dissolved Al in seawater samples was measured shipboard using a flow injection analysis (FIA) system (Brown and Bruland, 2008; Middag *et al.*, 2009) and is briefly summarized here. Samples were acidified to a pH of ~1.8 (0.024 M HCl) at least 1 h before analysis. Samples were introduced to the FIA system via an autosampler (CETAC ASX-260). The samples were buffered inline to a pH of 5.5 ± 0.1 with the sample buffer. The buffered sample was pre-concentrated on a column packed with Toyopearl AF-Chelate 650 M resin (TosoHaas, Germany). Samples from the Atlantic Ocean, with low concentrations of dAl, were preconcentrated for 150 s, while samples from the Mediterranean Sea, with higher concentrations of dAl, were pre-concentrated for 60 s. Following preconcentration, the column was rinsed for 60 s with MQ water to remove residual salts. The Al was subsequently eluted from the column with 0.10 M HCl and mixed with the reaction buffer containing the lumogallion (reaction pH of 5.4 ± 0.1) resulting in an Al-lumogallion chelate complex which was detected by its fluorescence. The chelation reaction continued along a 10 m reaction coil submerged in a water bath at 50 ˚C. Thereafter the 5% Brij-35 solution was mixed in to the solution along a 3 m length mixing coil to increase the sensitivity (Resing and Measures, 1994). The emission of the fluorescent complex was then detected by a FIA-lab PMT-LF detector with a 510-580 nm emission filter and a 480-490 nm excitation filter. Concentrations of dAl were calculated in units of nanomol L^{-1} (nM) from the peak heights and then converted to nmol kg^{-1} based on the density of seawater which was determined for each sample based on the measured salinity of the sample and a laboratory temperature of 20°C using the international one-atmosphere equation of state of seawater (Millero and Poisson, 1981).

2.3.5 Calibration and verification

The FIA system was calibrated each run using standard additions from a 1000 mg/L Al ICP stock standard to filtered acidified seawater with low Al concentration that was collected in the Atlantic Ocean. Each run consisted of a five point calibration, MQ water blank (also acidified to 0.024 M HCl), reference sample, and analysis of

approx. 24 samples collected from a single station. Stations with fewer than 24 samples were combined to make a full run. Each sample, blank, or standard was run in triplicate (three peak heights) and the average of the triplicate measurement is used as the final result. The standard deviation of the triplicate measurement was used to assess the precision of the measurement. The FIA system was calibrated to dAl concentrations up to 45 nM during analysis of samples collected from the Atlantic Ocean and up to 160 nM Al during analysis of samples collected from the Mediterranean Sea. The FIA system was rinsed regularly between runs with 0.1 M HCl. The dAl content of the MQ water blank was 0.5 ± 0.2 nM (1 SD; n= 50).

The accuracy and precision of the method was evaluated through the repeat analysis of reference samples. Every run included a triplicate analysis of an in-house reference sample. This was a sub-sample of a 25 L volume of filtered Mediterranean Outflow Water collected at the beginning of the cruise in the Atlantic Ocean off the coast of Portugal. The average concentration of dAl in the in-house reference sample during Leg 1 was 32.7 ± 0.9 nM (1 SD; n=29) and during Leg 2 was 34.2 ± 0.9 nM (1 SD; n=16). The increase in dAl in the in-house reference sample between Leg 1 and Leg 2 is likely an artefact of storage, as there was approximately one month between the end of Leg 1 and the start of Leg 2. Furthermore, a slight increasing trend in the concentration of dAl in the in-house reference sample was observed during Leg 1, which further supports the view that the 25L carboy used for the storage of the in-house reference sample may have been slowly releasing dAl. The internal reference sample was not used in the calculation of the final concentration of dAl in the samples and therefore has no influence on the results. The relative standard deviation of triplicate measurements of the in-house reference sample on single days was on average 1.9%. Furthermore, the GEOTRACES GS reference sample (GS-145) was analyzed in triplicate on six separate occasions. The average concentration of dAl in GS-145 was 27.4 ± 0.3 nmol kg^{-1} (1SD; n=6) which agrees with the consensus value of 27.5 ± 0.2 nmol kg^{-1} (GEOTRACES Consensus Values, May 2013; www.geotraces.org).

2.3.6 Additional analyses

A Seabird SBE 911+ CTD system was used to measure the conductivity (salinity), temperature, and pressure (depth) *in situ* at each sampling station. The temperature sensor was calibrated using a high-accuracy reference-thermometer

(Seabird SBE35), while the conductivity sensor was calibrated against shipboard salinity measurements of seawater samples.

Measurements of the inorganic major nutrients nitrate (NO_3), nitrite (NO_2), phosphate (PO_4) and silicic acid ($Si(OH)_4$; abbreviated as Si) followed the colorimetric procedures of Grasshoff *et al.* (1983). Nutrient samples were stored at 4 °C after collection and were analyzed within 18 hours on a Seal Analytical QuAAtro autoanalyzer. Accuracy and precision of the nutrient measurements was assessed every run by measuring an in-house mixed nutrient standard (containing NO_3, PO_4, and Si) and the Reference Material for Nutrients in Seawater (RMNS; lot BU) supplied by KANSO in Japan. The reproducibility of the mixed nutrient standard was better than 1% for NO_3, PO_4, and Si and the concentrations of NO_3, NO_2, PO_4 and Si measured in the RMNS were in agreement with the consensus values.

All data referred to in this study is included in the online Supplementary Data File and will be submitted to the GEOTRACES International Data Assembly Centre (www.bodc.ac.uk/geotraces).

2.4 Results

2.4.1 General Hydrography of the Mediterranean Sea

The Mediterranean Sea is a semi-enclosed concentration basin (*i.e.* evaporation exceeds precipitation and river runoff) connected to the Atlantic Ocean by the Strait of Gibraltar and to the Black Sea via the Dardanelles/Marmara Sea/Bosphorus system (Fig. 2.1). The western (WMED) and eastern (EMED) Mediterranean sub-basins are connected by the Channel of Sicily. The evaporative loss of water in the Mediterranean Sea is balanced by inflowing Atlantic Water (AW) through the Strait of Gibraltar, which can be identified as low salinity surface water flowing from the Strait of Gibraltar along the North African coast towards the EMED (Fig. 2.2a). The general basin scale circulation of AW forms along-slope anti-clockwise gyres in both the WMED and EMED (Millot and Taupier-Letage, 2005). Mesoscale gyres and eddies, which exhibit high spatial and temporal variability, can significantly alter the general cyclonic flow path of AW by forcing AW to move further offshore towards the central parts of the basins (Millot and Taupier-Letage, 2005). Before exiting the WMED, a portion of the inflowing AW splits from the main flow path and turns north flowing

along the western coast of Sardinia and Corsica (the west-Corsica vein). The remaining inflowing AW bifurcates at the Channel of Sicily in to two veins with one flowing in to the Tyrrhenian and one flowing in to the EMED (Millot and Taupier-Letage, 2005). The Tyrrhenian vein traverses the western coast of Sicily and Italy before entering the Channel of Corsica where it re-joins the west-Corsica vein, thereby forming the northern flow of the WMED gyre which continues along slope towards the Gulf of Lions (Millot and Taupier-Letage, 2005). In the EMED, inflowing AW generally flows in an eastward direction along the north African coast before turning northwards near the eastern boundary of the EMED. After turning north, inflowing AW then enters the southern reaches of Aegean Sea and then the Adriatic Sea. The salinity of AW progressively increases as it circulates through the Mediterranean Sea due to strong evaporation and mixing with surrounding surface and underlying intermediate Mediterranean waters.

The final transformation of AW into dense intermediate and deep Mediterranean waters occurs during strong wintertime cooling and further evaporation. Levantine Intermediate Water (LIW) is the most abundant water mass formed in the Mediterranean Sea and is very saline with a salinity ≥39 (Lascaratos, 1993). It is formed in the area south-southeast of the isle of Rhodes in the EMED (Millot and Taupier-Letage, 2005). After formation, LIW spreads through the entirety of the EMED and the WMED at intermediate depths generally following a basin scale cyclonic circulation pattern and can be identified as a subsurface salinity maximum at a depth range between 200 and 600 m (Fig. 2.2a). Furthermore, LIW has been identified as a major component of Mediterranean Outflow Water (MOW), which exits the Mediterranean Sea through the Strait of Gibraltar (Baringer and Price, 1997; Millot *et al.*, 2006) (Fig. 2.2b). Additional intermediate water masses may be formed together with denser waters at deep water formation sites in the EMED and WMED, although in much smaller volumes than LIW (Millot and Taupier-Letage, 2005). However, these other intermediate water masses are not easily distinguishable from pre-existing water masses due to their small volumes and therefore they are not considered further.

Deep water formation occurs in the northern regions of the Mediterranean Sea that experience intensely cold and dry continental northerly winds and are characterized by strong cyclonic circulation (Skliris, 2014). Salt preconditioning of intermediate and surface waters by very saline LIW also aids in the formation of Mediterranean deep waters in both the EMED and WMED (Skliris and Lascaratos, 2004). Deep water in the

EMED is a mixture of multiple water masses that have formed at different times and locations within the EMED (Fig. 2.2b) (Robinson et al, 2001). Adriatic Deep Water (AdDW) is the primary source of deep water in the EMED and is formed in the cyclonic gyre in the southern Adriatic Sea (Millot and Taupier-Letage, 2005; Skliris, 2014). Aegean Deep Water (AeDW) is a secondary source of deep water in the EMED and is formed in the southern Aegean Sea (Millot and Taupier-Letage, 2005; Skliris, 2014). During the "Eastern Mediterranean Transient" (EMT) event of the mid-1990s, AeDW became the main source of deep water in the EMED (Klein *et al.*, 1999; Lascaratos *et al.*, 1999). The newly formed AeDW was warmer, saltier, and denser than the old AdDW, which had previously filled most of the deep EMED basin. It is estimated that the old AdDW was uplifted by about 500 m (Roether *et al.*, 2007). Old uplifted deep water is clearly visible in Fig. 2.2b as the water mass between LIW and AeDW. About 75% of the total AeDW was delivered during the peak EMT between 1992 and 1994, with only 20% of the total being delivered between 1994 and 2002 (Roether *et al.*, 2007). AdDW has since returned as the dominant source of deep water in the EMED, although the EMT is an ongoing process that is still affecting the thermohaline circulation and hydrological properties of the Mediterranean Sea (Roether *et al.*, 2007). Based on thermohaline characteristics, the more saline (>38.75) water mass occupying the eastern portion of the deep EMED in Fig. 2.2b is identified as AeDW while the less saline (<38.75) water mass occupying the western part of the deep EMED is identified as AdDW. Both AdDW and AeDW form in relatively enclosed, shallow subbasins and then cascade down slope from their formation sites until reaching resident deep water with similar densities. They then circulate along slope, and in general tend to follow a basin scale cyclonic gyre. Deep waters formed each winter compete to fill the deepest parts of the EMED and therefore the upper deep waters (*i.e.* less dense) must outflow from the EMED through the Channel of Sicily and enter the WMED and Tyrrhenian basin.

Western Mediterranean deep water (WMDW) is relatively homogeneous compared to deep water in the EMED. The primary formation area of WMDW is in the Gulf of Lions during strong northerly winter winds and its thermohaline characteristics are strongly influenced by the characteristics of LIW and AW reaching the formation site. During 2004-2006, WMDW formation rates were exceptional high which resulted in the warming and salinification of the bottom layer (Schröeder *et al.*, 2006).

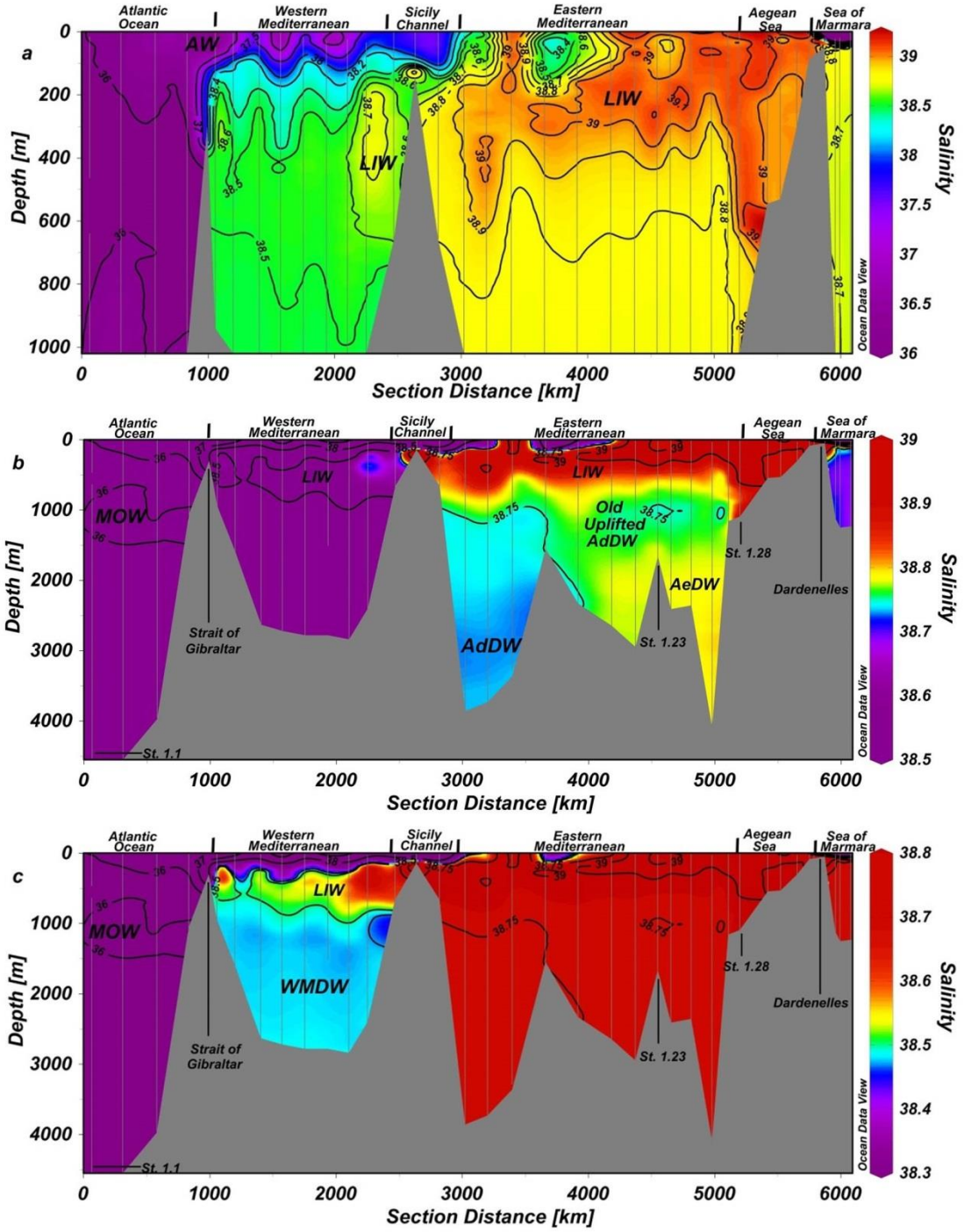

Fig. 2.2. (a) Cross-section plot of salinity of surface waters in the Atlantic Ocean and Mediterranean Sea at stations 1-37 occupied during 64PE370. (b) Cross-section plot of salinity over the full water column at stations 1-37 occupied during 64PE370 with the color bar scale optimized for visualization of the salinity differences in the deep eastern Mediterranean basin. (c) Same as (b) but the color bar scale is optimized for the visualization of the salinity differences in the deep western Mediterranean basin. Note the different scales for salinity. Contour lines represent isohalines. AdDW, Adriatic Deep Water; AeDW, Aegean Deep water; LIW, Levantine Intermediate Water; MOW, Mediterranean Outflow Water; WMDW, Western Mediterranean Deep Water.

2.4.2 Vertical profiles of dAl in the Atlantic Ocean and Mediterranean Sea

All measurements of dAl in the Atlantic Ocean and Mediterranean Sea from Leg 1 and Leg 2 are presented in Fig. 2.3 supported by measurements of salinity and Si (for clarity, data from the Aegean Sea and Sea of Marmara was omitted from Fig. 2.3). In the Atlantic Ocean, dAl concentrations in surface waters range between 2 to 7 nmol kg^{-1} and show a general increase with depth. A mid-depth maximum in the dAl concentration, between 30 to 40 nmol kg^{-1}, coincides with a mid-depth maximum in salinity centered around 1200 m, which is indicative of Mediterranean Outflow Water (MOW) (Hydes, 1983). Below 1200 m, dAl decreases to 15 to 20 nmol kg^{-1} at 2000 m and then slightly increases towards the bottom.

In the Mediterranean Sea, dAl displays a nutrient-type vertical distribution, similar to Si, with relatively low concentrations ranging between 10 to 80 nmol kg^{-1} in surface waters and increasing concentrations with depth. At most locations, the concentrations of dAl and Si reach a mid-depth maximum around 1000 to 1250 m and slightly decrease or remain constant towards the bottom. The concentration of dAl ranges between 125 to 170 nmol kg^{-1} in waters deeper than 1000 m.

In contrast, the concentration of dAl in the relatively shallow (maximum depths ~1000 m) Aegean Sea is relatively constant, ranging between 75 to 90 nmol kg^{-1}, in both surface and deep waters (Fig 4a). Significantly lower concentrations of dAl ranging between 15 to 40 nmol kg^{-1} are observed in the Sea of Marmara. The exchange of water between the Aegean Sea and the Sea of Marmara occurs solely through the Dardanelles Strait with saline water from the Aegean Sea with elevated dAl flowing along the bottom of the Dardanelle Strait, while relatively fresh water from the Sea of Marmara with lower levels of dAl flows along the surface (Fig. 2.4). The dissolved oxygen concentration in the Sea of Marmara is ~290 µmol kg^{-1} in surface waters and decreases to <50 µmol kg^{-1} in deep waters, indicating significant aerobic respiration of organic matter in deep waters. The dAl distribution in the Sea of Marmara is not discussed in detail but we note that intense scavenging of dAl by sinking organic matter may be responsible for the relatively low dAl concentration in deep waters of the Sea of Marmara.

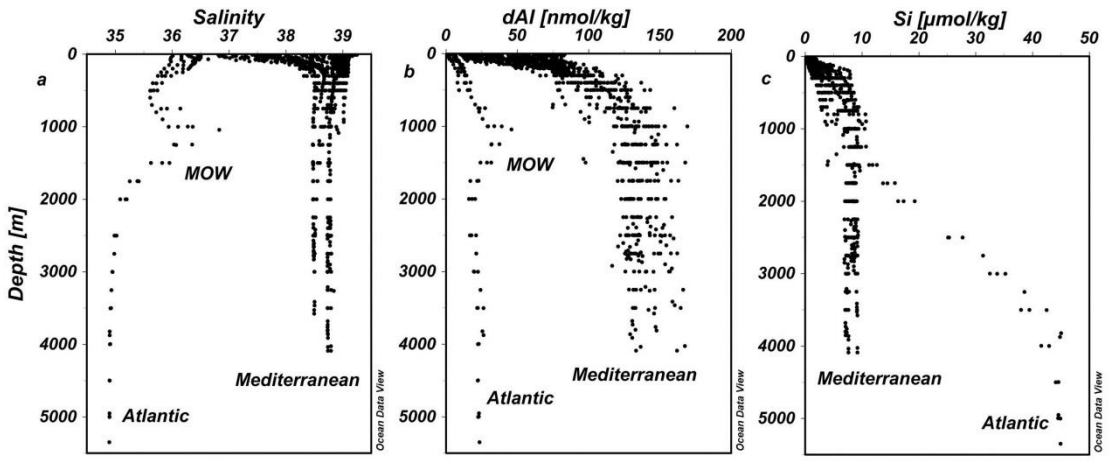

Fig. 2.3. Depth profiles of (a) salinity, (b) dAl, (c) and Si at stations 1.1‑1.28 occupied during Leg 1 (64PE370) and all stations occupied during Leg 2 (64PE374). Mediterranean Outflow Water (MOW) is observed in the salinity and dAl profiles and is centered at ~1200 m. Note that samples from the Aegean Sea and Sea of Marmara (stations 1.29-1.37) have been omitted from this figure.

2.4.3 Zonal distribution of dAl in the Mediterranean Sea

A strong west to east gradient in dAl concentrations is observed in both surface and deep waters of the Mediterranean Sea (Fig. 2.4). Atlantic Ocean surface waters display the lowest dAl concentrations of 2 to 7 nmol kg^{-1}, while the highest surface water dAl concentrations are observed in the EMED, ranging between 50 to 80 nmol kg^{-1} (Fig. 2.4a). Concentrations of dAl in WMDW range between 125 to 135 nmol kg^{-1}, whereas concentrations of dAl in deep waters of the EMED range between 130 to 165 nmol kg^{-1} (Fig. 2.4b). Furthermore, a west to east gradient in the concentration of dAl within EMED deep waters is evident (Fig. 2.4b). Specifically, the concentration of dAl in AdDW is between 130 to 135 nmol kg^{-1} while the concentration of dAl in AeDW eastward of AdDW is higher and ranges between 150 to 165 nmol kg^{-1} (Fig 4b).

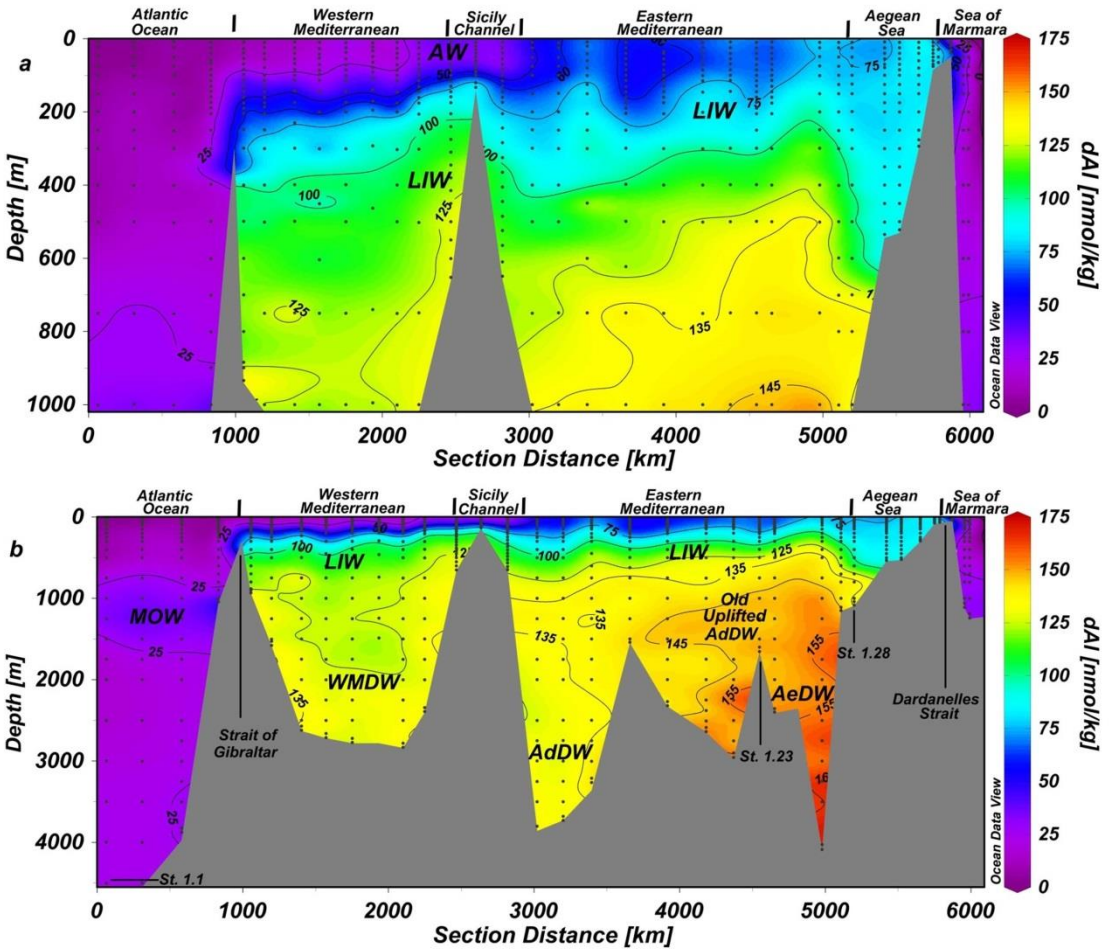

Fig. 2.4. (a) Cross-section plot of dAl concentrations (nmol kg^{-1}) in the upper 1000 m of the water column at stations 1-37 occupied during Leg 1 (64PE370). (b) Cross-section plot of dAl concentration (nmol kg^{-1}) over the full depth of the water column at stations 1-37 occupied during Leg 1 (64PE370). Discrete sampling depths are indicated by filled black circles. Contour lines represent surfaces with a constant dAl concentration. See Fig. 2.1 for location details. AdDW, Adriatic Deep Water; AeDW, Aegean Deep water; LIW, Levantine Intermediate Water; MOW, Mediterranean Outflow Water; WMDW, Western Mediterranean Deep Water.

2.5 Discussion

2.5.1 Distribution of dAl in Mediterranean surface and intermediate waters

The concentration of dAl in the upper water column of the Mediterranean Sea is strongly enriched compared to the Atlantic Ocean. This enrichment progressively increases west to east (Fig. 4, 5, and 6) from 2 to 7 nmol kg^{-1} in Atlantic surface waters to ~80 nmol kg^{-1} in EMED surface waters. A similar relationship between the concentration of dAl in surface waters and longitude has been previously observed in

the Mediterranean Sea (Guerzoni et al, 1999). The longitudinal gradient in dAl concentrations in surface waters is presumably due to advective mixing between inflowing AW and Mediterranean waters and the accumulative effect of continuous dust deposition along the advective flow path of the inflowing AW (Guerzoni *et al.*, 1999). Moreover, the Mediterranean Sea is an evaporative basin, which could lead to an increase in the dAl concentration, akin to the salinity, in Mediterranean surface waters relative to AW. Millot and Taupier-Letage (2005) estimate that 10% of inflowing AW evaporates during its journey through the Mediterranean and consequentially only leads to a ~10% increase in the concentration of dAl in inflowing AW (~5 nmol kg^{-1}). Thus, adopting a starting dAl concentration of ~5 nmol kg^{-1} for Atlantic surface water, it follows that evaporation can only account for ~0.5 nmol kg^{-1} increase in the concentration of dAl and is not an important control on the concentration of dAl in surface waters of the Mediterranean.

Previous studies have confirmed that atmospheric deposition of dust is the primary source of dAl to the Mediterranean responsible for the elevated dAl concentrations (*e.g.* Chou and Wollast, 1997; Hydes *et al.*, 1988). The input of dAl via dust deposition is approximately balanced by the export of dAl via MOW exiting the Mediterranean (Chou and Wollast, 1997; Measures and Edmond, 1988) so that the current Mediterranean system is close to steady state with respect to dAl. Although the elevated concentration of dAl in the Mediterranean is due to dust deposition, we can now show the final distribution of dAl is strongly influenced by internal processing. The concentration of dAl in the upper 30 m of Mediterranean surface waters along the general advective flow of AW (*i.e.* Leg 1 transect) is strongly correlated with salinity, indicating the surface distribution of dAl in the Mediterranean surface waters is primarily controlled by mixing (Fig. 2.5a). Mixing of inflowing AW with underlying Mediterranean intermediate waters (*e.g.* LIW) and older surface waters occurs over the entire eastward flow path of AW (Millot and Taupier-Letage, 2005), so that AW is only a minor component of surface waters in the EMED. The average concentration of dAl in LIW at ~350 m is ~100 nmol kg^{-1} in both the EMED and WMED (Fig. 2.4a). The concentration of dAl in incoming AW increases from <5 nmol kg^{-1} west of the Strait of Gibraltar to ~80 nmol kg^{-1} at the distal end of its flow path near the southern Aegean Sea (Fig. 2.6). Therefore, assuming simple two end member conservative mixing of dAl, AW represents only ~20% of the surface water at the distal end of its flow path in the EMED. Since LIW is formed directly from modified inflowing AW in the EMED,

the concentration of dAl in LIW must be maintained by either mixing with Mediterranean deep waters or by release of Al from sinking particles (see section 4.3.1).

Mixing is the primary control on dAl distribution in Mediterranean surface waters, but the effect of dust deposition on short time scales needs to be considered. If one assumes a constant dust input over the entire surface area of the Mediterranean, a constant solubility of Al from the dust and no removal processes, then a smooth zonal gradient in the concentration of dAl in surface waters along the path of inflowing AW could be expected, due to the accumulative effect of dust deposition. The magnitude of the increase in dAl along the AW flow path would depend on the chosen magnitude of dust deposition and Al solubility. However, Guieu *et al.* (2010) demonstrated the sporadic nature of dust deposition events in the Mediterranean and that the total annual atmospheric dust deposition for a particular location can be dominated by a single dust storm that may only last a couple of days. Specifically, a strong Saharan dust storm lasting two days on Nov. 11-12, 2001 deposited approximately 1.5 g Al/m^2 (21.9 g/m^2 total deposition of which approximately 7% is Al in the Saharan end-member (Guieu *et al.*, 2002)), which accounted for approximately 75% of the atmospheric deposition of Al for a 12 month period at a site in Corsica, France (Guieu *et al.*, 2010). If 5% of the Al deposited during this event dissolved in the surface mixed layer (Maring and Duce, 1987; Measures *et al.*, 2010) with a theoretical depth of 50 m, then this single event could have increased the dAl concentration of the effected water mass by 50 to 60 nmol kg^{-1}. Any such intense atmospheric deposition event occurring directly prior to this study may be expected to produce anomalously high dAl concentrations relative to the mixing line in Fig. 2.5a. The time scale over which such a deviation in the dAl concentration in surface waters is likely to persist depends on the residence time of surface water and surface dAl, neither of which are well constrained, but are on the order of several years (Chou and Wollast, 1997; Van Cappellen, 2014). The strong correlation between salinity and dAl in Fig. 2.5a implies that no intense dust deposition events can be directly inferred from the dAl concentration in Mediterranean surface waters during this study. This is possibly because advective and/or vertical mixing between surface and intermediate water occurs too quickly for any retention of an elevated dAl signal from dust deposition.

A few samples in the EMED, from in and around the Aegean Sea, depart from the general trend in Fig. 2.5a. The source of the apparently elevated dAl concentration

in Aegean Sea surface waters is currently not known although a number of scenarios can be envisioned such as locally enhanced atmospheric dust deposition or river discharges. The high dAl concentrations appear to be related to a slight decrease in the salinity which suggests a fresh water source (*e.g.* river discharge, submarine ground water discharge) is driving the dAl to higher concentrations in Aegean Sea surface waters.

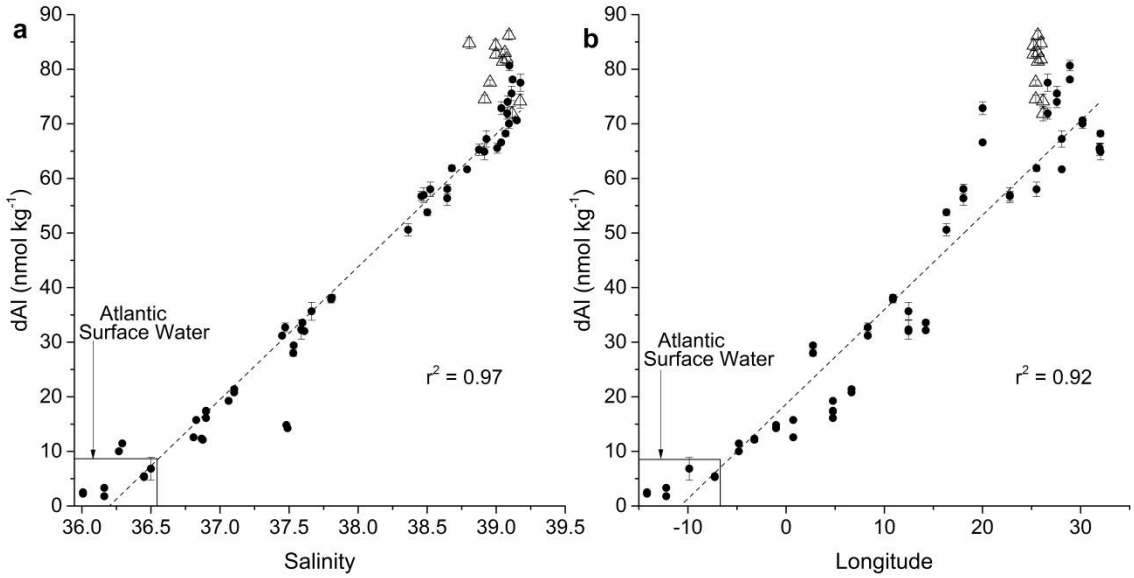

Fig. 2.5. (a) The concentration of dAl (nmol kg^{-1}) versus salinity in samples from the upper 30 m at stations occupied during Leg 1 (64PE370) in the Atlantic Ocean and the Mediterranean Sea (filled circles), and the Aegean Sea (open triangles). (b) Same as (a) but with dAl versus longitude. Dashed lines are best fit lines through Atlantic and Mediterranean samples.

2.5.2 Distribution of dAl in Mediterranean deep waters

The initial concentration of dAl in newly forming Mediterranean deep waters is controlled by the concentration of dAl in the surface and intermediate waters at their formation sites during times of deep water formation. In the southern Aegean Sea, where AeDW formation occurs, the surface water concentration of dAl is ~80 nmol kg^{-1}, while surface water in the southern Adriatic Sea, where AdDW formation occurs, has a slightly lower dAl concentration of ~70 nmol kg^{-1} (Fig. 2.6). Therefore, it is reasonable to expect the initial concentration of dAl in AeDW to possibly be ~10 nmol kg^{-1} higher than the initial dAl concentration in AdDW, which is similar to but less than the observed ~25 nmol kg^{-1} difference in the concentrations of dAl in AeDW and AdDW (Fig. 2.4b). However, both AeDW and AdDW, with dAl concentrations of ~155

nmol kg^{-1} and ~130 nmol kg^{-1} respectively, are enriched in dAl compared to their respective source waters by 60 to 75 nmol kg^{-1}. Therefore, an additional source of dAl to deep waters in the EMED is required.

The concentration of dAl in WMDW is 125 to 135 nmol kg^{-1} and is relatively homogeneous compared with deep waters in the EMED (Fig. 2.4b). This is because there is only one primary deep water mass in the WMED, while there are two separate deep water masses with different origins in the EMED. The Gulf of Lions region is the primary formation area of WMDW. Unfortunately, no stations were occupied in the Gulf of Lions, but the concentration of dAl in this region is likely elevated relative to the concentrations of dAl observed in the other WMED surface waters (~30 nmol kg^{-1}) for two main reasons. Firstly, surface waters in the northern WMED near the Gulf of Lions are a mixture of AW from the west-Corsica vein with (estimated dAl ~30 nmol kg^{-1} based on WMED surface waters) and AW from the Tyrrhenian vein with relatively higher dAl. The concentration of dAl in surface waters of the Tyrrhenian vein approaches ~55 nmol kg^{-1} (Fig. 2.6). Secondly, the concentration of dAl in surface waters near the Gulf of Lions may be significantly increased by fluvial runoff, namely the Rhone River (Chou and Wollast, 1997). Chou and Wollast (1997) observed an average dAl concentration of ~50 to 60 nmol kg^{-1} in surface waters near the Gulf of Lions during December 1988. Thus, the concentration of dAl in surface waters near the formation site of WMDW near the Gulf of Lions (assumed to be ~50 nmol kg^{-1}) is elevated relative to contemporaneous WMED surface waters sampled during this study. The enrichment of dAl in WMDW relative to surface waters near the Gulf of Lions (75 to 85 nmol kg^{-1}) is similar to the enrichment of dAl observed in deep waters of the EMED relative to EMED surface waters (60 to 75 nmol kg^{-1}), and thus an additional source of dAl to WMDW is also required (see Section 4.3.3).

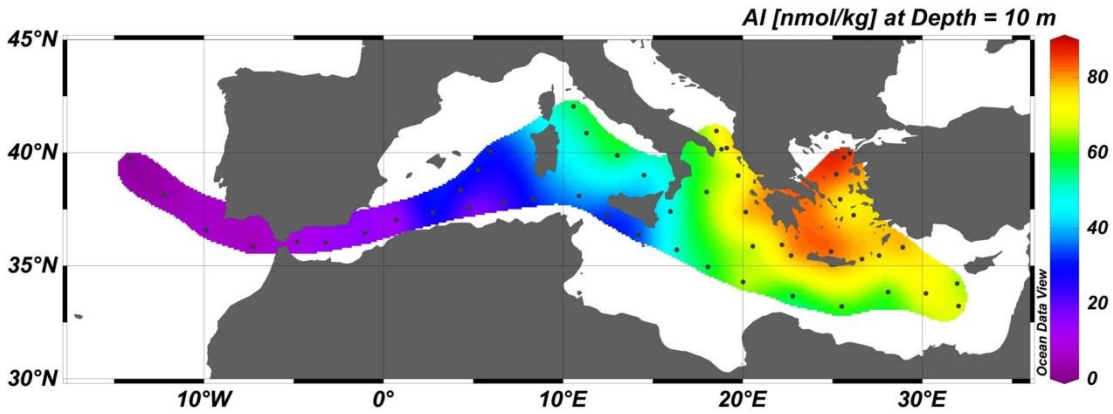

Fig. 2.6. Concentration of dAl (nmol kg^{-1}) at approximately 10 m deep for all stations occupied during Leg 1 (64PE370) and Leg 2 (64PE374). Black circles mark the station locations.

2.5.3 Correlations between dAl and Si in the Mediterranean Sea

A strong correlation between dAl and dissolved Si exists in samples collected from the Mediterranean Sea (Fig. 2.7a). If all of the data for the entire Mediterranean Sea is considered, then the resulting correlation of [dAl][nmol kg^{-1}]=10.6[Si][µmol kg^{-1}]+45.1 (R^2=0.77; n=952). When considered separately, samples collected in the WMED and EMED define distinctly different dAl:Si correlations (Fig. 2.7b). The dAl:Si correlation in the WMED is described by [dAl][nmol kg^{-1}]=13.8[Si][µmol kg^{-1}]+6.5 (R^2=0.98; n=234), while the dAl:Si correlation in the EMED is described by [dAl][nmol kg^{-1}]=10.0[Si][µmol kg^{-1}]+60.2 (R^2=0.93; n=539). Data from station 1.5 is not considered in the WMED dAl:Si correlation in Fig. 2.7b because this station is very close to the Strait of Gibraltar and is strongly influenced by inflowing Atlantic surface waters (see Fig. 2.1 for location). The dAl:Si relationship in the Sicily Channel and Tyrrhenian Sea falls between the relationship observed in the WMED and EMED.

Chou and Wollast (1997) reported a dAl:Si correlation of [dAl][nM]=10.9[Si][µM]+34.1 (R^2=0.86; n=300) for samples collected in the upper 1000 m of the water column at multiple locations in the WMED. Most of stations sampled by Chou and Wollast were in the Gulf of Lions region or near the southeast coast of Spain. The concentration of dAl in surface waters can be strongly influenced by river plumes. This is evident in the y-intercept of 34.1 reported by Chou and Wollast (1997). The dAl:Si correlation with a y-intercept of 6.5 in our study is very similar to the starting dAl concentration in inflowing AW. Therefore, the difference in the slopes

of the dAl:Si correlations between the two studies for WMED samples is likely due to differences in the water masses sampled.

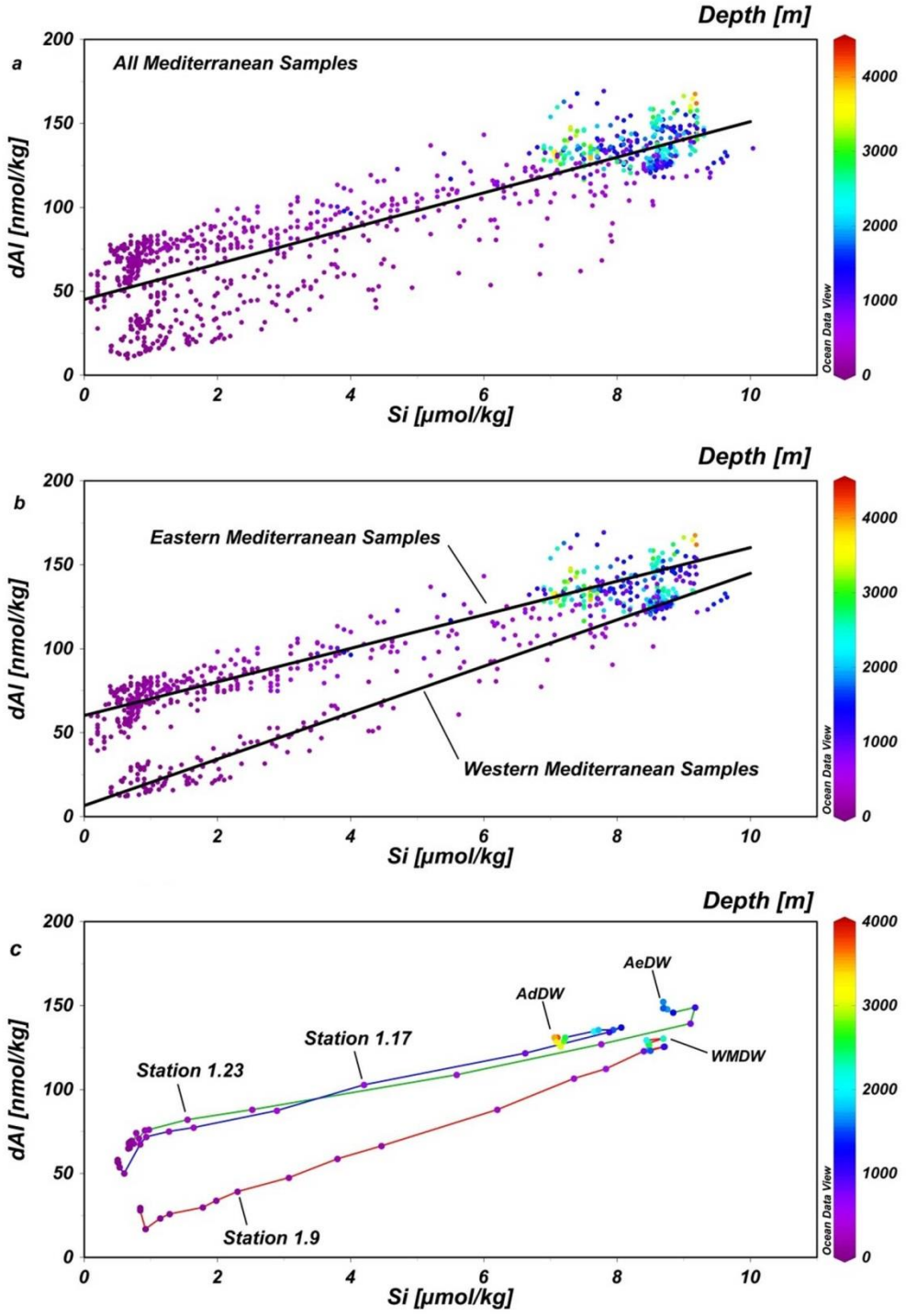

Fig.2.7. (a) Concentration of dAl (nmol kg^{-1}) versus dissolved Si (µmol kg^{-1}) for all stations in the Mediterranean Sea with associated trend line. The dAl:Si correlation is described by [dAl]=(10.6±5.9)[Si]+(45.1±32) (1 SD; R^2=0.77; n=952). (b) Concentration of dAl (nmol kg^{-1}) versus dissolved Si (µmol kg^{-1}) for stations in the western Mediterranean basin (WMED) and stations in the eastern Mediterranean basin (EMED) with individual trend lines. Samples from the Tyrrhenian and Channel of

Sicily are not included. The dAl:Si correlation in the WMED is described by [dAl]=(13.8±2.2)[Si]+(6.5±14) (1 SD; R^2=0.98; n=234). The dAl:Si correlation in the EMED is described by [dAl]=(10.0±2.7)[Si]+(60.2±14) (1 SD; R^2=0.93; n=539). (c) Concentration of dAl (nmol kg^{-1}) versus dissolved Si (µmol kg^{-1}) at stations 1.9, 1.17 and 1.23.

2.5.3.1 Correlation between dAl and Si in LIW

The dAl:Si correlation is strongest in intermediate waters and tends to be more convoluted in surface and deep waters. To illustrate this point more clearly, Fig. 2.7c displays the dAl:Si relationship at stations 1.9, 1.17, and 1.23. In the Mediterranean Sea, intermediate waters (*e.g.* LIW) are formed directly from surface waters and therefore the starting concentrations of dAl and Si in newly formed intermediate waters will be similar to their source surface waters and any addition of dAl or Si to intermediate waters will result in concentrations higher than those observed in surface waters. The concentrations of both dAl and Si are relatively low in surface waters and increase in tandem towards a mid-depth maximum around 1000-1250 m in both the EMED and WMED. Below this mid-depth maximum, the concentration of Si tends to slightly decrease towards the bottom while the concentration of dAl tends to behave more variably in deep waters, thereby convoluting the dAl:Si relationship. Therefore, most of the change in the concentration of both dAl and Si occurs at intermediate depths (100 to 1250 m), which is where the dAl:Si relationship is clearest (Fig. 2.7c). As discussed previously in section 3.1, for simplicity, the intermediate water mass at depths between 200 to 1000 m is identified as LIW (Fig. 2.2a). The water mass at 1000 to1250 m in the EMED is identified as old uplifted deep water (Klein *et al.*, 1999; Robinson *et al.*, 2001) (Fig. 2.2b), but similar uplifting of old deep water also occurs in the WMED.

The concentration of Si in surface waters is maintained at low levels (<1 µmol kg^{-1}) through biological utilization. Therefore, intermediate waters which form directly from surface waters, such as LIW, will also have a Si concentration of <1 µmol kg^{-1} immediately after formation. The concentration of dAl is about 78 nmol kg^{-1} in surface waters at station 1.26 near the isle of Rhodes, which is near the formation site of LIW. The aforementioned vertical increase in the Si and dAl concentrations between surface waters and old uplifted deep water at 1000-1250 m is therefore due to an addition of dAl and Si to LIW. The source of additional dAl and Si in LIW must either be dissolution of sinking particles or mixing between LIW and the old uplifted deep water.

A potential temperature-salinity (θ-S) diagram shows clear mixing between LIW (core at ~350 m for simplicity) and old uplifted deep water at 1000 to 1250 m in the WMED and EMED (Fig. 2.8). The θ-S relationship breaks down in shallower waters due to heating of surface waters (not shown). Linear correlations between Si and salinity (Fig. 2.9a) and dAl and salinity (Fig. 2.9b) at depths between ~350 to 1250 m indicate that the primary source of additional dAl and Si in LIW is through mixing with old uplifted deep waters that have elevated dAl and Si concentrations and lower salinity. Therefore, mixing can also account for the strong dAl:Si correlation observed in the Mediterranean at intermediate depths.

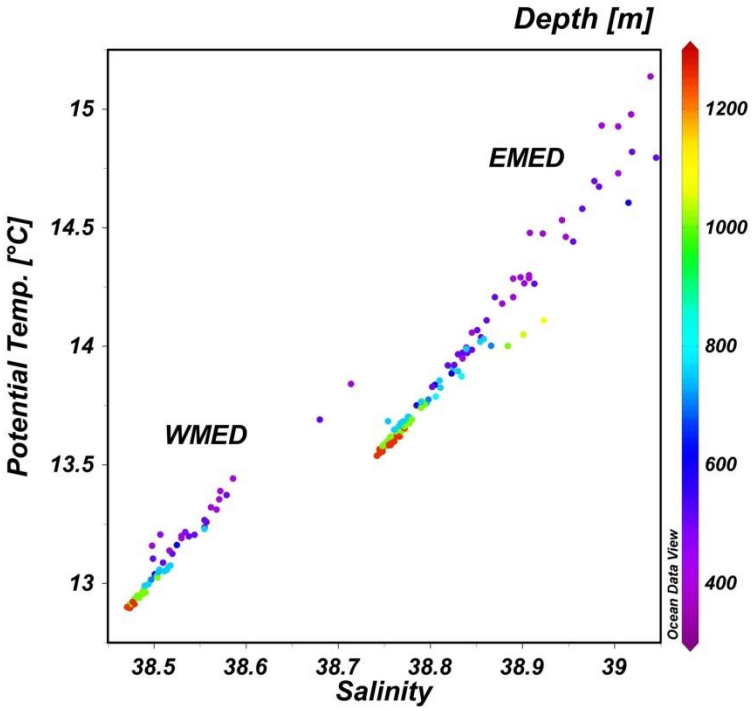

Fig. 2.8. θ-S diagram for 350-1300 m at all stations in the western Mediterranean basin (WMED) and eastern Mediterranean basin (EMED) except for stations 2.7, 2.8, and 2.9, which are located in the southern Adriatic Sea. The linear relationship between potential temperature and salinity indicates mixing between warm, saline Levantine Intermediate Water (core at ~350 m) with colder, less saline old uplifted deep water (core at 1000 to 1250 m).

Mixing between LIW and old uplifted deep water is clearest in the EMED due to the diminished effects of inflowing AW with relatively low Si, dAl, and salinity which is mixed to deeper depths in the WMED via mesoscale eddies (Fig. 2.2a) and because concentration gradients between LIW and underlying old uplifted deep water are greater in the EMED. As LIW spreads out from its formation site near the isle of

Rhodes, its core can be tracked by a salinity maximum at depths around ~200 m in the EMED and ~400 m in the WMED. The concentrations of the dAl and Si at the salinity maximum increase from ~80 nmol kg^{-1} to ~105 nmol kg^{-1} and <1 µmol kg^{-1} to ~7 µmol kg^{-1}, respectively, from the EMED to the WMED indicating a continual supply of dAl and Si to LIW as it travels through the Mediterranean, which is to be expected if mixing between LIW and underlying old uplifted deep water is occurring everywhere as is indicated by the θ-S diagram in Fig. 2.8. Therefore, the gradient in Si, dAl, and salinity between LIW and underlying old uplifted deep water is eroded away via mixing as LIW spreads from east to west (Fig. 2.8, 2.9, and 2.10). Consequentially, the vertical increase of dAl and Si concentrations observed in intermediate waters is clearly due to mixing between LIW and underlying old uplifted deep waters in the EMED, while in the WMED the vertical increase in the dAl and Si concentrations in intermediate waters is primarily due to mixing between inflowing AW and underlying LIW (Fig. 2.10). An additional subsurface water mass appears to be present in the WMED at ~120 m, possibly old surface water that has been trapped in the WMED and circulating just below new inflowing AW (Fig. 2.10). Furthermore, the different slopes of the dAl:Si trend lines in the WMED and EMED in Fig. 2.7b are therefore a result of the different concentrations of dAl and Si in LIW between the EMED and WMED and different mixing scenarios. Interestingly, the dAl:Si relationship in the WMED is maintained even though there is mixing between multiple water masses, strongly indicating that LIW is the dominant common source of dAl and Si to surface waters.

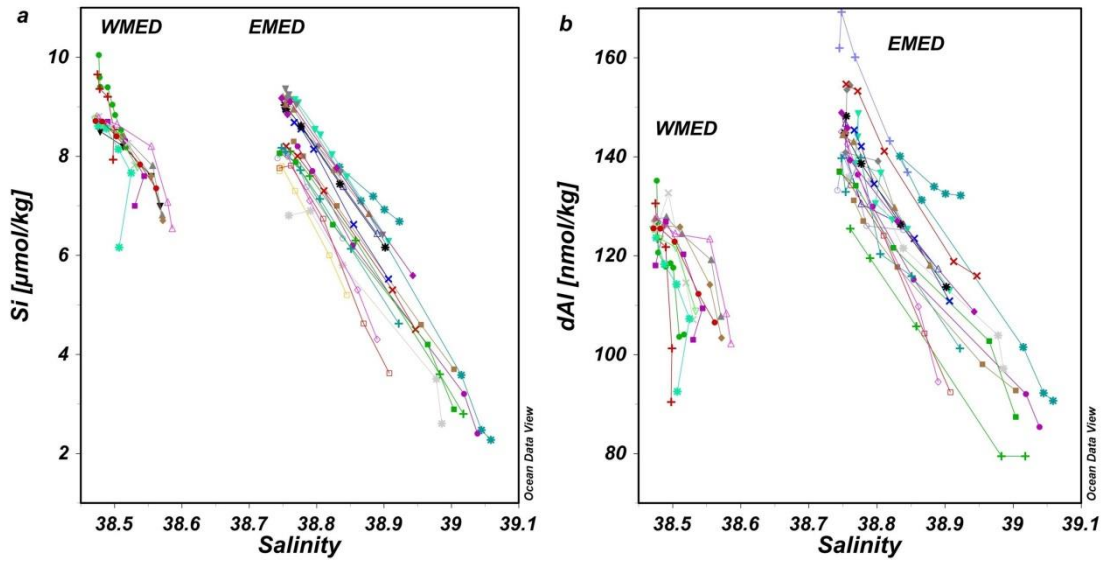

Fig. 2.9. (a) Plot of Si against salinity and (b) dAl against salinity at depths between 350-1300 m in the western Mediterranean basin (WMED) and eastern Mediterranean basin (EMED) except for stations 2.7, 2.8, and 2.9, which are located in the southern Adriatic Sea.

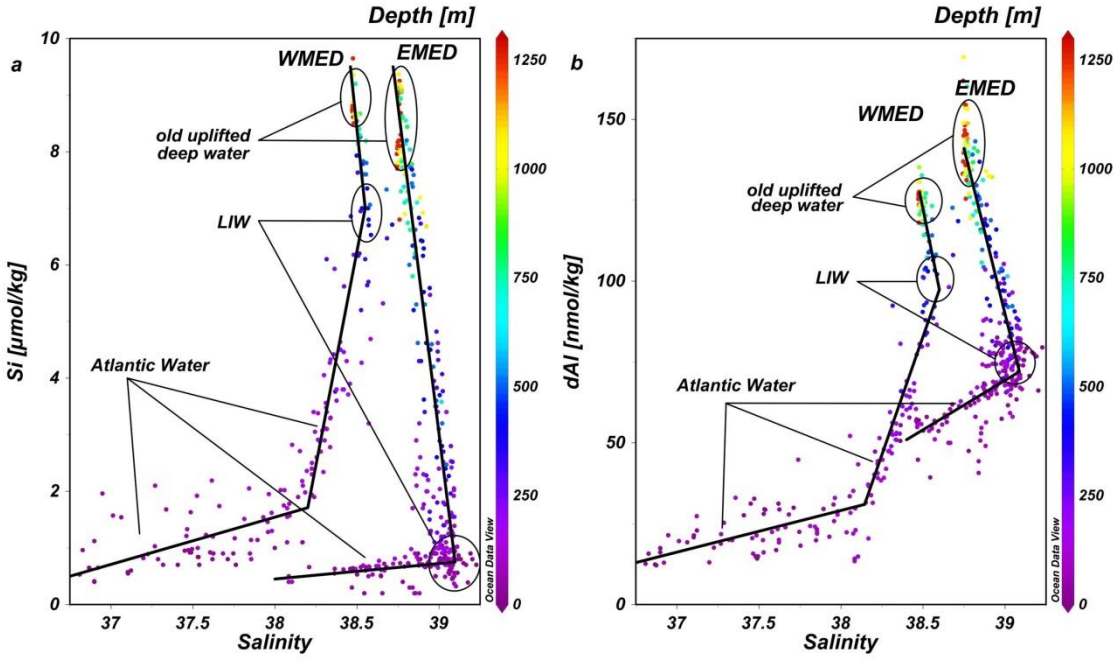

Fig. 2.10. (a) Plot of Si against salinity and (b) dAl against salinity at depths between 0-1300 m in the western Mediterranean basin (WMED) and eastern Mediterranean basin (EMED) except for stations 2.7, 2.8, and 2.9, which are located in the southern Adriatic Sea. The water with the highest salinity in both the EMED and WMED is the core of Levantine Intermediate Water (LIW).

2.5.3.2 Does vertical transport influence the dAl:Si relationship in the Mediterranean?

Mixing between LIW and uplifted deep water provides a source of dAl to LIW, while mixing between LIW and overlying AW provides a source of dAl to surface waters. Mixing between LIW and overlying AW is responsible for the zonal gradient in the dAl concentration in surface waters (see section 4.3.1). Similarly, LIW is also a source of Si to AW, especially in the WMED where LIW has a Si concentration of ~7 μmol kg^{-1}. However, a similar zonal gradient as observed for dAl in the Si concentration is lost due to rapid removal of Si from surface waters through utilization by diatoms. Subsequent transport of Si back to deep waters occurs via the dissolution of sinking biogenic opal. Experimental and field observations suggest that sinking biogenic diatom opal is the primary vector for vertical transport of dAl (Li *et al.*, 2013; Moran and Moore, 1988, 1992). The incorporation of dAl into biogenic opal is either through active uptake in the frustule (Gehlen *et al.*, 2002) or diatom cell (Li *et al.*, 2013) or surface adsorption onto the frustule (Li *et al.*, 2013; Moran and Moore, 1988, 1992) and is subsequently released either through dissolution or desorption, respectively, as the biogenic opal sinks and remineralizes. Furthermore, Middag *et al.* (2015) observe a clear increase in dAl across an oxygen minimum zone in the water column of the West Atlantic which supports the view that remineralization of biogenic particles can release dAl. However, Measures *et al.* (2014) did not observe an increase in dAl associated with the oxygen minimum zone in the highly productive Mauritanian shelf waters along the NW African. This contradiction may be due to the influence of low dAl Antarctic Intermediate Water corresponding with the deepest part of the oxygen minimum zone or due to scavenging being dominant over remineralization in the study of Measures *et al.* (2014) (see Middag *et al.* (2015) for further discussion).

Sinking dust particles may also transport dAl vertically via scavenging of dAl from surface waters and subsequent desorption at depth or through continuous dissolution of the dust particles themselves at depth. Sinking biogenic opal therefore transports both dAl and Si to deeper waters, while sinking dust particles may only transport appreciable amounts of dAl. If sinking dust particles transfer significant amounts of dAl from surface to deep waters then it is expected that in areas of high dust deposition, the dAl:Si relationship in intermediate waters, which has been established by conservative mixing, would breakdown due to excessive transport of dAl relative to Si (crustal Al/Si ratio is ~0.26 (Taylor, 1964)). No such breakdown of the dAl:Si relationship was observed in the present study, suggesting that sinking dust particles do

not transfer a significant amount of dAl from surface to intermediate waters in the Mediterranean relative to the effects of mixing. Similarly, if sinking biogenic particles are transferring significant amounts of dAl from surface to intermediate waters, then the Al/Si ratios of these sinking particles must be similar to the slope of the dAl:Si correlation, which is established through mixing. Otherwise, the dAl:Si, dAl-salinity, and Si-salinity relationships in intermediate waters would be lost. The slopes of the dAl:Si correlations in Fig. 2.7b are ~14×10^{-3} and ~10×10^{-3} mol/mol in the WMED and EMED, respectively, which are within the range of Al/Si ratios observed in natural diatoms (Gehlen *et al.*, 2002; Koning *et al.*, 2007; Ren *et al.*, 2013). This suggests that remineralization of biogenic opal could result in a similar dAl:Si correlation as mixing, and that the two processes cannot be distinguished from each other. However, the strong correlations between dAl and Si with salinity suggest mixing is the dominant process controlling the dAl:Si correlation in intermediate waters.

Although vertical transport of dAl through sinking biogenic particles is not directly evident at intermediate depths, it may be important for maintaining the elevated dAl and Si concentrations in deep waters that are in turn, the source of dAl and Si to LIW. As deep waters in the Mediterranean are initially formed with relatively low concentrations of dAl and Si, there must be a source of dAl and Si to increase the concentrations over time. For Si, it is generally accepted that dissolution of sinking biogenic opal increases the concentration of Si in deep waters over time. In the Mediterranean Sea, the maximum concentrations of both Si and dAl generally occur at the same depth in old uplifted deep water indicating the oldest waters are the most enriched in Si and dAl, although deep water formation obscures this relationship in some situations (see section 4.3.3). This implies a constant source of both dAl and Si to deep waters which thereby increases the concentrations of dAl and Si in deep waters as they age. Furthermore, the residence time of Mediterranean deep waters is on the order of 50-100 yrs (Millot and Taupier-Letage, 2005), which is significant relative to the residence time of dAl in the open ocean (~150 yrs (Orians and Bruland, 1985)), thereby necessitating the need for a continuous source of dAl to Mediterranean deep waters. As deep waters enriched in dAl and Si are uplifted, they begin to mix with overlying intermediate waters (*i.e.* LIW). The initial concentration of dAl and Si in new LIW is very low relative to old uplifted deep waters as LIW is formed from surface water. Therefore, the slope of the dAl:Si correlation observed in intermediate waters is driven by the high concentrations of dAl and Si in old uplifted deep water. Importantly, the

slope of the dAl:Si correlation in Mediterranean intermediate waters is in the range of the Al/Si ratios reported for diatoms, which we take as evidence that dissolution of biogenic opal could be responsible for maintaining the elevated levels of dAl in Mediterranean deep waters. To reiterate, given that LIW and deep waters all originate from surface waters in the Mediterranean, a source of both Al and Si is needed to account for their joint increase with depth. The release of Al and Si must be in a ratio similar to the slope of the dAl:Si correlation, otherwise the correlation would not be maintained. Involvement of Al in the biological cycle through either biological uptake or passive adsorption onto biological particles appears the most likely explanation for the joint source of Al and Si in subsurface waters. Furthermore, the slope of the dAl:Si correlation is relatively constant with time, which supports the hypothesis that the source of dAl and Si to deep waters is constant. Specifically, from the data of Hydes *et al.* (1988) we derive a slope in the dAl:Si correlation of ~$(9\text{-}10)\times10^{-3}$ in samples collected at three separate locations in the EMED in 1987, which is similar to the slope of the dAl:Si correlation observed in the EMED in this study in 2013. This suggests the dAl:Si correlation in intermediate waters in the EMED has remained relatively constant over nearly twenty-five years, which is significantly long relative to the <10 yr residence time of LIW in the EMED (Van Cappellen *et al.*, 2014). Interestingly, a major deep water renewal occurred in the EMED (*i.e.* EMT) between the time of the Hydes *et al.* study and the present study which has significantly altered the mixing scenario in the EMED (see section 3.1). The consistency of the dAl:Si correlation over time implies that the source of dAl and Si to deep waters (*i.e.* biogenic particles) has a relatively constant Al/Si ratio.

2.5.3.3 Impact of deep water formation on the dAl:Si relationship

Dense waters in the Mediterranean Sea are formed during episodes of winter cooling directly from a mixture of surface waters and intermediate waters (*e.g.* LIW) (see section 2.4.1). Depending on their formation density, newly formed dense waters descend to their equilibrium depth and begin to spread as a neutrally buoyant plume while mixing with older resident deep waters. Since Mediterranean surface waters and intermediate waters (in the EMED) have low concentrations of Si (<1 μmol kg^{-1}), the initial concentration of Si in newly formed deep waters will be low relative to older deep waters (*i.e.* old uplifted deep waters). However, mixing with resident deep waters can significantly erode the low Si (<1 μmol kg^{-1}) signature in newly formed deep water.

Similarly, the low dAl surface water signature (70 to 80 nmol kg^{-1} at dense water formation sites in the EMED) is obscured due to mixing with high dAl deep waters (~125 to 160 nmol kg^{-1}). Therefore, newly formed deep waters which still maintain a significant fraction of their initial surface water, should have lower dAl and Si concentrations relative to older resident deep waters, but maintain dAl and Si concentrations which fall on the dAl:Si correlation established in intermediate waters. At depths below the Si mid-depth maximum in old uplifted deep water at 1000 to 1250 m, the lowest Si concentration is ubiquitously found in bottom waters in the EMED, barring station 1.26 (see Fig. 2.7c for example), suggesting that recent dense water formation in the EMED has produced new deep water with sufficient density to reach the bottom. However, the dAl:Si relationship which gets imparted on deep water during its formation and mixing is only clearly preserved in AdDW (Fig. 2.7c) where AdDW plots along the dAl:Si correlation established in intermediate waters. Based on this simple conceptual model there appears to be excess dAl relative to Si in AeDW, which invokes the need for an additional source of dAl that is not a source of Si during the formation of AeDW.

Locally enhanced dust deposition in the southern Aegean Sea is a possible source of the elevated dAl in AeDW but is unlikely due to the magnitude of dust deposition required. If we consider the total volume of AeDW produced was ~2.8×10^{14} m^3 (Roether *et al.*, 2007) with a dAl concentration elevated by ~10 nmol kg^{-1} over resident deep waters, then an additional source of ~7.6×10^{19} ng of Al to AeDW is required. We again consider the extreme dust deposition event recorded in Corsica, France in Nov. 2001 by Guieu *et al.* (2010) which resulted in a total deposition of ~1.5×10^{9} ng/m^2 of Al. If an atmospheric deposition event of similar magnitude had occurred over the entire surface area of the southern Aegean Sea (~8×10^{10} m^2), it could have resulted in a total deposition of ~1.2×10^{20} ng of Al, of which only approximately 5% or ~6.0×10^{18} ng is expected to dissolve. Therefore, approximately ten of these extreme dust deposition events occurring during the primary formation period of AeDW (1992-1994) are necessary in order to achieve the total dAl input required to explain the high dAl in AeDW. This scenario is unlikely due to the unlikelihood that such extreme atmospheric deposition events would reoccur in the same location numerous times during a relatively short time interval.

Intense sediment resuspension has been extensively documented during times of dense shelf water cascading down through submarine canyons carved on continental

shelves at multiple locations in the Mediterranean Sea (*e.g.* Puig *et al.*, 2014). The formation of most AeDW occurred rapidly during the EMT of the mid-1990's. As the Aegean Sea is not normally a location of intense deep water formation, it is plausible that intense deep water formation during the EMT eroded sediments that had accumulated in submarine canyons in the southern Aegean Sea around the isle of Crete where AeDW enters the EMED. Moran and Moore (1991) experimentally demonstrated that resuspension of sediments leads to an increase of dAl in seawater. Furthermore, Middag *et al.* (2015) has demonstrated an increase in dAl associated with sediment resuspension during North Atlantic Deep Water formation. Contrarily to the formation of AeDW during the EMT, deep water formation occurs regularly in the southern Adriatic Sea and therefore easily eroded sediments are not likely to build up in submarine canyons along the flow path of AdDW in sufficient quantity to significantly increase the dAl concentration relative to Si in AdDW. The lack of a significant additional source of dAl to AdDW allows for the preservation of the dAl:Si relationship found in intermediate waters (Fig. 2.7c). Similarly, the production of WMDW regularly occurs in the Gulf of Lions region and therefore sediment resuspension is not expected to significantly influence the dAl:Si relationship in WMDW. However, the dAl:Si relationship in WMDW indicates there is a small additional source of dAl to WMDW (Fig. 2.7c). Small additions of dAl with respect to Si in WMDW could result from a number of different processes. One possibility is deep waters of the EMED with a relatively high dAl:Si ratio compared to WMDW enter the WMED after passing through the Channel of Sicily and Tyrrhenian Sea and mix with WMDW thereby providing an source of additional dAl relative to Si (Millot and Taupier-Letage, 2005). Alternatively, the dAl concentration of sinking surface water in the WMED could be increased relative to Si by river water discharging in to the Gulf of Lions region during times of WMDW formation (Chou and Wollast, 1997).

2.6 Conclusions

The concentration of dAl in Mediterranean surface and deep waters shows a strong zonal gradient. In surface waters, the concentration of dAl is strongly correlated with salinity, which suggests that mixing between surface waters of Atlantic origin with low dAl and Mediterranean surface and intermediate waters with high dAl is the

primary control on the concentration of dAl in Mediterranean surface waters. As the surface flow path of AW through the Mediterranean is, in general, west to east, the surface waters near the southern Aegean Sea are at the distal end of the AW flow path. Surface waters near the southern Aegean Sea have the highest concentration of dAl of all Mediterranean surface waters due to experiencing the most mixing, rather than the most direct atmospheric dust deposition. Dust deposition is eventually responsible for the elevated concentrations of Al, but no direct link between dust deposition and surface concentration was observed in the study. Nevertheless, large Saharan dust storms should be capable of creating resolvable increases in the concentration of dAl in surface waters. In this context, the lack of significant perturbations in the dAl-salinity relationship (Fig. 2.5a) indicate that no intense dust deposition events can be directly inferred from the dAl concentrations in Mediterranean surface waters during this study and that mixing is the dominant driver of the surface dAl distribution.

The concentration of dAl in LIW increases from ~80 nmol kg^{-1} in the EMED to ~105 nmol kg^{-1} in the WMED even though it experiences constant mixing with overlying AW, which has a very low dAl concentration (<5 nmol kg^{-1}). The comparatively high concentration of dAl in LIW must therefore be maintained by mixing between LIW and old underlying deep water at 1000 to 1250 m. This scenario is confirmed via a θ-S diagram indicating two end member mixing between depths of 350 to 1300 m (Fig. 2.8). Mixing between LIW and old uplifted deep waters in the EMED results in a strong correlation between dAl and Si. A slightly different mixing scenario occurs in the WMED. Mixing between surface waters and LIW dominate the dAl:Si correlation in the WMED, which results in a slightly different dAl:Si correlation than in the EMED. Therefore, significant vertical transport of dAl is not required to explain the long recognized dAl:Si relationship in the Mediterranean. Vertical transport of dAl via sinking biogenic particles is required however, to maintain the highest concentrations of dAl and Si in the oldest deep waters which in turn mix with overlying intermediate waters and thus maintain the dAl:Si relationship during overturning circulation in the Mediterranean.

Deep waters in the Mediterranean Sea are formed directly from surface and intermediate waters. Interestingly, AeDW has the highest concentration of dAl of all Mediterranean deep waters. Sediment resuspension as dense water cascades through submarine canyons is suspected to increase the concentration of dAl relative to Si in deep waters such as AeDW, thereby convoluting the dAl:Si relationship in deep waters.

As the formation of AeDW was a transient event, it is expected that new production of AdDW will eventually replace and uplift AeDW. Future research should include examining how the uplift of AeDW with a high concentration of dAl will affect the concentration of dAl in surface and intermediate Mediterranean waters.

CHAPTER 3

BASIN-SCALE DISTRIBUTIONS OF ANTHROPOGENIC DISSOLVED TRACE METALS IN THE MEDITERRANEAN SEA

3.1 Abstract

Many trace metals exist in the ocean at vanishingly low concentrations, yet are essential nutrients for the photosynthetic microorganisms that makeup the base of marine food webs (*e.g.* iron). Some trace metals can also be toxic at concentrations elevated above certain threshold values (*e.g.* cadmium). As the Mediterranean Sea is a small semi-enclosed marine basin subject to intense anthropogenic pressures owing to the large industrial centers that border its shores, it is at risk of becoming severely polluted with trace metals. Although there are many known anthropogenic sources of trace metals to the Mediterranean Sea, particularly around large urban centers and historical mining sites, the distributions of dissolved trace metals at the basin-scale are not well characterized. Here the basin-scale distributions of dissolved iron (Fe), zinc (Zn), cadmium (Cd), and lead (Pb), from the 2013 GEOTRACES expeditions to the Mediterranean Sea are presented. Basin-scale atmospheric deposition of lithogenic particles leads to elevated dissolved Fe concentrations of ~1 to greater than 3 nM in Mediterranean surface waters compared to deep waters with concentrations generally well below 1 nM. Significant enrichments of dissolved Zn (up to >5 nM), Cd (up to >80 nM), and Pb (up to >100 nM) in the western Mediterranean basin cannot be ascribed to elevated concentrations of these metals in water entering the basin through the straights. This implies that internal sources of these metals within the western Mediterranean basin are responsible for the elevated concentrations. As the distribution of dissolved Pb is known to be significantly impacted by anthropogenic sources of Pb to the marine environment, the similar patterns of enrichments observed between dissolved Zn, Cd, and Pb in the Mediterranean Sea provides strong evidence that anthropogenic activities are also a significant source of Zn and Cd to the western Mediterranean and that the concentrations of dissolved Zn and Cd are elevated over their baseline levels at a basin-scale due to these anthropogenic sources.

3.2 Introduction

The Mediterranean Sea is a semi-enclosed marine basin which supports diverse ecosystems that are of vital socioeconomic importance to the many countries that border its shores (UNEP, 2005). The small size and enclosed nature of the Mediterranean Sea make it especially vulnerable to environmental change, such as changing climate and intensified metal pollution. Elevated concentrations of trace metals with known anthropogenic sources to the environment, such as lead (Pb), cadmium (Cd) and zinc (Zn), have been observed in the water column (*e.g.* Boyle *et al.*, 1985; Migon and Nicolas, 1998; Morley *et al.*, 1997; Statham *et al.*, 1985; van Geen *et al.*, 1988, 1991), marine sediments (*e.g.* Azoury *et al.*, 2013; Castillo *et al.*, 2013; Cossa *et al.*, 2014; Elbaz-Poulichet *et al.*, 2011; Martin *et al.*, 2009; Miralles *et al.*, 2006) and marine organisms (*e.g.* Benedicto *et al.*, 2011; Copat *et al.*, 2012; Yilmaz, 2003) at different locations in the Mediterranean Sea. These observations indicate that anthropogenic activities significantly impact the trace metal fluxes to coastal zones of the Mediterranean Sea. The delivery of trace metals from anthropogenic sources to the Mediterranean Sea is dominated by atmospheric transport processes and by continental runoff. Both of these trace metal transport vectors have received significant attention. Rivers receive and transport trace metals derived from various anthropogenic sources including agricultural runoff (Dumas *et al.*, 2015), urban runoff (Nicolau *et al.*, 2012), industrial effluent, acid mine drainage (Nieto *et al.*, 2007) and treated wastewater discharges (Oursel *et al.*, 2013). The atmospheric transport of natural and anthropogenic aerosols delivers trace metals to surface waters throughout the Mediterranean (Guieu *et al.*, 1997; Migon and Caccia, 1990). Recent observations have demonstrated decreased levels of phytoplankton biomass over large swaths of the western Mediterranean Sea after pulses of atmospheric deposition of copper-rich anthropogenic aerosols (Jordi *et al.*, 2012), highlighting the deleterious effects of high levels of trace metals on marine ecosystems. Although, much work has been done focusing on the sources of trace metals to the Mediterranean Sea and the accumulation of trace metals in sediments, there has been less focus on the distributions of dissolved trace metals, due to the challenging sampling and analytical methods required for acquiring reliable open ocean dissolved trace metal concentrations.

Trace metals are essential nutrients to phytoplankton at the base of the marine food web, yet can also be toxic at high levels. Thus, the distributions of dissolved trace

metals can significantly influence biological productivity. For example, availability of dissolved Fe limits primary productivity in high-nutrient low-chlorophyll (HNLC) regions, which account for over 30% of the world's ocean (de Baar *et al.*, 1990; Martin and Fitzwater, 1988; Moore *et al.*, 2013). In the Mediterranean Sea, the supply of trace metals through atmospheric deposition is extremely high compared to the open ocean (*e.g.* Guerzoni *et al.*, 1999) ensuring that biological productivity is not limited by the availability of essential trace metals. More concerning for the Mediterranean Sea, however, are the effects of the industrialization of Europe on the dissolved trace metal concentrations. As demonstrated by Jordi *et al.* (2012), the delivery of metal-laden aerosols to the surface ocean has detrimental effects on phytoplankton communities within the Mediterranean Sea. It is, however, the dissolved species of trace metals that are generally bioavailable to marine biota and it is therefore important to understand the distributions of trace metals in the Mediterranean Sea and how they influence modern marine ecosystems.

To date, there is a paucity of high-quality data available covering the full basin-scale distribution of dissolved trace metals in the Mediterranean Sea, which hinders our ability to understand the true scale of pollution in this vital marine basin. Here we report data from the Dutch GEOTRACES zonal transect in the Mediterranean Sea on the distributions of dissolved Fe, Zn, Cd and Pb. These elements were chosen based on current knowledge about the balance between natural and anthropogenic sources of these metals to the Mediterranean Sea. The data reveal a striking enrichment of anthropogenic dissolved trace metals in the western Mediterranean basin, relative to the known primary sources of water to the western Mediterranean, which are Atlantic Ocean surface waters and intermediate and deep waters formed in the eastern Mediterranean basin.

3.3 Materials and Methods

3.3.1 Study area

Samples were collected during GEOTRACES cruises 64PE370 (Lisbon-Istanbul; hereafter referred to as leg 1) and 64PE374 (Istanbul-Lisbon; hereafter referred to as leg 2) in the Mediterranean Sea aboard RV Pelagia during May-June 2013 and July-August 2013, respectively (Fig. 3.1). All stations were sampled for

dissolved trace metals with the exception of stations 1.25 and 1.37 during leg 1 and station 2.16 during leg 2. Leg 1 followed a west to east transect from the Atlantic Ocean to the eastern Mediterranean basin before turning north through the Aegean Sea (red outline in Fig. 3.1). Specifically, stations 1.1 to 1.4 were in the Atlantic Ocean, stations 1.5 to 1.12 were in the western Mediterranean basin, stations 1.13 to 1.15 were across the relatively shallow Channel of Sicily with bottom depths shallower than 1000 m (sill depth ~300 m), and stations 1.16 to 1.28 were in the eastern Mediterranean basin with station 23 being the most eastward. Stations 1.29 to 1.37 were in the Aegean Sea and the Sea of Marmara. Leg 2 generally followed an east to west transect beginning in the southern Aegean Sea and ending in the western Mediterranean basin. Specifically, station 2.1 was located in the southernmost region of the Aegean Sea, just to the north of the isle of Crete. Stations 2.2-2.11 were in the eastern Mediterranean basin and southern Adriatic Sea, stations 2.12-2.15 were in the Tyrrhenian basin, and stations 2.16-2.19 were in the western Mediterranean basin.

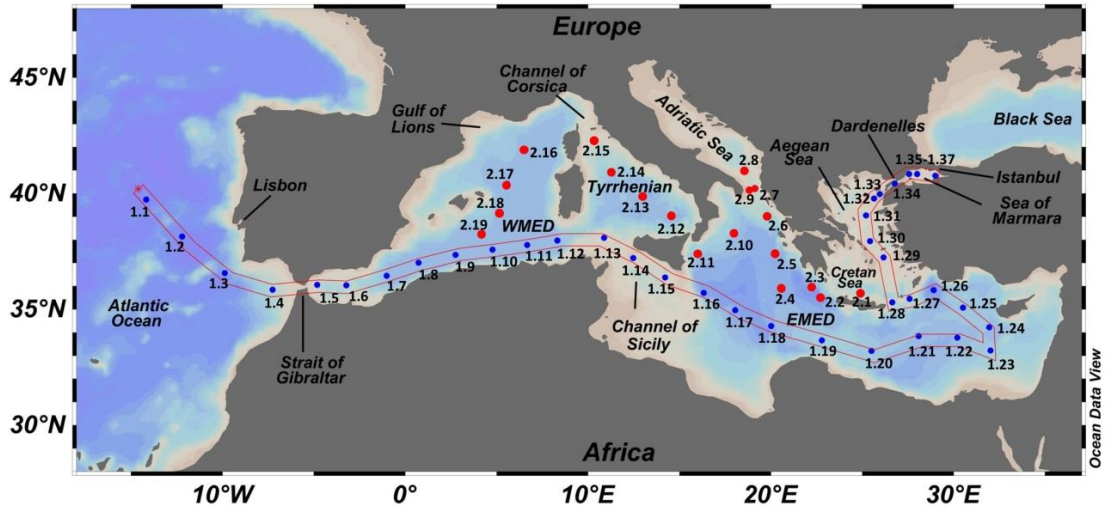

Fig. 3.1. Map of the sampling stations occupied during the GEOTRACES Mediterranean cruises 64PE370 (leg 1; blue circles) in May-June 2013 and 64PE374 (leg 2; red circles) in July-August 2013. Leg 1 followed a west to east track from the Atlantic Ocean through the Atlantic Ocean through the southern Mediterranean and finally through the Aegean Sea and Sea of Marmara as indicated by the red outline. Leg 2 followed an east to west track through the northern reaches of the Mediterranean Sea. WMED, western Mediterranean basin; EMED, eastern Mediterranean basin. This figure was made using Ocean Data View software (Schlitzer, 2015).

3.3.2 Sample collection

Seawater samples were collected using an ultraclean all-titanium framed TITAN CTD sampling system (de Baar *et al.*, 2008) outfitted with 24x24 L novel PRISTINE sample bottles constructed from ultrapure polyvinylidene fluoride (PVDF) and titanium (Rijkenberg *et al.*, 2015). Immediately upon recovery, the TITAN system was placed inside a purpose-built class 100 clean room container (de Baar et al, 2008). Inside the clean room container, seawater was filtered directly from the PRISTINE samplers using 0.2 µm filter cartridges (Sartobran-300, Sartorius) under nitrogen pressure (1.5 atm) and collected in 40 mL low density polyethylene (LDPE) bottles (Nalgene^{TM}, Fisher Scientific). All LDPE sample bottles were rigorously acid cleaned following the 'Sample and Sample-handling protocols for GEOTRACES cruises' (http://www.geotraces.org). Immediately after collection, samples were acidified to 0.024 M HCl using ultra-high purity 12 M HCl (SeastarTM Baseline®).

A Seabird SBE 911+ CTD system was used to measure the conductivity (salinity), temperature, pressure (depth), and dissolved oxygen *in situ* at each sampling station. The temperature sensor was calibrated using a high-accuracy reference-thermometer (Seabird SBE35), while the conductivity sensor was calibrated against shipboard salinity measurements of seawater samples.

3.3.3 Shipboard pre-concentration of trace metals from seawater

Detailed descriptions of the methods used for pre-concentrating trace metals from seawater are presented by Biller and Bruland (2012) and Middag *et al.* (2015). Slight modifications were made in order to make the methods more amenable to working while at sea. Briefly, a version of the off-line pre-concentration system described by Biller and Bruland (2012), which employs the Nobias- PA1 chelating resin to extract trace metals from seawater, was installed in a laminar flow bench inside a laboratory container aboard RV Pelagia. The system was composed of 8 individual micro-columns (~40 µL resin bed) and was therefore capable of pre-concentrating 8 samples simultaneously. The seawater samples remained acidified for at least 5 h before the pre-concentration was commenced. Exactly 40 mL of acidified seawater was then transferred from the original 40 mL LDPE sample bottle in to a second acid cleaned 40 mL LDPE using a 10 mL pipette. The 40 mL sample was then spiked with 50 µL of a Lu-In spike (resulting in a final concentration of 5 nM for both Lu and In in the final 40 mL sample assuming negligible Lu and In open ocean seawater), which

served as internal standards allowing for the calculation of the concentration of trace metals present in seawater based on an 'element dilution' approach (see Middag *et al.* (2015) for further details). The samples were then allowed 2 h to equilibrate before metal extraction. Immediately prior to the extraction, 20 µL of 1.2 M HF was added and the pH of the samples was adjusted to 5.8 ± 0.2 with ~500 µL of a 3.7 M ammonium acetate (NH_4Ac) buffer. Trace metals were then extracted by passing ~35 mL of the buffered samples across columns packed with clean Nobias resin. After loading of the sample, the columns were rinsed with 0.05 M NH_4AC to remove sea salt before elution. The metals were eluted in ~2 mL of 1 M HNO_3 containing 10 ng g^{-1} Rh which acts as an internal standard to monitor instrumental drift (described below). The eluent acid was collected in 8 mL acid cleaned LDPE bottles. The pre-concentration method results in a concentration factor of ~17.5 and the removal of >99.9% of salts present in the original seawater sample, allowing for the analysis of a suite of trace metals by high resolution ICP-MS, as described below.

The pre-concentration method was calibrated following the standard addition approach. A multi-elemental stock standard containing Ti, V, Mn, Fe, Co, Ni, Cu, Zn, Ga, Y, Zr, Cd, La and Pb with natural isotopic abundances was added to natural seawater containing low concentrations of metals. The Fe, Zn, Cd, and Pb will be discussed in this report while the other metals will be dealt with in separate reports. Five standard additions were used for the construction of the calibration curve. The standards were also spiked with the Lu-In spike to a concentration of 5 nM each. The standards were then processed alongside samples in an identical fashion. A standard addition calibration was performed approximately every 8 stations.

The performance of the shipboard pre-concentration method was verified and validated by processing SAFe Surface and Deep reference samples during every calibration. The trace metal concentrations in these reference materials analyzed by the shipboard pre-concentration method during the Dutch GEOTRACES expeditions to the Mediterranean and Black Sea in 2013 (cruises 64PE370, 64PE373, and 64PE374) are in good agreement with the GEOTRACES consensus values (Table 1; Middag *et al.*, 2015). Furthermore, 4 x 1 L samples of Mediterranean Outflow Water collected at station 1.1 were sub-sampled and processed during each of the calibrations to assess the reproducibility of the method. In total, the Mediterranean Outflow Water in-house reference same was processed 32 times and the average concentration and standard

deviation of the analyzed elements are shown in Table 2. The results of these reference materials demonstrate that the shipboard pre-concentration with 'element dilution' method and subsequent ICP-MS analysis (described in section 2.4) produces accurate and reproducible concentrations of multiple dissolved trace metals.

Table 3.1. Measured and consensus values of SAFe Surface (S) and Deep (D) reference samples (n = 4) with 1SD uncertainty.

Metal	SAFe S1 564		SAFe D1 323		SAFe D2 54	
	measured	consensus	measured	consensus	measured	consensus
Ti (pmol kg^{-1})	16 ± 1		103 ± 19		116 ± 7	
Mn (nmol kg^{-1})	0.81 ± 0.01	0.79 ± 0.06	0.37 ± 0.02		0.38 ± 0	0.35 ± 0.05
Fe (nmol kg^{-1})	0.10 ± 0.02	0.093 ± 0.008	0.64 ± 0.03	0.67 ± 0.04	0.94 ± 0.01	0.933 ± 0.023
Ni (nmol kg^{-1})	2.28 ± 0.02	2.28 ± 0.09	8.66 ± 0.12	8.58 ± 0.26	8.62 ± 0.2	8.63 ± 0.25
Zn (nmol kg^{-1})	0.08 ± 0.02	0.069 ± 0.010	7.43 ± 0.09	7.40 ± 0.35	7.44 ± 0.07	7.43 ± 0.25
Ga (pmol kg^{-1})	11.2 ± 0.1		7.3 ± 1.1		8.5 ± 1.2	
Y (pmol kg^{-1})	63 ± 1		194 ± 3		197 ± 2	
Zr (pmol kg^{-1})	7 ± 5		115 ± 9		33 ± 6	
Cd (pmol kg^{-1})	1.5 ± 0.1	1.1 ± 0.3	992 ± 13	991 ± 31	976 ± 12	986 ± 23
La (pmol kg^{-1})	4.7 ± 0.1		31.4 ± 0.2		31.4 ± 0.4	
Pb (pmol kg^{-1})	49.1 ± 0.2	48.0 ± 2.2	24.5 ± 0.3	27.7 ± 2.6	27.4 ± 0.2	27.7 ± 1.5

Consensus values are from the May 2013 intercomparison (www.geotraces.org).
Table is adapated from Middag et al. (2015) with the addition of the SAFe D1 sample and the Zr data.

Table 3.2. Results obtained for the Mediterranean Overflow Water in-house reference sample (n = 32).

	Ti (pM)	Mn (nM)	Fe (nM)	Ni (nM)	Zn (nM)	Ga (pM)	Y (pM)	Zr (pM)	Cd (pM)	La (pM)	Pb (pM)
Average	78	0.26	0.70	3.86	1.96	43	158	167	192	21.9	49.9
1 SD	9	0.02	0.03	0.09	0.09	2	3	10	3	0.4	1.3
RSD (%)	11%	7%	4%	2%	5%	4%	2%	6%	2%	2%	3%

3.3.4 Analysis of metals by ICP-MS

The metal analysis protocol used in the present study is described in detail elsewhere (Biller and Bruland, 2012; Middag *et al.*, 2015). Briefly, the pre-concentrated samples in ~2 mL of 1 M HNO_3 were analyzed directly on a Thermo Element XR magnetic sector inductively coupled plasma mass spectrometer (ICP-MS)

at the Institute of Marine Science, University of California, Santa Cruz. The ion beam intensities of $^{89}Y^{+}$, $^{90}Zr^{+}$, $^{111}Cd^{+}$, $^{139}La^{+}$, $^{208}Pb^{+}$, and $^{95}Mo^{+}$ were measured in low resolution mode, while the intensities of $^{47}Ti^{+}$, $^{51}V^{+}$, $^{55}Mn^{+}$, $^{56}Fe^{+}$, $^{59}Co^{+}$, $^{60}Ni^{+}$, $^{63}Cu^{+}$, $^{66}Zn^{+}$ and $^{69}Ga^{+}$ were measured in medium resolution. The ion beam intensities of $^{115}In^{+}$, $^{175}Lu^{+}$, and $^{103}Rh^{+}$ were measured in both low and medium resolution. The presence of Rh in the elution acid was used to monitor changes in the instrumental sensitivity. The concentration of metals in the initial seawater sample were calculated by dividing the ion beam intensities of each metal by the ion beam intensity of Lu, which normalizes the ion beam intensities of the metals to the concentration factor as the Lu ion beam intensity is proportional to the amount of sample loaded and the amount of elution acid used. Since the concentration of Lu in the initial seawater sample is known exactly (*i.e.* spiked to 5 nM), the concentration of the metals can then be determined. Similarly, in a separate calculation, the metal ion beam intensities can be divided by the ion beam intensity of In, thereby providing two independent determinations of the concentration factor with the average of the two values used for the final determination of the metal concentrations (see Middag *et al.* (2015) for further details). The presence of the polyatomic interference of $^{95}Mo^{16}O^{+}$ on $^{111}Cd^{+}$ was corrected by monitoring $^{95}Mo^{+}$ and calculating an oxide production rate based on Mo standards (Biller and Bruland, 2012). All samples, standards, blanks and reference materials which were processed using the shipboard pre-concentration method during the Dutch GEOTRACES expeditions in 2013 to the Mediterranean (cruises 64PE370 and 64PE374) and Black Seas (cruise 64PE373) were analyzed during one analytical session on the ICP-MS (~150 h total instrument time required for the analysis of ~2100 samples, standards, blanks, and reference samples).

3.4 General hydrography of the Mediterranean Sea

The thermohaline circulation in the Mediterranean Sea is complex and there are numerous reviews which cover the topic in detail (*e.g.* Millot and Taupier-Letage, 2005; Skliris, 2014). The hydrographic results obtained during the Dutch GEOTRACES expeditions in 2013 have been previously presented by Rolison *et al.* (2015) and are briefly summarized here. The Mediterranean Sea is a concentration basin (evaporation exceeds precipitation and runoff) and is connected to the Atlantic

Ocean via the Strait of Gibraltar. Due to net evaporation, the sea surface height of the Mediterranean Sea is slightly lower than the Atlantic Ocean, thereby promoting the inflow of surface Atlantic Water (AW; Millot and Taupier-Letage, 2005). The general flow path of AW can be tracked by a salinity minimum in surface Mediterranean waters (Fig. 3.2). The salinity of AW is ~36 as it enters the western Mediterranean basin (WMED), while the salinity of surface waters in the eastern Mediterranean basin (EMED) reaches >39. The salinity gradient in Mediterranean surface waters is a result of mixing between inflowing low salinity AW with high salinity Mediterranean surface waters and net evaporation. The high salinity surface waters of the EMED promote the formation of Levantine Intermediate Water (LIW) during winter time cooling. A second intermediate water mass formed in the EMED known as Cretan Intermediate Water (CIW), is less saline yet denser than LIW and is produced in smaller volume than LIW (Velaoras *et al.*, 2014). We note that LIW and CIW are difficult to distinguish from each other based on thermohaline characteristics alone and thus LIW is often used to denote all intermediate water present in the EMED and WMED, although new terminology for intermediate waters has been suggested (Millot, 2013). After formation, LIW spreads throughout the entire EMED and WMED and can be identified as a subsurface salinity maximum in the upper ~300 m in the EMED and across a depth range between ~200 and 600 m in the WMED before it eventually flows out of the Mediterranean Sea as the primary component of Mediterranean Outflow Water (MOW; Fig. 3.2). The core of MOW can be tracked as it spreads through the North Atlantic Ocean by a mid-depth salinity maximum centered around 1250 m. Deep water formation also occurs during winter time cooling in the northern regions of the Mediterranean Sea. The primary site of deep water formation in the EMED is the southern Adriatic Sea, but also forms in significant volume in the southern Aegean Sea under certain environmental conditions (Fig. 3.1). In the deep EMED, Adriatic Deep Water (AdDW) can be identified as the water mass with a salinity of <38.75, while Aegean Deep Water (AeDW) has a salinity >38.75 (Fig. 3.2). Deep waters exiting the EMED at the Sicily Channel is termed Eastern Mediterranean Deep Water (EMDW) and consists of contributions from both AdDW and AeDW. In the WMED, Western Mediterranean Deep Water (WMDW) is the only significant deep water and primarily forms in the region of the Gulf of Lions (Fig. 3.1).

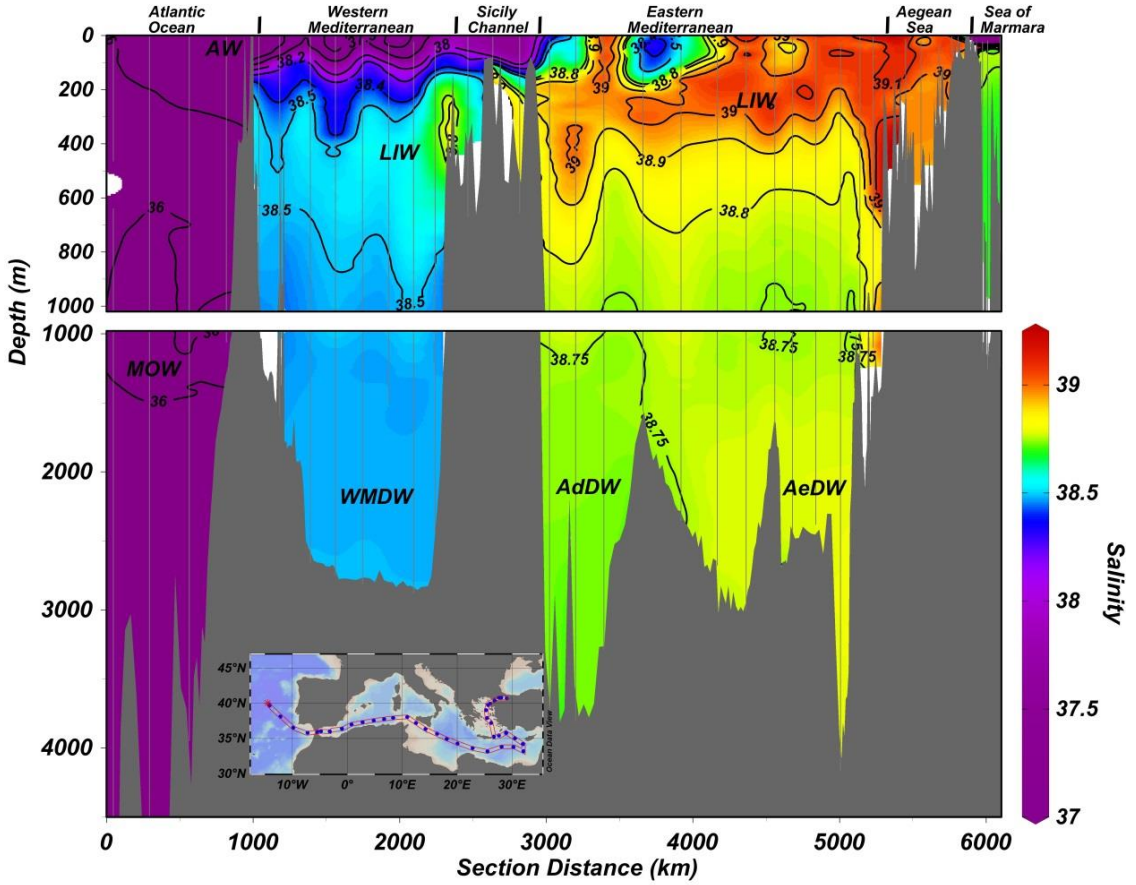

Fig. 3.2. Cross-section plot of salinity in surface waters (upper panel) and over the full depth of the water column (lower panel) in the Mediterranean Sea during the Dutch GEOTRACES cruise 64PE370. Contour lines represent isohalines. AdDW, Adriatic Deep Water; AeDW, Aegean Deep water; LIW, Levantine Intermediate Water; MOW, Mediterranean Outflow Water; WMDW, Western Mediterranean Deep Water.

3.5 Results

3.5.1 Zonal distribution of dissolved iron, zinc, cadmium, and lead in the Mediterranean Sea

The full depth zonal distributions of dissolved Fe, Zn, Cd, and Pb in the Mediterranean Sea are displayed in Fig. 3.3, 3.4, 3.5, and 3.6, respectively. The data reveal enrichments of dissolved Fe, Zn and Pb in the Mediterranean Sea relative to the Atlantic Ocean. Furthermore, within the Mediterranean Sea itself, there is a clear enrichment of dissolved Zn, Cd, and Pb in the sub-surface WMED relative to the sub-surface EMED.

3.5.1.1 Dissolved Fe

The vertical profiles of dissolved iron (Fe_d) at stations in the Atlantic Ocean display a mix of nutrient-type and scavenged-type behavior, known as a hybrid distribution (Bruland and Lohan, 2003; Johnson *et al.*, 1997), typical of open ocean environments. Minimum Fe_d concentrations of <0.1 nM are observed in Atlantic surface waters and increase to relatively constant values of ≥0.5 nM in Atlantic deep waters, with >0.7 nM in the core of Mediterranean Outflow Water. The distribution of Fe_d in the Mediterranean is, in general, opposite to that observed in the Atlantic Ocean. Specifically, the highest concentrations of Fe_d of >>1 nM are observed in the upper 100 m of the Mediterranean Sea water column, while deep waters are generally characterized by Fe_d concentrations of <0.5 nM. At intermediate depths between ~200 and 800 m, the concentration of Fe_d is highly variable. The distribution of Fe_d in WMED deep waters below 1000 m is relatively homogeneous with concentrations between ~0.3 and 0.5 nM in WMDW, while there is considerable structure in the distribution of Fe_d in EMED deep waters. The concentration of Fe_d ranges between ~0.1 and 0.75 nM in AdDW and ~0.3 and 1.25 nM in AeDW.

3.5.1.2 Dissolved Zn

Dissolved zinc (Zn_d) displays typical nutrient-like behavior in the Atlantic Ocean, as is expected in open ocean environments (Bruland *et al.*, 2014). Minimum Zn_d concentrations of <0.10 nM are observed in Atlantic surface waters, while concentrations increase to values >3 nM in Atlantic deep waters. The concentration of Zn_d in the core of Mediterranean Outflow Water is ~2 nM. The vertical distribution of Zn_d in the Mediterranean Sea is strikingly different compared to the Atlantic Ocean with an increase in absolute concentrations at similar depths. The concentration of Zn_d in upper 100 m of the Mediterranean Sea water column is generally >1 nM, increases rapidly with depth to values >4 nM at 200 m at a few localities in the WMED, and is relatively homogeneous with an average concentration of 4.3 ± 0.3 nM (1SD) at depths deeper than 500 m in the WMED. In the EMED, the concentration of Zn_d is relatively homogenous (~1 to 1.5 nM) in the upper ~300 m and increases to ~2 to 2.5 nM present at depths between ~300 and 750 m. The distribution of Zn_d in EMED deep waters is relatively homogenous with concentrations ranging between ~1.7 to 2.2 nM, with small patches of >2.2 nM. In general, the concentration of Znd is much higher in the WMED relative to the EMED, especially in intermediate and deep waters.

3.5.1.3 Dissolved Cd

Similar to Zn_d, dissolved cadmium (Cd_d) displays nutrient-like behavior in the Atlantic Ocean. Concentrations of Cd_d of ≤10 nM are observed in upper 100 m of Atlantic surface waters, while concentrations steadily increase to values >375 pM in Atlantic deep waters. The concentration of Cd_d in the core of Mediterranean Outflow Water is ~160 pM, which is higher than observed value in the Mediterranean Sea indicating significant mixing between MOW and Atlantic waters has likely already occurred. The distribution of Cd_d in the Mediterranean is similar to that of Zn_d. In the WMED, the concentration of Cd_d increases from ~40 to 50 pM in surface waters to a mid-depth maximum of ~80-90 pM across a depth range of ~150 to 500 m, and is relatively homogeneous at depths deeper than 500 m with concentrations between ~75 and 80 pM. In the EMED, the concentration of Cd_d in surface waters is ~50 to 60 pM while mid-depth maxima of ~70 to 80 pM are observed across a depth range of ~200 to 600 m. There is limited variability in the Cd_d concentrations in EMED deep waters below 1000 m. The concentration of Cd_d is ~60 to 65 pM in AdDW and is~55 to 60 pM in AeDW. Again similar to Zn_d, the concentration of Cd_d is generally elevated in deep waters in the WMED relative to EMED deep waters.

3.5.1.4 Dissolved Pb

The vertical profiles of dissolved Pb (Pb_d) in the Atlantic Ocean are punctuated by mid-depth maxima associated with Mediterranean Outflow Water. The concentration of Pb_d in the upper 100 m of Atlantic surface waters ranges between ~25 and 35 pM and increases to >50 pM at depths of 1000 to 1250 m in the core of MOW. Below 1250 m, the concentration of Pb_d steadily decreases with increasing depth to ≤20 pM below 4000 m. The concentration of Pb_d is, in general, elevated in the Mediterranean Sea relative to the Atlantic Ocean and is elevated in Mediterranean surface waters relative to deep waters. Surface waters of the WMED display the highest Pb_d concentrations with maximum values of ~150 pM observed. The concentration of Pb_d in EMED surface waters is generally lower than in WMED surface waters and ranges between ~60 and 80 pM. The distribution of Pb_d is relatively homogenous below 300 m in the WMED and ranges between ~75 and 85 pM in WMDW. The concentration of Pb_d is lower in deep waters of the EMED relative to WMDW, with

AdDW displaying Pb_d concentrations of ~60 to 65 pM and AeDW displaying Pb_d concentrations between ~55 and 60 pM.

3.5.2 Surface distribution of dissolved iron, zinc, cadmium and lead

Similar to the full depth distributions, the surface distributions of Fe_d, Zn_d, Cd_d, and Pb_d across the Mediterranean Sea at the shallowest depth sampled at each station (Fig. 3.7) also reveal an overall enrichment of trace metals in the Mediterranean Sea relative to inflowing Atlantic Water originated west of the Strait of Gibraltar. In general, the concentrations of Fe_d and Cd_d are highest in the eastern and northern regions. Excluding the stations in the Sea of Marmara, both Zn_d and Pb_d display the highest concentrations at to the west of the Sicily Channel (stations 1.12 and 1.13), and Pb_d is elevated in surface waters of the WMED and Tyrrhenian relative to the EMED.

3.5.3 Distribution of dissolved iron, zinc, cadmium and lead in the Sea of Marmara

Sub-surface water in the Sea of Marmara is primary composed of high salinity (>38.5) water inflowing from the EMED and Aegean Sea through the Dardanelles Strait. Low salinity (<30 at 25 m depth) surface water in the Sea of Marmara is significantly influenced by low salinity Black Sea water flowing in to the Marmara Sea through the Bosphorus Strait. The strong salinity stratification results in limited renewal of deep water, leading to low levels of dissolved oxygen (Fig. 3.8). Elevated levels of Fe_d, Zn_d, and Cd_d in the Sea of Marmara relative to the EMED were observed (Stations 1.35 and 1.36; Fig. 3.8). A maximum Fe_d concentration of ~9 nM is observed in surface waters and lower values between ~0.4 to 1 nM are observed a depths >150 m. The concentration of Zn_d ranges between a minimum of ~3 nM in deep waters and a maximum of ~8 nM at a depth of 100 m at station 1.36. The concentration of Cd_d ranges between a minimum of ~90 pM in surface water and a maximum ~128 pM at 400 m at both stations 1.35 and 1.36. In contrast, the concentration of Pb_d is lower in the Sea of Marmara relative to the Mediterranean Sea. The concentration of Pb_d steadily decreases with increasing depth from a maximum of ~65 pM in surface waters to <20 pM at depths below ~500 m (Fig. 3.8).

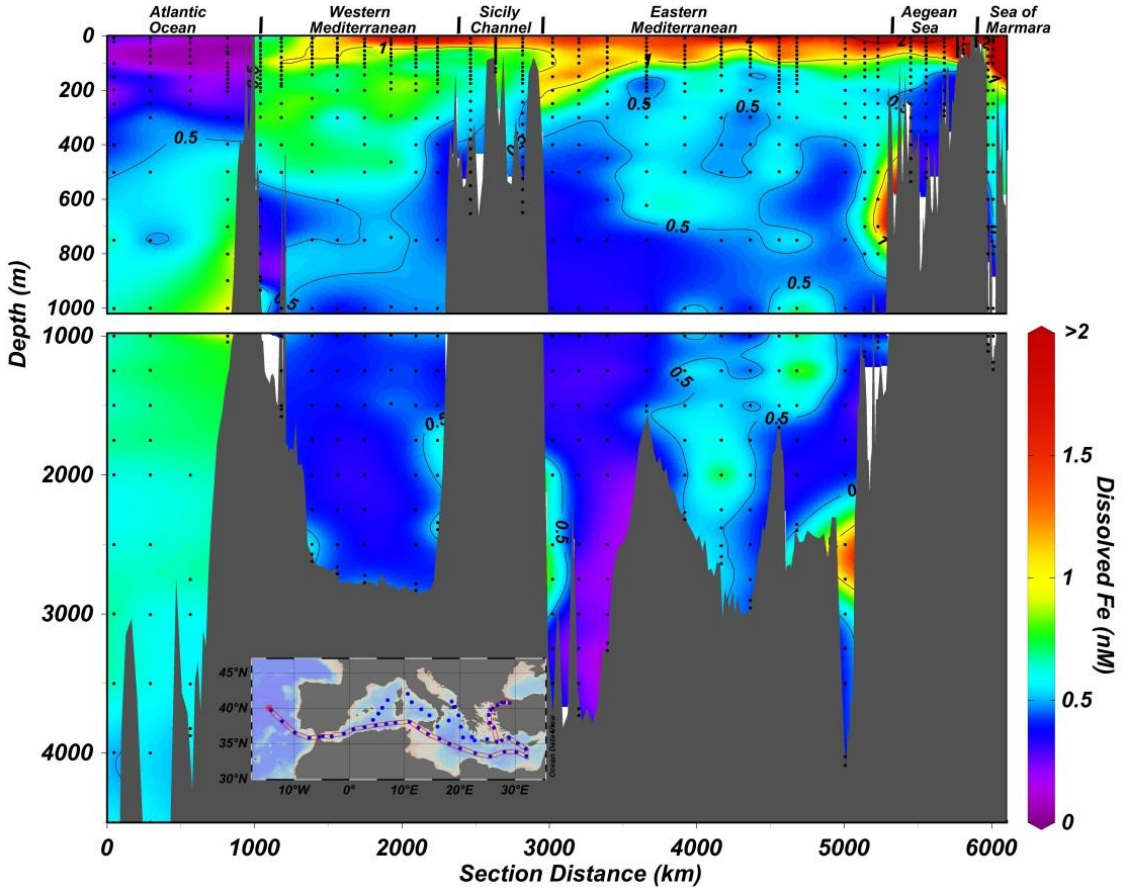

Fig. 3.3. Zonal distribution of dissolved iron in the upper 1000 m of the water column (upper panel) and at depths greater than 1000 m (lower panel) in the Mediterranean Sea during the Dutch GEOTRACES cruise 64PE370. The cruise track of cruise 64PE370 is highlighted by the red outline in the inset map.

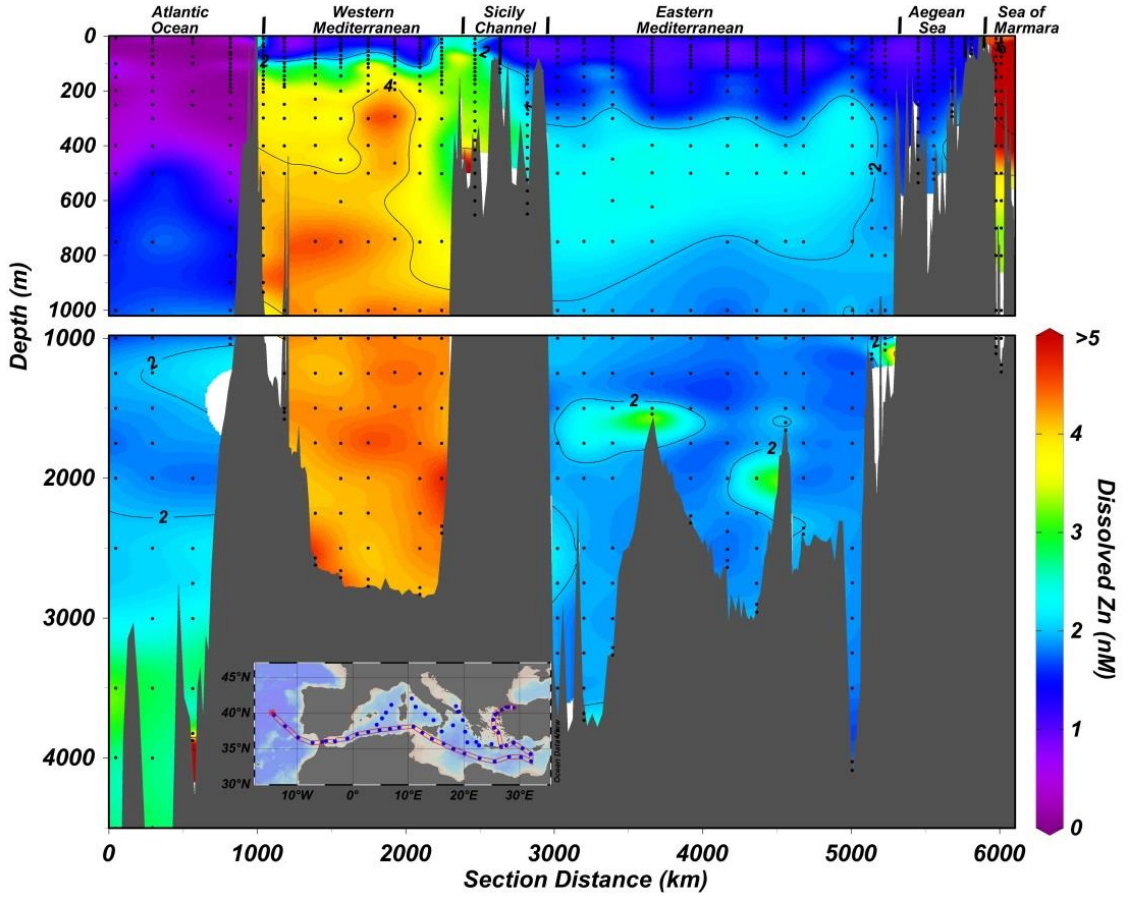

Fig. 3.4. Zonal distribution of dissolved zinc in the upper 1000 m of the water column (upper panel) and at depths greater than 1000 m (lower panel) in the Mediterranean Sea during the Dutch GEOTRACES cruise 64PE370. The cruise track of cruise 64PE370 is highlighted by the red outline in the inset map.

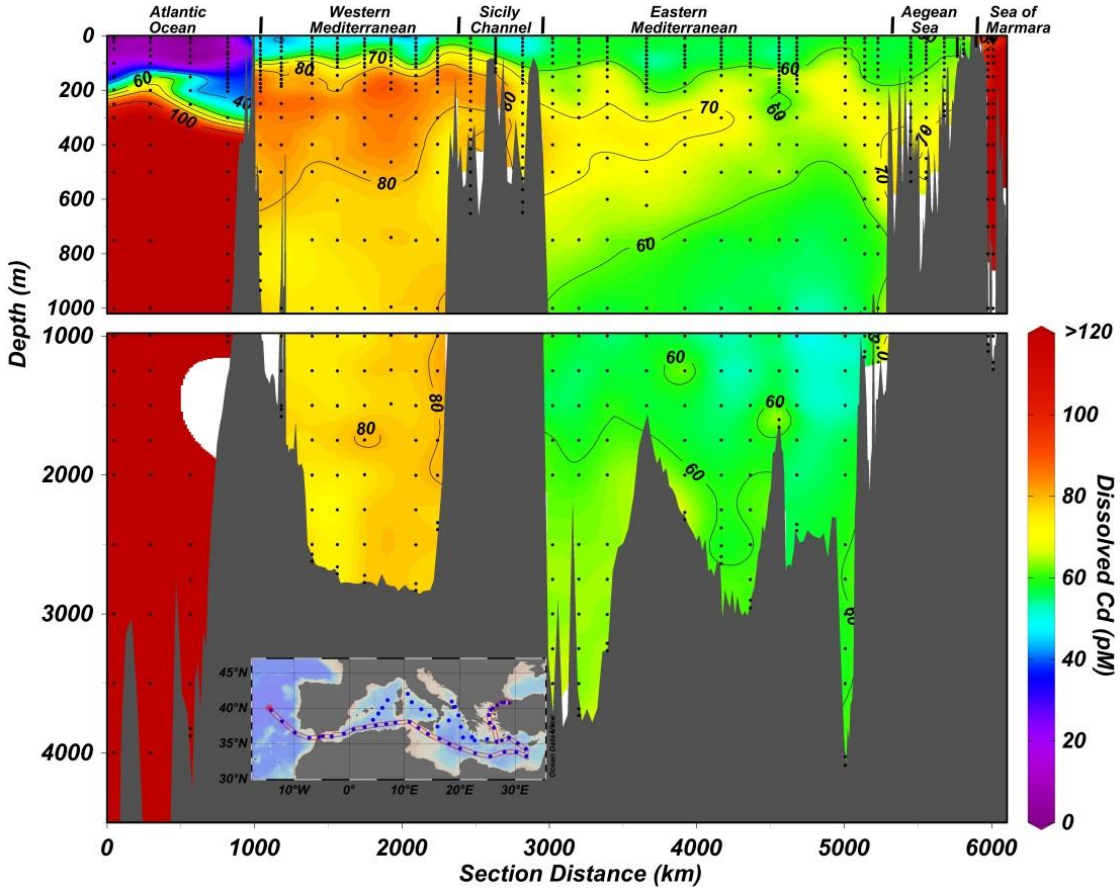

Fig. 3.5. Zonal distribution of dissolved cadmium in the upper 1000 m of the water column (upper panel) and at depths greater than 1000 m (lower panel) in the Mediterranean Sea during the Dutch GEOTRACES cruise 64PE370. The cruise track of cruise 64PE370 is highlighted by the red outline in the inset map.

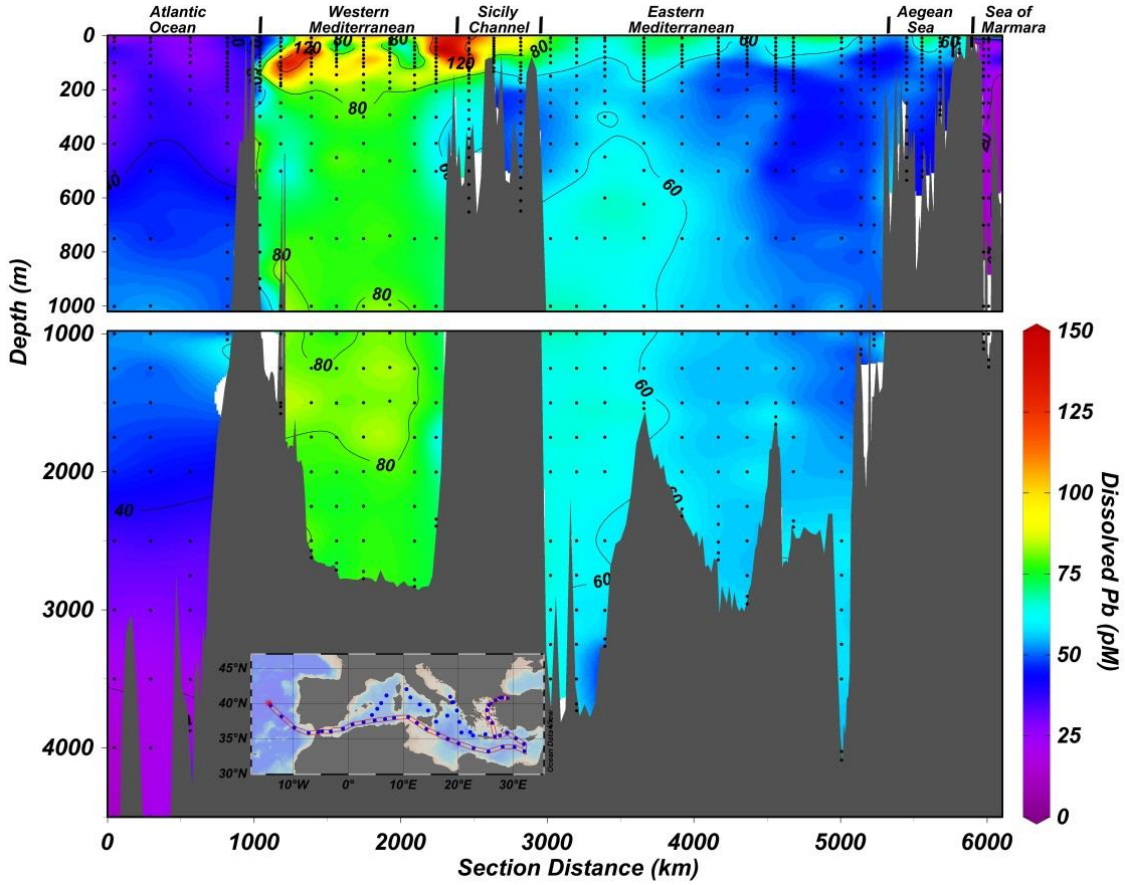

Fig. 3.6. Zonal distribution of dissolved lead in the upper 1000 m of the water column (upper panel) and at depths greater than 1000 m (lower panel) in the Mediterranean Sea during the Dutch GEOTRACES cruise 64PE370. The cruise track of cruise 64PE370 is highlighted by the red outline in the inset map.

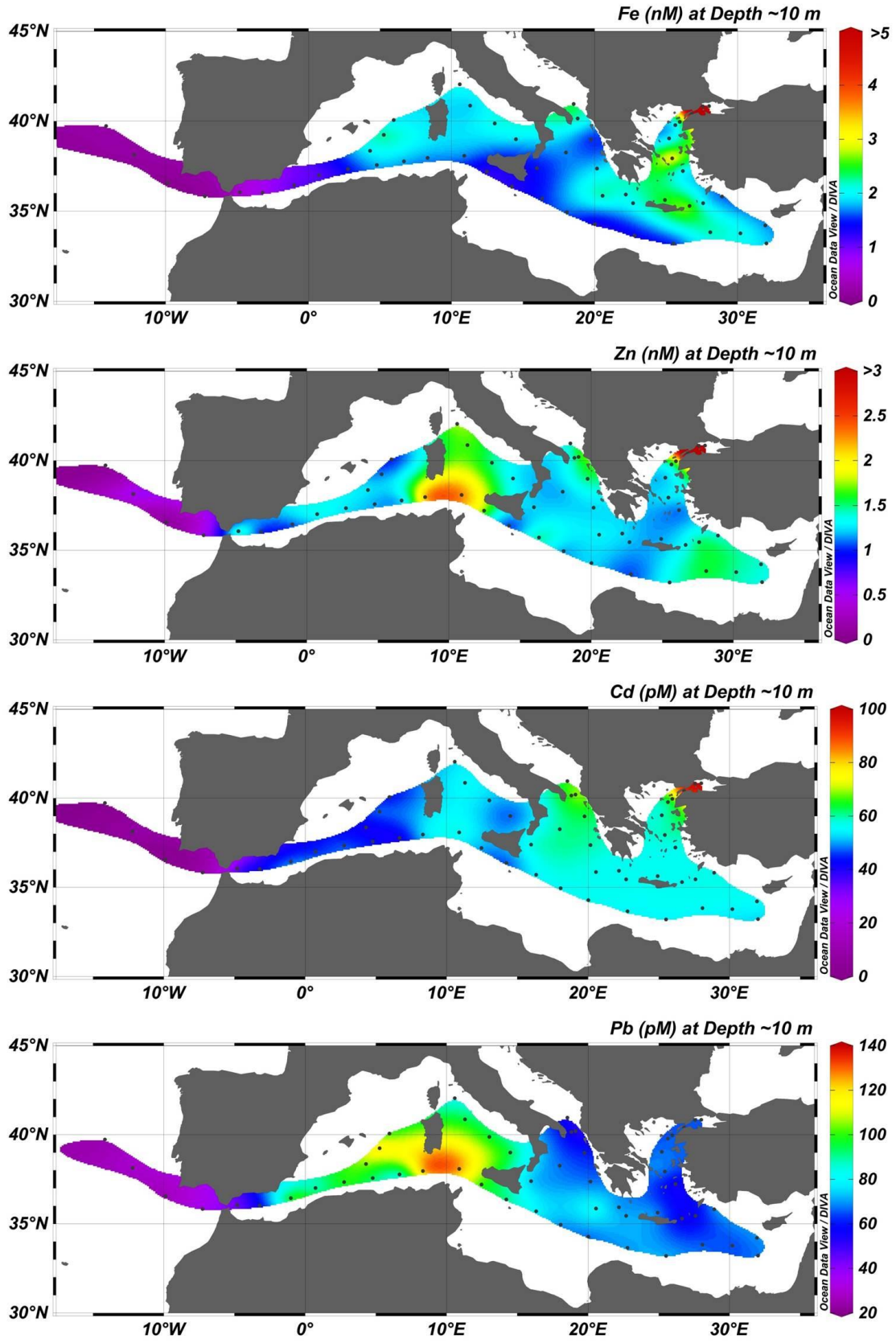

Fig. 3.7. Surface contour plots of dissolved Fe, Zn, Cd, and Pb in the Mediterranean Sea during the 2013 Dutch GEOTRACES cruises 64PE370 and 64PE374.

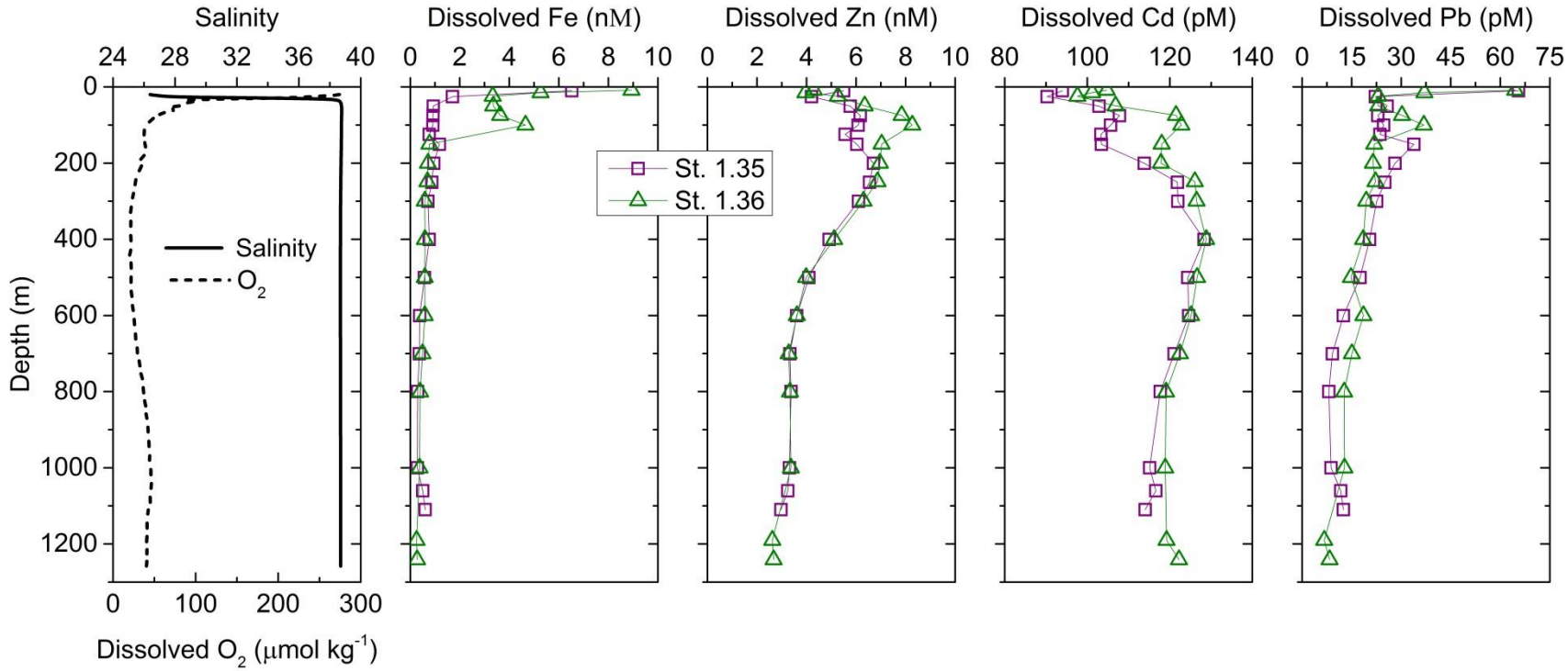

Fig. 3.8. Vertical profiles of salinity, dissolved O_2, Fe_d, Zn_d, Cd_d, and Pb_d at stations 1.35 (square symbols) and 1.36 (triangle symbols) in the Sea of Marmara. The salinity and dissolved O_2 profiles displayed are from station 1.36.

3.6 Discussion

The remarkable patterns observed in the zonal distributions of dissolved Fe, Zn, Cd, and Pb in the Mediterranean Sea reflects the net input and removal of these metals at the basin boundaries and the internal biogeochemical cycling of these metals within the different basins. We consider the Atlantic Ocean, the western Mediterranean, the eastern Mediterranean, and the Sea of Marmara as four separate basins that exchange water with adjacent basins. Thus, circulation represents a flux of metals out of one basin and into another. Additional fluxes of metals at basin boundaries include continental runoff, submarine groundwater discharge, atmospheric deposition, sedimentary sources/sinks, and hydrothermal sources/sinks. Internal biogeochemical processes affecting the distributions of trace metals include the uptake by living organisms, scavenging on to particle surfaces, release/regeneration during bacterial degradation of sinking particles, and burial when particles reach the seafloor before they are completely degraded. The formation of water masses (*i.e.* intermediate and deep waters) within individual basins also contribute to the distributions of dissolved metals. In the following discussion we will consider the effects of boundary fluxes and internal processes in each of individual basins in order to gain a better understanding of the primary controls on the distributions of dissolved Fe, Zn, Cd, and Pb in the Mediterranean Sea with special consideration for the importance of known anthropogenic versus natural sources of these metals.

3.6.1 Atlantic Ocean

The bioactive metals Fe, Zn, and Cd all display typical open ocean behavior at the four stations in the Atlantic Ocean. The lowest concentrations of Fe_d, Zn_d, and Cd_d are observed in surface waters (Fig. 3.3, 3.4, 3.5) primarily as a result of cellular uptake and utilization by photosynthetic microorganisms growing in sunlit surface waters. Metals can also be removed from solution in the surface ocean due to the process of scavenging which is the adsorption of metals to the external surfaces of suspended particles. For the case of Fe, Zn, and Cd, biological uptake is primarily responsible for maintain the low surface concentrations (*e.g.* Bruland *et al.*, 2015). Incorporated and scavenged metals are transported to the ocean interior by sinking particles and can be returned to the dissolved phase upon microbial degradation of organic matter associated with the host particle and/or dissolution of the calcareous or siliceous structural

components. Thus, the concentrations of bioactive metals increase with depth in the Atlantic Ocean (Fig. 3.3, 3.4, 3.5) with the oldest, deepest water masses tending to have the highest concentrations of bioactive metals, as is the case for Zn and Cd. The hybrid-type behavior of Fe results in relatively minor enrichments of Fe_d in deep waters comparted with enrichments observed for nutrient-type trace metals due to scavenging in deep waters (Bruland *et al.*, 2014).

Metals that are not essential to biology, such as Pb, tend to have distributions that differ significantly from the bioactive metals in the open ocean. Anthropogenic sources of Pb, especially leaded gasoline, have significantly increased the content of Pb_d of the upper North Atlantic Ocean since the industrial revolution (Kelly *et al.*, 2009; Shen and Boyle, 1988). Deposition of fine atmospheric aerosols transports anthropogenic Pb to the surface ocean where it is later transported to the ocean interior during mixing and ventilation of thermocline waters. Due to the phasing-out of leaded gasoline in North America and Europe, the concentration of Pb_d in North Atlantic surface waters has decreased dramatically by 5-10 fold since the 1980s, but the legacy of anthropogenic Pb_d still persists in thermocline water masses which were ventilated well before the phase-out resulting in a current day Pb_d maximum at intermediate depths across the North Atlantic Ocean (Noble *et al.*, 2015). The maximum Pb_d concentrations observed in North Atlantic thermocline waters have steadily decreased and deepened due to mixing with uncontaminated deep waters, ventilation, and scavenging and release (Noble *et al.*, 2015). Furthermore, the strong scavenging of Pb_d from solution results in old deep waters with lower concentrations of Pb_d than younger surface and intermediate waters.

The preformed concentrations of metals (*i.e.* the metal concentration present in source waters at the time water masses are formed) exert a strong control on the oceanographic distributions of metals. In the Atlantic Ocean, Mediterranean Outflow Water contains preformed metal concentrations that differ from the adjacently located water masses present in the Atlantic Ocean. Specifically, the concentrations of Fe_d, Zn_d, and Pb_d in MOW are all elevated relative to water masses residing shallower and deeper than MOW in the water column of the Atlantic Ocean, while the concentration of Cd_d is lower in MOW. Thus, the presence of MOW centered at ~1250 m in the Atlantic Ocean, and the vertical transport processes and anthropogenic perturbation of the Pb distribution discussed previously, account for the overall distributions of Fe_d, Zn_d, Cd_d and Pb_d in this small region of the Atlantic Ocean.

3.6.2 Mediterranean Sea

The distributions of dissolved metals in the Mediterranean Sea display striking inter-basin fractionations with elevated concentrations of Zn_d, Cd_d, and Pb_d in the deep water of the western Mediterranean basin relative to the deep water of the eastern Mediterranean basin. In contrast, elevated concentrations of Fe_d are observed in surface waters relative to deep waters of both the EMED and WMED, with no obvious inter-basin fractionation of the deep waters. As the concentration of Fe_d of inflowing AW is very low, the surface maximum of Fe_d in both the EMED and WMED is indicative of a source of Fe to Mediterranean surface waters, such as continental runoff and/or atmospheric deposition. The influence of continental runoff is expected to be strongest in the coastal zone (Bruland *et al.*, 2014) and a recent assessment of available data on the metal concentrations in rivers draining in to the Mediterranean Sea suggests rivers are a minor source of metals to the Mediterranean Sea relative to sources from atmospheric deposition and inflowing AW at the Strait of Gibraltar (Elbaz-Poulichet, 2005). Thus, the primary source of metals to surface waters of the Mediterranean Sea is likely atmospheric deposition, especially during times of limited vertical mixing due to strong stratification.

Atmospheric deposition in the Mediterranean Sea is a source of metals with variable anthropogenic and natural origins (Guieu *et al.*, 2010; Migon and Caccia, 1990). The natural lithogenic contribution to atmospheric deposition of metals to surface waters can be estimated by analyzing the ratio of the metal content to the aluminium (Al) content in the atmospheric aerosol particles themselves and comparison of these ratios to the metal/Al ratios (Me/Al) in the source lithogenic material. In the Mediterranean Sea, the primary source of lithogenic material in atmospheric particles is Saharan dust (Guieu *et al.*, 2002; Guieu *et al.*, 2010). Elevated Me/Al ratios in atmospheric particles relative to the background Me/Al ratios in the Saharan dust end member indicate an additional source (*i.e.* anthropogenic) of metals to atmospheric deposition in the Mediterranean Sea. This normalization method assumes that anthropogenic sources of Al in atmospheric particles are negligible and that Al in atmospheric particles is nearly completely derived from a single lithogenic source with known Me/Al ratios. Using this method, Guieu *et al.* (2010) estimated that at the scale of the entire Mediterranean Sea the atmospheric deposition of Fe is ~89% lithogenic in origin, while Zn, Cd, and Pb are ~88%, 96%, and 81% anthropogenic in origin,

respectively. Furthermore, no significant spatial gradients were evident in the atmospheric deposition of these metals in the Mediterranean Sea during the study of Guieu *et al.* (2010), but the temporal and spatial patterns of deposition are expected to be highly variable. Thus, the elevated concentrations of Fe_d in Mediterranean surface waters relative to inflowing AW (Fig. 3.3) can be tentatively ascribed to the accumulative effect of atmospheric deposition, with a primarily lithogenic origin. Furthermore, given that atmospheric deposition is the primary source of metals to the Mediterranean and that atmospheric deposition of Zn, Cd and Pb is supposedly dominantly derived from anthropogenic sources, implies that the elevated concentrations of Zn_d, Cd_d, and Pb_d in Mediterranean surface and deep waters relative to inflowing AW are possibly a consequence of atmospheric deposition of anthropogenic particles. The elevated concentrations of Zn_d, Cd_d, and Pb_d observed in WMED deep waters relative to EMED deep waters may be related to spatial gradients in atmospheric deposition of anthropogenic particles and/or other processes that may redistribute dissolved metals within the confines of the Mediterranean Sea, as discussed below.

3.6.2.1 Western Mediterranean basin

Using simple calculations we demonstrate that fluxes of metals associated with water exchange at the basin boundaries cannot account for the elevated levels of metals in the WMED relative to the EMED. The water budget in the WMED is dominated by the fluxes at the Strait of Gibraltar and the Sicily Channel, which vary significantly between winter and summer. At the Strait of Gibraltar, AW flows into the WMED at a rate of ~1 Sverdrup (Sv = 10^6 m^3 s^{-1}) which is approximately <10% greater than the flux of MOW exiting the WMED, resulting in a net exchange of <0.1 Sv (Tsimplis *et al.*, 2006; Soto-Navarro *et al.*, 2010). Similar fluxes are estimated at the Sicily Channel such that modified AW exits the WMED at the Sicily Channel at a rate of ~1 Sv and LIW flows in the reverse direction at a similar rate (Van Cappellen *et al.*, 2014). For simplicity, all fluxes considered here are assumed to be identical and equal to 1 Sv. The estimated dissolved metal contents of inflowing AW, modified AW, LIW, and MOW are summarized in Table 3. At the Strait of Gibraltar, the metal concentrations in inflowing AW are estimated from the average concentrations in samples from the upper 100 m at stations 1.1-1.3 and the metal concentrations in outflowing MOW are estimated from the average concentrations in samples from depths between 200 and

500 m at station 1.5. At the Sicily Channel, the metal concentrations inflowing LIW are estimated from the average concentrations in samples from depths between 200 and 500 m at stations 1.16-1.17 and the metal concentrations in outflowing modified AW are estimated from the average concentration in samples from the upper 100 m at stations 1.11-1.12. The concentrations of Fe_d, Zn_d, Cd_d, and Pb_d are all higher in MOW than in inflowing AW, resulting in a net flux of metals out of the WMED at the Strait of Gibraltar. At the Sicily Channel, the concentrations of Fe_d and Pb_d are higher in modified AW than in LIW, while the concentrations of Zn_d and Cd_d are similar (within the stated uncertainty) in modified AW than in LIW, resulting in a net flux of Fe_d and Pb_d out of the WMED and a near zero net flux of Zn_d and Cd_d. Thus, water mass fluxes at the boundaries of the WMED result in a total net flux of Fe_d, Zn_d, Cd_d, and Pb_d out of the WMED and physical circulation cannot account for the patterns of enrichment observed for these metals in the Mediterranean Sea, and additional sources of these metals to the WMED are required to maintain the elevated concentrations. Importantly, small changes in the water fluxes or concentrations of dissolved metals in the different water masses will not change the general observation that the physical circulation results in a net flux of metals out of the WMED.

The effect of the flux of particulate trace metals through straits on the dissolved trace metal budget of the WMED is more difficult to constrain as particulate data is not yet available for this cruise. Atlantic surface waters possibly contain elevated concentrations of trace metals in the particulate phase due to biological uptake and atmospheric deposition. As Atlantic surface water circulates through the Mediterranean Sea, the particulate trace metals could be released to the dissolved phase thereby contributing to the flux of trace metals through the straights. Of primary concern is the labile fraction of the particulate trace metals which can be readily transferred to the dissolved phase upon remineralization of the particle. The labile fraction is generally associated with soft organic tissue rather than the more refractory lithogenic fraction. Twinning *et al.* (2015) reported levels of labile particulate Fe, Zn, and Cd from Atlantic surface waters off the coast of Portugal determined as part of the 2010/2011 U.S. GEOTRACES North Atlantic Zone Transect. The labile fractions of particulate trace metals were on average less than 0.25 nM Zn, 5 pM Cd, and 1 nM Fe in the upper 150 m. Elevated concentrations of particulate Fe were observed near the continental margin close to Lisbon, but quickly diminished moving offshore. Thus, fluxes of particulate Zn and Cd are not likely to strongly influence the net flux of trace metals across the Strait

of Gibraltar or change the general observation that the distributions of dissolved Zn and Cd in the Mediterranean Sea require sources of these metals internal to the WMED. The influence of particulate Fe is likely more prominent, but it is expected that the WMED receives strong internal fluxes of particulate Fe due to the small size of the Mediterranean Sea and that these internal fluxes would far exceed the flux of particulate Fe fluxing through the Strait of Gibraltar.

Table 3.3. Average concentrations of dissolved metals observed in water masses entering and exiting at the western Mediterranean boundaries. (± 1 standard deviation)

		Strait of Gibraltar		Sicily Channel	
		Input	Output	Input	Output
		AW	MOW	LIW	Modified AW
Fe_d	(nM)	0.1 ± 0.1	0.7 ± 0.1	0.6 ± 0.2	1.1 ± 0.4
Zn_d	(nM)	0.2 ± 0.2	4.0 ± 0.1	1.9 ± 0.3	2.1 ± 1.3
Cd_d	(pM)	7 ± 6	85 ± 5	69 ± 6	56 ± 14
Pb_d	(pM)	30 ± 4	68 ± 13	54 ± 2	101 ± 37

AW - Atlantic Water; MOW - Mediterranean Outflow Water;
LIW - Levantine Intermediate Water.

The distributions of Zn_d and Cd_d in the WMED are quite similar with both elements displaying lower concentrations in surface waters compared to intermediate and deep waters. Morely *et al.* (1997) suggested that mixing between inflowing AW with underlying LIW controls the distribution of Cd_d in the upper water column of the WMED. Our data supports their conclusions and we further demonstrate that the distributions of both Zn_d and Cd_d correlate with salinity in the upper water column of the WMED (Fig. 3.9a, b), with low concentrations of Zn_d and Cd_d in inflowing AW and elevated concentrations in underlying LIW. Furthermore, Rolison *et al.* (2015) demonstrated that the distribution of dissolved Al (Al_d) in the WMED is primarily controlled by conservative mixing between the different water masses present in the basin including AW, LIW and WMDW (Fig. 3.9c). The strong relationships between Zn_d and Cd_d with Al_d (Fig. 3.9e, f) provide additional evidence that the distributions of Zn_d and Cd_d are strongly controlled by mixing over the full depth of the water column in the WMED. Specifically, upward advection and turbulent mixing between LIW and WMDW supplies the upper water column with Zn_d and Cd_d, resulting in the strong relationship between the two metals (Fig. 3.9d). The relatively high concentrations of

Zn_d and Cd_d in LIW and WMDW must therefore be supported by a source of these metals to intermediate and deep waters, assuming the distributions of Zn_d and Cd_d in the WMED are in steady state. Since atmospheric deposition of anthropogenic particles is considered to be the primary source of Zn and Cd to the Mediterranean Sea, there also must be vertical transport of Zn and Cd from surface waters to deep waters, such as deep water formation or vertical transport via sinking particles. The formation of WMDW primarily occurs in the region of the Gulf of Lions (Millot and Taupier-Letage, 2005), and therefore it is important to constrain the concentrations of dissolved metals in this region in order to better understand how deep water formation controls the dissolved metal concentrations in WMDW. Unfortunately, no stations were occupied in this region during the 2013 GEOTRACES expeditions precluding a detailed discussion of the dissolved metal concentrations in WMDW precursor water. The homogenous distribution of Zn_d and Cd_d in WMDW indicates that inter-annual variability in the preformed concentrations of Zn_d and Cd_d in newly forming WMDW has little impact on the overall distribution of these metals. This is likely due to the preformed concentrations of Zn_d and Cd_d in new WMDW being similar to concentrations of these metals in resident WMDW and rapid mixing preventing preservation of small inter-annual variability in the preformed metal concentrations of WMDW. A constant vertical flux of metal laden particles dissolving through the water column of the WMED could also account for the relatively homogenous concentrations of Zn_d and Cd_d in WMDW. As atmospheric deposition is highly variable, the homogeneous distributions of Zn_d and Cd_d in WMDW are likely due to low variability of Zn_d and Cd_d concentrations in WMDW precursor waters. Interestingly, the average concentration of Zn_d of 4.3 ± 0.3 nM (1SD) at depths deeper than 500 m in the WMED is very similar to the average Zn_d concentration of 3.9 ± 0.5 nM (1SD) at depths deeper than 300 m in the WMED in 1983 as reported by Ruiz-Pino *et al.* (1991). The similarity of the two estimates suggests that the source of Zn to the WMED has remained relatively constant for at least three decades. Time-series measurements show an ~54% decrease in the Zn concentrations in atmospheric aerosols at Cap Ferrat, France in the north-west Mediterranean between 1998 and 2008 (Heimbürger *et al*., 2010), implying that other sources, such as vehicle tire wear and waste incineration, are responsible for maintain the elevated Zn concentrations in WMDW. Alternatively, the relatively stable Zn concentration in WMDW may reflect a stable concentration of Zn binding ligands which help keep Zn dissolved in solution and that may effectively set the upper limit

for the Zn concentration in WMDW. In this scenario, the magnitude of the source of Zn is less important so long as enough Zn is supplied to maintain saturation of the Zn binding ligands.

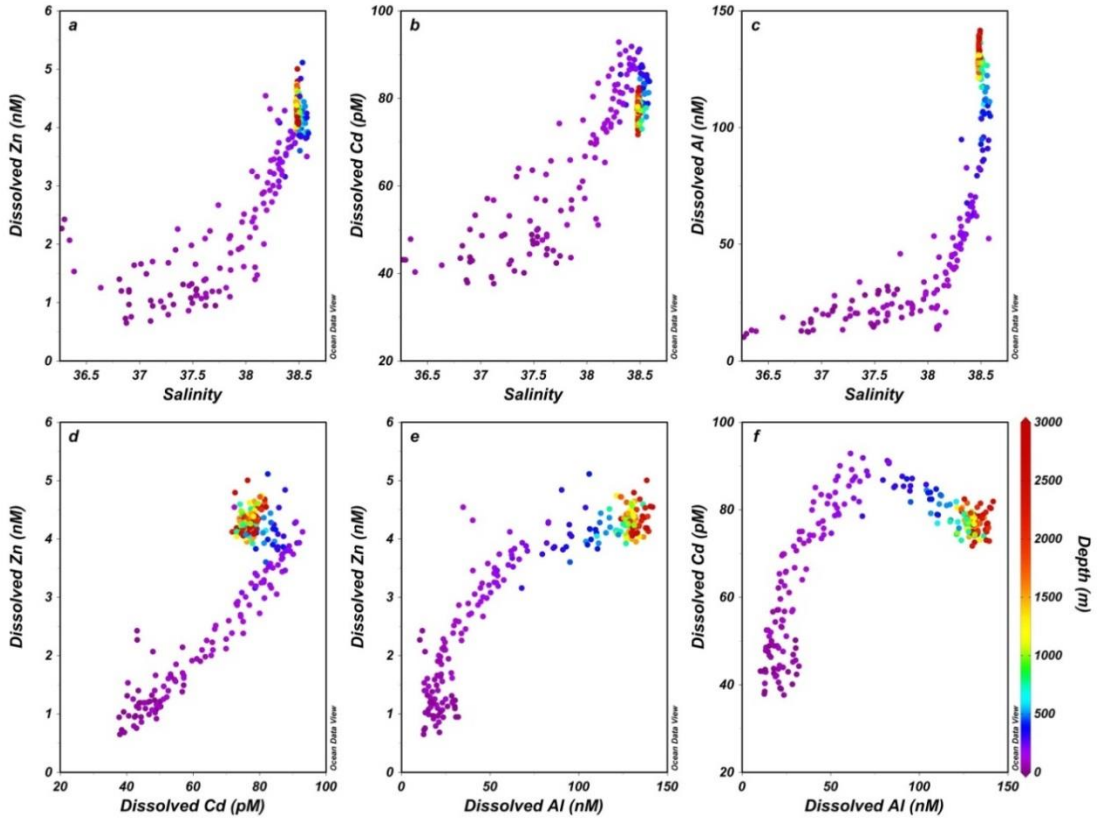

Fig. 3.9. Relationships between salinity and dissolved Zn (a), salinity and dissolved Cd (b), salinity and dissolved Al (c), dissolved Cd and Zn (d), dissolved Al and Zn (e), and dissolved Al and Cd (f) over the full water column of the western Mediterranean basin. The color bar scale for depth in (f) applies to all panels. Data is from stations 1.5-1.11 and 2.17-2.19 occupied during the 2013 Dutch GEOTRACES cruises 64PE370 and 64PE374.

In contrast to the distributions of Zn_d and Cd_d in the WMED, the distributions of Fe_d and Pb_d display elevated concentrations in surface waters relative to intermediate and deep waters, indicating that atmospheric deposition exerts a strong control on the distribution of these metals. The highest concentrations of Pb_d (*i.e.* >100 pM; max = 161 pM) are spatially limited to surfaces waters in the WMED, while the elevated concentrations of Fe_d in surface waters also extend throughout the EMED. To a first order, these observations suggest that atmospheric deposition of Pb to surface waters is strongest in the WMED, while atmospheric deposition of Fe to surface waters is more evenly distributed across the entire Mediterranean Sea. The study of Guieu *et al.* (2010)

reported approximately a factor of two higher atmospheric deposition of Fe in the WMED than in the EMED during one year of continuous sampling of wet and dry deposition at nine locations spanning the entire Mediterranean Sea, but this result was likely biased by the sampling of an intense Saharan dust storm that only impacted one sampling site which was located in the WMED. No difference in the atmospheric deposition of Pb between the WMED and EMED was observed during the same study, but the authors did observe a slight increase in the atmospheric deposition of Pb in the southern sampling sites relative to the northern sampling sites (Guieu *et al.*, 2010). As atmospheric deposition is highly variable both spatially and temporally, longer records with more spatial coverage of the sampling sites are required to better constrain overall atmospheric depositional patterns. Importantly, the distributions of Fe_d and Pb_d in surface waters of the Mediterranean Sea may reflect an integrated pattern of atmospheric deposition over the residence time of surface water in the Mediterranean Sea, which is not well constrained but estimated to be on the order of ~10 years based on a mixed layer depth of 100 m, total surface area of 2.5×10^6 km^2, and inflowing AW at a rate of 1 Sv. However, if the residence times of Fe and Pb are much shorter than 10 y in Mediterranean surface waters then distributions of Fe_d and Pb_d observed here only reflect the average atmospheric deposition of these metals during their respective residence times. Based on the Fe_d inventory in surface waters and concurrent measurements of atmospheric dry deposition, Croot *et al.* (2004) estimated a residence time of Fe_d in surface waters of ~1 to 10 yr in the highly dust impacted equatorial Atlantic Ocean. The residence time of Pb_d in surface waters of the Atlantic Ocean is estimated to be <1 yr (Nozaki *et al.*, 1976) and may be shorter in the Mediterranean Sea due to elevated rates of scavenging associated with the high atmospheric deposition. Thus, we attribute the elevated concentrations of Pb_d in WMED surface waters to the atmospheric deposition of anthropogenic Pb, although we note that the source of Pb could also be related to terrestrial inputs, such as runoff, as most stations occupied during leg 1 are <100 km away from the nearest land mass and can therefore still be influenced by coastal processes (Morely *et al.*, 1997). The distribution of Fe_d in Mediterranean surface waters (Fig. 3.3 and 3.7a) suggests that atmospheric deposition of Fe continuous in both the WMED and EMED and that the residence time of Fe_d is long enough in Mediterranean Surface waters for it to continuously accumulate in surface waters as they circulate following a roughly west to east flow path. If shorter residence times of Fe_d in surface waters are assumed (*e.g.*<1 month; Sarthou *et al.*,

2003), then the distribution of Fe_d in surface waters of the Mediterranean Sea may indicate a stronger flux of atmospheric deposition of Fe in the EMED relative to the WMED in the in the spring of 2013.

The distribution of Pb_d in intermediate and deep waters of the WMED is relatively homogenous (Fig. 3.6; average Pb_d = 76 ± 5 pM (1SD) below 500 m). Similar to the Atlantic Ocean, the concentration of Pb_d in the Mediterranean Sea has decreased dramatically since the phasing-out of leaded gasoline in the 1980s (Migon and Nicolas, 1998; Migon, 2005). The average concentration of Pb_d at depths >500 m at the DYFAMED site located north of Corsica steadily decreased from ~180 pM in 1987 to ~100 pM in 1998 (Migon, 2005). Comparison of the DYFAMED site with the data obtained in this study demonstrates Pb_d concentrations at depths >500 m in the WMED have possibly decreased by a further ~25 pM in the past ~15 y. The slowing rate of decreasing Pb_d concentrations in WMED intermediate and deep waters reflects the trend in decreasing atmospheric Pb concentrations over the WMED which have also markedly slowed down (Migon et al, 2008). In contrast to intermediate and deep waters, surface waters in the WMED display concentrations of Pb_d values of >100 pM, suggesting the concentration of Pb_d has remained constant or perhaps slightly increased in surface waters of the WMED since 1998 (Migon, 2005). Although the use of leaded gasoline has been phased-out in Europe, other anthropogenic sources of Pb are still active, such as sewage treatment plants and waste incinerators, which are likely contributing to maintaining the elevated concentrations of Pb_d in WMED surface waters and to the slowing rate of decreasing Pb_d concentrations in intermediate and deep waters. Additionally, leaded gasoline is still being used in the North African country Algeria (UNEP, 2015) which may be contributing to the elevated Pb_d concentrations in WMED surface waters. As part of the continuing effort of the GEOTRACES program, additional analyses of Pb isotope ratios in the same samples discussed in this study are in progress and will no doubt be useful for differentiating between the different sources of Pb in the WMED.

3.6.2.2 Eastern Mediterranean basin

The concentrations of Zn_d, Cd_d, and Pb_d are generally lower in the EMED than in the WMED in both surface and deep waters, while surface waters of the EMED display slightly elevated concentrations of Fe_d relative to surface waters of the WMED.

The distributions of Zn_d and Cd_d again resemble each other in the EMED, as in the WMED, and both display maximum concentrations over a broad depth range of ~200 to 750 m. Within this depth range there are two intermediate water masses. The intermediate water masses formed in the EMED in the largest volume and with the highest salinity is LIW. Cretan Intermediate Water (CIW), which forms in the Cretan Sea, a sub-basin of the southern Aegean Sea, forms with a slightly greater density than LIW and therefore resides below LIW in the water column (Velaoras *et al.*, 2014). As LIW has a higher salinity than CIW, the maximum Zn_d and Cd_d concentrations observed across the depth range of ~200 to 750 m should correlate with the highest salinities if the Zn_d and Cd_d maxima originate in LIW. However, Fig. 3.10 clearly demonstrates that the maximum Zn_d and Cd_d concentrations across this depth range do not correlate with the highest salinities (and therefore LIW), but rather correlate with a denser, less saline water mass deeper in the water column. The maximum Zn_d and Cd_d concentrations cluster around a potential density anomaly (σ) between ~29.10 and 29.17 kg/m^3 which is within the range of the observed σ of CIW (29.1 to 29.2 kg/m^3) produced between 2007 and 2009 (Velaoras *et al.*, 2014). Station 2.1 is the only station from the 2013 GEOTRACES expedition located within the Cretan Sea. Elevated concentrations of Zn_d and Cd_d are observed in deep waters with σ >29.15 at station 2.1 (Fig. 3.11), and support the role of CIW as the source of elevated Zn_d and Cd_d concentrations observed in the EMED across a depth range of ~200 to 750 m. Thus, the primary features of in the distributions of Zn_d and Cd_d in the EMED appear to be related their preformed concentrations in water masses produced within the EMED. Interestingly, the concentrations of Zn_d and Cd_d in AeDW, which also forms in the Cretan Sea, are not elevated (Fig. 3.4, 3.5) implying different water masses are utilized during intermediate versus deep water formation or temporal differences in the dissolved metal content in dense water residing within the Cretan basin.

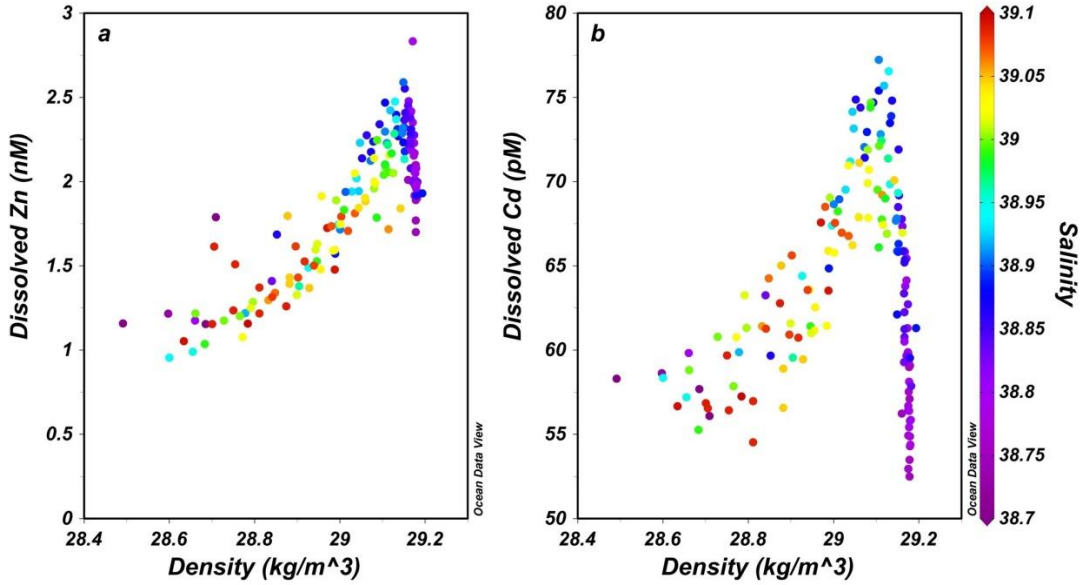

Fig. 3.10. Plot of dissolved Zn (a) and Cd (b) versus density (σ) in the eastern Mediterranean basin at depths of 100 to 1000 m. The color bar scale for salinity applies to both panels. The highest concentrations of Zn_d and Cd_d cluster around a density between ~29.11 and 29.17 kg/m^3 which is similar to the observed density of Cretan Intermediate Water (CIW). The data used to generate this figure is from stations 1.16-1.28 (excluding 1.23 and 1.25), 2.2-2.5, and 2.10-2.11 occupied during the 2013 Dutch GEOTRACES cruises 64PE370 and 64PE374.

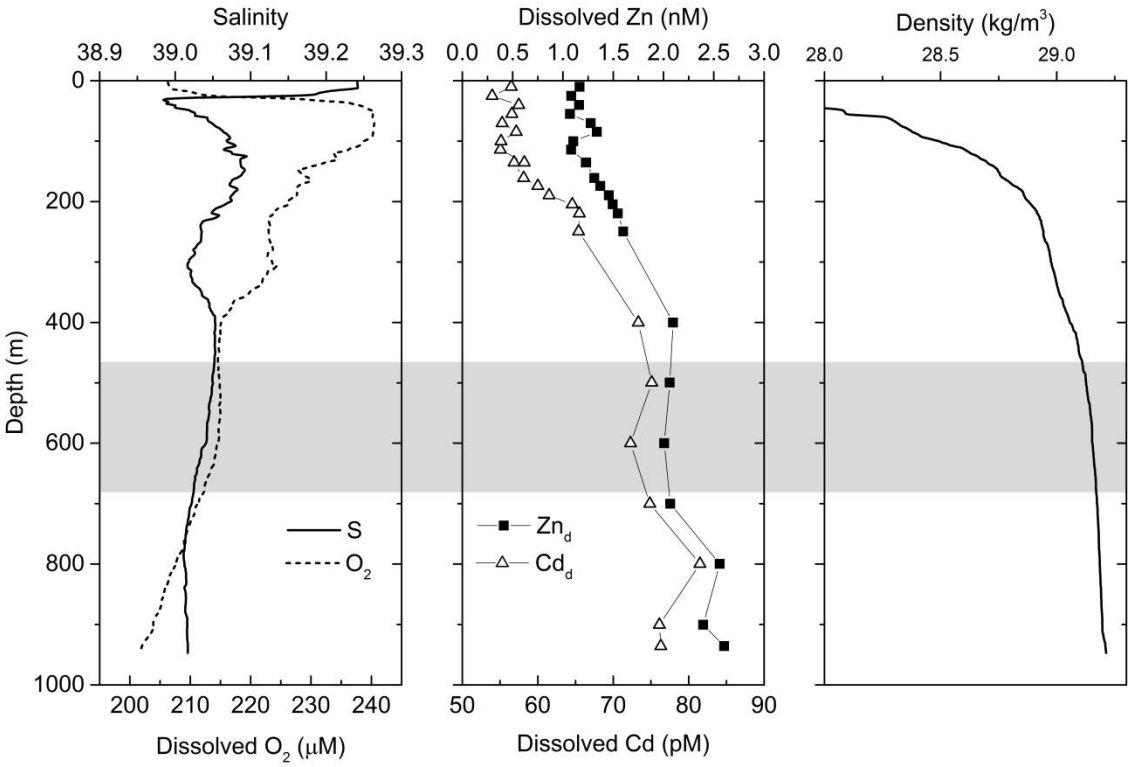

Fig. 3.11. Vertical profiles of salinity, dissolved oxygen, Zn_d, and Cd_d at station 2.1 in the Cretan Sea. The elevated concentrations of Zn_d and Cd_d at depths >400 m support the role of Cretan Intermediate Water as the source of elevated Zn_d and Cd_d

concentrations observed in the EMED across a depth range of ~200 to 750 m. The grey shading indicates a density (σ) between 29.11 and 29.17 kg/m^3.

The distribution of Pb_d in the EMED is similar to that in the WMED, with relatively elevated concentrations observed in surface waters relative to underlying intermediate and deep waters. However, the concentrations of Pb_d are generally lower in the EMED than in the WMED. Most striking is the sharp decrease in Pb_d in modified AW as it flows through the Sicily Channel with concentrations >100 pM observed immediately to the west of the channel at stations 1.12 and 1.13 and concentrations of <80 pM observed in surface waters throughout the entirety of the EMED. After exiting the Sicily Channel into the EMED, modified AW mixes with underlying LIW which has relatively low concentrations of Pb_d. Thus, the dilution of modified AW by LIW in the EMED results in decreasing Pb_d concentrations as modified AW circulates through the EMED. The linear relationships between Pb_d and salinity, and Al_d, in the upper 75 m of the water column along the flow path of modified AW in the southern EMED (stations 1.14-1.23; Fig. 3.12) confirms that physical mixing is the dominant process influencing the distribution of Pb_d and that no additional source of Pb_d besides inflowing modified AW is required to explain the distribution of Pb_d in surface waters of the EMED. The average concentration of Pb_d in EMED deep waters (>500 m) is 59 ± 5 pM (1SD) and is lower than the average deep water concentration of Pb_d in the WMED (76 ± 5 pM). There is a small difference between the Pb_d concentrations in the different deep water masses with AdDW displaying slightly higher concentrations than AeDW (Fig. 3.6). Overall, the zonal gradient in the Pb_d distribution, displaying higher concentrations in the WMED relative to the EMED (Fig. 3.6, 3.7), is suggestive of a larger anthropogenic source of Pb to the WMED than the EMED over the residence time of deep water in the Mediterranean Sea which is estimated to be 50-100 yrs (Millot and Taupier-Letage, 2005).

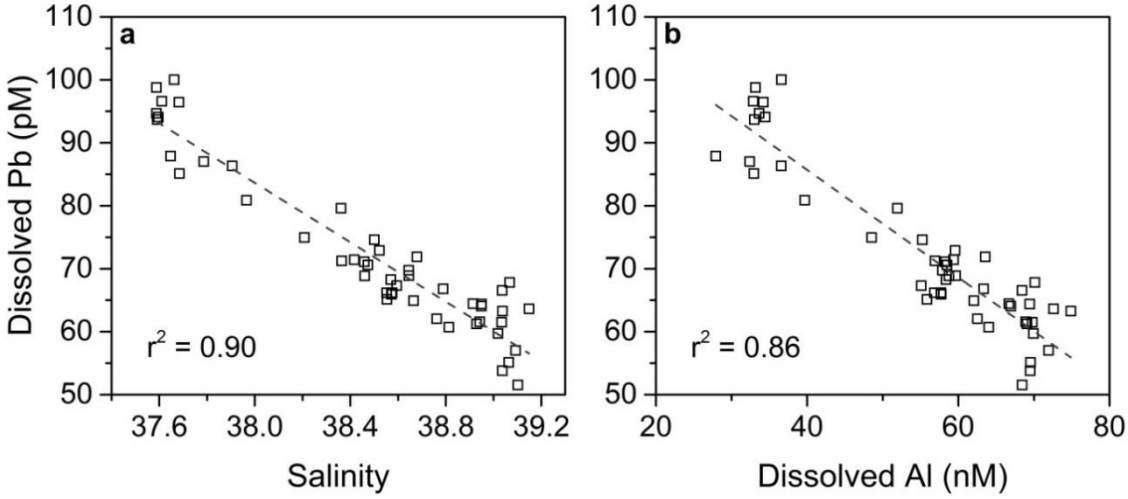

Fig. 3.12. Concentration of dissolved Pb versus salinity (a) and dissolved Al (b) in the upper 75 m of the water column along the flow path of modified Atlantic water within the eastern Mediterranean basin at stations 1.14-1.23.

3.6.2.3. Impact of anthropogenic sources of trace metals

The role of anthropogenic activities in the distribution of Pb_d is well established. Higher concentrations of Pb_d in the WMED indicate that sources of anthropogenic Pb are stronger in the WMED relative to the EMED. Anthropogenic sources of Zn and Cd are also well known and the concentrations of Zn_d and Cd_d are higher in the WMED relative to the EMED. The regional similarities between the distributions of Pb_d, Zn_d, Cd_d, is a perhaps an important indication that the WMED is strongly impacted by anthropogenic sources of these metals, at least significantly more so than the EMED. Furthermore, the lack of any relationship between the distributions of Zn_d and Cd_d with the distribution of Fe_d, which is likely a tracer of natural dust deposition, indicates that the largest natural source of trace metals to the Mediterranean Sea (*i.e.* dust deposition) cannot account for the distributions of Zn_d and Cd_d.

3.6.3 Sea of Marmara

The steep halocline present in the Sea of Marmara prevents efficient overturning of deep water which results in the consumption of dissolved oxygen (<50 µmol kg^{-1} below ~100 m) due to aerobic respiration of sinking particulate organic matter whose production in surface waters is supported by runoff of nutrients from anthropogenic sources in the region (Fig. 3.8; Beşiktepe *et al.*, 1994; Polat and Tugrul, 1995). Scavenging of Fe_d and Pb_d onto sinking particles is an important control on the distributions of these metals in the open ocean and we suspect that scavenging is also

responsible for the surprisingly low concentrations of Fe_d and Pb_d in sub-surface waters of the Sea of Marmara. Under low oxygen conditions, preservation of particulate organic matter is increased due to low respiration rates which should act to enhance scavenging efficiency. Surface maximum of Fe_d and Pb_d (Fig. 3.8) up to ~9 nM and ~65 pM, respectively, indicate the low salinity water residing at the surface is enriched in these metals. The low salinity surface water originates in the Black Sea before entering the Sea of Marmara via the Bosporus Strait. Low concentrations of Fe_d of <1 nM (Chapter 4; Lewis and Landing, 1991) in Black Sea surface waters suggest that the Bosporus Strait is a significant source of Fe to water flowing into the Sea of Marama, while elevated Pb_d concentrations of >100 pM have been observed in Black Sea surface waters (Lewis and Landing, 1992) indicating no additional source of Pb within the Bosporus Strait is required to explain the elevated Pb_d concentrations in surface waters of the Sea of Marmara. The concentrations of Zn_d and Cd_d are both elevated in surface and sub-surface waters of the Sea of Marmara relative to inflowing Mediterranean waters from the Aegean Sea (Fig. 3.4, 3.5) and to surface waters in the Black Sea (Chapter 4). Both Zn_d and Cd_d display concentrations in surface waters that are slightly depleted relative to immediately underlying waters (Fig. 3.8), possibly suggesting nutrient-type behaviour, at least in the upper water column, and/or that low salinity surface waters originating in the Black Sea are depleted in Zn_d and Cd_d relative to sub-surface waters of the Sea of Marmara. Regardless, the Sea of Marmara appears to contain elevated concentrations of Zn_d and Cd_d thereby requiring an internal source of these metals to the basin. Interestingly, both Zn_d and Cd_d concentrations also show a slight decreasing trend with depth, indicating scavenging is affecting the distribution of these metals in sub-surface waters but to a lesser extent than Fe_d and Pb_d.

3.7 Conclusions

We present a full depth zonal transect of dissolved Fe, Zn, Cd, and Pb in the Mediterranean Sea. The data reveal enrichments of these metals within the Mediterranean Sea compared to the concentrations observed in inflowing surface Atlantic water to the west of the Strait of Gibraltar. There is also a strong enrichment of Zn, Cd, and Pb in the WMED relative to the EMED. The overall enrichment of metals in the Mediterranean Sea compared to surface Atlantic water is indicative of an internal

source of these metals to the Mediterranean Sea. The distribution of dissolved Fe in surface waters reflects atmospheric deposition occurring across the entirety of the Mediterranean Sea. The distribution of Pb_d also potentially reflects atmospheric deposition, but the source largely appears to be present in the WMED, whereas the distribution of Pb_d in EMED surface waters is controlled by mixing between surface and intermediate waters. The elevated concentrations of Pb_d in WMED deep waters relative to EMED deep waters suggest that Pb fluxes to the WMED have been elevated over fluxes of Pb to the EMED over the mixing time of deep waters in the Mediterranean Sea (~50-100 yrs). The similarity between the distributions of Zn_d and Cd_d in the WMED reflect mixing between inflowing Atlantic water depleted in Zn_d and Cd_d with underlying intermediate and deep waters enriched in Zn_d and Cd_d. In the EMED, Cretan intermediate water displays elevated concentrations of Zn_d and Cd_d relative to adjacent intermediate and deep waters. Overall, the results suggest that the distributions of trace metals in the WMED are more heavily impacted by anthropogenic activities than in the EMED. Furthermore, the results provide more evidence for the continuing existence of elevated levels of dissolved Pb in the oceans due to the legacy of burning leaded gasoline in addition to other current sources, and demonstrate that anthropogenic sources have generated basin-scale enrichments of dissolved Zn and Cd in the Mediterranean Sea.

CHAPTER 4

BEHAVIOR OF LITHOGENIC AND REDOX SENSITIVE TRACE METALS ACROSS THE REDOX GRADIENT IN THE BLACK SEA WATER COLUMN

4.1 Abstract

The Black Sea is the world's largest marine basin and is an ideal natural laboratory for examining the behavior of trace metals through the redox zonation within the water column. The distributions of a suite of dissolved trace metals, including aluminum, titanium, manganese, iron, copper, zinc, gallium, yttrium, zirconium, cadmium, and lanthanum, over the full depth of the water column at multiple stations in the deep central basin are reported. The primary controls on the distributions of trace metals in the Black Sea are redox reactions that induce changes in solubility of the metals, the formation of insoluble metal-sulfides in the deep sulfidic basin, and scavenging onto sinking particles that have formed within the upper water column. The distributions of dissolved manganese, iron, copper, zinc, cadmium and lanthanum are very similar to previous reports, while this study represents the first investigation of the distributions of dissolved aluminum, titanium, gallium, yttrium, and zirconium in the Black Sea or any other anoxic marine basin. The distribution of yttrium tracks the distribution of lanthanum very closely, demonstrating its rare earth element characteristics. The distributions of dissolved aluminium and gallium appear to be dominated by scavenging processes with very similar patterns in their vertical profiles, as would be expected from their adjacent positions on the periodic table indicating similar chemistry. Contrary to this reasoning, the distribution of dissolved titanium is strikingly different than that of zirconium although they also are expected to display similar chemistry. The distribution of dissolved zirconium is similar to that of aluminium and gallium, while the concentration of titanium increases by nearly two orders of magnitude from <30 pM in the upper water column to ~2000 pM in the deep basin and has a distribution that is more similar to that of dissolved iron around the redoxcline.

4.2 Introduction

The distributions of trace metals in the world's ocean serve as tracers of many physical, chemical and biological oceanographic processes in the modern ocean. Stratigraphic records of trace metals in marine sediments are used to investigate how these oceanographic processes may have differed during important intervals in Earth's history when the climate was much different than today (*e.g.* Algeo and Maynard, 2008). Some redox sensitive trace metals (*e.g.* Cu, Zn, Cd) form insoluble metal-sulfides in the presence of free H_2S which are transferred from the water column to underlying sediments. Enrichments of redox sensitive trace metals in marine sediments may therefore indicate the presence euxinic conditions, *i.e.* anoxic and sulfidic, at the time the sediments were deposited. Significant enrichments of redox sensitive trace metals in organic rich sediments deposited during the Cretaceous are thought to indicate widespread euxinia in the early Atlantic Ocean during so called oceanic anoxic events (*e.g.* Brumsack, 2006; Jenkyns, 2010). Oxygen depletion in the water column also leads to the enhanced preservation of organic matter, such that organic rich sediments are a reliable indicator of low bottom water oxygen concentration at the time of sediments deposition. Two distinct oceanographic scenarios are generally assumed to be responsible for oxygen depletion and associated accumulation of organic rich sediments. In the first scenario, oxygen depletion is the result of enhanced primary productivity in surface waters due to upwelling leading to oxygen minimum zones caused by high rates of aerobic respiration of sinking organic matter (Suess and Thiede, 1983). In the second scenario, restricted circulation prevents efficient transport of oxygen to deep waters, eventually leading to water column euxinia such as in the Black Sea (Demaison and Moore, 1980), which is the focus of this study. Sedimentary patterns of trace metal abundances can possibly distinguish between the two modes of organic rich sediment deposition. However, successful interpretation of trace metal patterns requires a sound knowledge of how the elements of interest behave during their biogeochemical cycling in modern endmembers of these two distinct anoxic environments for calibration purposes (*e.g.* Brumsack, 2006, Little *et al.*, 2015). A complex assemblage of biogeochemical processes, including the prevailing redox state, controls the distributions of trace metals in the ocean and the incorporation of trace metals into marine sediments.

Redox chemistry is an especially crucial component of the biogeochemical cycles of many elements. In natural aqueous systems with high primary productive and/or limited mixing, dissolved oxygen (O_2) can be fully consumed by aerobic biological respiration and inorganic chemical reactions. At depths below the oxic zone, biological respiration proceeds predominately through nitrate reduction, manganese reduction, iron reduction, sulfate reduction, and methanogenesis. A classic example of such a system is anoxic marine sediments (*e.g.* Canfield and Thamdrup, 2009). Froelich *et al.* (1979) produced the first high-quality marine pore water sediment profiles of the chemical by-products of these respiration processes and showed that the order of appearance of the respiration pathways tracked with the amount of energy released during the respiration of organic matter. Information on the redox chemistry of trace metals can also be gained by examining their concentration gradients across strong redox zonation, such as those observed in anoxic marine sediments or within the water column of anoxic marine basins.

The Black Sea is the world's largest anoxic basin, and as such, it is an important natural laboratory for investigating the redox chemistry of dissolved trace metals. The chemical and physical characteristics of the Black Sea water column are controlled by its hydrological balance (Caspers and Schmidt, 1957; Sorokin, 1983). European rivers (primarily the Danube, Dniester, Dnieper, Don, and Kuban) supply freshwater to the upper surface layer of the Black Sea. The only source of saltwater to the Black Sea is from the Mediterranean Sea which enters through the Bosporus straight (sill depth ~60 m). Consequentially, a vertical salinity gradient exists, with a salinity of ~18 to 18.5 in surface waters and >22 in deep waters (Murray and Yakushev, 2006). The vertical stratification effectively limits the rate at which deep waters are renewed, resulting in a well oxygenated surface waters (0 to ~100 m) and euxinic (*i.e.* anoxic and sulfidic) deep waters (100 to ~2200 m). Oxygen is depleted due to aerobic respiration of sinking organic matter which also fuels the progression of other respiration pathways. The full progression of the respiration pathways and redox zonation, known as the redoxcline, occurs in the water column across a depth range of tens of meters thick, centered at ~100 m, which is a very large spatial window compared to marine sediments where the full progression from oxic to euxinic conditions can occur across centimetre scale depth intervals. Thus, the Black Sea water column represents an ideal location to examine the behavior of trace metals across variable redox conditions (*e.g.* Brewer and Spencer, 1974; German *et al.*, 1991; Guieu *et al.*, 1998; Haraldsson and Westerlund, 1988;

Lewis and Landing, 1991, 1992; Schijf *et al.*, 1991; Tankéré *et al.*, 2001; Yiğiterhan *et al.*, 2011).

Here we report the distributions of dissolved aluminum (Al), titanium (Ti), manganese (Mn), iron (Fe), copper (Cu), zinc (Zn), gallium (Ga), yttrium (Y), zirconium (Zr), cadmium (Cd), and lanthanum (La) over the full depth of the water column across a full zonal transect of the Black Sea. The distributions of many of these elements (Mn, Fe, Cu, Zn, Cd, and La) have been previously reported in the Black Sea but generally only for a limited number of locations. The distributions of Mn and Fe are influenced by changes in their oxidation states which lead to increased solubility under reducing conditions and precipitation of insoluble sulfides under euxinic conditions (*e.g.* Jacobs *et al.*, 1985; Lewis and Landing, 1991). The metals Cu, Zn, and Cd do not change oxidation state and their distributions in the anoxic basins are dominated by the formation of metal-sulfides that either precipitate from solution directly or are scavenged from solution on the surfaces of other sinking particles (*e.g.* Jacobs *et al.*, 1985; Lewis and Landing, 1992). Currently, there are no data available on the distributions of dissolved Al, Ti, Ga, Y, and Zr in anoxic marine basins. In marine sediments, the abundances of Al, Ti, Ga and Zr are dominated by the lithogenic fraction. It is common practice to normalize sedimentary redox sensitive trace metal concentrations to the concentration of a lithogenic element (commonly Al) as a means to evaluate their enrichments relative to the background lithogenic fraction and it also serves to diminish variability in the trace metal records resulting from variable contributions from the lithogenic fraction (*e.g.* Brumsack, 2006). This normalization technique is only valid if the assumption that the concentrations of lithogenic elements in sediments are not themselves effected by different redox processes. In this context, this study aims to investigate the behavior of lithogenic and redox sensitive trace metals in the Black Sea with the objective of gaining a better understanding of the processes that control the behavior of different trace metals across a water column redox gradient.

4.3 Methods

4.3.1 Sampling stations and seawater collection

Seawater samples were collected during the Dutch MedBlack GEOTRACES expedition (cruise 64PE373) to the Black Sea in July 2013 aboard R/V *Pelagia* (Fig.

4.1). A total of 12 stations were occupied during the expedition with 6-48 discrete seawater samples collected at each station. The concentrations of dissolved trace metals were determined for all stations. Seawater samples were collected using an ultraclean all-titanium framed 'TITAN' CTD sampling system (de Baar *et al.*, 2008; Rijkenberg *et al.*, 2015). Immediately upon recovery, the TITAN system was placed inside a purpose-built class 100 clean room container. Inside the clean room container, seawater was filtered directly from sampling bottles using 0.2 µm filter cartridges (Sartobran-300, Sartorius) under nitrogen pressure (1.5 atm). Filtered seawater samples were collected in 40 mL low density polyethylene (LDPE) bottles which had been acid cleaned following GEOTRACES guidelines (www.geotraces.org). Sample bottles were rinsed 5 times with sample seawater prior to sample collection. Immediately after collection, seawater samples were acidified to 0.024 M HCl using ultra-high purity 12 M HCl (Seastar^{TM} Baseline®), except for the separately collected sample for dissolved Al which was acidified to 0.024 M HCl approximately 1 to 2 h before analysis (see Chapter 2).

Seawater samples were collected for analysis of major nutrients (nitrate (NO_3), nitrite (NO_2), ammonia (NH_3), phosphate (PO_4), and silica (Si)) and hydrogen sulfide (H_2S) in high density polyethylene (HDPE) syringes with a three way valve to limit exposure to air during sampling from the CTD. The syringes were rinsed three times with the sample before being completely filled and were immediately processed shipboard.

A Seabird SBE 911+ CTD system was used to measure the conductivity (salinity), temperature, and pressure (depth) *in situ* at each sampling station. The temperature sensor was calibrated using a high-accuracy reference-thermometer (Seabird SBE35), while the conductivity sensor was calibrated against shipboard salinity measurements of seawater samples.

4.3.2 Analysis of dissolved trace metals in seawater

The concentration of dissolved Al was determined using the methods described in Chapter 2 section 2.2. The multi-element preconcentration and HR-ICP-MS methods used for determining the concentrations of the other dissolved trace metals are detailed in Chapter 3 section 3.2. The concentration of dissolved Mn was outside the range of the calibration in deep anoxic waters of the Black Sea and the results obtained from thepreconcentration using Nobias PA-1 resulted in unreliable data. Therefore, the

concentration of dissolved Mn was therefore determined by directly diluting seawater samples 30x with acidified MQ water (0.024 M HCl) and subsequent analysis via quadrupole ICP-MS (Agilent 7500) at the University of Otago. The smooth vertical profiles obtained for most elements analyzed and the agreement between the data presented here with data from other analytical techniques and with data from the literature where available suggests that the issues encountered with Mn did not negatively affect the measurements of the other metals.

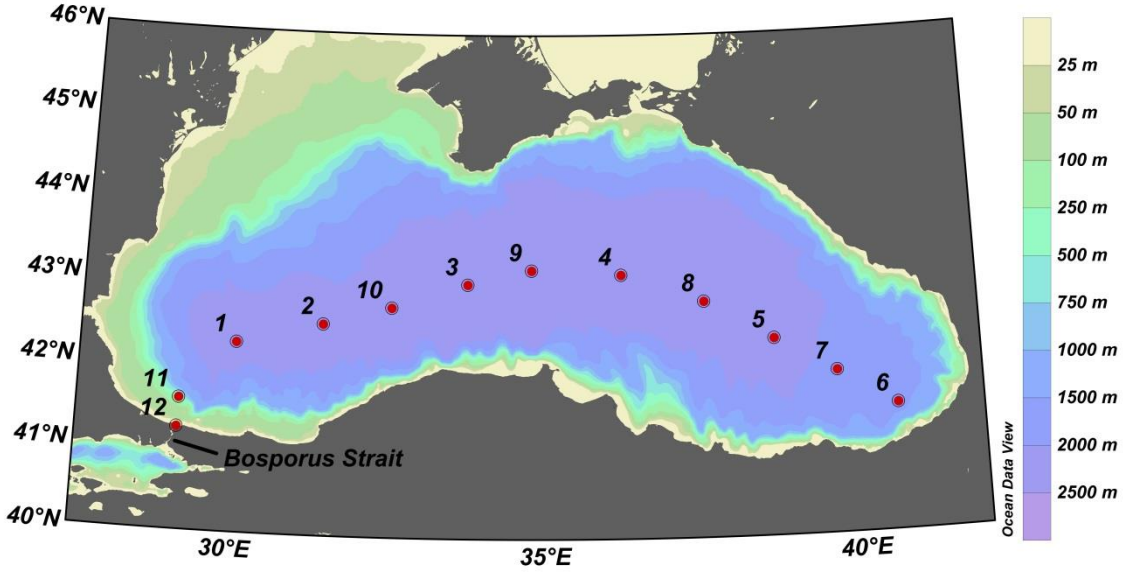

Fig. 4.1. Map of the sampling locations during the 2013 GEOTRACES Black Sea expedition (cruise 64PE373). Figure made using Ocean Data View (Schlitzer, 2015).

4.4 Results and Discussion

At the central basin stations 1 to 10, two CTD casts were performed with a total of 48 discreet samples collected at each station. The first cast at each station was a full depth profile, with the deepest sample taken at ~10 m above the seafloor at each station. The second cast at each station was intended to achieve high vertical sampling resolution with 12 samples collected every ~5 m above and below the depth of oxic-anoxic interface at ~100 m. At station 2, all 48 samples were preconcentrated and analyzed using the multi-element trace metal method. At stations 1, 3, 4, 5, 6, 8, 9 and 10, half of the samples from the second cast were processed, resulting in 36 samples at each station. The upper 12 samples from the first cast at station 7 were processed for

dissolved Al while none were processed for the multi-element method. The concentration of dissolved Al was determined for the 24 samples from the first casts at the other stations. The concentration of dissolved Mn was only determined for the first cast from station 2 as it was included in the elemental analysis for the initial uranium concentration measurement as described in Chapter 6.

4.4.1 Redox zonation

The vertical redox zonation in the Black Sea water column and the associated behavior of dissolved trace metals at station 2 are illustrated in Fig. 4.2 and 4.3. The pycnocline (represented by the salinity gradient) at depths between ~50 and 150 m separates the upper surface layer from deep waters, and initiates the formation of the strong redoxcline. The depletion of dissolved O_2 coincides with the upper portion of the pycnocline with concentrations decreasing from ~330 µmol kg^{-1} at ~25 m to below the detection limit at ~95 m. The first detection of H_2S occurs at ~105 m and increases to >400 µmol kg^{-1} in the deep basin. The concentration of NO_3 increases sharply to a maximum of ~4 µmol kg^{-1} at ~65 m before decreasing to below the detection limit at ~100 m. A maximum concentration of dissolved Mn of ~9 µM occurs at ~140 m before decreasing to ~5 µM below ~500 m while the maximum concentration of dissolved Fe of >400 nM occurs at ~160 m, slightly deeper than the Mn maximum, and decreases to <20 nM at depths below 1000 m.

The depth of the pycnocline is slightly variable across the Black Sea which induces shifts in the depth of the redox zonation. Wind driven surface currents force isopycnal surfaces to dome upwards in the central basin, such that the pycnocline is found at shallower depths in the central basin relative to the margins. Similarly, all of the gradients in the vertical profiles of different parameters are found at shallower depths in the central basin but are almost always associated with the same isopycnal surface. This is clearly visible in the cross-section zonal distributions of H_2S and dissolved Fe (Fig. 4.4). Therefore, it is preferable to compare vertical profiles from different stations by plotting the various parameters versus density rather than depth. All stations in the central basin display similar vertical profiles of all parameters investigated when compared in this way (Fig. 4.5, 4.6). The concentration of O_2 decreases to below the detection limit at a density (σ_θ) of $\leq$ 16 kg/m^3 and the onset of euxinic conditions occurs at $\sigma_\theta \geq$ ~16.2 kg/m^3 which is in agreement with previous studies (Konovalov *et al.*, 2004; Murray and Yakushev, 2006).

The parameters O_2, NO_3, Mn, Fe, and H_2S are indicative of the prevailing respiration processes occurring at different depths throughout the water column. In the presence of O_2, aerobic respiration of organic matter is the highest energy yielding respiration process available to microorganisms (Froelich *et al.*, 1979). Dissolved O_2 is rapidly depleted through the pycnocline because the rate of aerobic respiration out paces the rate of O_2 replenishment through physical mixing. Respiration of organic matter releases NO_3 back to the dissolved phase were it accumulates to maximum concentrations of ~4 µmol kg^{-1} around σ_θ = ~15.4 kg/m^3, similar to previous investigations (Murray and Yakushev, 2006). Below this density horizon the concentration of O_2 is low enough for the commencement of nitrate reduction and denitrification which consumes the accumulated nitrate, which yield less energy than aerobic respiration but more energy than metal reduction (Froelich *et al.*, 1979). Below the zone of nitrate reduction, microbial respiration occurs through Mn and Fe reduction. Sinking particles of Mn(III/IV) and Fe(III) oxides provide the source of these metals to the microbial communities. Reduction of Mn and Fe oxides through microbial metal reduction releases dissolved Mn(II) and Fe(II) back to the dissolved phase where it accumulates, generating the observed maximum in the vertical profiles. The concentration of dissolved Mn reaches a maximum of ~9 µM at slightly shallower depths than maximum concentrations of dissolved Fe of >400 nM which occur at σ_θ = ~16.5 kg/m^3. The energy available from microbial Mn reduction is slightly higher than during Fe reduction which explains why Mn reduction, and thus the dissolved Mn maximum, occurs slightly above microbial Fe reduction and the dissolved Fe maximum in the Black Sea water column. Sulfate reduction provides lower energy yields than metal reduction and the accumulation of H_2S, the product of sulfate reduction, occurs below the zone of metal reduction. The production of H_2S in the water column affects the solubility of Mn(II) and Fe(III), resulting in the decreasing concentrations of dissolved Mn and Fe in the deep Black Sea due to the precipitation of Mn and Fe sulfides (Konovalov *et al.*, 2004). Precipitation of other metal-sulfides (*e.g.* CdS, ZnS) is also occurring, as discussed in the following sections.

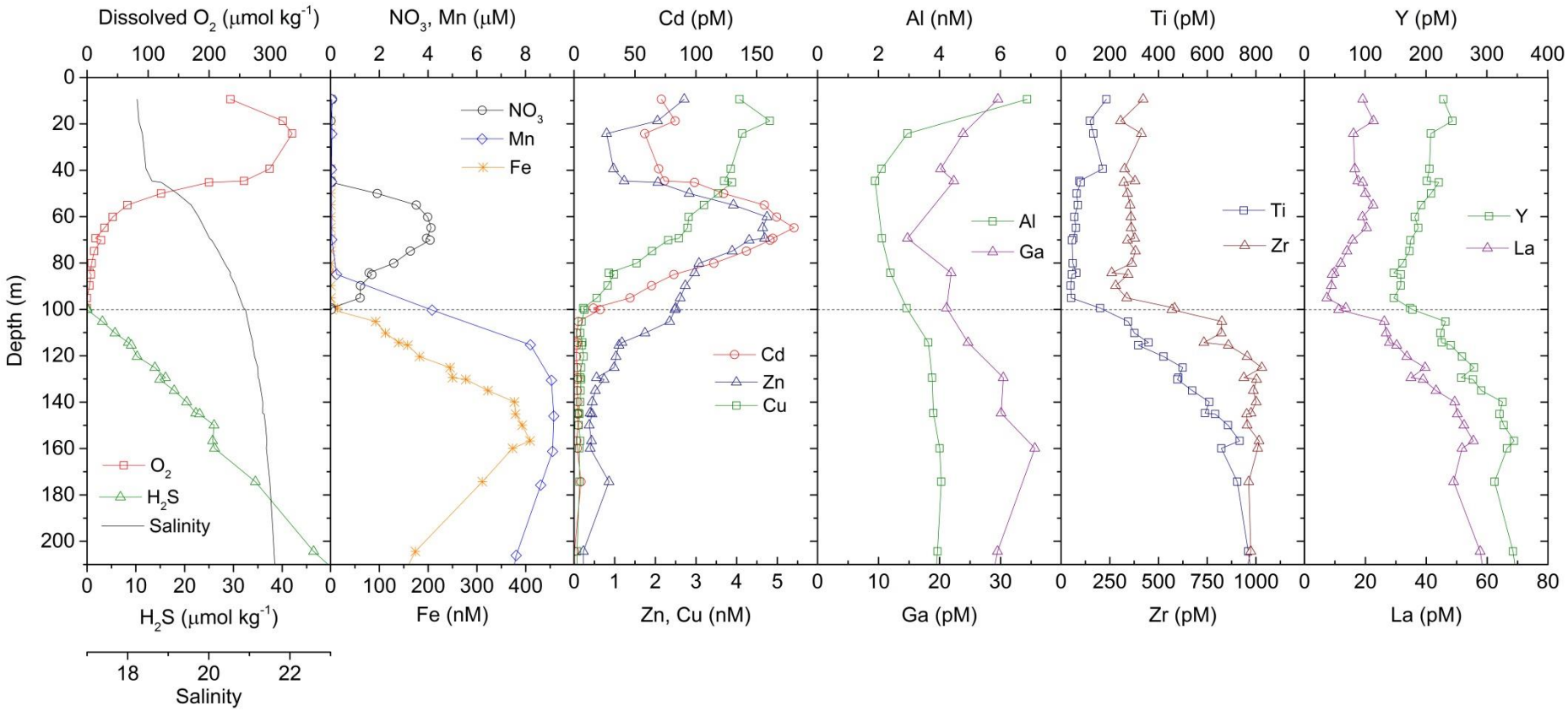

Fig 4.2. Vertical profiles of salinity, O_2, H_2S, NO_3 and dissolved trace metals in the upper 200 m of the water column at station 2. The horizontal dashed line at 100 m denotes the transition from oxic surface waters to anoxic and sulfidic deep waters.

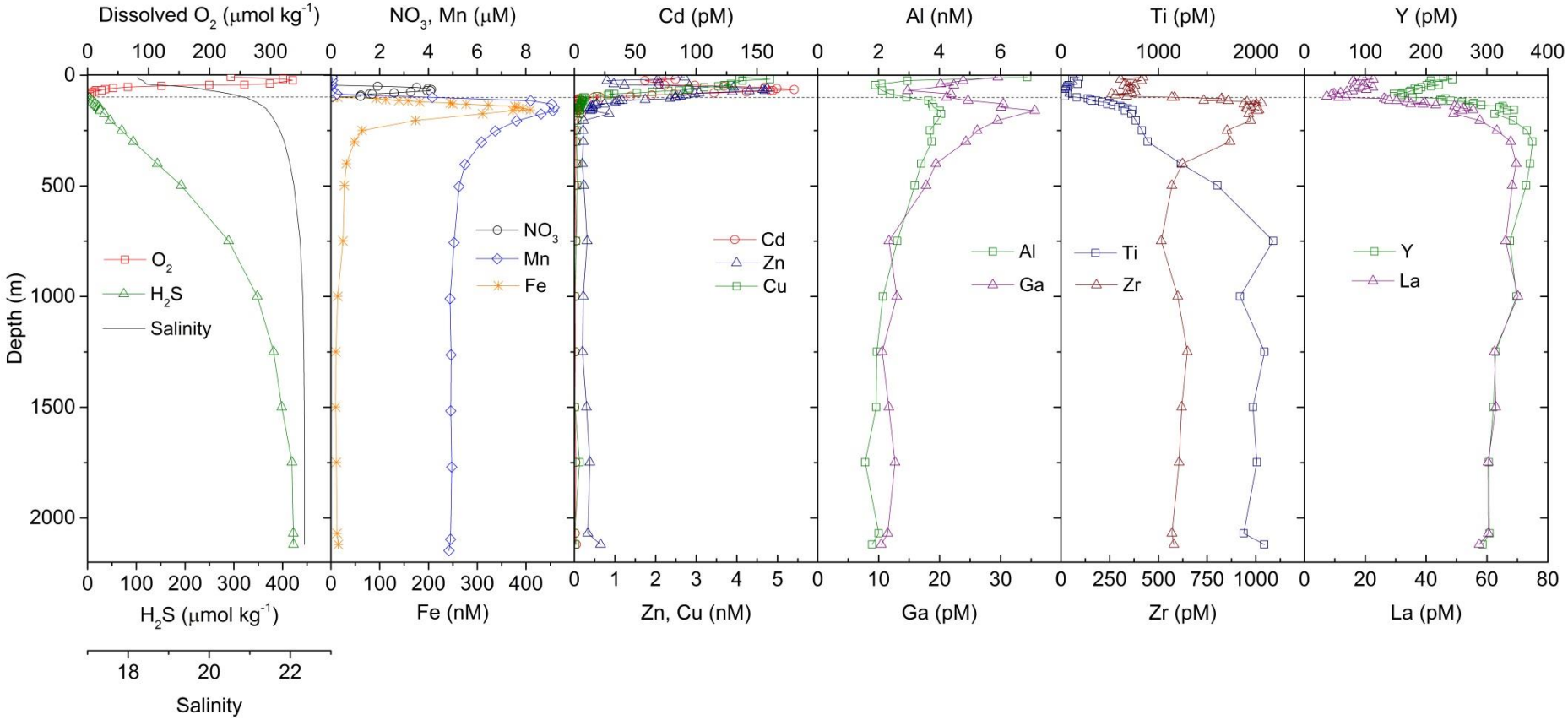

Fig. 4.3. Vertical profiles of salinity, O_2, H_2S, NO_3 and dissolved trace metals over the full depth of the water column at station 2. The horizontal dashed line at 100 m denotes the transition from oxic surface waters to anoxic and sulfidic deep waters.

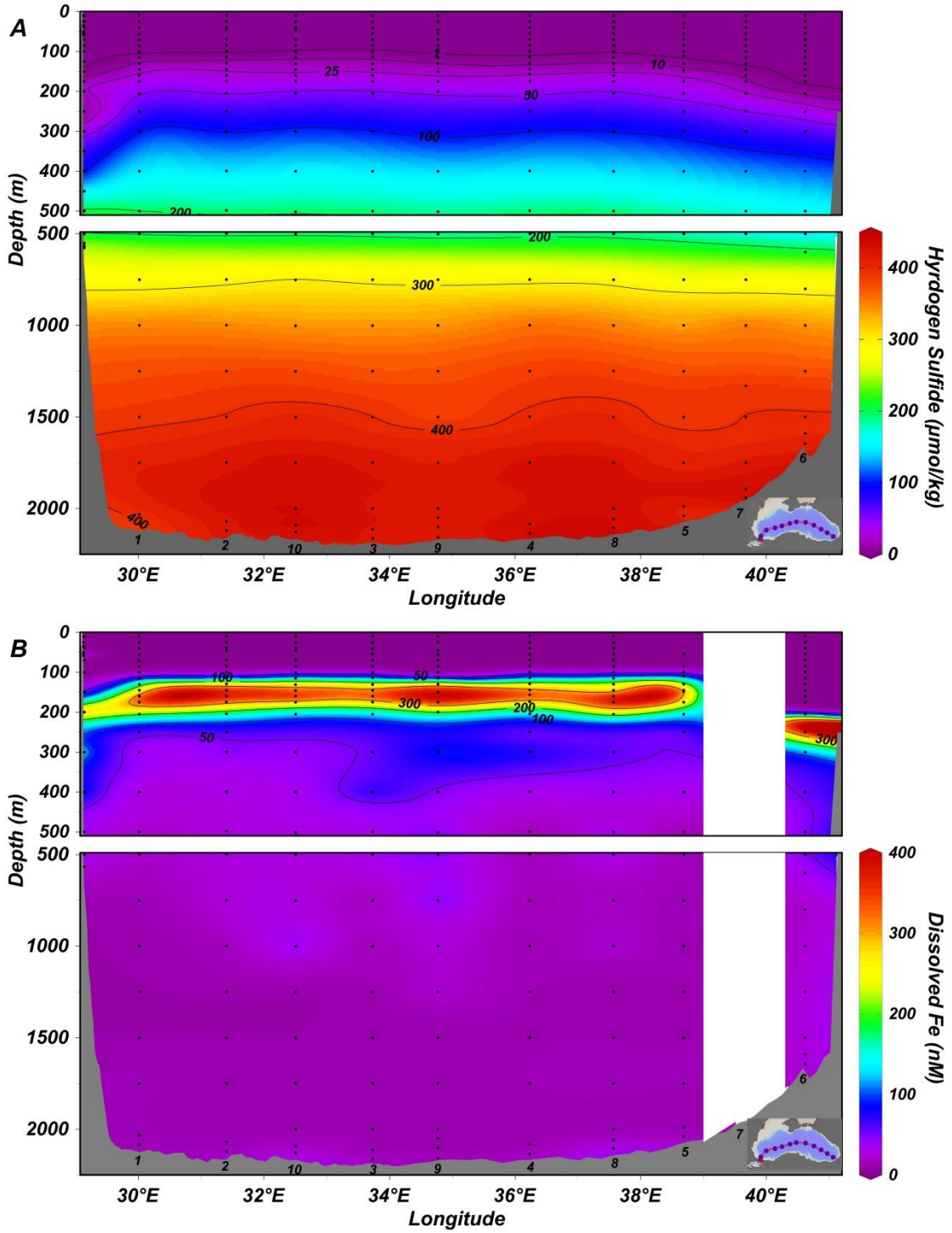

Fig. 4.4. Cross-section zonal distribution of H_2S (A) and dissolved Fe (B) in the Black Sea during 2013 GEOTRACES cruise display the effects of isopycnal doming which forces the redoxcline to shallower depths in the central basin. Discrete sample depths are indicated by black circles. The upper panel in both A and B display the upper 500 m of the water column and the lower panel in both A and B display the water column below 500 m. The color bar applies to both the upper and lower panels.

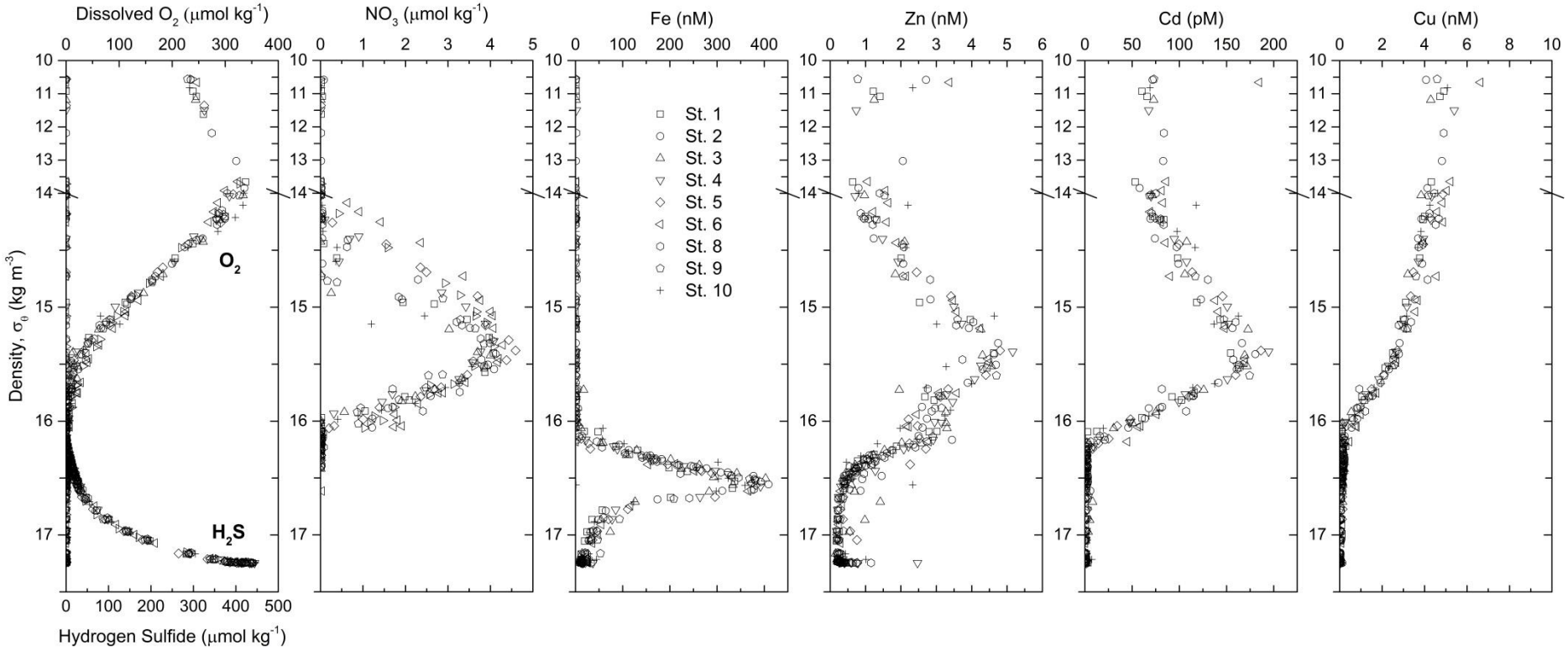

Fig. 4.5. Vertical profiles from all central basin stations of O_2, H_2S, NO_3, Fe, Cd, Zn and Cu plotted versus density (σ_θ). Note the break in the y-axis scale at 14 kg/m^3.

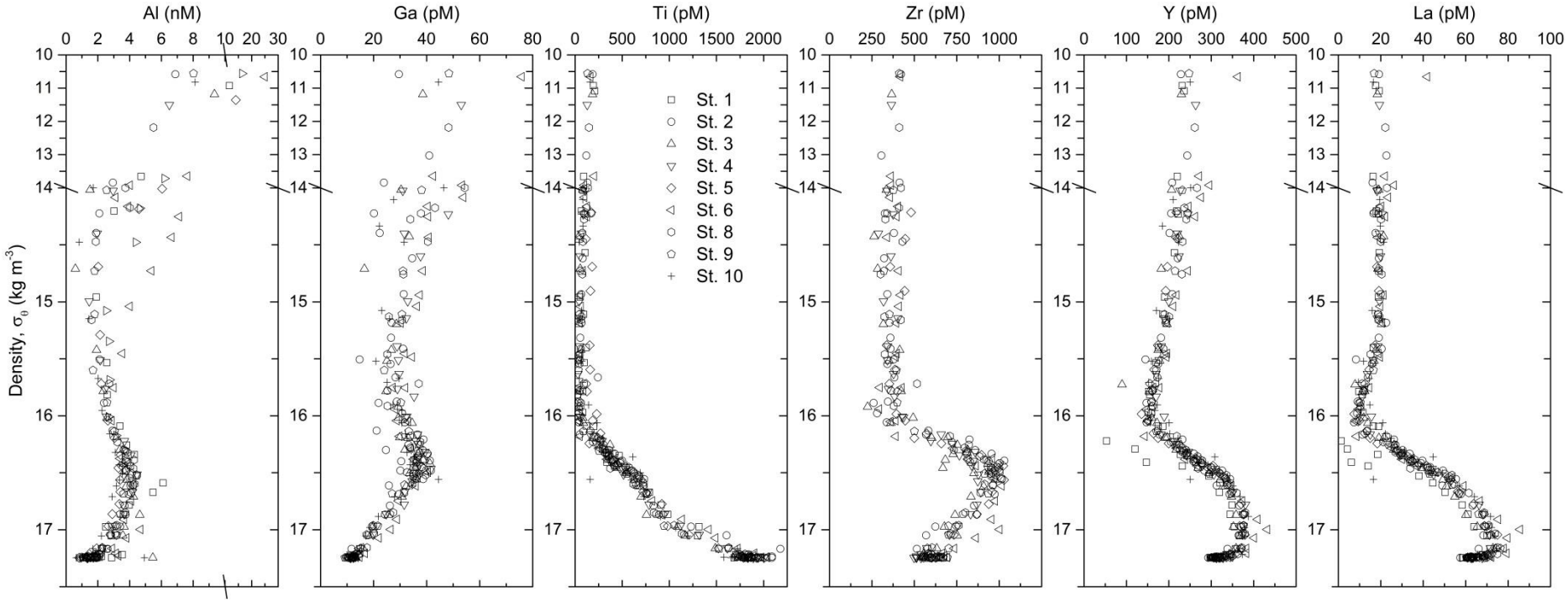

Fig. 4.6. Vertical profiles from all central basin stations of dissolved Al, Ga, Ti, Zr, Y, and La plotted versus density (σ_θ). Note the break in the y-axis scale at 14 kg/m^3 and in the Al scale at 10 nM.

4.4.2 Distributions of trace metals

4.4.2.1 Cadmium

The concentration of dissolved Cd in surface waters varies from 50 to 75 pM at $10 < \sigma_\theta < 14$ kg/m^3 before increasing to a maximum concentration of >175 pM at σ_θ = ~15.4 kg/m^3. The concentration of dissolved Cd then drops dramatically to values of <1 pM below the sulfide interface at $\sigma_\theta \geq$~16.2 kg/m^3 (Fig. 4.5). The general shape of the vertical profiles of dissolved Cd and the magnitude of the concentration change is similar previous reports by Haraldsson and Westerlund (1988), Lewis and Landing (1992), and Tankéré *et al.*(2001). The relatively low concentrations of dissolved Cd in the upper surface layer are in part maintained through biological uptake. Remineralization of sinking particulate organic matter is likely responsible for the maximum concentrations of dissolved Cd and NO_3 at σ_θ = ~15.4 kg/m^3. The relationship between dissolved Cd and NO_3 in the water column of the Black Sea is illustrated in Fig. 4.7. The slope of the Cd/NO_3 relationship at $14 < \sigma_\theta < 15.4$ kg/m^3 is ~17.6×10^{-6} mol/mol and is similar to the Cd/NO_3 ratio of ~6×10^{-6} to 19×10^{-6} mol/mol observed in phytoplankton from the North Atlantic Ocean (Twining *et al.*, 2015), which further supports the role of remineralization in supporting the elevated concentration of dissolved Cd at σ_θ = ~15.4 kg/m^3. The role of biological uptake and remineralization in determining the distribution of dissolved Cd in the upper surface waters of the Black Sea was also suggested by Tankéré *et al.* (2001). The Cd/NO_3 relationship is different for samples with $15.4 < \sigma_\theta < 16.2$ kg/m^3, which likely reflects the removal rates of NO_3 through nitrate reduction and the removal of dissolved Cd through sulfide formation and physical mixing. Although biological uptake and remineralization appear to result in the vertical transport of dissolved Cd from surface waters to deeper waters where σ_θ = ~15.4 kg/m^3, the strong correlations between dissolved Cd and salinity (Fig. 4.8) suggests that the gradient in the dissolved Cd concentration through the redoxcline is also a consequence of conservative mixing between deep waters ($\sigma_\theta \geq$ ~16.2 kg/m^3) depleted in dissolved Cd with overlying intermediate waters (σ_θ = ~15.4 kg/m^3) enriched in dissolved Cd, and mixing between surface waters ($\sigma_\theta \leq$ ~14 kg/m^3) with underlying intermediate waters (σ_θ = ~15.4 kg/m^3).

Cadmium occurs in the environment only in the Cd(II) oxidation state. Thus, depletion of dissolved Cd across the redoxcline is not driven by precipitation of reduced Cd species, but by the formation of insoluble Cd-sulfides (Landing and Lewis, 1991; Lewis and Landing, 1992), which results in a sharp increase in the particulate Cd

concentration at the onset of sulfidic conditions (Yiğiterhan *et al.*, 2011). Cadmium released from decaying organic matter immediately forms insoluble sulfides, which maintains the dissolved Cd concentration at <1 pM in the deep water column (Fig. 4.3, 4.5).

4.4.2.2 Zinc

The vertical distribution of dissolved Zn in the Black Sea is very similar to that of Cd, as previously recognized (Haraldsson and Westerlund, 1988; Lewis and landing, 1992). Relatively low, yet variable, concentrations of ~0.5 to 3 nM are observed in the upper surface layer due in part to biological uptake (Fig. 4.2, 4.5). The concentration of dissolved Zn then increases from ~1 nM at σ_θ = ~14 to a maximum of >4.5 nM at σ_θ = ~15.4 kg/m^3, which, similarly to Cd, is at the same density as the maximum NO_3, indicating Zn is also being released during aerobic respiration of sinking organic matter (Fig. 4.5). The slope of the Zn/NO_3 relationship at 14 < σ_θ < 15.4 kg/m^3 is ~0.67×10^{-3} mol/mol (Fig. 4.7) and is similar to the Zn/NO_3 ratio observed of ~0.2×10^{-3} to 0.7×10^{-3} mol/mol in phytoplankton from the North Atlantic Ocean (Twining *et al.*, 2015), which supports the role of remineralization as the primary driver of the increase in dissolved Zn concentrations across this density interval. Interestingly, Yiğiterhan *et al.* (2011) observed a Zn/Al ratio in particles at σ_θ = ~15.4 kg/m^3 above background ratios, indicating scavenging of Zn onto particles or elevated levels of organic particulate matter as σ_θ = ~15.4 kg/m^3 also coincides with the NO_3 maximum. The elevated dissolved concentrations of Zn and excess particulate Zn suggests remineralization of particulate Zn is controlling the Zn distribution in the upper water column. However, the relationship between salinity and dissolved Zn indicates that mixing between surface waters ($\sigma_\theta \leq$ ~14 kg/m^3) depleted in the dissolved Zn with underlying intermediate water (σ_θ = ~15.4 kg/m^3) enriched in dissolved Zn is also an important control on the distribution of dissolved Zn in the upper water column of the Black Sea (Fig. 4.8). Like Cd, Zn only occurs naturally as Zn(II), even under reducing conditions, but forms sulfides under euxinic conditions (Haraldsson and Westerlund, 1988; Landing and Lewis, 1991). The concentration of dissolved Zn in the deep basin is maintained at <0.5 nM through Zn-sulfide precipitation and scavenging on to sinking particles (Lewis and Landing, 1992). There are instances of slight increases in the dissolved Zn concentration near the seafloor, indicating a small benthic source of Zn (Fig. 4.5). Across the redoxcline, dissolved Zn displays a non-linear decrease, which is

clearly observed at station 2 (Fig. 4.2). All stations display a similar pattern, resulting in a cluster of variable dissolved Zn concentrations at σ_θ = ~16 kg/m^3 (Fig. 4.5). This feature in the vertical distribution of dissolved Zn corresponds to the density at which the concentration of dissolved Mn begins rapidly increasing. Scavenging of Zn onto Mn oxides and subsequent release during dissolution of these particles as they sink due to microbial metal reduction may explain why the concentration of dissolved Zn does not decrease as smoothly as dissolved Cd.

4.4.2.3 Labile copper

Copper is strongly complexed by organic ligands in seawater and obtaining accurate concentrations of the true concentration of dissolved Cu requires the destruction of these ligands via *e.g.* UV-oxidation. Since no strong oxidation of the samples was performed prior to processing, the concentrations presented here only represent the operationally defined 'labile' fraction of the dissolved Cu pool which is fraction of the dissolved Cu pool that is able to interact with the functional groups of the Nobias PA-1 resin and therefore be extracted from the seawater matrix. Similar to both Cd and Zn, Cu is biologically utilized and forms sulfide complexes under euxinic conditions. The primary oxidation state of Cu is Cu(II) but experiments and equilibrium calculations suggest that Cu(I)-sulfide complexes are favourable under euxinic conditions (Landing and Lewis, 1991; Lewis and Landing, 1992). The vertical profile of dissolved Cu is very consistent at all stations across the central basin, characterized by concentrations of ~4 to 6 nM in the upper water column and a sharp unidirectional decrease in concentration through the redoxcline to <0.2 nM at $\sigma_\theta \geq$ 16 kg/m^3 (Fig. 4.5), consistent with previous reports (Haraldsson and Westerlund, 1988; Lewis and Landing, 1991; Tankéré *et al.*, 2001). Elevated Cu/Al ratios relative to crustal background ratios in particles below the redoxcline suggest the formation of insoluble Cu-sulfides (Yiğiterhan *et al.*, 2011).

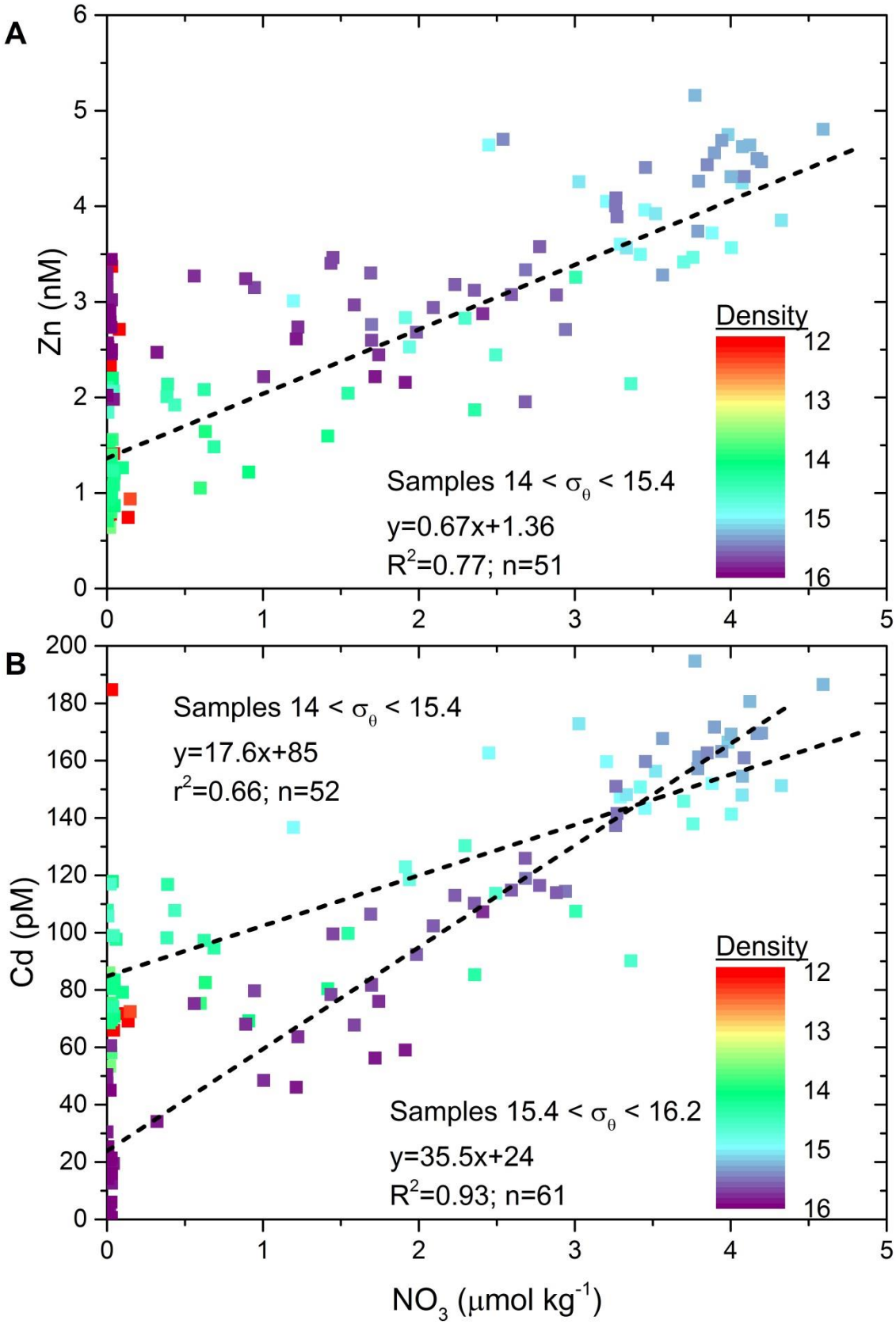

Fig. 4.7. Relationship between nitrate and dissolved Zn (A) and dissolved Cd (B) in the water column of the Black Sea. Color scale corresponds to density (σ_θ).

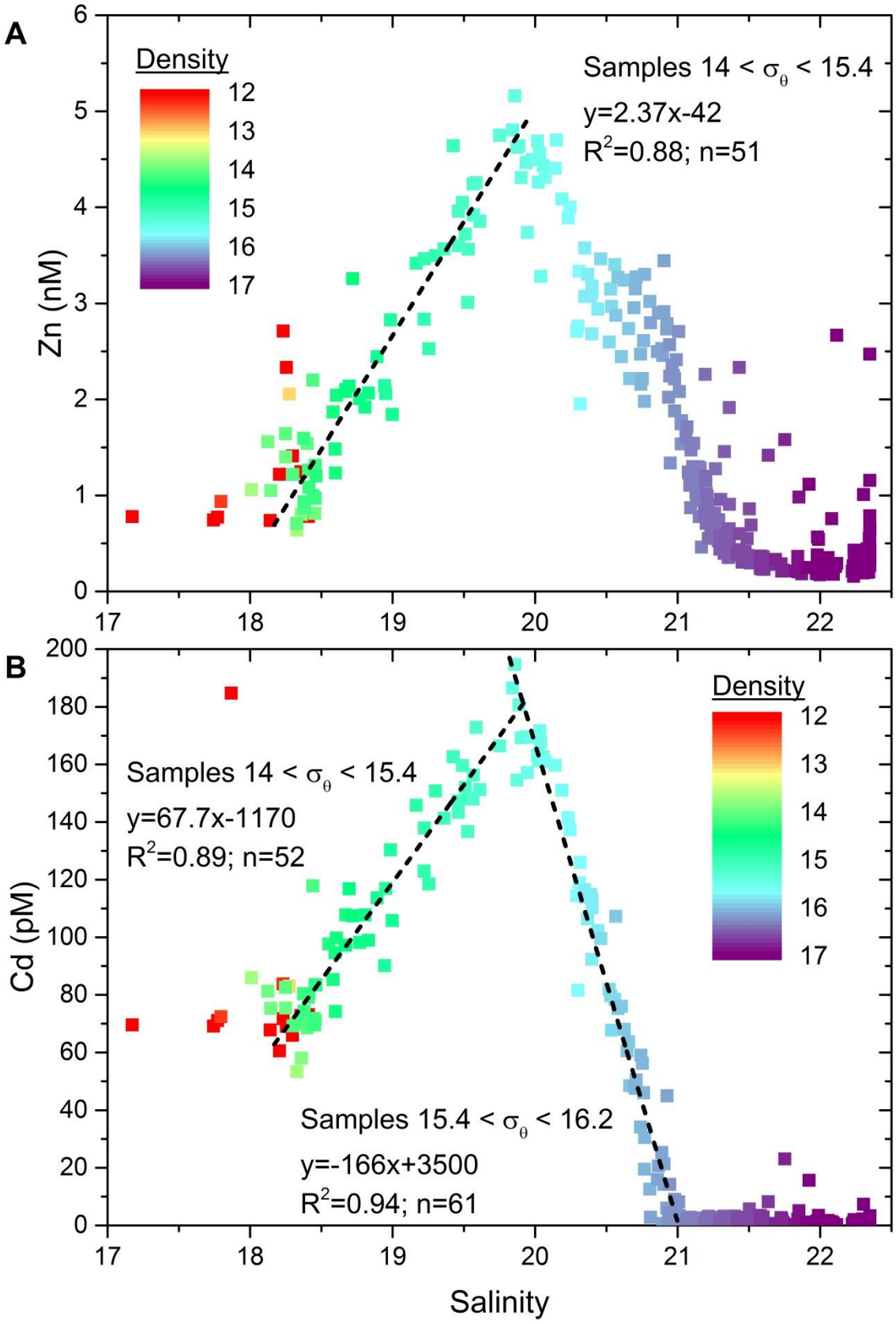

Fig. 4.8. Relationship between salinity and dissolved Zn (A) and dissolved Cd (B) in the water column of the Black Sea. Color scale corresponds to density (σ_θ).

4.4.2.4 Aluminum and gallium

No previous data exists on the distribution of dissolved Al and Ga in the Black Sea. The vertical profiles of dissolved Al and Ga in the Black Sea are very similar, which is not surprising given their relative positions in the periodic table would predict very similar chemistry between the two elements. Neither element is expected to undergo a change in redox state under anoxic conditions. Maximum concentrations of both elements are observed in surface waters indicating atmospheric deposition is a source of these metals to surface waters in the central basin (Fig. 4.2, 4.6) while fluvial sources are likely more important on the continental shelf. The concentration of dissolved Al reaches >10 nM in surface waters before decreasing sharply to <2 nM at σ_θ = ~14.5 kg/m^3, slightly increasing to ~4 nM at σ_θ = ~16.5 kg/m^3, and again decreasing to ≤ 2 nM in the deep basin. The concentration of dissolved Ga in surface waters is ~40 to 50 pM, decreasing to <30 pM at σ_θ = ~15.5 kg/m^3, then increases to >40 pM at σ_θ = ~16.5 kg/m^3 and finally decreases to ~10 pM in the deep basin. The surface maxima suggest atmospheric deposition is an important source of Al and Ga to surface waters. Decreasing concentrations in surface waters below the maxima likely reflect scavenging of dissolved Al and Ga onto the surfaces of organic particles. Further scavenging is probably occurring in the region of Mn and Fe oxide formation within the redoxcline. The increase in dissolved Al and Ga at σ_θ = ~16.5 kg/m^3 coincides with the increase in dissolved Mn and Fe concentrations, indicating that Al and Ga are released during the dissolution of Mn and Fe oxides as they sink into anoxic waters. Finally, the decrease in dissolved Al and Ga concentrations in the deep basin likely reflect scavenging onto metal-sulfides that are forming in the water column of the deep basin. These results demonstrate that the distributions of Al and Ga reflect the effects of the redox driven particulate formation and dissolution cycle in the Black Sea water column but the effects of the redox cycle on the concentrations of Al and Ga are relatively minimal. As the solubility of Al and Ga are not significantly controlled by the redox state of the marine environment, it is suitable to utilize Al and Ga as normalizing lithogenic elements when quantifying the enrichments of redox sensitive trace metals. The transfer of Al (and other lithogenic elements) to sediments with biogenic particulate matter is also an important consideration when evaluating the behavior of lithogenic normalizing element. For Al, this is especially important in regions with high diatom abundances (*e.g.* Dymond *et al.*, 1997).

4.4.2.5 Titanium and zirconium

Similar to Al and Ga, Ti and Zr reside in the same column of the periodic table, do not undergo active redox chemistry, and no previous data exists on their distributions in the Black Sea or in any other anoxic marine basin. Unlike the close relationship observed between Al and Ga, the distributions of dissolved Ti and and Zr are strikingly different (Fig. 4.2, 4.3, 4.6). Dissolved Zr displays relatively consistent concentrations of ~250 to 500 pM in surface waters ($10 < \sigma_\theta < 16$), a sharp increase to >1000 pM at σ_θ = ~16.5 kg/m^3 and a slight decrease to <750 pM in the deep basin (Fig 4.6). The vertical profile of dissolved Zr is very similar to that of dissolved Al and Ga, indicating similar processes are controlling their distributions. One exception is the lack of a surface maximum in the distribution of dissolved Zr, indicating the atmospheric deposition is less important for Zr than for Al and Ga. The vertical profile of dissolved Ti is characterized by a slight maximum in surface waters up to ~200 pM, decreasing concentrations down to ~30 pM at $\sigma_\theta \leq$ ~16 kg/m^3, and a rapid increase in concentration up to >2000 pM at $\sigma_\theta \geq$ ~16 kg/m^3 (Fig. 4.2, 4.3. 4.6).

The rapid rise in the dissolved Ti concentration appears to occur at two different depths. The initial rise occurs just below the redoxcline at a depth of ~95 to 160 m at station 2 and is coincident with the rise in dissolved Fe (Fig 4.2). The strong correlation between the dissolved Fe and Ti concentrations across all stations between depths of ~80 to 160 m (Fig. 4.9) suggests that they have a common source, which for Fe is known to be the dissolution of Fe oxide minerals in shelf-sediments under reducing conditions (Raiswell and Canfield, 1998; Wijsman *et al.*, 2001; Anderson and Raiswell, 2004, Lyons and Severmann, 2006). Once in the dissolved phase, Fe is transported from shelf regions to the central basin within the redoxcline via diffusion and advection. Similarly, dissolved Ti sourced from Fe minerals bearing Ti within shelf-sediments that is transport laterally to the central basin, could account for the correlation between dissolved Fe and Ti. The second increase in dissolved Ti occurs deeper in the water column at a depth range of 300 to 1000 m at station 2 (Fig. 4.3). Dissolution of Fe oxide minerals in the sediment, or possibly sinking atmospheric dust particles, in the deep basin releases both Fe and Ti to the dissolved phase. However, unlike in the redoxcline where Fe is stable in the dissolved phase, dissolved Fe quickly reacts with H_2S in the deep basin to form FeS (mackinawite) and ultimately pyrite. Thus, the release of dissolved Fe and Ti are decoupled in the deep basin. This hypothesis is supported by previous studies which have measured a benthic diffusive

flux of Ti out of reducing marine sediments and into the overlying water column (Skrabal, 2006; Skrabal and Terry, 2002). It is currently unclear why Ti is not scavenged from solution on to sinking metal-sulfides as is observed for Al, Ga, and Zr.

The mass of Ti required to support the deep water concentration (~2000 pM) over a water column depth of 1000 m (Fig. 4.3) is approximately 96 mg over an area of 1 m^2 or approximately 9600 ng over an area of 1 cm^2. The average concentration of Ti in shale is ~0.46 wt% (Li and Schoonmaker, 2003) which is a reasonable approximation of sediments deposited in the deep Black Sea. A water column 1000 m deep with an area of 1 cm^2 containing 9600 ng Ti represents only ~0.2% of the total Ti in 1 g of sediment. Thus, it is expected that any diffusive benthic flux of Ti to the deep Black Sea will have an inconsequential effect on the Ti concentration of the sediments supplying the Ti and that the normalization of sedimentary records of redox sensitive trace metals to Ti should be unaffected by the mobility of Ti under anoxic conditions. However, the mobility of Ti in marine sediments observed in the Black Sea in this study and in estuarine and pelagic sediments (Skrabal, 2006; Skrabal and Terry, 2002) suggests that benthic fluxes of Ti may be an important component of the marine biogeochemical cycle of Ti.

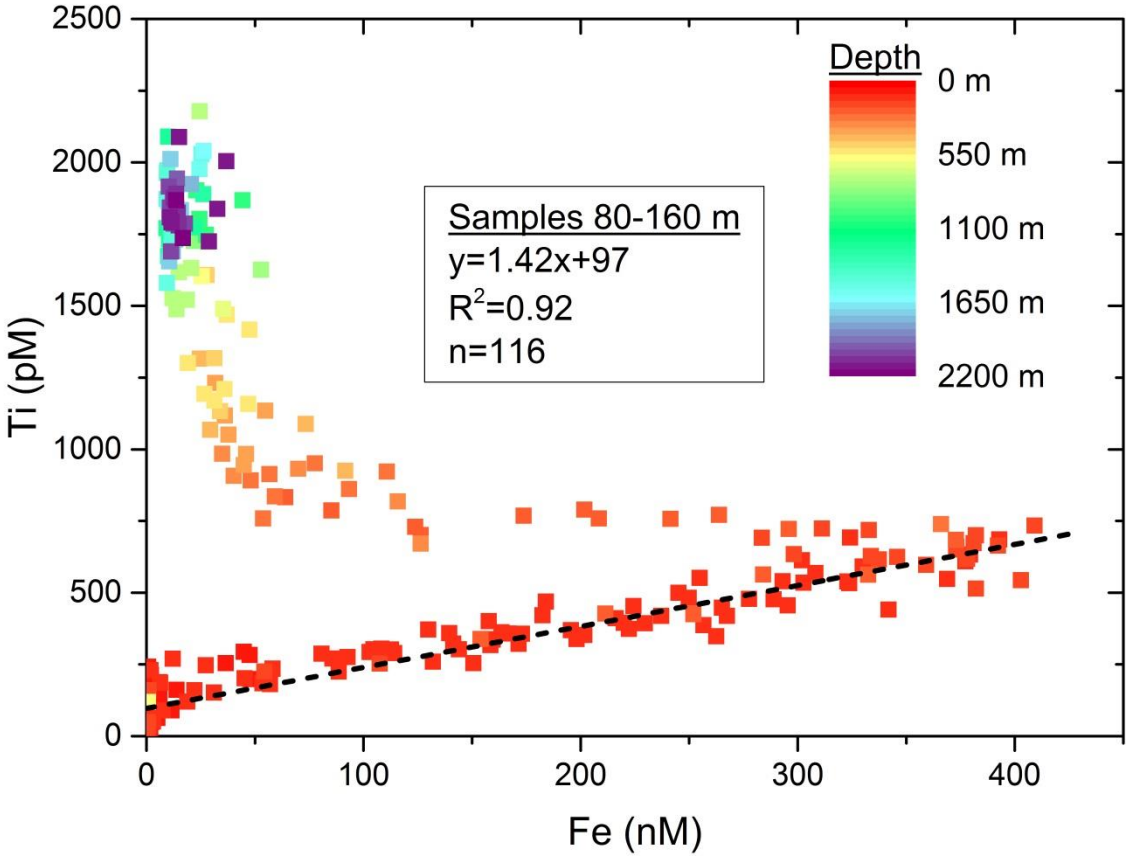

Fig. 4.9. Relationship between dissolved Ti and Fe in the water column of the Black Sea.

4.4.2.6 Yttrium and lanthanum

The behavior of the rare earth elements in the water column of the Black Sea have been discussed in detail previously by German *et al.* (1991) and Schijf *et al.* (1991). The general shape of the vertical profiles of dissolved La and the magnitude of the concentration changes of dissolved La observed in this study (Fig. 4.2, 4.3, 4.6) are nearly identical to the previously reported observations. Furthermore, the distribution of dissolved Y is tightly coupled to that of La, suggesting very similar controls on their distributions. The oxidation state of both Y and La is +3 and is not expected to change under reducing conditions. Both elements show slight surface maxima, with concentrations of dissolved Y of ~200 to 300 pM and dissolved La of ~20 pM. The concentrations of both elements display minimum concentrations at σ_θ = ~16 kg/m^3 with dissolved Y approaching ~150 pM and dissolved La of <10 pM. The maximum concentrations of both elements are observed at $\sigma_\theta \geq$ ~17 kg/m^3. Dissolved Y reaches a maximum concentration of ~375 pM, while dissolved La reaches ~75 pM. The elevated concentrations in the anoxic deep basin of the Black Sea suggest that reduced marine

waters, such as anoxic pore waters, are a likely source of Y and La, and perhaps other rare earth elements, to overlying oxygenated waters as suggested in recent literature (*e.g.* Abbott *et al.*, 2015 and references therein). Both elements show a slight decrease in near bottom waters, possibly due to scavenging. The tightly coupled behavior between Y and the rare earth elements has been previously observed in the open ocean (*e.g.* Alibo and Nozaki, 1999; Zhang *et al.*,1994) and this relationship is also observed in the Black Sea (Fig. 4.10). One notable difference in their distributions occurs in the upper ~75 m (σ_θ < ~15.5 kg/m^3) of the water column where the concentration of dissolved Y increases with only a slight, if any, increase in La, suggesting a source of Y to surface waters that is not associated with La, or contrarily, the removal of La without the associated removal of Y (Fig. 4.10b). The general shape of the vertical profiles of dissolved Y and La are similar to those of dissolved Al, Ga, and Zr, in that minimum concentrations are observed at $\sigma_\theta \leq$ ~16 kg/m^3 and maximum concentrations are observed at $\sigma_\theta \geq$ ~16.5 kg/m^3. These similarities suggest that the distributions of these elements are dominated by scavenging and dissolution processes related to the redox cycling of sinking particles, such as Mn and Fe oxides.

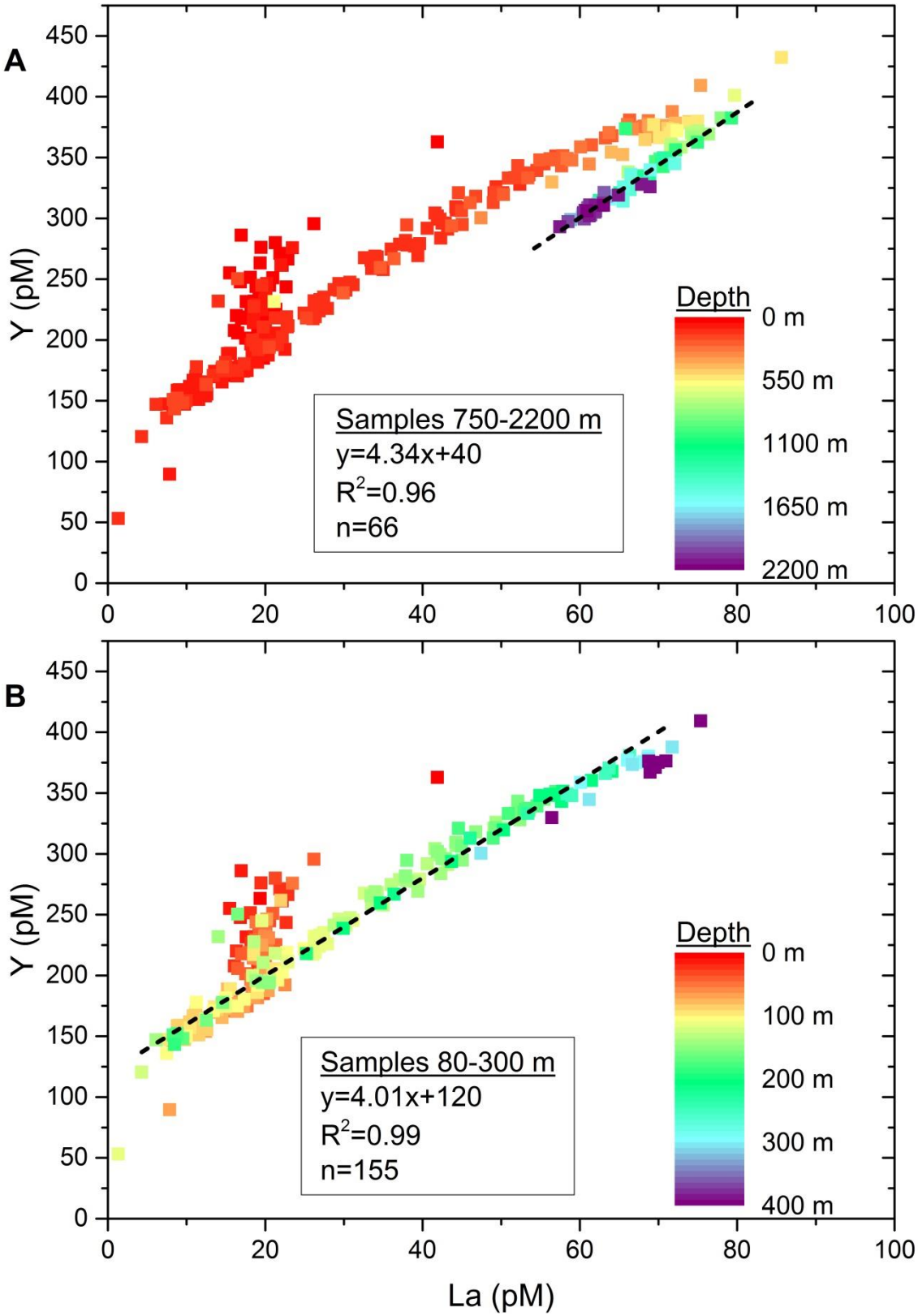

Fig. 4.10. Relationship between dissolved Y and La in the Black Sea water column over the full depth range (A) and over the upper 400 m (B).

4.5 Conclusions

The vertical profiles of dissolved trace metals including Fe, Mn, Cd, Zn, Cu, Al, Ga, Ti, Zr, Y, and La from the 2013 GEOTRACES expedition to the Black Sea are reported. The distributions of Fe, Mn, Cd, Zn, Cu, and La are all very similar to previous studies. Both dissolved Fe and Mn display strong maximum concentrations within the upper layer of the sulfidic deep basin which is due to the dissolution of sinking metal oxide particles which formed in the upper oxygenated water column. Dissolved Cd and Zn display evidence of regeneration associated with aerobic respiration in the upper portion of the redoxcline. Dissolved Cd, Zn and Cu are severely depleted in the euxinic deep basin due to the formation of insoluble sulfide species. The distributions of dissolved Al, Ga, Ti, Zr, and Y are reported for the first time for the Black Sea. Scavenging onto sinking oxides and subsequent release during dissolution are the primary controls on the distributions of Al, Ga, Zr, Y and La. The distributions of dissolved Al, Ga, and Zr indicate that these elements respond to redox processes in the marine environment, but the effects are insufficient to compromise their suitability as normalizing lithogenic elements when quantifying enrichments of redox sensitive trace metals in marine sediments. The distribution of dissolved Ti is enigmatic and appears to show limited effects of scavenging. Elevated concentrations of dissolved Ti up to ~2000 pM indicate an increase in solubility under euxinic conditions. Although the effect in the Black Sea appears to be insignificant, this observation may be a cause for concern when Ti is used as a normalizing lithogenic element in quantifying the enrichments of redox sensitive trace metals in sedimentary records and warrants further investigations of the geochemical behavior of Ti under anoxic and sulfidic marine conditions.

CHAPTER 5

IRON ISOTOPE FRACTIONATION DURING PYRITE FORMATION IN A SULFIDIC PRECAMBRIAN OCEAN ANALOGUE

5.1 Abstract

The iron isotope composition of sedimentary pyrite is commonly utilized as a tracer of the evolution of microbial and redox controls on the iron cycle in the Precambrian ocean, yet the intrinsic iron isotope fractionation accompanying pyrite formation is not well constrained. We demonstrate, for the first time, a large shift in the isotope composition of dissolved iron in the euxinic water column of the Black Sea that is best explained by an iron isotope fractionation factor of approximately 2.75 permil (‰) accompanying syngenetic (water column) pyrite formation and much smaller iron isotope fractionation associated with Fe(II) to Fe(III) oxidation in near surface waters. Pyrite formation results in the largest iron isotope fractionation yet to be reported for reactions that do not involve iron redox chemistry. In light of these findings, the sedimentary pyrite iron isotope record suggests a fundamental shift towards more sulfidic conditions in the Precambrian oceans around 2.3 billion years ago coinciding with the timing of the Great Oxidation Event in the early Proterozoic.

5.2 Introduction

Reliable reconstruction of the rise and fall of oxygen (O_2) in the past ocean-atmosphere system is crucial for understanding the evolution of life on Earth and evaluating the potential for life on inter- and extra-solar planets. Redox-sensitive trace metals, such as iron (Fe), provide robust tracers of oxygenation and de-oxygenation due to pronounced changes in their speciation, biogeochemical cycling, and concomitant stable isotope fractionation, when environmental conditions transition between oxic, anoxic, and euxinic (anoxic and sulfidic) states (Lyons *et al.*, 2009). The persistence of widespread anoxic conditions in the Precambrian ocean-atmosphere system resulted in oceans rich in dissolved iron and an iron cycle that was much different than today's where oxygenated conditions prevail (Holland, 2005). The iron isotope composition

($\delta^{56}Fe$) of Precambrian sedimentary pyrite (FeS_2) suggests a perturbation of the iron cycle and the chemistry of the oceans, perhaps to more oxidizing conditions, around 2.3 billion years (Ga) ago, coincident with the permanent rise in atmospheric O_2 in the early Paleoproterozoic, known as the 'Great Oxidation Event' or GOE (Fig. 1.2, 1.3; Holland, 2002; Rouxel et al, 2005). The $\delta^{56}Fe$ of pyrites formed before the GOE between ca. 2.8 to 2.3 Ga ago commonly display large negative values ranging between +0.5 to -3.5‰, which contrasts strongly with the near zero $\delta^{56}Fe$ values of bulk continental and oceanic crust, while pyrites younger than ca. 2.3 Ga display more positive $\delta^{56}Fe$ values ranging between +1.2 to -0.5‰ (Fig. 1.3; Rouxel *et al.*, 2005, Archer and Vance, 2006). However, the exact character in which the Archean ocean transitioned from dominantly anoxic to oxic is not well constrained, in large part because the origin of the large, negative $\delta^{56}Fe$ signatures of Archean pyrite is highly contentious. By implication, models describing the rise of oxygen and the evolution of life are also uncertain for this crucial time interval.

As iron isotope fractionation occurs during both abiotic and biologically-mediated reactions (*e.g.* Johnson *et al.* 2008), different biogeochemical scenarios have been invoked, and debated, to explain the variations in the $\delta^{56}Fe$ record preserved in Precambrian sedimentary pyrite. However, all of these scenarios rely on the assumption that pyrite is essentially a passive recorder of seawater $\delta^{56}Fe$ whereby no iron isotopic shift occurs during its precipitation from oceanic waters. Based on this assumption, negative $\delta^{56}Fe$ signatures in pyrite are generally considered as being inherited from a dissolved oceanic Fe(II) reservoir depleted in ^{56}Fe (Rouxel *et al.*, 2005). To date, reactions involving a change in oxidation state between highly soluble Fe(II) and poorly soluble Fe(III) are generally assumed to produce the largest iron isotope fractionations. Thus, mechanisms proposed for generating a marine Fe(II) reservoir heavily depleted in ^{56}Fe commonly include extensive abiotic oxidation, on the order of 90%, of the oceanic dissolved Fe(II) reservoir to Fe(III) followed by deposition of ^{56}Fe-enriched iron oxides and/or microbial iron reduction (MIR) which produces Fe(II) depleted in ^{56}Fe (*e.g.* Beard *et al.*, 1999; Welch *et al.*, 2003; Icopini *et al.*, 2004; Rouxel *et al.*, 2005; Yamaguchi *et al.*, 2005; Johnson *et al.*, 2008).

Importantly, the assumption that pyrite is a passive recorder of seawater $\delta^{56}Fe$ is unfounded because the intrinsic iron isotope fractionation associated with the process of pyrite formation is not well constrained, leading to uncertainty in reconstructions of the Precambrian iron cycle based on sedimentary pyrite $\delta^{56}Fe$. Uncertainty in the

interpretation of sedimentary pyrite δ^{56}Fe records is largely due to conflicting constraints on iron isotope fractionation during pyrite formation from laboratory-controlled experiments. For example, experimental data suggests that precipitation of mackinawite (FeS_m), a precursor to pyrite, is governed by a unidirectional, mass-dependent kinetic process, leading to the residual dissolved Fe(II) being ca. 0.9‰ heavier that the precipitated mackinawite, described by a kinetic isotope fractionation factor $\varepsilon_{Fe(II)-FeSm}$ of up to +0.9 ± 0.3‰ (see supplementary material; Butler *et al.*, 2005). Subsequent conversion of FeS_m to pyrite formation is accompanied by an additional kinetic isotope fractionation factor ($\varepsilon_{FeSm-pyrite}$) of +2.2 ± 0.7‰ (Guilbaud *et al.*, 2011). Taken together, these results suggests a total kinetic isotope fractionation factor ($\varepsilon_{Fe(II)-pyrite}$) of +3.1 ± 1.0‰ for the formation of pyrite from dissolved Fe(II). Contrarily, separate experiments conducted by Wu *et al.* (2012) suggest that pyrite formation is likely dominated by an equilibrium exchange reaction between Fe(II) and FeS_m described by an equilibrium isotope fractionation factor $\varepsilon_{Fe(II)-FeSm}$ that is almost an order of magnitude smaller and between -0.32 ± 0.29‰ to -0.64 ± 0.36‰. Therefore, the combination of kinetic and equilibrium iron isotope fractionation during pyrite formation can potentially account for the full range of δ^{56}Fe observed in Precambrian sedimentary pyrite (Guilbaud *et al.*, 2011), without invoking additional fractionation mechanisms, such as abiotic Fe(II)-Fe(III) oxidation or MIR. However, the experimental conditions leading to kinetic iron isotope fractionation during pyrite formation in the experiments of Guilbaud *et al.*, (2011) are far from what can be expected in nature and thus the findings have been intensely debated, and largely considered inapplicable (Czaja *et al.*, 2012; Guilbaud *et al.*, 2012; Wu *et al.*, 2012; Yoshiya *et al.*, 2015). Consequently, scenarios for pyrite formation in the Archean oceans have only been considered in the context of the comparatively minor iron isotope fractionation observed under equilibrium conditions.

Here we report, for the first time, the observed iron isotope fractionation associated with abiotic pyrite formation in a natural setting, represented by the water column of the Black Sea, which provides a unique opportunity to contribute to the abovementioned debate. The Black Sea is the world's largest anoxic marine basin, and serves as a useful analogue to the dominantly anoxic and potentially euxinic conditions present in the Precambrian ocean. Seawater samples were collected during the 2013 MedBlack GEOTRACES expedition (cruise 64PE373) (Fig. S1). Samples collected at

Station 2 in the western central basin and Station 5 in the eastern central basin were analyzed for $\delta^{56}Fe$ and other supporting parameters (see supplementary material).

5.3 Results and Discussion

The vertical profiles of dissolved O_2, H_2S, iron (Fe_d) and $\delta^{56}Fe$ in the water column of the Black Sea at Stations 2 and 5 are presented in Fig. 5.1. The transition from oxic to anoxic to euxinic conditions (*i.e.* the redoxcline) occurs in the water column over a depth range between ~90 to 100 m at Station 2 and between ~100 to 115 m at Station 5. The distribution of Fe_d is controlled by the redox gradient in the water column of the Black Sea (Lewis and Landing, 1991). Three distinct zones of Fe_d and $\delta^{56}Fe$ can be discerned; (1) surface waters (*i.e.* above the redoxcline) are characterized by low Fe_d (<1 nmol kg^{-1}) and variable $\delta^{56}Fe$ between ca. -0.09 and -1.46‰. Low Fe_d concentrations are typical of oxygenated surface waters due to the low solubility of Fe(III) and biologic utilization. The large range of $\delta^{56}Fe$ in surface waters likely reflects many processes that are not well understood and is not the focus of this report. (2) Below the redoxcline Fe_d increases to a maximum of ca. 400 nmol kg^{-1} between 150 and 160 m at Station 2 and at 175 m at Station 5, while $\delta^{56}Fe$ falls within a narrow range between ca. -0.67 and -1.12‰. (3) Below the Fe_d maximum, Fe_d decreases sharply to values of ca. 10 to 15 nmol kg^{-1} at depths below 1000 m, while $\delta^{56}Fe$ increases in parallel to a maximum value of +2.36 ± 0.05‰. Thus, there is a >3‰ gradient in the dissolved $\delta^{56}Fe$ in the Black Sea water column while Fe_d changes by up to three orders of magnitude. The concomitant gradients in Fe_d and $\delta^{56}Fe$ in the water column can be understood based on current models of iron cycling in the Black Sea, as discussed below.

It is well established that reductive dissolution of reactive iron (hyrd)oxides in Black Sea shelf sediments mobilizes Fe(II) which is subsequently exported offshore along isopycnals associated with the redoxcline where both O_2 and H_2S are present at trace levels. This iron 'shuttle' results in the pronounced wedge of elevated Fe_d in the central basin water column and prominent enrichments of reactive iron in deep central basin sediments (Raiswell and Canfield, 1998; Wijsman *et al.*, 2001; Anderson and Raiswell, 2004; Lyons and Severmann, 2006; Fig. 5.1). The $\delta^{56}Fe$ of the Fe_d exported from shelf sediments has been estimated to be -1.3 ± 0.3‰ based on $\delta^{56}Fe$ signatures of

bulk sediments and pyrite from the deep central basin (Severmann *et al.*, 2008). We argue that the $\delta^{56}Fe$ of the laterally exported Fe_d that reaches the central basin is instead ca. -0.70 ± 0.08‰ based on the compositions of the two samples from 150 and 160 m at Station 2 and the sample from 175 m at Station 5 which have the highest Fe_d and should therefore be most representative of the laterally exported Fe_d (Fig. 5.1). The negative $\delta^{56}Fe$ signature of the exported Fe_d supports the role of MIR as an important process supplying Fe_d to the central basin (Severmann *et al.*, 2008).

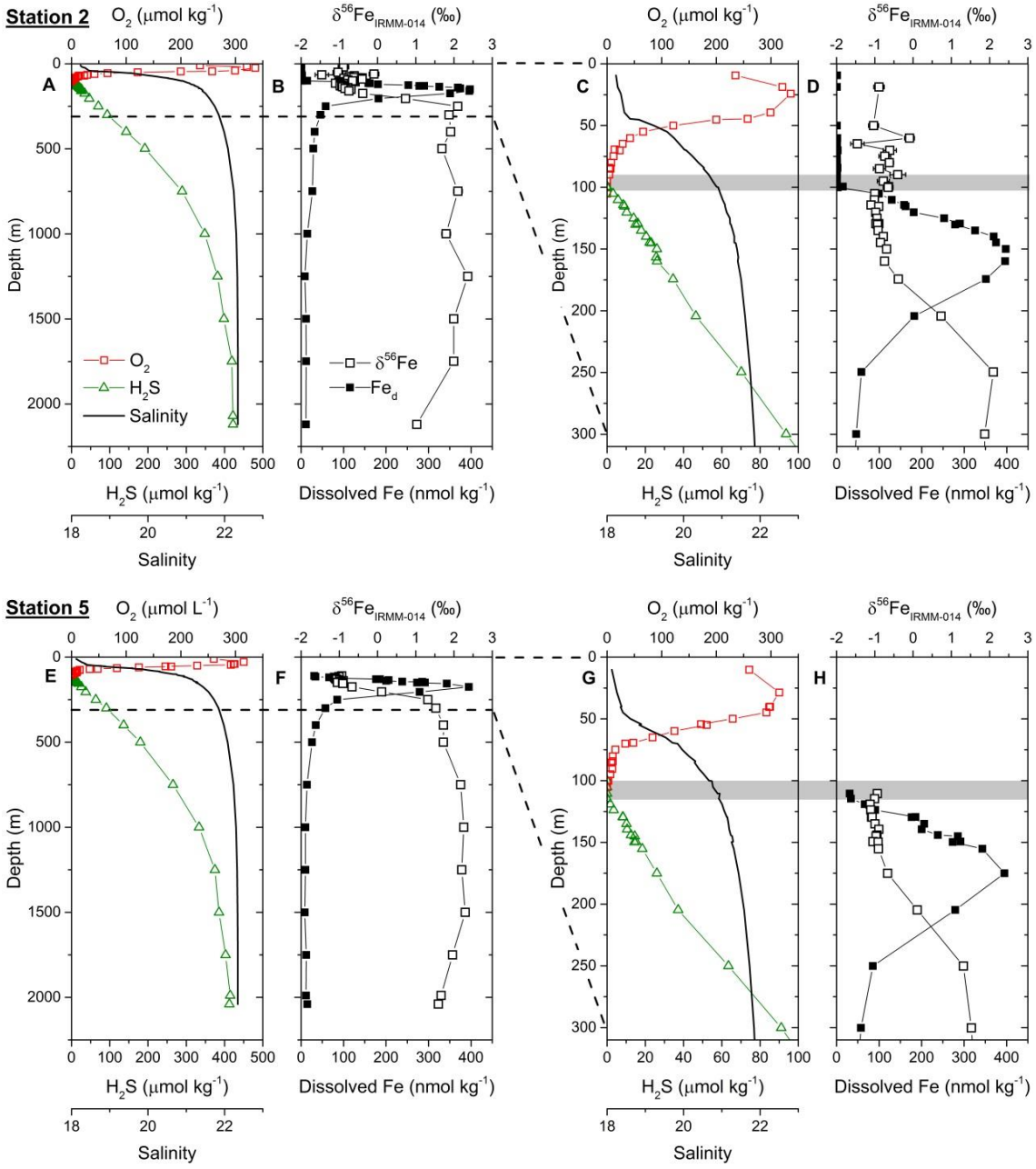

Fig. 5.1. Water column depth profiles of dissolved oxygen, hydrogen sulfide, salinity, Fe_d, and $\delta^{56}Fe$ in the Black Sea. The full depth profiles from Station 2 (**A**, **B**) and Station 5 (**E**, **F**) are shown in addition the upper 300 m from Station 2 (**C**, **D**) and

Station 5 (**G**, **H**). Oxygenated surface waters are separated from euxinic (anoxic and sulfidic) deep waters by the redoxcline at ~90 to 100 m at Station 2 and 100 to 115 m at Station 5, denoted by the grey horizontal bar in (**C**, **D**, **G**, **H)**. Oxygenated surface waters are characterized by low Fe_d (<1 nmol kg^{-1}). The wedge of elevated Fe_d centered at ~150 to 160 m at Station 2 and ~175 m at Station 5 results from shelf to basin transport of iron released from shelf sediments during reductive dissolution and represents the primary source of iron to the deep central basin. Fe_d diffuses upwards away from the center of the wedge and into the redoxcline where it is oxidized and precipitated, thereby driving the gradient in Fe_d and $\delta^{56}Fe$ at depths between the redoxcline and the Fe_d maximum. Below the Fe_d maximum, Fe_d is sequestered by syngenetic pyrite formation. Iron isotope fractionation accompanies both oxidation and pyrite formation, leading to a ca. 3‰ gradient in $\delta^{56}Fe$ over the water column. See text for details. Error bars on $\delta^{56}Fe$ represent the analytical internal error (2SE).

Samples from the upper part of the Fe_d wedge, between 105 and 160 m depth at Station 2 and between 115 and 175 m depth at Station 5, display a large positive gradient in Fe_d and a small, but resolvable gradient in $\delta^{56}Fe$ towards heavier values. The upward diffusion of Fe_d away from the center of the wedge and into the redoxcline leads to the oxidation of Fe(II) to Fe(III) and precipitation of iron (hydr)oxides. This upwards loss of Fe_d accounts for the observed gradient in Fe_d across this depth range. It is likely that the small shift in $\delta^{56}Fe$ from ca.-1.1‰ to -0.7‰ reflects the iron isotope fractionation associated with progressive oxidation and removal of Fe_d, rather than precipitation of iron-sulfides because the H_2S concentration at these depths is not sufficiently high to support the latter process (Landing and Lewis, 1991). By combining both datasets from Stations 2 and 5 and assuming the highest Fe_d at each station represents the initial Fe_d, the fraction of Fe_d removed at each depth through Fe(II)-Fe(III) oxidation can be calculated and the corresponding isotope fractionation factor associated with this removal process, operating under equilibrium or kinetic conditions, can be modelled. Using this approach, the covariation between Fe_d and $\delta^{56}Fe$ in samples from depths between the redoxcline and the Fe_d maximum can be described equally well by both an equilibrium fractionation model with $\varepsilon_{Fe(II)-Fe(III)}$ = -0.40 ± 0.12‰ (2SE) and a Rayleigh fractionation model with $\varepsilon_{Fe(II)-Fe(III)}$ = -0.19 ± 0.07‰ (2SE) (Fig. 5.2a; see supplementary material). These values are significantly smaller than experimentally derived $\varepsilon_{Fe(II)-Fe(III)}$ values of up to ca. -3‰ during equilibrium isotope exchange (Welch *et al.*, 2003). The apparently subdued $\varepsilon_{Fe(II)-Fe(III)}$ may indicate Fe(III) is recycled back into the Fe(II) reservoir as oxidized particles sink out of the redoxcline into underlying anoxic waters and/or that additional kinetic isotope

fractionation during the adsorption of Fe(III) to particles counteracts the expression of the full equilibrium isotope fractionation factor (Beard and Johnson, 2004).

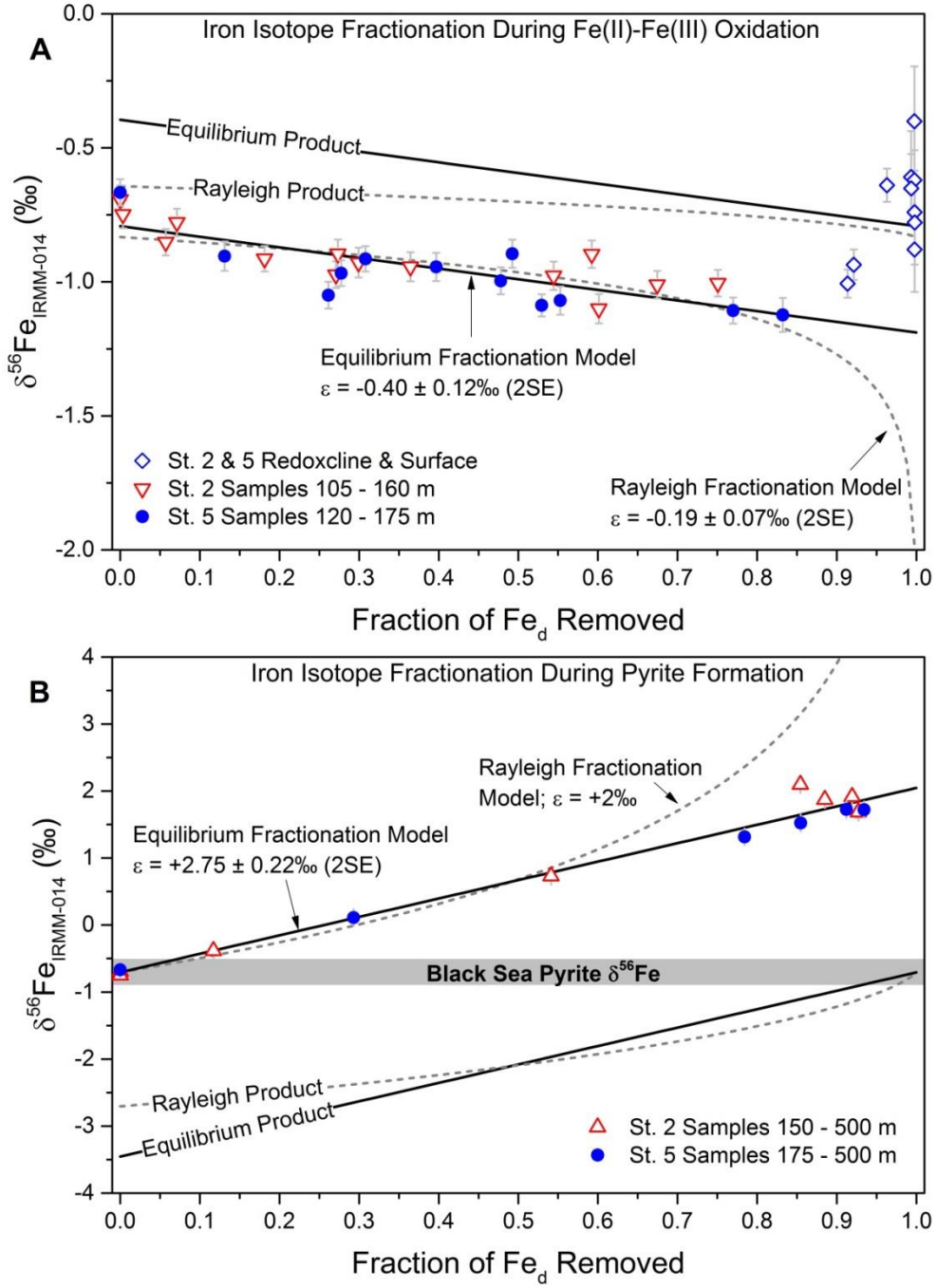

Fig. 5.2. Plot of fraction of Fe_d removed versus $\delta^{56}Fe$ from both Stations 2 and 5 in the Black Sea. In (**A**), the removal of upward diffusing Fe_d due to oxidation in the redoxcline results in iron isotope fractionation which can be explained equally well by both an equilibrium fractionation model (solid lines) with $\varepsilon_{Fe(II)-Fe(III)} = -0.40 \pm 0.12‰$ (2SE) and a kinetic Rayleigh fractionation model (dashed lines) with $\varepsilon_{Fe(II)-Fe(III)} = -0.19 \pm 0.07‰$ (2SE). Samples from within and just above the redoxcline may contain residual Fe(III) that still remains in solution and are characterized by $\delta^{56}Fe$ values that

approach the modelled Fe(III) product. In (**B**), syngenetic pyrite formation at depths between the Fe_d maximum and ~500 m results in iron isotope fractionation that is best described by an equilibrium isotope fractionation model (solid lines) with $\varepsilon_{Fe(II)-pyrite}$ = +2.75 ± 0.22‰ (2SE). A Rayleigh fractionation model (dashed lines) with $\varepsilon_{Fe(II)-pyrite}$ = +2‰ is shown for reference but is not a good fit to all data. The range in $\delta^{56}Fe$ measured in pyrite from euxinic Black Sea sediments is denoted by the horizontal grey bar (Severmann *et al.*, 2008). Error bars on $\delta^{56}Fe$ represent the analytical internal error (2SE).

Below the Fe_d maximum at 150 to 160 m at Station 2 and 175 m at Station 5, Fe_d decreases sharply primarily due to pyrite formation directly from the water column (syngenetic) of the Black Sea (Lewis and Landing, 1991; Wilkin and Arthur, 2001), in parallel with rapidly increasing H_2S concentrations and the establishment of intense water column euxinia (Fig 5.1). At 500 m, ~93% of Fe_d has been removed through pyrite formation, with <30 nmol kg^{-1} remaining. Below 500 m, pyrite formation becomes less dominant and secondary processes such as scavenging may influence Fe_d and $\delta^{56}Fe$ (see supplementary material). Figures 5.1 and 5.2b unequivocally demonstrate that syngenetic pyrite formation in the Black Sea preferentially removes light iron isotopes from solution resulting in a residual dissolved Fe(II) reservoir characterized by positive $\delta^{56}Fe$ values and a striking covariation between Fe_d and $\delta^{56}Fe$ at depths between the Fe_d maximum and 500 m. The removal of Fe_d and concomitant iron isotope fractionation with increasing depth is best described by an equilibrium isotope fractionation model with $\varepsilon_{Fe(II)-pyrite}$ = +2.91 ± 0.34‰ (2SE) for Station 2 (Fig. S3) and $\varepsilon_{Fe(II)-pyrite}$ = +2.56 ± 0.08‰ (2SE) for Station 5 (Fig. S4). The combination of datasets from both Stations 2 and 5 is best described by $\varepsilon_{Fe(II)-pyrite}$ = +2.75 ± 0.22‰ (2SE; Fig. 5.2b). It is however, unlikely that Fe(II) and pyrite reach isotopic equilibrium because pyrite is only sparingly soluble and pyrite formation is thus essentially a unidirectional reaction. Iron isotope fractionation during experimental pyrite formation at 100 °C was recently shown to follow a unidirectional, multistep pathway involving isotopic equilibration between the pyrite precursors FeS_m and aqueous iron sulfide (FeS^0_{aq}) which resulted in an 'apparent' equilibrium isotope fractionation for the overall reaction of FeS_m to pyrite (Guilbaud *et al.*, 2011). We propose a similar process is occurring in the Black Sea water column and that our calculated $\varepsilon_{Fe(II)-pyrite}$ of +2.75 ± 0.22‰ is a robust estimate of the total combined iron

isotope fractionation during syngenetic pyrite formation. The $\varepsilon_{\mathrm{Fe(II)-pyrite}}$ determined here is very close to the sum of the experimentally derived kinetic isotope fractionation factors, $\varepsilon_{\mathrm{Fe(II)-FeSm}}$ and $\varepsilon_{\mathrm{FeSm\text{-}pyrite}}$ of +3.1 ± 1.0‰ (Butler *et al.*, 2005; Guilbaud *et al.*, 2011), indicating that kinetic isotope fractionation dominates during syngenetic pyrite formation and that the experimental conditions used by Guilbaud *et al.* (2011) produced results that are applicable to natural systems.

Furthermore, since Fe_d is nearly quantitatively removed in iron-limited deep waters, syngenetic pyrite accumulating in sediments in the deep central basin of the Black Sea should have an iron isotope composition similar to the initial δ^{56}Fe of the Fe(II) reservoir (*i.e.* Fe_d exported from shelf sediments). Previously reported δ^{56}Fe values of pyrite from the deep euxinic Black Sea basin are scarce. One study reports an average sedimentary pyrite δ^{56}Fe of ~ -0.63‰ (Severmann *et al.*, 2008; recalculated relative to IRMM-014), which is slightly more positive than the δ^{56}Fe of Fe_d exported from shelf sediments observed in the present study of -0.70 ± 0.08‰. Textural evidence suggests that syngenetic pyrite derived from the euxinic water column accounts for >85% of the total pyrite in sediments in the deep central basin of the Black Sea, while the other <15% is diagenetic pyrite formed from detrital reactive iron in the sediment (Wilkin and Arthur, 2001) with an assumed δ^{56}Fe overlapping bulk continental and oceanic crust of 0.1‰. A simple isotope mass balance calculation, taking into consideration the above δ^{56}Fe signatures and relative contributions of syngenetic pyrite and diagenetic pyrite to the total sedimentary pyrite, suggests that syngenetic pyrite accumulating in sediments in the deep central basin of the Black Sea has a δ^{56}Fe between -0.63 to -0.76‰. This is nearly identical to the δ^{56}Fe of the Fe_d exported from shelf sediments observed in the upper water column, and provides independent evidence that the δ^{56}Fe of the Fe_d exported from shelf sediments reported in this study is a robust conclusion.

The utilization of Precambrian sedimentary pyrite δ^{56}Fe as a tracer of microbial metabolism and redox evolution of the ocean-atmosphere system requires careful consideration of the intrinsic iron isotope fractionation during pyrite formation. Our study shows, for the first time, that syngenetic pyrite formation in a natural euxinic setting results in a large, permil-level δ^{56}Fe shift away from the composition of the Fe(II) oceanic reservoir from which it precipitated, and gives rise to a fractionation factor of ca. 2.5 to 3‰ for the Fe(II)-FeS_2 system. Moreover, the magnitude of iron

isotope fractionation during syngenetic pyrite formation observed in the euxinic Black Sea water column is the largest yet to be reported for non-redox reactions and is comparable in magnitude to the extent of fractionation associated with experimental Fe(II)-Fe(III) redox reactions. By implication, the large negative $\delta^{56}Fe$ values recorded in Archean pyrites formed between ca. 2.8 to 2.3 Ga (Fig. 1.3; Rouxel *et al.*, 2005; Archer and Vance, 2006) can be explained entirely by pyrite formation under sulfide-limiting conditions whereby only a small fraction of the dissolved Fe(II) reservoir is consumed, thereby allowing for the expression of the maximum Fe(II)-Fe_2S fractionation of ca. 3‰. During the Archean, hydrothermal inputs with an estimated $\delta^{56}Fe$ of 0 to -0.5‰ likely supported a vast oceanic reservoir of dissolved Fe(II) (Yamaguchi *et al.*, 2005). Thus, this simplistic scenario, combining the intrinsic iron isotope fractionation associated with pyrite formation with an oceanic Fe_d reservoir characterized by a $\delta^{56}Fe$ of -0.5‰ is able to account for Archean pyrite with $\delta^{56}Fe$ as low as -3.5‰. Oxidation of Fe(II) and the input of isotopically light iron from MIR may have acted to further decrease the $\delta^{56}Fe$ of the hydrothermally derived dissolved Fe(II) reservoir, but this secondary process is not required to account for the negative $\delta^{56}Fe$ in Precambrian sedimentary pyrite. Under iron-limited conditions, such as in the modern Black Sea, sedimentary pyrite may retain the $\delta^{56}Fe$ signature of the initial dissolved Fe(II) reservoir due to quantitative removal of Fe(II). However, variability in the contributions of syngenetic pyrite and diagenetic pyrite to the total sedimentary pyrite may complicate interpretations of the pyrite $\delta^{56}Fe$ record.

By utilizing the iron isotope fractionation factors determined in the Black Sea, end-member scenarios of vertical profiles of $\delta^{56}Fe$ in the Precambrian ocean can be envisioned (Fig. 5.3). Appreciable levels of atmospheric O_2 after the GOE would have increased the supply of sulfate to the Precambrian oceans through the oxidative weathering of pyrite on the continents. Elevated levels of sulfate in the oceans would have supported the expansion of euxinic conditions in highly productive continental margin settings where the supply of organic carbon was sufficient. In this scenario, a wedge of euxinic water would extend away from the continental margin towards the open ocean. Similar processes occur in modern ocean minimum zones. Under euxinic conditions such as post-GOE, pyrite formation is iron-limited and the $\delta^{56}Fe$ of the residual seawater reservoir is shifted to more positive values as the extent of Fe removed from solution increases. As the extent of Fe removal approaches completion, the $\delta^{56}Fe$ of pyrite produced would approach the $\delta^{56}Fe$ of the initial seawater reservoir

while at the same time the δ^{56}Fe of the residual seawater reservoir approaches its maximum value. Under open ocean conditions with little to no pyrite formation, or sulfide-limited pyrite formation such as is expected pre-GOE, the vertical profile of δ^{56}Fe would have been relatively uniform throughout the deep water column and the δ^{56}Fe of any pyrite that is formed under these conditions would record maximum negative values. Oxidation of Fe(II) to Fe(III) and precipitation of iron oxides in surface waters also results in iron isotope fractionation and can shift the δ^{56}Fe of the residual seawater reservoir, but the magnitude of the fractionation associated with this process is smaller than that of the pyrite formation processes based on the data from the Black Sea. This scenario predicts surface water near the continental margins would be characterized by δ^{56}Fe values that are elevated relative to off shore surface waters.

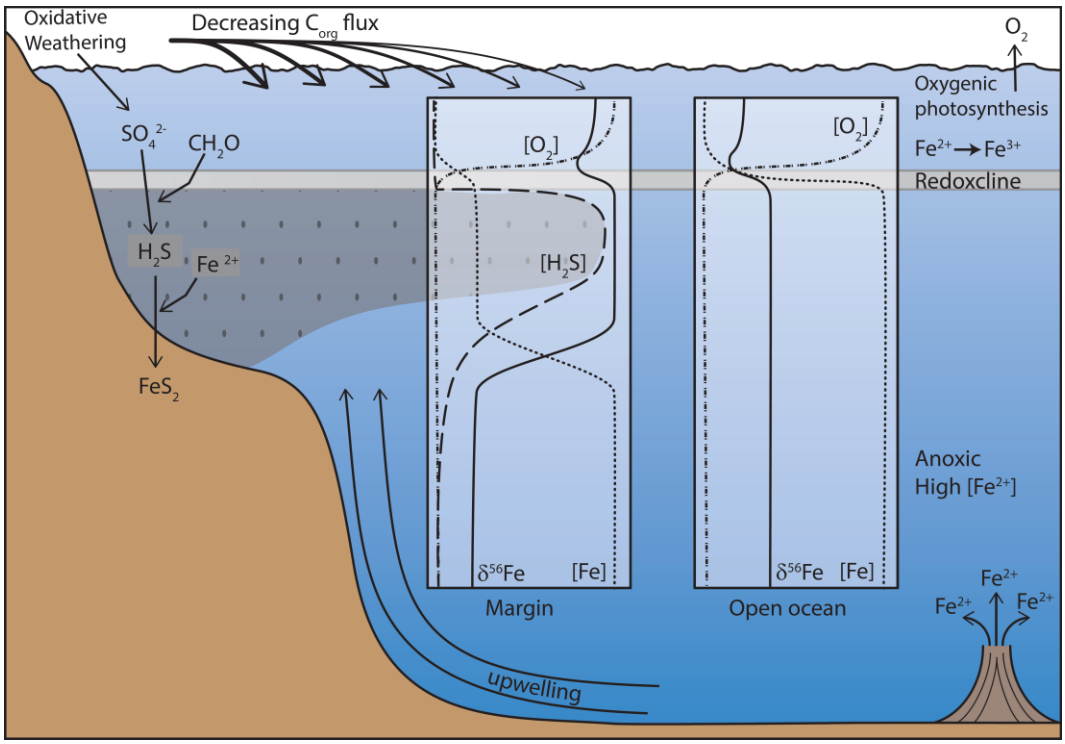

Fig. 5.3. Schematic model depicting possible vertical profiles of δ^{56}Fe in the Precambrian ocean. The Precambrian ocean was likely characterized by a redox stratified water column with anoxic deep waters overlain by oxygenated surface waters, and with sulfidic zones developing along the continental margin as a result of high productivity in surface waters which is driven in part by upwelling of deep waters. Hydrothermal venting supplied Fe with δ^{56}Fe around 0‰ was the primary source of Fe to the Precambrian ocean and supported high concentrations of Fe in anoxic deep waters. Pyrite formation and oxidation reactions in continental margin settings draw down Fe concentrations and generate a residual seawater reservoir with δ^{56}Fe positively fractionated from the initial hydrothermal signature. In open ocean settings, no pyrite formation occurs and oxidation reactions generate a residual seawater reservoir with δ^{56}Fe that is only slightly fractionated from the original hydrothermal signature.

5.4 Supplementary Material

5.4.1 Materials and Methods

5.4.1.1 Sample Collection and Study Site

Seawater samples were collected during the Dutch MedBlack GEOTRACES expedition (cruise 64PE373) in the Black Sea in July 2013 aboard R/V *Pelagia* (Fig. S1). The hydrologic balance in the Black Sea results in a strong vertical stratification with respect to salinity (Fig. 5.1), resulting in slow ventilation rates of the deep central basin. Seawater from the Mediterranean flows along the bottom of the Bosporus Strait into the Black Sea where it mixes with existing water masses and forms the salty, dense water that fills the deep central basin. Several European rivers flowing into the Black Sea keep the salinity of the surface layer low. Since ventilation rates are slow, oxidation of organic matter in the deep basin consumes dissolved O_2 faster than it can be replenished leading to anoxic conditions. Microbial sulfate reduction occurs in the water column and in sediments (Konovalov *et al.*, 2006), resulting in maximum H_2S concentrations of >400 µmol L^{-1} in bottom waters (Fig. 5.1). A total of 12 stations were occupied during the expedition with 6-48 discrete seawater samples collected at each station. The concentrations of dissolved trace metals were determined at all stations while the dissolved Fe isotope composition was determined at Stations 2 and 5 (Fig. S1). Seawater samples were collected using an ultraclean all-titanium framed 'TITAN' CTD sampling system (de Baar *et al.*, 2008; Rijkenberg *et al.*, 2015). Immediately upon recovery, the TITAN CTD system was placed inside a purpose-built class 100 clean room container. Inside the clean room container, seawater was filtered directly from the CTD sampling bottles using 0.2 µm filter cartridges (Sartobran-300, Sartorius) under nitrogen pressure (1.5 atm). Filtered seawater samples were collected in 1 L low density polyethylene (LDPE) bottles and cubitainers ranging in volume from 4 to 10 L which had been acid cleaned following GEOTRACES guidelines (www.geotraces.org). Sample bottles were rinsed five times with sample seawater prior to sample collection. Immediately after collection, seawater samples were acidified to 0.024 M HCl using ultra-high purity 12 M HCl (Seastar™ Baseline®).

Seawater samples were collected for analysis of major nutrients (nitrate, nitrite, ammonia, phosphate, and silicic acid) and hydrogen sulfide (H_2S) in high density polyethylene (HDPE) syringes with a three way valve to limit exposure to air during

sampling from the CTD. The syringes were rinsed three times with the sample before being completely filled and were immediately processed shipboard.

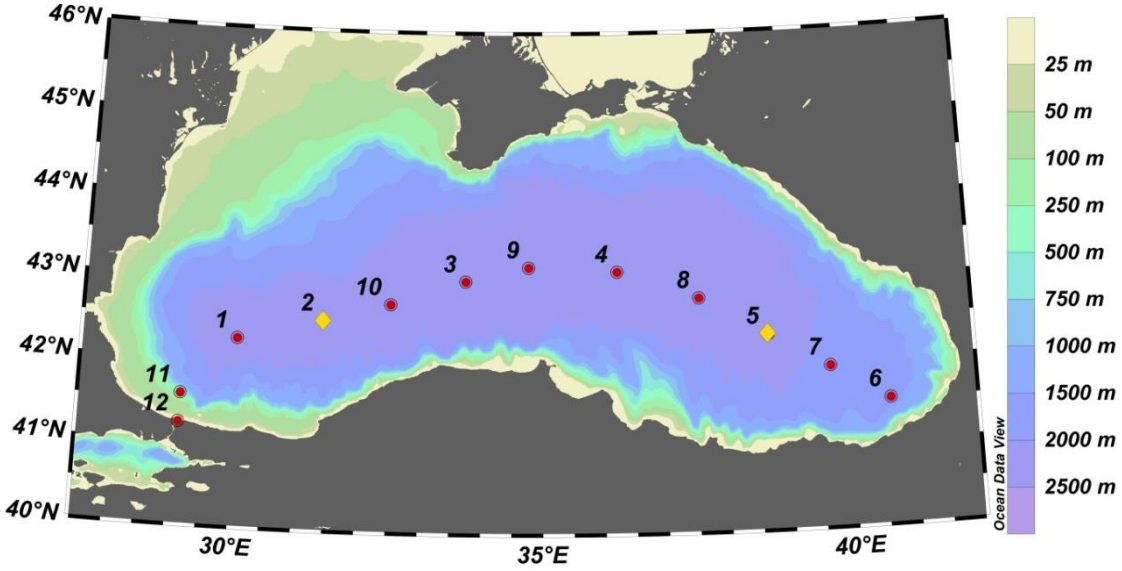

Fig. S1. Map of the station locations in the Black Sea during the MedBlack GEOTRACES expedition to the Black Sea in July 2013 (cruise 64PE373). Water column depth profiles from Stations 2 and 5 are investigated in this study. The Black Sea Fe isotope intercomparison samples were collected at Station 10.

5.4.1.2 Reagents and equipment

The preparation of samples for Fe isotope analysis was performed in the Centre for Trace Element Analysis within the Department of Chemistry, University of Otago, New Zealand. All sample processing and reagent preparation was carried out in Class 10 laminar flow benches within a Class 100 clean laboratory. Ultra-high purity de-ionized water (>18.2 MΩ) supplied by a Milli-Q Element purification system (Millipore, U.S.A) was used for all reagent and equipment preparation. Ultra-high purity acids (HCl, HNO_3 and CH_3COOH) were prepared by sub-boiling quartz distillation. Ultra-high purity NH_4OH and H_2O_2 were purchased from Fisher Scientific (Optima^{TM}). Teflon vials (Savillex, U.S.A.) were used throughout for sample digestion and collection during the chemical preparation of samples. All sample processing equipment was rigorously acid cleaned before use following standard protocols.

5.4.1.3 Extraction of Fe from seawater

For each sample, dissolved Fe was extracted from the seawater matrix by passing it across a column packed with Nobias PA-1 chelating resin (Hitachi High

Technologies, Japan). The procedure utilized here is fundamentally similar to previous methods utilizing Nobias resin in the extraction of dissolved metals from seawater (*e.g.* Sohrin *et al.*, 2008; Biller and Bruland, 2012; Conway *et al.*, 2013; Middag *et al.*, 2015), with some minor modifications developed to aid in the processing of large volumes samples of up to 10 L. Briefly, pre-cleaned Bio-Rad Poly-Prep® chromatography columns (Bio-Rad Laboratories, U.S.A.) were packed with 2 mL of clean Nobias resin. The resin and columns were further cleaned with 2 M HNO_3 and then pre-conditioned with ultra-high purity water. Prior to loading onto the column, the seawater samples were buffered to 0.02 M ammonium acetate and the pH was then adjusted to 4.75 ± 0.20 by the addition of ammonia hydroxide. Seawater samples were then loaded in to HDPE reservoirs attached to the top of the columns. The samples were then passed across the Nobias resin, aided either by gravity flow or by a peristaltic pump attached to the bottom of the columns via Teflon tubing. After the sample loading was complete, the Nobias resin was rinsed with ultra-high purity water and trace metals were then eluted in ~12 mL of 2 M HNO_3. The total Fe blank for the extraction procedure was ca. 0.15 ng and the average recovery of Fe was ca. 80%, both of which are similar to values reported in previous studies employing Nobias resin for extracting Fe from large volumes of seawater (Conway *et al.*, 2013).

5.4.1.4 Purification of Fe

After extraction, Fe was purified by anion-exchange chromatography using a method adapted from Conway *et al.*, 2013. Before anion-exchange purification was commenced, pre-concentrated samples were evaporated to dryness and refluxed in H_2O_2/HNO_3 (1:1) at 120 °C for >12 h to destroy organics which may affect the performance of the anion-exchange protocol. Samples were again evaporated to dryness and re-dissolved in 1 mL of 6 M HCl + 0.0001 M H_2O_2. Chromatography columns were constructed by adding 100 µL of pre-cleaned AG-MP1 resin to pre-cleaned customized columns made from heat-shrink Teflon tubing. Once loaded onto the column, the resin was pre-cleaned with 6 M HCl followed by 2 M HNO_3, and then pre-conditioned with 6M HCl + 0.0001 M H_2O_2. The samples were then loaded on to the resin in 1 mL of 6 M HCl + 0.0001 M H_2O_2 and the resin was subsequently rinsed with 6 M HCl + 0.0001 M H_2O_2 to remove the residual matrix elements remaining in the pre-concentrated sample. Iron was then eluted in 1 M HCl. The Fe containing fraction was then evaporated to dryness and re-dissolved in 1 mL 6 M HCl + 0.0001 M H_2O_2,

and the AG-MP1 purification procedure was repeated to remove residual matrix elements to negligible levels. Samples were then evaporated to dryness and re-dissolved in 2% (v/v) HNO_3 in preparation for MC-ICPMS analysis. The final solution was subsampled and analyzed via Q-ICPMS to calculate the recovery of Fe and to check the purity of the final sample prior to Fe isotope analysis. The total Fe blank for the purification procedure was ca. 0.15 ng. The combined Fe blank for the extraction and purification method is thus ca. 0.3 ng, which is negligible compared to the >300 ng Fe typically recovered from the deep Black Sea samples.

5.4.1.5 Fe isotope analysis by MC-ICPMS

All samples were analyzed for their Fe isotope composition using a Nu Instruments Nu Plasma HR multiple-collector inductively coupled plasma mass spectrometer (MC-ICPMS) in the Centre for Trace Element Analysis at the University of Otago, New Zealand following methods adapted from Millet *et al.*, 2012. In brief, samples were introduced to the plasma via a Nu Instruments DSN 100 desolvating nebulizer system and a 100 µL min^{-1} PFA nebulizer. Analysis of Fe isotope ratios via the Nu Plasma HR requires the utilization of the pseudo-high resolution mode to resolve the $^{54}Fe^+$, $^{56}Fe^+$ and $^{57}Fe^+$ ion beams from their primary plasma based polyatomic interferences $^{40}Ar^{14}N^+$, $^{40}Ar^{16}O^+$ and $^{40}Ar^{16}OH^+$, respectively. Pseudo-high resolution is achieved by reducing the source slit to 0.03 mm and eliminating beam aberrations by closing the alpha slits. Each Fe isotope analysis consisted of 1 block of 60 cycles with 5 s integrations, during which the beam intensities on $^{54}Fe^+$, $^{56}Fe^+$, $^{57}Fe^+$, and $^{58}Fe^+$ were recorded. The detector array on the Nu Plasma HR does not allow for simultaneous detection $^{60}Ni^+$ and $^{53}Cr^+$, which could be used to correct for the presence of $^{58}Ni^+$ and $^{54}Cr^+$ isobaric interferences on $^{58}Fe^+$ and $^{54}Fe^+$, respectively. However, all samples were checked for purity prior to Fe isotope analysis and always displayed negligible concentrations of Ni and Cr in the final Fe cut. The measured ion beam intensities were 'blank-corrected' at the cycle level by subtracting the on-peak zeros measured in pure 2% (v/v) HNO_3 for 60 s before each analysis. On-peak zeros were generally around 0.5 mV for the $^{56}Fe^+$ ion beam and negligible for the other beams. On-peak zero measurements characterize the electronic baseline and the background ion beams due to memory effects from the desolvating nebulizer. The measured Fe isotope ratios were then corrected for instrumental mass fractionation at the cycle level using an off-line data reduction procedure, discussed further below. Cycles were discarded if the

reduced, double-spike corrected Fe isotope ratios were outside 2SD of the 60 cycle average, and the new average was re-calculated. The washout protocol between sample and standard measurements consisted of 5% (v/v) HNO_3 for 3 min and 2% (v/v) HNO_3 for an additional 3 min before the on-peak zeros were measured.

5.4.1.6 ^{57}Fe-^{58}Fe double spike and mass fractionation correction

The double spike technique is an effective method for correcting instrumental mass fractionation during isotope ratio analysis via MC-ICPMS (Siebert *et al.*, 2001) and can account for isotope fractionation during sample processing resulting from non-quantitative yields. Furthermore, the double spike method allows for the accurate determination of the initial elemental concentration via isotope dilution if the mass of the double spike added and the sample mass is accurately known.

A ^{57}Fe-^{58}Fe double spike was added to all samples >24 h prior to the extraction procedure. The double spike was prepared from purified mono-isotopic ^{57}Fe and ^{58}Fe spikes obtained from Oak Ridge National Lab and Isoflex USA, respectively. The final isotope composition of the double spike was $^{54/56}$Fe = 0.0161, $^{57/56}$Fe = 14.4589, $^{58/56}$Fe = 18.7430. Samples were double-spiked to give a ^{58}Fe/^{56}Fe spike/sample ratio of ~1, in order to minimize the uncertainty calculation of the mass fractionation corrected Fe isotope ratios (Rudge *et al.*, 2009). The mass of double spike addition needed to achieve a final ^{58}Fe/^{56}Fe ratio of ~1 in each sample was calculated based on the mass of natural iron in the sample, which was in turn determined from the mass of the sample together with the initial concentration of dissolved Fe in the sample based on a separate pre-concentration method that was performed shipboard (see Middag *et al.*, 2015 for details). The final dissolved Fe concentrations reported here are calculated via isotope dilution equations using the mass fractionation corrected ^{58}Fe/^{58}Fe isotope ratio data from MC-ICPMS analysis. The uncertainty in the Fe concentrations determined by isotope dilution is <1% (2SD).

The measured Fe isotope ratios therefore represent a mixture of the added double spike and the natural Fe present in the sample. The iterative double spike data reduction scheme described in detail by Siebert *et al.* (2001) was applied off-line, at the cycle level to correct the Fe isotope ratios for both instrumental mass fractionation and the contribution from the double spike. For each ratio, the final corrected composition was based on the average of the ~60 corrected ratios. Each sample analysis was bracketed by two analyses of the widely utilized 'zero-permil' IRMM-014 Fe isotope

standard (Institute for Reference Materials and Measurements (IRMM), Belgium) which was concentration-matched and double spiked in the same way as samples. The final Fe isotope ratios of the samples are reported relative to the average of the two bracketing IRMM-014 standard measurements, using delta notation (δ^{56}Fe) as follows:

$$\delta^{56}\text{Fe}\ (‰) = \left(\frac{(^{56}\text{Fe}/^{54}\text{Fe})_{\text{sample}}}{(^{56}\text{Fe}/^{54}\text{Fe})_{\text{IRMM}-014}} - 1\right) \times 10^3 \quad (1)$$

In most cases, each sample was analyzed once for its Fe isotope composition. The reported error associated with the analysis of each sample (2SE) accounts for analytical internal error in the measured isotope ratios of the sample itself and that in the two bracketing standards using standard error propagation:

$$2\text{SE} = 2 \times \sqrt{SE_{\text{samp}}^2 + \frac{(SE_{\text{std}_1})^2 + (SE_{\text{std}_2})^2}{4}} \quad (2)$$

where SE_{samp} is the analytical standard error on the measurement of the sample and SE_{std} is the analytical standard error on the measurements of the two bracketing standards. The total 2SE uncertainty for samples determined in this manner is typically ±0.05‰ when ~300 ng of natural Fe consumed during each measurement. Larger uncertainties, up to ~ ±0.2‰, are associated with samples that yielded <<300 ng natural Fe.

To assess the performance of the above protocols, the United States Geological Survey (USGS) standard reference materials BCR-2 and NOD-A1 were acid digested, double-spiked with the ^{58}Fe-^{57}Fe tracer, purified for Fe, and analyzed for their Fe isotope composition alongside the Black Sea seawater samples. Replicate analysis over a protracted period of 6 months of BCR-2 yielded an average δ^{56}Fe of 0.09 ± 0.07‰ (n=19, 2SD) and NOD-A1 yielded an average δ^{56}Fe of -0.43 ± 0.07‰ (n=18, 2SD) (Table S3; Fig S24), which agree very well with literature values (Dideriksen *et al.*, 2006; Craddock and Dauphas, 2011; He *et al.*, 2015).

Table S1. Iron isotope composition of reference materials and method validation samples.

Sample	n	$\delta^{56}Fe_{IRMM-014}$ (‰)	2SD[a] (‰)	2 SE[b] (‰)
USGS Standard Reference Materials				
BCR-2	19	0.09	0.07	
NOD-A1	18	-0.43	0.07	
Black Sea Fe Isotope Intercomparison Sample				
BS-Fe-IC-Anoxic (1)	13	-0.77	0.08	
BS-Fe-IC-Anoxic (2)	6	-0.80	0.08	
BS-Fe-IC-Anoxic (3)	7	-0.80	0.07	
BS-Fe-IC-Anoxic (4)	3	-0.79	0.09	
BS-Fe-IC-Anoxic (5)	3	-0.79	0.03	
BS-Fe-IC-Anoxic (6)	5	-0.81	0.14	
grand average	***6***	***-0.79***	***0.03***	
Trace metal free seawater doped with IRMM-014[c]				
TM Free SW - 1 (500 ng)	1	-0.05		0.05
TM Free SW - 2 (500 ng)	1	-0.02		0.04
TM Free SW - 3 (250 ng)	1	-0.07		0.07
TM Free SW - 4 (250 ng)	1	-0.04		0.07
TM Free SW - 5 (200 ng)	1	-0.05		0.07
TM Free SW - 6 (200 ng)	1	0.00		0.06
TM Free SW - 7 (100 ng)	1	-0.08		0.09
TM Free SW - 8 (100 ng)	1	0.03		0.10
grand average	***8***	***-0.04***	***0.07***	

[a] 2SD is the uncertainty on >1 MC-ICPMS analyses of the same sample or when multiple aliquots of a sample have been processed independently.

[b] 2SE refers to the analytical internal error on a single MC-ICPMS analysis.

[c] 125 mL aliquots of trace metal free seawater were doped with 100 to 500 ng of Fe isotope standard IRMM-014 and subsequently processed alongside samples.

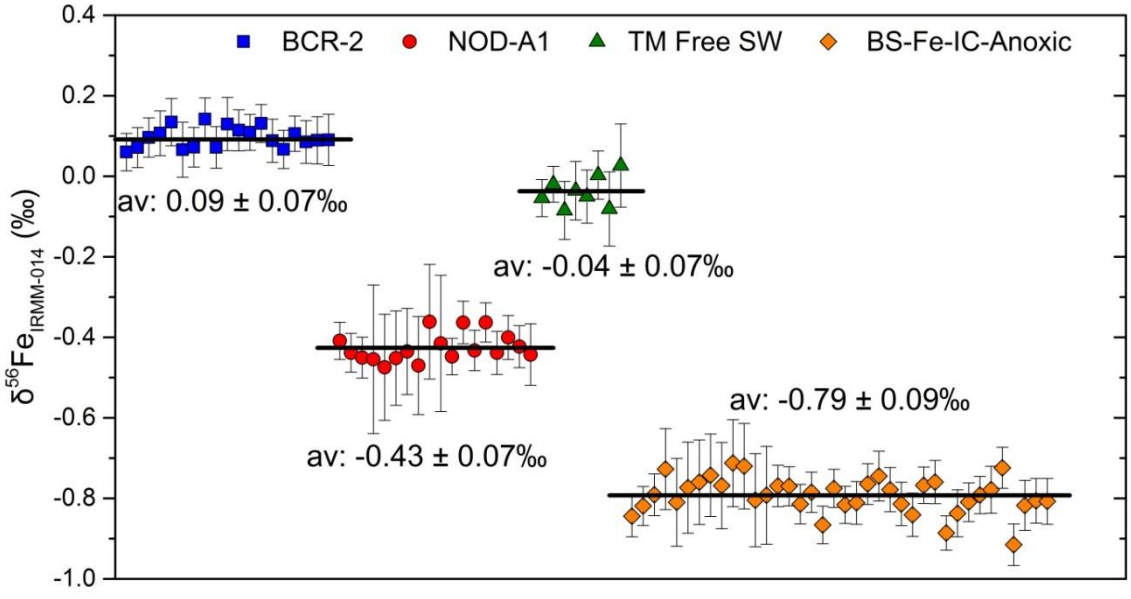

Fig. S2. Iron isotope composition of reference materials and validation samples. Error bars on $\delta^{56}Fe$ represent the analytical internal error (2SE). Black lines represent the average value for each sample. Larger internal error is associated with diluted samples so that <100 ng of Fe is consumed during each analysis.

5.4.1.7 Validation of the seawater Fe isotope method

The accuracy and precision of the Fe isotope data obtained with the aforementioned seawater Fe isotope method was assessed through the analysis of Fe isotope intercomparison seawater samples and trace metal free seawater that was doped with variable concentrations of IRMM-014. Trace metal free seawater was prepared by repeating the extraction procedure described in *'Extraction of Fe from Seawater'* three times with the same sample of seawater. After the third and final extraction, the seawater, now free of trace metals, was re-acidified to pH ~1.8. Eight aliquots of 125 mL were doped with 100 to 500 ng of Fe isotope standard IRMM-014, double-spiked, and chemically processed alongside the Black Sea Fe isotope seawater samples. The $\delta^{56}Fe$ values determined for the trace metal free seawater samples doped with IRMM-014 are all similar to the expected value of 0.0‰ within the uncertainty of the measurement (Table S1; Fig S2), indicating that there is no systematic inaccuracy associated with the seawater Fe isotope method.

Iron isotope intercomparison seawater samples were collected at Station 10 during the Dutch GEOTRACES Black Sea (cruise 64PE373) expedition. Three samples collected at different depths labelled as 'oxic' (30 m), 'suboxic' (100 m), and 'anoxic' (150 m) were distributed to 10 different laboratories. The Black Sea Fe intercomparison

sample from the anoxic water column (BS-Fe-IC-Anoxic) is most similar to the samples reported here, and was therefore chosen for repeated analyses. Six 125 mL aliquots of BS-Fe-IC-Anoxic were independently double-spiked and processed alongside the Black Sea Fe isotope seawater samples. The δ^{56}Fe values determined for the six aliquots of the BS-Fe-IC-Anoxic sample are identical, within uncertainty of the measurements. The average δ^{56}Fe of the six samples is -0.79 ± 0.03‰ (2SD, n=6) (Table S1; Fig S2), indicating that external sources of error are small and that the internal uncertainty reported for the δ^{56}Fe values of Black Sea seawater samples is an appropriate estimate of the total uncertainty. Previous studies have also demonstrated that the total uncertainty in seawater δ^{56}Fe analyses is dominated by internal sources of error (*i.e.* Johnson noise and counting statistics) and that external sources of error are negligible (John, 2012; Conway *et al.*, 2013).

5.4.2 Results and Fe isotope fractionation models

The water column Fe_d data, δ^{56}Fe data and other supporting parameters from Stations 2 and 5 are summarized in Tables S2 and S3. Iron isotope fractionation during chemical reactions in the Black Sea can be understood using standard isotope fractionation models. In the case of Fe, the isotope fractionation factor, α, is equal to the quotient of the ^{56}Fe/^{54}Fe ratio of the reactant, A, and the ^{56}Fe/^{54}Fe ratio of the product, B:

$$\alpha_{\mathrm{A-B}} = \frac{^{56/54}\mathrm{Fe_A}}{^{56/54}\mathrm{Fe_B}} \quad (3)$$

As α values are generally close to unity, it is convenient to convert α values to enrichment factors, ε, which are reported in permil (‰):

$$\varepsilon_{\mathrm{A-B}}(‰) = (\alpha_{\mathrm{A-B}} - 1) * 1000 \quad (4)$$

Furthermore, when δ values are <10‰, the following approximation is valid:

$$\varepsilon_{\mathrm{A-B}} \approx \delta^{56}\mathrm{Fe_A} - \delta^{56}\mathrm{Fe_B} \approx 1000 \ln \alpha_{\mathrm{A-B}} \quad (5)$$

5.4.2.1 Rayleigh Fractionation Model

The evolution of the reactant δ^{56}Fe ($\delta^{56}Fe_{reactant}$) during the progression of a unidirectional reaction can be described by a Rayleigh fractionation model:

$$\delta^{56}\mathrm{Fe}_{\mathrm{reactant}} = \delta^{56}\mathrm{Fe}_{\mathrm{initial}} + \varepsilon \ln f \quad (6)$$

where $\delta^{56}Fe_{initial}$ is the initial Fe isotope composition of the reactant and *f* is the fraction of the reactant remaining (*i.e.* Fe_d). This model assumes that the reactant reservoir is finite and that, after formation, the product is permanently removed from the system with no back reaction. These boundary conditions also describe a kinetic reaction. Thus, the Rayleigh model may also be used to model kinetic isotope fractionation. The evolution of the accumulated product δ^{56}Fe ($\delta^{56}Fe_{product}$) can be calculated as

$$\delta^{56}\mathrm{Fe}_{\mathrm{product}} = \delta^{56}\mathrm{Fe}_{\mathrm{initial}} + \varepsilon \ln(f) - \frac{\varepsilon \ln f}{1-f} \quad (7)$$

5.5.2.2 Equilibrium Fractionation Model

The evolution of $\delta^{56}Fe_{reactant}$ during the progression of a reaction where isotope exchange reaches equilibrium can be described by an equilibrium fractionation model:

$$\delta^{56}\mathrm{Fe}_{\mathrm{reactant}} = \delta^{56}\mathrm{Fe}_{\mathrm{initial}} - \varepsilon(1-f) \quad (8)$$

The equilibrium model assumes a finite reservoir of the reactant and that the product and reactant reach isotope exchange equilibrium at each time point of the reaction. The evolution of $\delta^{56}Fe_{product}$ can be calculated as:

$$\delta^{56}\mathrm{Fe}_{\mathrm{product}} = \delta^{56}\mathrm{Fe}_{\mathrm{initial}} - \varepsilon(1-f) + \varepsilon \quad (9)$$

Table S2. Water column depth profile of dissolved oxygen, hydrogen sulfide, Fe_d, and $\delta^{56}Fe$ at Station 2 in the Black Sea.

Sample ID[a]	Depth	Salinity	O_2	H_2S	Fe_d	$\delta^{56}Fe_{IRMM-014}$	2SE
station.cast.bottle#	(m)		(μmol kg^{-1})	(μmol kg^{-1})	(nmol kg^{-1})	(‰)	(‰)
2.1.24	9	18.23	234.9	0.0	n.d.	n.d.	n.d.
2.3.24	19	18.28	320.8	0.0	0.7	-0.89	0.14
2.1.23	24	18.36	336.1	0.0	n.d.	n.d.	n.d.
2.1.22	39	18.45	299.1	0.0	n.d.	n.d.	n.d.
2.1.21	45	18.60	257.3	0.0	n.d.	n.d.	n.d.
2.3.23	45	18.83	199.8	0.0	n.d.	n.d.	n.d.
2.3.22	50	19.22	121.2	0.0	0.6	-1.03	0.13
2.3.21	55	19.57	66.1	0.0	n.d.	n.d.	n.d.
2.3.20	60	19.75	42.1	0.0	1.6	-0.09	0.13
2.3.19	65	19.89	28.7	0.0	1.0	-1.46	0.17
2.1.20	69	20.02	13.9	0.0	n.d.	n.d.	n.d.
2.3.18	70	20.07	23.1	0.0	2.6	-0.61	0.17
2.3.17	75	20.23	11.8	0.0	0.9	-0.74	0.16
2.3.16	80	20.39	7.7	0.0	1.0	-0.62	0.11
2.1.19	84	20.54	4.3	0.0	n.d.	n.d.	n.d.
2.3.15	85	20.52	6.4	0.0	0.9	-0.88	0.16
2.3.14	90	20.66	4.0	0.0	1.0	-0.40	0.21
2.3.13	95	20.76	0.0	0.0	0.8	-0.78	0.16
2.1.18	99	20.86	0.0	0.0	14.7	-0.64	0.06
2.3.12	100	20.90	0.0	0.0	2.6	-0.65	0.13
2.3.11	105	20.96	0.0	3.2	99.2	-1.01	0.05
2.3.10	110	21.02	0.0	5.7	129.4	-1.01	0.05
2.1.17	114	21.09	0.0	8.5	158.6	-1.10	0.05
2.3.9	115	21.09	0.0	9.1	162.1	-0.90	0.05
2.3.8	120	21.13	0.0	10.3	181.2	-0.98	0.05
2.3.7	125	21.21	0.0	13.9	252.7	-0.94	0.05
2.1.16a	129	21.22	0.0	16.1	288.9	-0.90	0.05
2.1.16b	129	21.22	0.0	16.1	289.9	-0.97	0.05
2.3.6	130	21.24	0.0	14.9	278.6	-0.93	0.06
2.3.5	135	21.29	0.0	17.8	325.6	-0.91	0.05
2.3.4	140	21.33	0.0	20.4	369.3	-0.78	0.05
2.1.15	145	21.33	0.0	22.3	374.9	-0.85	0.05
2.3.3	145	21.36	0.0	23.1	n.d.	n.d.	n.d.
2.3.2	150	21.40	0.0	26.0	397.6	-0.69	0.05
2.3.1	157	21.43	0.0	25.7	n.d.	n.d.	n.d.
2.1.14	160	21.42	0.0	26.1	396.3	-0.75	0.05
2.1.13	174	21.50	0.0	34.5	351.1	-0.39	0.05
2.1.12	204	21.61	0.0	46.4	182.4	0.73	0.05
2.1.11	250	21.74	0.0	70.2	58.0	2.10	0.05
2.1.10	300	21.85	0.0	93.6	45.8	1.87	0.05
2.1.9	399	21.99	0.0	143.1	32.1	1.91	0.07
2.1.8	498	22.09	0.0	192.0	29.0	1.68	0.09
2.1.7	749	22.24	0.0	289.1	26.8	2.10	0.11
2.1.6	999	22.31	0.0	348.0	14.8	1.79	0.12
2.1.5	1249	22.33	0.0	381.6	9.0	2.36	0.05
2.1.4	1499	22.34	0.0	398.3	11.8	1.99	0.06
2.1.3	1749	22.35	0.0	419.2	12.1	1.99	0.06
2.1.2	2070	22.35	0.0	421.9	n.d.	n.d.	n.d.
2.1.1	2120	22.35	0.0	422.2	11.7	1.03	0.05

Table S3. Water column depth profile of dissolved oxygen, hydrogen sulfide, Fe_d, and $\delta^{56}Fe$ at Station 5 in the Black Sea.

Sample ID[a]	Depth	Salinity	O_2	H_2S	Fe_d	$\delta^{56}Fe_{IRMM-014}$	2SE
station.cast.bottle#	(m)		($\mu mol\ kg^{-1}$)	($\mu mol\ kg^{-1}$)	($nmol\ kg^{-1}$)	(‰)	(‰)
5.1.24	10	18.12	260.4	0.0	n.d.	n.d.	n.d.
5.1.23	29	18.26	315.2	0.0	n.d.	n.d.	n.d.
5.4.24	40	18.38	298.3	0.0	n.d.	n.d.	n.d.
5.1.22	40	18.35	296.8	0.0	n.d.	n.d.	n.d.
5.4.23	45	18.41	291.6	0.0	n.d.	n.d.	n.d.
5.4.22	50	18.61	229.9	0.0	n.d.	n.d.	n.d.
5.1.21	54	18.89	172.1	0.0	n.d.	n.d.	n.d.
5.4.21	55	18.84	182.3	0.0	n.d.	n.d.	n.d.
5.4.20	60	19.17	123.3	0.0	n.d.	n.d.	n.d.
5.4.19	65	19.53	83.1	0.0	n.d.	n.d.	n.d.
5.1.20	69	19.71	48.0	0.0	n.d.	n.d.	n.d.
5.4.18	70	19.84	33.4	0.0	n.d.	n.d.	n.d.
5.4.17	75	19.96	15.1	0.0	n.d.	n.d.	n.d.
5.4.16	80	20.14	10.3	0.0	n.d.	n.d.	n.d.
5.1.19	84	20.31	10.4	0.0	n.d.	n.d.	n.d.
5.4.15	85	20.29	8.0	0.0	n.d.	n.d.	n.d.
5.4.14	90	20.40	9.6	0.0	n.d.	n.d.	n.d.
5.4.13	95	20.53	6.0	0.0	n.d.	n.d.	n.d.
5.4.12	100	20.66	2.3	0.0	n.d.	n.d.	n.d.
5.1.18	100	20.74	0.4	0.0	n.d.	n.d.	n.d.
5.4.11	105	20.77	0.0	0.0	n.d.	n.d.	n.d.
5.4.10	110	20.89	0.0	0.0	n.d.	n.d.	n.d.
5.1.17	110	20.95	0.0	0.0	31.1	-0.94	0.06
5.4.9	115	20.92	0.0	0.0	34.1	-1.01	0.05
5.4.8	119	21.01	0.0	1.7	66.3	-1.12	0.06
5.4.7	124	21.06	0.0	3.5	90.9	-1.11	0.05
5.4.6	129	21.13	0.0	8.2	185.8	-1.09	0.04
5.1.16	130	21.14	0.0	8.4	176.6	-1.07	0.05
5.4.5	135	21.17	0.0	10.2	206.2	-1.00	0.05
5.4.4	139	21.19	0.0	10.5	200.4	-0.90	0.05
5.4.3	144	21.23	0.0	12.5	238.2	-0.94	0.05
5.1.15	145	21.27	0.0	14.5	285.3	-0.97	0.05
5.1.14	149	21.30	0.0	15.1	291.7	-1.05	0.05
5.4.2	150	21.25	0.0	14.3	273.3	-0.91	0.05
5.4.1	155	21.31	0.0	18.4	343.1	-0.90	0.05
5.1.13	175	21.44	0.0	26.0	394.9	-0.67	0.05
5.1.12	205	21.58	0.0	37.2	279.2	0.11	0.05
5.1.11	250	21.73	0.0	63.5	85.2	1.31	0.04
5.1.10	300	21.84	0.0	91.1	57.4	1.52	0.06
5.1.9	400	21.98	0.0	136.5	34.7	1.72	0.05
5.1.8	500	22.08	0.0	180.1	26.0	1.72	0.06
5.1.7	750	22.23	0.0	265.2	14.0	2.17	0.09
5.1.6	1000	22.30	0.0	333.3	10.3	2.26	0.06
5.1.5	1250	22.33	0.0	374.8	10.2	2.20	0.07
5.1.4	1500	22.34	0.0	385.5	8.9	2.29	0.06
5.1.3	1751	22.35	0.0	402.6	12.2	1.96	0.05
5.1.2	1989	22.35	0.0	414.8	11.8	1.67	0.06
5.1.1	2040	22.35	0.0	412.6	14.7	1.59	0.05

[a] Two ultraclean CTD casts were collected at Station 5, casts 1 and 4, with 24 samples collected during each cast.
n.d. - not determined.

5.4.2.3 Application of the fractionation models to the Black Sea iron isotope profiles

The vertical profiles of Fe_d and $\delta^{56}Fe$ in the Black Sea can be modelled as the progression of different reactions using the aforementioned Fe isotope fractionation models and the values of the isotope fractionation factors for the different water column processes can be determined. The fractionation factors derived from the Rayleigh models are calculated from the slope of the best fit lines in plots of $\delta^{56}Fe$ versus ln*f*. The fractionation factors derived from equilibrium models are calculated from the slope of the best fit lines in plots of $\delta^{56}Fe$ versus 1-*f*. The uncertainties in the respective slopes are used to calculate the uncertainty in the fractionation factors.

For Station 2, the Fe_d concentration reaches a maximum of ca. 400 nmol kg^{-1} at 150 to 160 m. The sample at 150 m serves as the initial Fe_d in the calculation of *f* (*i.e.* the fraction of Fe_d remaining). Vertical diffusion transports Fe(II) away from the Fe_d maximum and upwards into the redoxcline where it is oxidized to Fe(III) and precipitated as (hydr)oxides or to deeper depths in the water column where it reacts with H_2S to form pyrite. The parallel change in Fe_d and $\delta^{56}Fe$ between the redoxcline at ~100 m and the Fe_d maximum at 160 m is equally well described by both a Rayleigh fractionation model with $\varepsilon_{Fe(II)-Fe(III)}$ = -0.19 ± 0.10‰ (2SE) and an equilibrium fractionation model with $\varepsilon_{Fe(II)-Fe(III)}$ = -0.35 ± 0.14‰ (2SE) (Fig. S3a). Below the Fe_d maximum, pyrite formation removes iron from solution. At 500 m depth, ~93% of Fe_d has been removed due to pyrite formation. The associated change in Fe_d and $\delta^{56}Fe$ between the Fe_d maximum at 150 m and 500 m is best described by an equilibrium fractionation model with $\varepsilon_{Fe(II)-Fe(III)}$ = +2.90 ± 0.34‰ (2SE) (Fig. S3b).

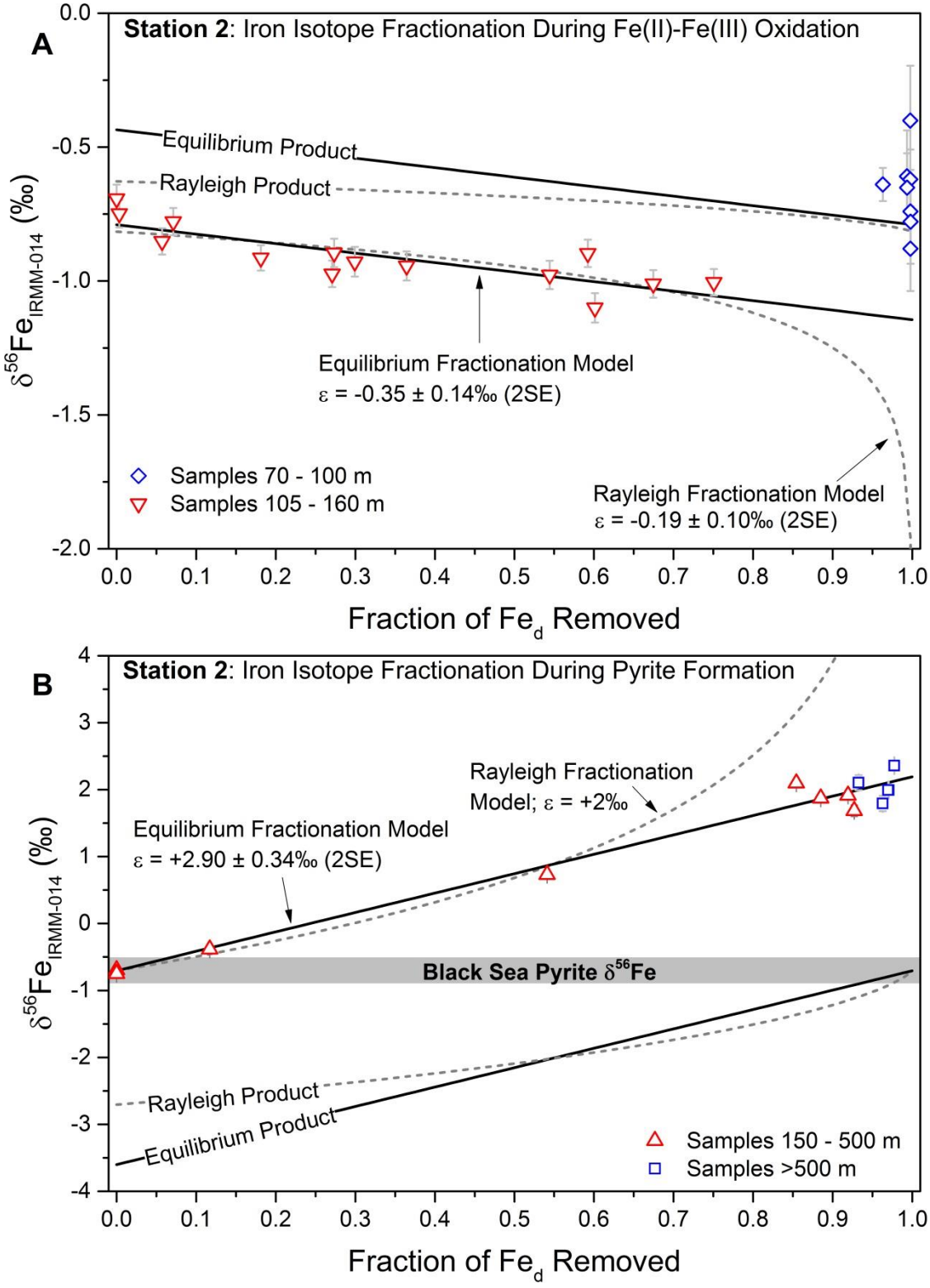

Fig. S3. Iron isotope fractionation model for the water column Fe_d and $\delta^{56}Fe$ data from Station 2 in the Black Sea. The process of oxidation of Fe(II) to Fe(III) and subsequent precipitation of iron (hydr)oxides results in a concomitant gradient in Fe_d and $\delta^{56}Fe$ across a depth range of 105 to 160 m [(A) red triangles] that is reasonably well described by both a Rayleigh fractionation model with $\varepsilon_{Fe(II)-Fe(III)} = -0.19 \pm 0.10‰$ (2SE) and an equilibrium fractionation model with $\varepsilon_{Fe(II)-Fe(III)} = -0.35 \pm 0.14‰$ (2SE). Samples from depths within and above the redoxcline [(A) blue diamonds] may

represent product Fe(III) that has yet to precipitate and are characterized by $\delta^{56}Fe$ values that roughly fit with the fractionation models. Syngenetic pyrite formation results in a concomitant gradient in Fe_d and $\delta^{56}Fe$ across a depth range of 500 to 160 m [(B) red triangles] that is best described by an equilibrium fractionation model with $\varepsilon_{Fe(II)-Fe(III)} = +2.90 \pm 0.34‰$ (2SE). A Rayleigh fractionation model with $\varepsilon_{Fe(II)-Fe(III)} = +2‰$ is shown for reference but is not a good fit to the data. Additional processes are required to explain the data below 500 m; see text for details. The range in $\delta^{56}Fe$ measured in pyrite from euxinic Black Sea sediments is denoted by the horizontal grey bar (Severmann *et al.*, 2008). Error bars on $\delta^{56}Fe$ represent the analytical internal error (2SE).

For Station 5, the Fe_d concentration reaches a maximum of ca. 400 nmol kg^{-1} at 175 m, which serves as the initial Fe_d in the calculation of f (*i.e.* the fraction of Fe_d remaining). The parallel change in Fe_d and $\delta^{56}Fe$ between the redoxcline at ~115 m and the Fe_d maximum at 175 m is equally well described by both a Rayleigh fractionation model with $\varepsilon_{Fe(II)-Fe(III)} = -0.18 \pm 0.10‰$ (2SE) and an equilibrium fractionation model with $\varepsilon_{Fe(II)-Fe(III)} = -0.42 \pm 0.20‰$ (2SE) (Fig. S4a). At 500 m depth, ~93% of Fe_d has been removed due to pyrite formation. The associated change in Fe_d and $\delta^{56}Fe$ between the Fe_d maximum at 175 m and 500 m is best described by an equilibrium fractionation model with $\varepsilon_{Fe(II)-Fe(III)} = +2.56 \pm 0.08‰$ (2SE) (Fig. S4b).

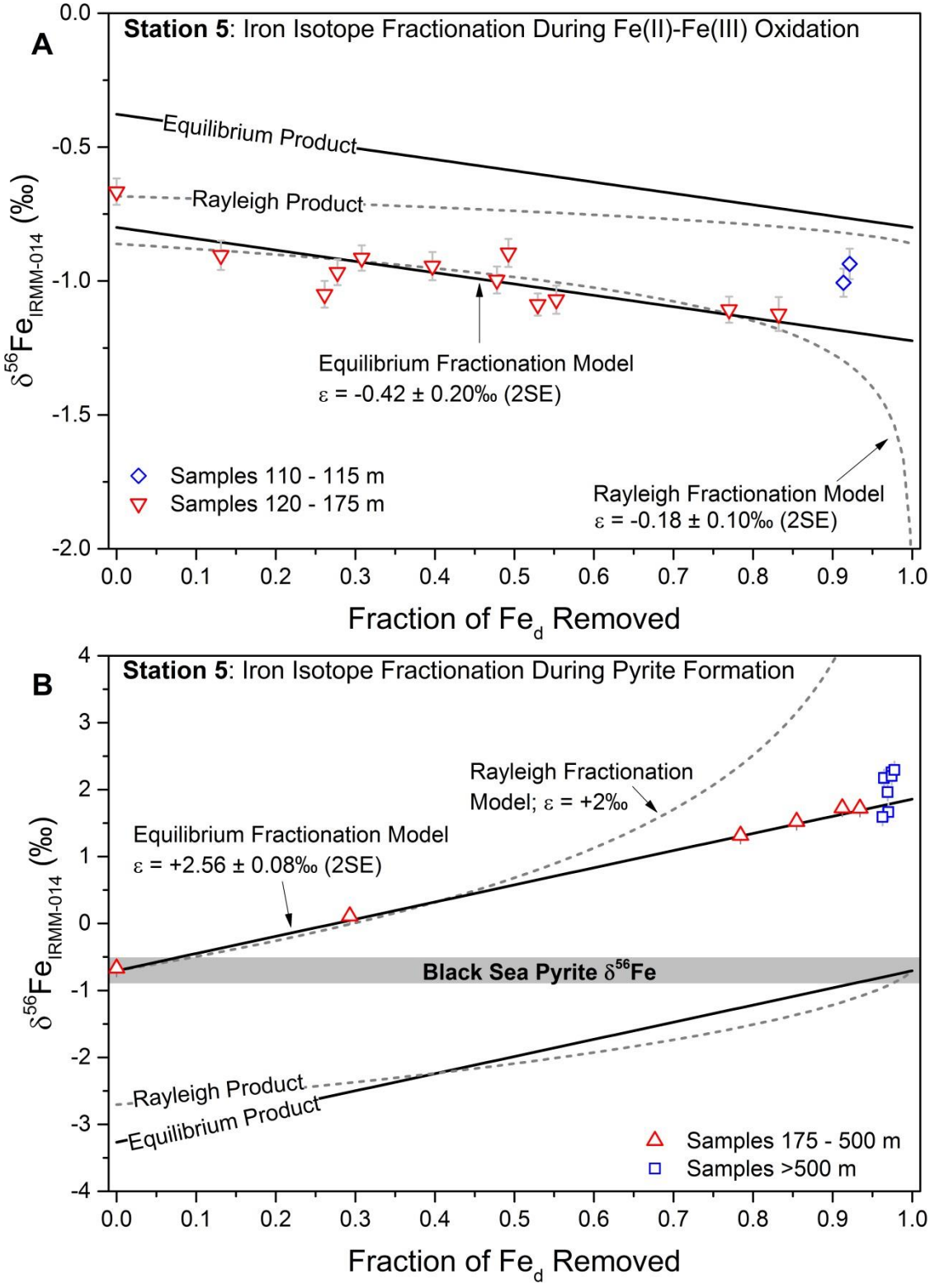

Fig. S4. Iron isotope fractionation model for the water column Fe_d and $\delta^{56}Fe$ data from Station 5 in the Black Sea. The process of oxidation of Fe(II) to Fe(III) and subsequent precipitation of iron (hydr)oxides results in a concomitant gradient in Fe_d and $\delta^{56}Fe$ across a depth range of 120 to 175 m [(A) red triangles] that is reasonably well described by both a Rayleigh fractionation model with $\varepsilon_{Fe(II)-Fe(III)} = -0.18 \pm 0.10‰$ (2SE) and an equilibrium fractionation model with $\varepsilon_{Fe(II)-Fe(III)} = -0.42 \pm 0.20‰$ (2SE). Samples from depths within the redoxcline [(A) blue diamonds] may represent a

mixture of product Fe(III) and residual Fe(II) and are characterized by $\delta^{56}Fe$ values that fall between the modelled reactant Fe(II) and product Fe(III). Syngenetic pyrite formation results in a concomitant gradient in Fe_d and $\delta^{56}Fe$ across a depth range of 175 to 500 m [(B) red triangles] that is best described by an equilibrium fractionation model with $\varepsilon_{Fe(II)\text{-}Fe(III)} = +2.56 \pm 0.08‰$ (2SE). A Rayleigh fractionation model with $\varepsilon_{Fe(II)\text{-}Fe(III)} = +2‰$ is shown for reference but is not a good fit to the data. Additional processes are required to explain the data below 500 m; see text for details. The range in $\delta^{56}Fe$ measured in pyrite from euxinic Black Sea sediments is denoted by the horizontal grey bar (Severmann *et al.*, 2008). Error bars on $\delta^{56}Fe$ represent the analytical internal error (2SE).

The Fe_d and $\delta^{56}Fe$ data from both Stations 2 and 5 is ultimately combined to calculate the final fractionation factors (Fig. 5.2). Considering the combination of data from both Stations 2 and 5, the Fe isotope fractionation accompanying the combined process of Fe(II) to Fe(III) oxidation and precipitation is equally well described by both a Rayleigh model with $\varepsilon_{Fe(II)\text{-}Fe(III)} = -0.19 \pm 0.07‰$ (2SE) and an equilibrium model with $\varepsilon_{Fe(II)\text{-}Fe(III)} = -0.40 \pm 0.12‰$ (2SE) (Fig. 5.2a). Considering the combination of data from both Stations 2 and 5 the Fe isotope fractionation accompanying syngenetic pyrite formation is best described by an equilibrium fractionation model with $\varepsilon_{Fe(II)\text{-}pyrite} = +2.75 \pm 0.22‰$ (2SE) (Fig. 5.2b).

At both Stations 2 and 5, the removal of Fe_d due to pyrite formation imparts the greatest influence on $\delta^{56}Fe$ at depths between the Fe_d maximum and ~500 m. Secondary removal processes may be important in deep waters away from the primary site of pyrite formation. There is considerably more scatter in the $\delta^{56}Fe$ data from deep samples at Station 2 compared to Station 5. Therefore, we limit the following discussion to the data for deep samples from Station 5. Below 500 m, the Fe_d concentration stabilizes at depths between 750 and 1500 m and shows a slight increase near the seafloor (Table S2). The four samples from depths between 750 and 1500 m display constant $\delta^{56}Fe$ values of $+2.23 \pm 0.10‰$ (2SD), which is significantly larger than the sample at 500 m with a $\delta^{56}Fe$ value of $+1.72 \pm 0.06‰$ (2SE). There is a slight change in Fe_d from 26 nmol kg^{-1} at 500 m to an average of ~11 nmol kg^{-1} at depths between 750 and 1500 m. These samples do not fit the equilibrium isotope model established by samples from 175 to 500 m at Station 5. Thus, a secondary removal process appears to result in additional Fe isotope fractionation across this depth range. For example, scavenging of Fe(II) on the surfaces of sinking particles with $\varepsilon_{Fe(II)\text{-}particulate} = +0.5$ to $0.85‰$ could account for the additional Fe isotope fractionation.

At Station 5 an increase in Fe_d near the seafloor is accompanied by a negative shift in $\delta^{56}Fe$ to +1.59 ± 0.05‰ (2SE). Reductive dissolution of Fe (hydr)oxides at the sediment-water interface could result in the release of Fe(II) with a $\delta^{56}Fe$ near 0.0‰ if the Fe (hydr)oxides are lithogenic in origin, or with $\delta^{56}Fe$ approaching -0.7‰ if the Fe (hydr)oxides are authigenic in origin and formed in the redoxcline in the upper water column. In both cases, reductive dissolution at the sediment-water interface would drive the $\delta^{56}Fe$ of bottom waters to lower values.

CHAPTER 6

URANIUM STABLE ISOTOPE FRACTIONATION IN THE BLACK SEA: MODERN CALIBRATION OF THE $^{238}U/^{235}U$ PALEOREDOX PROXY

6.1 Abstract

The isotopic compositions of redox-sensitive metals, including uranium (U), in marine sediments have recently emerged as powerful diagnostic tracers of the redox state of the ancient ocean-atmosphere system. Interpretation of sedimentary isotopic information requires a thorough understating of the environmental controls on isotopic fractionation in modern anoxic environments before being applied to the paleo-record. In this study, the relationship between ocean anoxia and the isotopic fractionation of U was investigated in the water column and sediments of the Black Sea, the world's largest anoxic basin. Removal of U from the water column occurs during the redox transition of soluble U(VI) to relatively insoluble U(IV). The primary results of this study are two-fold. First, significant $^{238}U/^{235}U$ variability was observed in the water column of the Black Sea, suggesting the reduction of U induces $^{238}U/^{235}U$ fractionation. Second, the $^{238}U/^{235}U$ of underlying sediments is related to the water column through the isotope fractionation factor of the reduction reaction but is influenced by mass transport processes and changes in the sedimentary environment. These results provide important constraints on the use of $^{238}U/^{235}U$ as a proxy of the redox state of ancient oceans.

6.2 Introduction

The history of free oxygen (O_2) in Earth's ocean-atmosphere system is intimately connected to the evolution of life. The timing and nature of the initial rise of O_2 in Earth's early atmosphere is thus immensely important for understanding the environmental conditions which led to the rise of complex life forms on Earth. The relative abundances of redox sensitive metals and their isotopes in sedimentary archives can effectively track changes in the redox condition of Earth's atmosphere and oceans, and thus approximate the progression of oxidizing conditions in the environment (*e.g.*

Lyons *et al.*, 2014). For instance, oxidation of metal bearing sulfide minerals on Earth's surface during the initial rise of atmospheric O_2 would have released metals, such molybdenum (Mo) and rhenium (Re), to rivers, and subsequently the oceans where metals are ultimately fixed in sediments. Enrichments of metals in marine sediments deposited during the Archean may therefore reflect subaerial oxidative weathering of the continents implying the existence of atmospheric O_2. Additionally, enrichments of redox sensitive elements in coeval Phanerozoic marine sediments provide strong evidence of global scale shifts in the prevailing redox conditions in the oceans, and evidence for widespread ocean anoxia, such as during the so called 'oceanic anoxic events' or OAEs of the Mesozoic Ocean (*e.g.* Jenkyns, 2010). Accurately dating such sediments provides an estimate of the timing of O_2 accumulation or depletion in Earth's ocean-atmosphere system. Such reconstructions advance our understanding of the complex interplay between the chemical state of the oceans, the marine carbon cycle and global climate. Importantly, accurate interpretations of trace metal records rely on a thorough understanding of how trace metal patterns in sediments relate to the redox of the ocean-atmosphere system. Much of the current understanding of trace metal paleoredox proxies comes from investigations in modern anoxic marine basins, such as the Black Sea.

Recent advances in analytical capabilities, most notably multiple-collector inductively coupled plasma mass spectrometry (MC-ICPMS), now enable routine analyses of many redox sensitive metal stable isotope systems, including the emerging uranium (U) 'stable' isotope system ($^{238}U/^{235}U$), which offers the potential to provide new insight concerning the redox conditions of ancient environments. Uranium has three naturally occurring radioisotopes, ^{238}U ($t_{1/2} \approx 4.5$ Ga), ^{235}U ($t_{1/2} \approx 700$ Ma) and ^{234}U ($t_{1/2} \approx 245$ ka), the latter of which is the longest lived intermediate daughter of ^{238}U. The two primordial isotopes form the basis of the U-Pb and U-series dating methods, but are sufficiently long-lived so that the ^{238}U-^{235}U system can essentially be regarded as a stable isotope tracer. However, as is the case with all stable isotope paleoredox proxies, utilization of the $^{238}U/^{235}U$ isotope system to its full potential requires a strong understanding of the physicochemical processes which result in isotope fractionation under varying environmental conditions. Progress in this area is ongoing and warrants further investigation in modern hydrological settings.

The utility of U isotopes as a marine paleoredox proxy is based on the sensitivity of the U marine geochemical cycle to the redox state of seawater. Under the

oxygenated conditions of the modern open ocean, dissolved U occurs as oxidized U(VI) and forms soluble uranyl carbonate complexes, resulting in conservative behavior with a concentration of ~3.2 ng/g at a salinity of 35 (Ku *et al.*, 1977; Owens *et al.*, 2011), homogenous $^{238}U/^{235}U$ and $^{238}U/^{234}U$ (Andersen *et al.*, 2010, 2014; Stirling *et al.*, 2007; Tissot and Dauphas, 2015; Weyer *et al.*, 2008), and a long residence time of ~0.5 Ma relative to the deep ocean renewal time of ~1 ka (Dunk *et al.*, 2002; Ku *et al.*, 1977). In contrast, under oxygen-depleted conditions, the chemical reduction of U(VI) to poorly soluble U(IV), sometimes mediated by biological activity, results in removal of U from solution to sediments. In the modern global ocean, suboxic and anoxic marine sediments only cover ~6% of the seafloor, yet they account for ~56% of U removal from the modern ocean (Dunk *et al.*, 2002), highlighting the potential sensitivity of the marine geochemical cycle of U to fluctuations in the levels of dissolved O_2. Significant U isotope fractionation occurs during the reduction of U(VI) to U(IV) and changes in the extent of oceanic anoxia could therefore significantly influence the U concentration and isotope composition of seawater. In this regard, variations in the U isotope composition recorded in ancient marine sediments have recently been interpreted as changes in the seawater U isotope composition. To a first order, these variations are believed to reflect changes in the marine redox conditions (*e.g.* Brennecka *et al.*, 2011a; Dahl *et al.*, 2014; Kendall *et al.*, 2013; Kendall *et al.*, 2015; Montoya-Pino *et al.*, 2010; Weyer *et al.*, 2008), as to date, other U removal processes have been shown to result in only minor $^{238}U/^{235}U$ fractionation (Romaniello *et al.*, 2013).

Significant U isotope fractionation is associated with the chemical reduction of U(VI) to U(IV) and the subsequent removal of U(IV) from solution. Therefore, this process exerts a strong control on the U isotope composition of seawater and underlying sediment. It is thus crucial to quantify the magnitude of the fractionation associated with this process for the accurate application of U isotopes as a paleoredox proxy. Recent studies have begun addressing this issue by measuring the U isotope composition of the water column and sediments from different anoxic marine settings, including the Baltic Sea, the Black Sea, the Cariaco Basin and Saanich Inlet (Andersen *et al.*, 2014; Holmden *et al.*, 2015; Montoya-Pino *et al.*, 2010; Noordman, *et al.*, 2015). Laboratory and field experiments have also been conducted to ascertain the sense and magnitude of U isotope fractionation during abiotic and biotic U(VI)-U(IV) reduction under variable conditions (Basu *et al.*, 2014; Bopp *et al.*, 2010; Rademacher *et al.*, 2006; Stirling *et al.*, 2007; 2015; Stylo *et al.*, 2015). All studies thus far, with the

exception of Rademacher *et al.* (2006), report that microbially mediated U(VI)-U(IV) reduction results in the preferential reduction and immobilization of ^{238}U over ^{235}U. In contrast, purely abiotic reduction results in minor U isotope fractionation in the opposite direction with enrichment of ^{238}U in the remaining U(VI) pool occurring as the reaction progresses (Stylo *et al.*, 2015). Enrichment of ^{238}U in sediments relative to seawater from anoxic marine basins suggests removal of U under reducing conditions is dominated by microbially-mediated reduction (Andersen *et al.*, 2014; Holmden *et al.*, 2015; Montoya-Pino *et al.*, 2010; Noordmann *et al.*, 2015; Weyer *et al.*, 2008). Similarly, studies of U isotope systematics during U(VI)-U(IV) reduction in groundwater and assimilation into mineralised sediment indicate preferential reduction of ^{238}U over ^{235}U (Bopp *et al.*, 2009; 2010; Brenneca *et al.*, 2010; Murphy *et al.*, 2014). This sense of fractionation results from the dominance of nuclear volume effects during U isotope fractionation (Abe *et al.*, 2008; Bigeleisen, 1996; Schauble, 2007), which acts in opposition to mass dependent fractionation and is expected to be an order of magnitude smaller, given uranium's heavy mass. The study of Rademacher *et al.* (2006) reported the opposite sense of fractionation (*i.e.* preferential removal of ^{235}U) during U(VI) reduction experiments by metal reducing bacteria but it is possible that their results were influenced by preferential sorption of ^{235}U to mineral surfaces rather than U(VI)-U(IV) reduction (Basu *et al.*, 2014; Brennecka *et al.*, 2011b; Rademacher *et al.*, 2006; Stirling *et al.*, 2015).

This study builds upon previous studies of $^{238}U/^{235}U$ fractionation in natural environments by investigating the U isotope systematics in the permanently anoxic Black Sea. We have measured the concentration and isotope composition of U in the water column of the Black Sea at three separate locations and in one sediment core collected from the deep central basin. As the world's largest anoxic marine basin, the Black Sea is an ideal natural laboratory for examining the behavior of uranium isotopes under environmental conditions similar to ancient oceans which were, on occasion, devoid of oxygen.

6.3 Methods

6.3.1 Study site and Sample collection

Seawater and sediment samples were collected during the Dutch MedBlack GEOTRACES expedition (cruise 64PE373) to the Black Sea in July 2013 aboard R/V *Pelagia* (Fig. 6.1). The Black Sea is the world's largest restricted marine basin with depths reaching ~2250 m in the deep central basin. The physical and chemical structure of the Black Sea is controlled by its hydrologic balance (Murray and Yakushev, 2006). Eurasian rivers supply freshwater to the surface while very saline water from the Mediterranean Sea enters through the Bosporus Strait below the surface (sill depth ~60 m). Consequentially, surface waters (0-100 m) in the Black Sea have a salinity of ~18, while deep waters (100-2250 m) are significantly denser with a salinity of ~22. The strong pycnocline prevents efficient vertical mixing which results in the development of a sharp chemocline. In the central basin, well oxygenated surface waters persist to a depth of ~100 m, while deep waters (100 m to 2250 m) are euxinic (*i.e.* anoxic and sulfidic) with H_2S concentrations >400 µM.

A total of 12 stations were occupied during the expedition with 6-48 discrete seawater samples collected at each station. The concentrations of dissolved trace metals were determined for all stations while the concentration and isotope composition of dissolved U was determined for stations 2, 5 and 9 (Fig. 6.1). Seawater samples were collected using an ultraclean all-titanium framed 'TITAN' CTD sampling system (de Baar *et al.*, 2008; Rijkenberg *et al.*, 2015). Immediately upon recovery, the TITAN system was placed inside a purpose-built class 100 clean room container. Inside the clean room container, seawater was filtered directly from sampling bottles using 0.2 µm filter cartridges (Sartobran-300, Sartorius) under nitrogen pressure (1.5 atm). Filtered seawater samples were collected in low density polyethylene (LDPE) bottles and cubitainers ranging in volume from 60 mL to 10 L which had been acid cleaned following GEOTRACES guidelines (www.geotraces.org). Sample bottles were rinsed 5 times with sample seawater prior to sample collection. Immediately after collection, seawater samples were acidified to 0.024 M HCl using ultra-high purity 12 M HCl (Seastar™ Baseline®).

Unfiltered seawater samples were collected for analysis of major nutrients in high density polyethylene (HDPE) bottles that were rinsed three times with sample water and then stored in the dark at 4 ˚C until analyzed within 8-12 hours.

A small gravity corer tethered to the bottom of the TITAN CTD frame via a ~10 m rope was used to collect the upper ~30 cm of sediment. Successfully collected cores were sectioned shipboard at ~1 cm intervals using a plastic knife and then stored in plastic bags and frozen. Sediment samples were then freeze-dried at the University of Toulouse and stored in plastic vials until further processing. The sediment core investigated in this study was collected at station 2 from a depth of 2157 m.

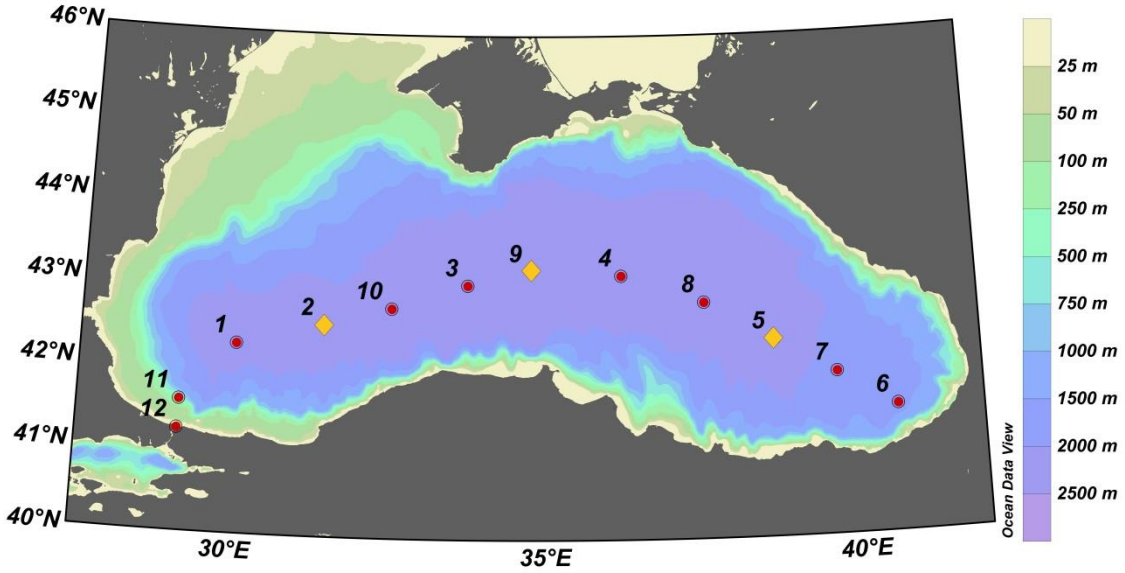

Fig. 6.1. Map of the station locations in the Black Sea during the Dutch MedBlack GEOTRACES expedition to the Black Sea in July 2013 (cruise 64PE373). Water column profiles from stations 2, 5, and 9 and a sediment core from station 2 are investigated in this study.

6.3.2 Seawater trace metal analysis

A suite of trace metal concentrations were measured in seawater samples collected in the Black Sea using methods similar to Biller and Bruland (2012). The full method and Black Sea trace metal dataset are described in detail by Middag *et al.* (2015) and Chapter 4, respectively, with only a brief description of the method provided here. Approximately 40 mL of buffered seawater was preconcentrated on Nobias PA-1 chelating resin and all metals were subsequently eluted in 1 M HNO_3. The eluent was analyzed for all metals using high-resolution ICP-MS (Element 2, Thermo Scientific) at the University of California, Santa Cruz. The preconcentration factor was determined by spiking the initial 40 mL of seawater with a known amount of In and Lu, which are both quantitatively retained on the Nobias PA-1 resin. The concentration of In and Lu in the final eluent was then used to calculate the pre-concentration factor,

which was in turn used to calculate the initial seawater concentration of the dissolved trace metals.

6.3.3 Sediment trace metal analysis

All acids used (HNO_3, HCl, and HF) for digestion and subsequent U extraction and purification (section 2.4) were purified by sub-boiling quartz distillation. High purity Milli-Q water (>18.2 MΩ cm; Millipore) was used for all dilutions. Ultra-high purity H_2O_2 was purchased from Fisher Scientific (Optima). All fluorinated ethylene propylene (FEP) and perfluoroalkoxy (PFA) labware (Savillex Ltd, U.S.A.) was cleaned by sequential soaking in warm 2% Citranox detergent (Alconox Inc, U.S.A.) for ~24 hr, warm 8 M HNO_3 for at least one week, and in warm 6 M HCl for at least one week, with each step followed by rinsing with copious amounts of Milli-Q water.

Sediment samples (~300 mg) were weighed out in 60 mL PFA beakers. Sediments were then digested in a mixture concentrated HNO_3 and HF acid (1:8 ratio) for 96 h at ~120 °C. The samples were then dried down and then refluxed in 7 M HNO_3 at ~120 °C for ~48 h. Samples were again dried down and then refluxed in 6 M HCL at ~120 °C for ~48 h. After appropriate dilution, elemental concentrations were measured via quadrupole ICP-MS (Agilent 7500) using an in-house multi-element standard for instrumental calibration at the Centre for Trace Element Analysis, University of Otago. An in-house multi-element internal standard was added to all samples to correct for instrumental drift. The performance of the sediment digestion and elemental analysis methods were checked by processing the United States Geological Survey (USGS) standard reference material Brush Creek Shale (SBC-1). Recoveries of 100 ± 5% were obtained for SBC-1 for the elements reported here.

6.3.4 Chemical preparation of samples for uranium isotopic analysis

Uranium isotopic composition was determined using a ^{236}U-^{233}U double spike to correct for instrumental mass fractionation following methods reported previously (Murphy *et al.*, 2014; Amelin *et al.*, 2010; Stirling *et al.*, 2007). In brief, seawater samples were first subsampled, diluted by a factor of 30 and analyzed via quadrupole ICP-MS (Agilent 7500) at the University of Otago to initially determine the approximate U concentration in order to inform the double spike addition calculation. Based on this U concentration, samples were again subsampled into 60 mL PFA vials to achieve a total uranium mass of 60 to 100 ng and spiked with the ^{236}U-^{233}U double

spike to attain a final $^{236}U/^{235}U$ of ~3. The spiked samples were then allowed to equilibrate for 48-72 hours on a hotplate at 120 °C. After equilibration, the samples were dried down, refluxed in 7 M HNO_3, and dried down again before final re-dissolution in 1.5 M HNO_3. Uranium was then chemically separated and purified from the residual seawater matrix using a two-stage ion exchange chromatographic procedure which utilized TRU and UTEVA® resins (Eichrom Technologies, U.S.A.) following previously reported methods (Murphy *et al.*, 2014; Potter *et al.*, 2005; Stirling *et al.*, 2007). Sediment digests were subsampled to obtain ~200 ng uranium then spiked with the ^{236}U-^{233}U double spike and allowed to equilibrate for ~24 h before being dried down and re-dissolved in 1.5 M HNO_3 for U extraction and purification using the same two-stage ion exchange chromatographic procedure as utilized for the seawater samples.

Following U extraction and purification, samples were dried down, refluxed in a HNO_3-H_2O_2 mixture (1:1 ratio) to breakdown any residual organics arising from the resin. The U fractions were then dried down again and re-dissolved in 0.24 M HCl + 0.28 M HF in preparation for U isotope ratio analysis.

6.3.5 Uranium isotopic analysis

Uranium isotope measurements were made on a multiple-collector ICP-MS (MC-ICPMS; Nu Plasma HR, Nu Instruments Ltd, U.K.) at the Centre for Trace Element Analysis, University of Otago following previously reported methods (Murphy *et al.*, 2014; Stirling *et al.*, 2007). Samples were introduced to the MC-ICPMS via a DSN 100 desolvating nebulizer fitted with a 60 uL/min PFA nebulizer. Uranium isotope data, denoted by $^{238}U/^{235}U$ and $^{234}U/^{238}U$, are presented in the delta-notation (δ) following Eq. (1) and Eq. (2), respectively:

$$\delta^{238}\mathrm{U} = \left(\frac{(^{238}\mathrm{U}/^{235}\mathrm{U})_{\mathrm{sample}}}{(^{238}\mathrm{U}/^{235}\mathrm{U})_{\mathrm{CRM-145}}} - 1\right) \quad (1)$$

$$\delta^{234}\mathrm{U} = \left(\frac{(^{234}\mathrm{U}/^{238}\mathrm{U})_{\mathrm{sample}}}{(^{234}\mathrm{U}/^{238}\mathrm{U})_{\mathrm{sec.eq.}}} - 1\right) \quad (2)$$

The reference material CRM-145 (National Institute of Standards and Technology, U.S.A.) is the internationally recognized δ-zero standard with a $^{238}U/^{235}U$ ratio of

137.837 ± 0.015 (Richter *et al.*, 2010) and sec. eq. refers to the $^{234}U/^{238}U$ atomic ratio at radioactive secular equilibrium of 5.497×10^{-5} (Cheng *et al.*, 2013). The determined δ values are converted to units of permil (‰) by multiplying by a factor of 10^3. In brief, the ^{238}U, ^{236}U, ^{235}U, and ^{233}U ion beams were measured during a static sequence using Faraday collects configured with 10^{11} Ω resistors while the low-level ^{234}U ion beam was measured simultaneously using a coupled electron multiplier – ion counting detector system. After correction for the electronic baseline by deflecting the ion beams off-axis, all U isotope ratios were corrected for the contribution of natural ^{238}U, ^{235}U and ^{234}U in the ^{236}U-^{233}U mixed spike (Stirling *et al.*, 2007). Instrumental mass fractionation was then corrected for by normalizing the measured $^{236}U/^{233}U$ against the 'true' ratio and the exponential mass fractionation law (Habfast, 1998; Hart and Zindler, 1989). Furthermore, each pair of sample measurements were bracketed by, and normalized to, measurements of U concentration-matched CRM-145 which was double spiked in the same way as samples. Each isotope measurement of a sample is therefore calculated relative to the average of the two bracketing CRM-145 standards. This sample-standard bracketing approach allows for calibration of the Faraday-ion counter gain for mixed-mode $^{238}U/^{234}U$ measurement. The final uncertainty in the isotope measurement of a sample for which there is only one analysis is reported as twice the standard error (2SE) and accounts for the internal error (*i.e.* instrumental error) in all three measurements using standard error propagation following Eq. (3):

$$2\mathrm{SE} = 2 \times \sqrt{\mathrm{SE}_{samp}^2 + \frac{(\mathrm{SE}_{std1})^2 + (\mathrm{SE}_{std2})^2}{4}} \quad (3)$$

where SE_{samp} is the internal error on the measurement of the sample and SE_{std} is the internal error on the measurements of the two bracketing standards. Uncertainty for samples determined in this manner is typically ±0.06-0.10‰ for $\delta^{238}U$ and ±5‰ for $\delta^{234}U$ with ~60 ng of U consumed during each measurement.

Based on the $^{238}U/^{236}U$ composition of the double spike, the mass of each seawater sample and the mass of added double spike, the U concentration in the original seawater sample was determined simultaneously with the isotope measurements using isotope dilution equations. The overall method for both seawater and sediment samples produces a blank of <15 pg U, which is considered negligible and therefore no correction is made for the U isotope composition. The validity of the

methods was assessed by analyzing three independently processed open ocean seawater samples from the deep Pacific Ocean and the USGS reference material SBC-1. The Pacific Ocean seawater samples resulted in an average $\delta^{238}U$ of -0.39 ± 0.03‰ (2SD; n=5; Table 6.1). The SBC-1 reference material yielded $\delta^{238}U$ of -0.21± 0.04‰ (2SD; n=3; Table 6.2).

Table 6.1. Uranium isotope and concentration data for Black Sea water column and open ocean seawater samples.

Sample ID	n[c]	Depth (m)	Salinity	H_2S (μmol kg^{-1})	$\delta^{238}U_{CRM-145}$ (‰)	2 S.E. (‰)	[U] (ppb)	2 S.E. (ppb)
Black Sea Samples[a]								
station.cast.bottle#								
2.1.1		2120	22.35	422	-0.63	0.06	1.41	0.02
2.1.2		2070	22.35	422	-0.68	0.06	1.38	0.02
2.1.3		1749	22.35	419	-0.77	0.06	1.40	0.02
2.1.4		1499	22.34	398	-0.86	0.07	1.42	0.02
2.1.6		999	22.31	348	-0.69	0.06	1.51	0.02
2.1.8		498	22.09	192	-0.55	0.06	1.75	0.02
2.1.10		300	21.85	94	-0.55	0.07	1.96	0.02
2.1.12		204	21.61	46	-0.48	0.05	2.04	0.02
2.1.16		129	21.22	16	-0.45	0.06	2.11	0.02
2.1.18		99	20.86	0	-0.44	0.06	2.14	0.02
2.1.22		39	18.45	0	-0.52	0.06	2.16	0.02
2.1.24		9	18.23	0	-0.35	0.06	2.14	0.02
5.1.1		2040	22.35	413	-0.73	0.08	1.44	0.02
5.1.2		1989	22.35	415	-0.66	0.06	1.40	0.02
5.1.3		1751	22.35	403	-0.84	0.05	1.40	0.02
5.1.4		1500	22.34	385	-0.75	0.07	1.43	0.02
5.1.6		1000	22.30	333	-0.74	0.07	1.50	0.02
5.1.8		500	22.08	180	-0.55	0.06	1.78	0.02
5.1.10		300	21.84	91	-0.52	0.07	1.97	0.02
5.1.12		205	21.58	37	-0.41	0.06	2.08	0.02
5.1.16		130	21.14	8	-0.45	0.06	2.09	0.02
5.1.18		100	20.74	0	-0.43	0.06	2.17	0.02
5.1.22		40	18.35	0	-0.49	0.07	2.14	0.02
5.1.24		10	18.12	0	-0.39	0.06	2.16	0.02
9.1.1		2157	22.35	414	-0.74	0.09	1.40	0.02
9.1.2		2101	22.35	419	-0.69	0.07	1.43	0.02
9.1.3		2050	22.35	423	-0.60	0.11	1.40	0.02
9.1.4		2000	22.35	416	-0.66	0.09	1.40	0.02
9.1.5		1750	22.35	414	-0.72	0.11	1.44	0.02
9.1.6		1500	22.34	379	-0.75	0.09	1.48	0.02
9.1.7		1250	22.33	375	-0.67	0.10	1.53	0.02
9.1.8		1000	22.30	339	-0.71	0.10	1.57	0.02
9.1.9		750	22.23	289	-0.56	0.09	1.66	0.02
9.1.10		501	22.08	186	-0.54	0.09	1.77	0.02
9.1.11		400	21.98	142	-0.52	0.10	1.86	0.02
9.1.12		300	21.84	87	-0.54	0.09	1.96	0.02
9.1.13		200	21.60	44	-0.55	0.10	2.05	0.02
9.1.14		175	21.50	31	-0.50	0.09	2.05	0.02
9.1.15		150	21.36	17	-0.46	0.09	2.09	0.02
9.1.16		130	21.22	10	-0.43	0.09	1.99	0.02
9.1.17		115	21.09	4	-0.40	0.08	2.07	0.02
9.1.18		100	20.87	0	-0.43	0.06	2.13	0.02
9.1.19		85	20.53	0	-0.43	0.08	2.14	0.02
9.1.20		70	20.15	0	-0.37	0.09	2.11	0.02
9.1.21		55	19.46	0	-0.41	0.08	2.17	0.02
9.1.22		46	18.95	0	-0.37	0.09	2.11	0.02
9.1.23		25	18.40	0	-0.41	0.08	2.11	0.02
9.1.24		10	18.41	0	-0.33	0.09	2.12	0.02
Open Ocean Seawater[b]								
Pacific SW	1	3500	34.69	n.d.	-0.40	0.08	3.08	0.02
Pacific SW	1	4000	34.72	n.d.	-0.38	0.09	3.10	0.02
Pacific SW	2	4000	34.72	n.d.	-0.39	0.08	3.10	0.02
Pacific SW	1	4500	34.71	n.d.	-0.36	0.08	2.80	0.02
Pacific SW	2	4500	34.71	n.d.	-0.39	0.07	2.80	0.02

[a] Black Sea samples were collected in July 2013 during the Dutch GEOTRACES expedtion (cruise 64PE373).

[b] Open ocean seawater samples were collected at 32.5°S and 165°W during the 2011 New Zealand GEOTRACES expedtion.

[c] Number of MC-ICPMS analysis on a single processed sample.

Table 6.2. Trace element and uranium isotope data for the Black Sea Station 2 sediment core and the geologic reference material USGS SBC-1.

Sample ID	Depth (cmbsf)	[Fe] (wt%)	[Al] (wt%)	[Ca] (wt%)	[Mn] (wt%)	[Mo] (ppm)	[U] (ppm)	$[U]_{auth}$ %	$\delta^{238}U$ (‰)	2 SE (‰)	$\delta^{238}U_{auth}$ [a] (‰)	$\delta^{234}U_{sec.\ eq.}$ (‰)	2 SE (‰)
Black Sea St. 2 Sediment Core													
2A	1	1.42	1.54	16.0	0.029	22.0	7.0	0.89	-0.06	0.06	-0.03	134	0.5
2B	2	2.30	2.84	12.2	0.041	32.9	7.8	0.88	-0.12	0.06	-0.09	122	0.5
2C	3	2.36	2.83	19.7	0.045	25.8	12.1	0.91	-0.16	0.07	-0.14	129	1.0
2D	4	2.64	3.16	19.4	0.047	28.1	13.3	0.91	-0.02	0.06	0.02	132	0.5
2E	5	2.83	3.33	18.0	0.051	30.2	16.8	0.93	-0.01	0.06	0.02	134	0.5
2F	6	3.10	3.65	17.1	0.053	33.7	16.7	0.93	0.00	0.06	0.02	134	0.4
2G	7	2.13	2.53	24.7	0.043	24.6	18.6	0.93	-0.10	0.08	-0.09	130	0.7
2H	8	2.78	3.06	19.9	0.050	35.1	17.9	0.93	0.01	0.07	0.03	142	0.4
2I	9	2.68	2.86	19.6	0.048	34.2	18.3	0.94	0.03	0.06	0.05	140	0.5
2J	10	1.39	1.34	30.2	0.035	21.2	17.7	0.93	-0.16	0.07	-0.14	139	0.5
2K	11	1.21	1.20	31.7	0.032	19.0	14.7	0.92	-0.16	0.06	-0.14	131	0.5
2L	12	1.04	1.03	33.4	0.030	17.0	14.6	0.91	-0.15	0.06	-0.12	130	0.4
2L-duplo	12	1.01	1.04	32.0	0.029	15.9	14.6	0.92	-0.21	0.06	-0.20	130	0.4
2M	13	1.98	2.00	25.6	0.040	27.4	16.7	0.93	-0.04	0.06	-0.01	134	0.4
2N	14	2.31	2.50	22.2	0.043	30.2	18.6	0.94	0.10	0.06	0.13	126	0.4
2O	15	1.94	2.04	25.9	0.039	27.3	18.1	0.93	-0.03	0.06	0.00	132	0.4
2P	16	1.80	1.86	26.9	0.036	26.8	18.4	0.93	-0.05	0.06	-0.03	131	0.4
2R	18	2.99	3.41	19.9	0.049	34.0	14.9	0.92	0.17	0.06	0.21	120	0.4
2S	19	4.50	7.02	7.3	0.072	21.2	4.1	0.63	-0.26	0.06	-0.23	27	0.4
2T	20	4.34	7.06	7.4	0.068	11.0	3.0	0.49	-0.28	0.06	-0.24	-7	0.4
2U	21	3.45	5.10	11.0	0.060	16.9	4.3	0.70	n.d.	n.d.	n.d.	n.d.	n.d.
2V	22	1.60	1.70	28.5	0.034	28.5	12.8	0.90	0.09	0.06	0.14	124	0.4
2V-duplo	22	1.66	1.79	28.9	0.035	28.3	12.8	0.90	0.04	0.06	0.09	136	0.5
2W	23	0.93	0.89	33.4	0.026	20.2	13.9	0.91	n.d.	n.d.	n.d.	n.d.	n.d.
2X	24	1.55	1.53	27.0	0.032	35.9	15.3	0.92	n.d.	n.d.	n.d.	n.d.	n.d.
2Y	25	2.18	2.87	24.4	0.038	31.9	12.5	0.89	-0.07	0.06	-0.04	120	0.5
Reference Materials	*n* [b]												
USGS SBC-1	1	7.11	10.78	2.2	0.113	2.47	5.83		-0.21	0.06		-25	0.4
USGS SBC-1	2								-0.19	0.07		-26	0.4
USGS SBC-1	3								-0.23	0.06		-26	0.4

[a] $\delta^{238}U$ of authigenic U ($\delta^{238}U_{auth}$) is calculated by correcting the bulk $\delta^{238}U$ for detrital and biogenic carbonate fractions. See text for details.

[b] Number of MC-ICPMS analysis on a single SBC-1 digestion.

6.4 Results

6.4.1 Black Sea Water Column

6.4.1.1 Distribution of dissolved redox-sensitive metals

Surface waters in the Black Sea at station 2 are characterized by a very sharp chemocline at ~100 m, which marks the transition from anoxic to euxinic conditions (Fig. 6.2). The classical redox sequence defined as the transitioning of respiration processes from aerobic oxidation to nitrate reduction, Mn and Fe reduction, and finally sulfate reduction is clearly discernible in the water column of the Black Sea. The distribution of dissolved trace metals are strongly affected by the change in redox potential due to changes in oxidation states which leads to an increase or decrease in solubility, the formation of insoluble sulfides, or due to the effects of scavenging by authigenic particles. The chemical zonation and distribution of trace metals observed at station 2 is representative of that observed at all stations occupied in this study, with only slight variations in the depth of the chemocline across the deep basin (see Chapter 4). A decrease in O_2 coincides with the halocline and approaches 0.0 µmol kg^{-1} at ~95-100 m. The first occurrence of detectable H_2S is at ~105 m. Increases in nitrate (NO_3), Cd, Zn, and V are coincident with the O_2 decrease, indicating that elements are being released during aerobic respiration of organic matter. Nitrate reduction then consumes the released NO_3 before the onset of reduction of Mn and Fe oxides which increases the dissolved concentrations of Mn and Fe. The increase in H_2S below the zone of Mn and Fe reduction marks the upper zone of the euxinic deep waters. Removal of Fe, through precipitation of Fe sulfides, keeps the concentration of Fe relatively low in deep waters. The precipitation of Fe sulfides is thought to scavenge other metals that form soluble sulfide complexes, as is the case for Cd, Zn, Cu, Co, and Mo. Scavenging of V and Ni onto precipitated Mn and Fe oxides at the bottom of the oxic zone, followed by release during dissolution of the oxides at the top of the euxinic zone may be responsible for the observed vertical profiles of V and Ni.

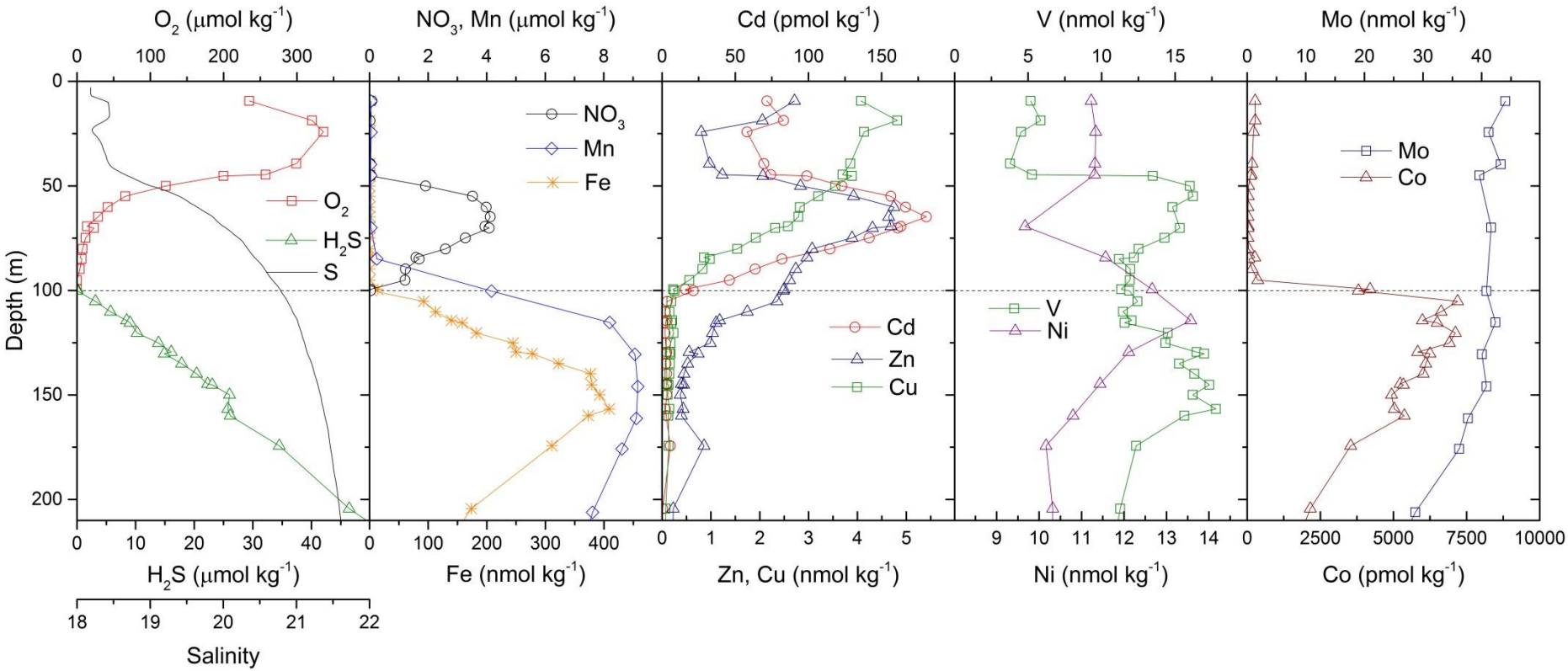

Fig. 6.2. Chemical zonation in the upper 200 m of the Black Sea water column at station 2. The horizontal dashed line denotes the transition from anoxic to euxinic conditions ~100 m.

The U concentration in the Black Sea water column at stations 2, 5, and 9 is presented in Table 6.1 and Fig. 6.3. All three U depth profiles have the same general shape. Surface waters (<100 m) display U concentrations of 2.1- 2.2 ng g^{-1}, while the deepest waters (~10 m above the seafloor) display lower concentrations of ~1.4 ng g^{-1}. The U concentration begins to decrease systematically at a depth of ~100 m which coincides with the transition from anoxic to euxinic conditions. Most of the decrease in the U concentration occurs between 100 m and 1000 m, with a less pronounced decrease below 1000 m. The general shape of the U distribution is very similar to that observed in previous studies of dissolved U in the Black Sea (Anderson *et al.*, 1989; Wei and Murray, 1991), although Anderson *et al.* (1989) observed uniform dissolved U concentrations between the surface layer and a depth of ~400 m, while only at depths of >400 m were decreasing U concentrations observed.

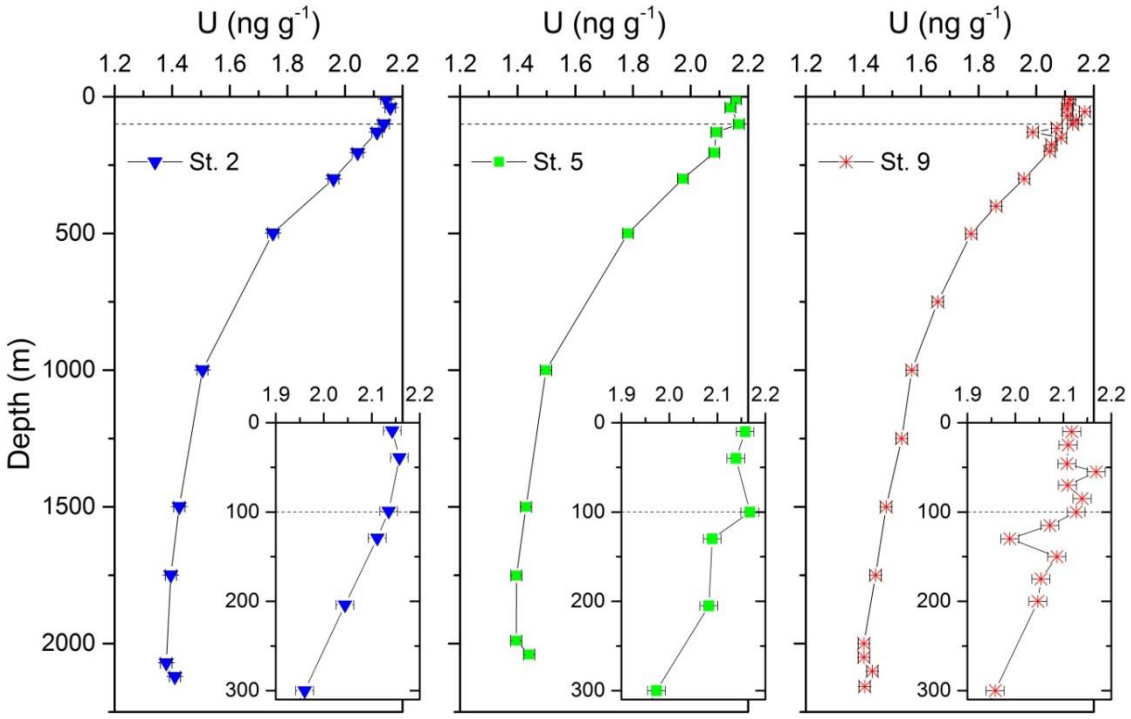

Fig. 6.3. Uranium concentration over the full water column in the Black Sea at stations 2, 5, and 9. The U concentration in the upper 300 m of the water column at each station is displayed in the insets. The horizontal dashed line indicates the transition from anoxic to euxinic conditions at ~100 m depth, which also denotes the depth at which the U concentration systematic begins to decrease. The deepest sample at each station is ~10 m above the seafloor.

6.4.1.2 Dissolved $^{238}U/^{235}U$ isotope composition

The isotopic composition of dissolved U in the water column for stations 2, 5, and 9 are shown in Table 6.1 and Fig. 6.4. At all three stations, the behavior of $\delta^{238}U$ closely mirrors the U concentration. The uppermost surface waters (depth ~10 m) in the Black Sea are characterized by $\delta^{238}U$ values between -0.33 ± 0.09‰ and -0.39 ± 0.06‰ (average = -0.36‰, n=3), which is identical, within error, to the open ocean seawater composition of -0.39 ± 0.02‰ (Andersen *et al.*, 2014; Stirling *et al.*, 2007; Tissot and Dauphas, 2015; Weyer *et al.*, 2008). Below ~100 m, the dissolved U becomes increasingly depleted in the heavy ^{238}U isotope, which is reflected in more negative $\delta^{238}U$ values between -0.60 ± 0.09‰ and -0.86 ± 0.07‰ at depths >1000 m (Fig. 6.4). At station 2, and possibly station 5, samples from below 2000 m are characterized by higher $\delta^{238}U$ values relative to overlying samples at depths between 1500-2000 m.

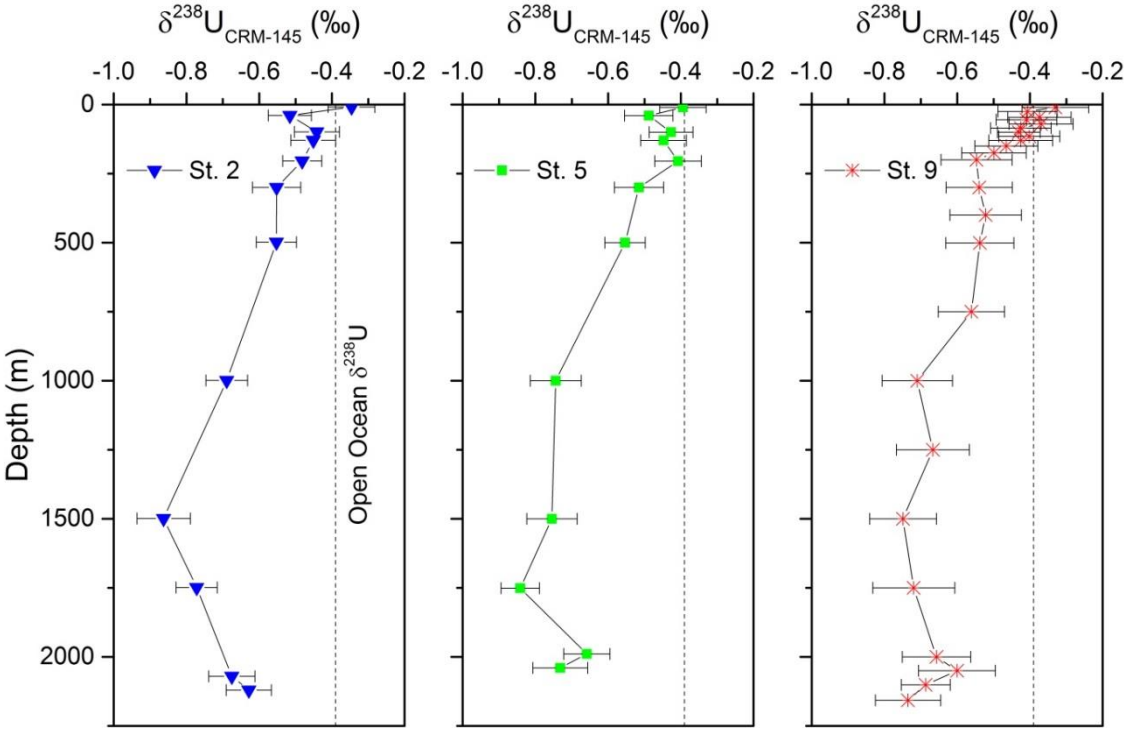

Fig. 6.4. Dissolved uranium isotope composition ($\delta^{238}U$) of the Black Sea water column at stations 2, 5, and 9. The vertical dashed lines represent an open ocean seawater $\delta^{238}U$ of -0.39 ± 0.02‰ (Andersen *et al.*, 2014; Stirling *et al.*, 2007; Tissot and Dauphas, 2015; Weyer *et al.*, 2008). Error bars represent analytical uncertainty (2SE) determined for each sample.

6.4.2 Black Sea Sediments

6.4.2.1 Distributions of redox-sensitive metals in the sedimentary record

In the Black Sea sedimentary sequence, the concentrations of a suite of redox-sensitive metals in the sediment depth profile from station 2 are present in Table 6.2 and Fig. 6.5. The sediment concentrations of Ca, Mn, Fe, and Mo are normalized to the aluminum (Al) concentration. Aluminum is used as a tracer of detrital lithogenic input and normalizing to Al removes any variability in the sedimentary record due to changes in the flux of lithogenic material. Sediments were sampled from the surface to a depth of ~25 cm, spanning the upper section of unit I in the Black Sea sedimentary sequence, and representing the last ~1000 y of sediment deposition, assuming a sedimentation rate of ~25 cm kyr^{-1} for unit I sediments (Hay, 1988). At station 2, the upper 25 cm of unit I is punctuated by an ~3-5 cm thick turbidite layer (sediment deposited by a gravity flow) centered at 20 cm depth in the core. Turbidites are composed primarily of lithogenic material and can serve as a useful reference layer within a core sequence for assessing the authigenic (formed from seawater) enrichments of metals in the non-turbidite core material. The unit I Black Sea sediment core from station 2 is characterized by high metal to aluminum (Me/Al) ratios (Fig. 6.5), compared to the turbidite, which has Me/Al ratios similar to local background lithogenic material (Little *et al.*, 2015). Assuming that detrital material represents the only source of Al to Black Sea sediments, then Me/Al ratios above those in the turbidite (Fe/Al ~ 0.6 wt%/wt%; Mo/Al ~ 1.5 ppm/wt%; Mn/Al ~ 100 ppm/wt%; Ca/Al ~ 1 wt%/wt%) represent a non-detrital source of the metal to the sediment. The sediment depth profile is characterized by intervals of elevated Me/Al ratios with Fe/Al up to 1.0 wt%/wt%, Mo/Al up to 23 ppm/wt%, Mn/Al up to 295 ppm/wt% and Ca/Al above 35 wt%/wt%. The Ca/Al maxima at depths of ~23 cm and ~12 cm may represent periods of increased carbonate deposition as noted by Hay (1988) with total sediment Ca concentrations of ~33%.

6.4.2.2 Sedimentary record of U, $\delta^{238}U$, and $\delta^{234}U$

In the Black Sea sedimentary sequence, the concentration of U increases from ~7 ppm to ~17 ppm in the upper ~5 cm, and remains relatively stable over the rest of the core aside from the turbidite layer. The sediment depth profile of U/Al ratios reveals strong enrichment of U over the detrital background evidenced by elevated U/Al ratios of up to >15 ppm/wt% (compared with <1 ppm/wt% in the turbidite) and absolute U concentrations >18 ppm (compared with <3 ppm in the turbidite) (Fig. 6.5). The

sediment depth profile of U/Al ratios closely follows the profiles of Ca/Al and Mn/Al (Fig. 6.5, 6.6).

The sediment depth profile of $\delta^{238}U$ is shown in Table 6.2 and Fig. 6.5. The turbidite is characterized by a bulk sediment $\delta^{238}U$ value of -0.27‰, while the rest of the core is characterized by an average authigenic $\delta^{238}U$ of -0.01 ± 0.10‰ (1SD). The relationship between $\delta^{238}U$ and U/Al is displayed in Fig. 6.6.

The $\delta^{238}U$ of the authigenic U fraction ($\delta^{238}U_{auth}$; Table 6.2) is determined by assuming the total U in the sediment core is comprised of authigenic, detrital, and carbonate fractions. Following Andersen *et al.* (2014), the bulk $\delta^{238}U$ is corrected for detrital and carbonate fractions using $[Ca]_{meas}$ and $[Al]_{meas}$, the measured Ca and Al concentrations in the bulk sediment, and by assuming a fixed detrital U/Al_{det} ratio of $1.8x10^{-5}$ (g/g) and $\delta^{238}U_{det}$ of -0.3‰ and a fixed carbonate U/Ca_{carb} ratio of $3.25x10^{-6}$ (g/g) and $\delta^{238}U_{carb}$ of -0.4‰ via the equation:

$$\delta^{238}U_{auth} = \left(\frac{\delta^{238}U_{bulk} * [U]_{bulk} - \delta^{238}U_{det} * U/Al_{det} * [Al]_{meas} - \delta^{238}U_{carb} * U/Ca_{carb} * [Ca]_{meas}}{[U]_{bulk} - U/Al_{det} * [Al]_{meas} - U/Ca_{carb} * [Ca]_{meas}} \right)$$

For all samples, other than the turbidite, the authigenic U fraction accounts for >90% of the U and therefore the $\delta^{238}U$ correction is relatively minor (~0.03‰) and does not influence the following discussion. The $\delta^{234}U$ of the turbidite is close to 0‰ indicating that U in the turbidite is primarily lithogenic in origin and in radioactive equilibrium with respect to ^{238}U and ^{234}U and older than 1 Ma. The U/Al ratio of the turbidite at 20 cm depth is 4.2×10^{-5} (g/g) which may indicate the assumed lithogenic U/Al of 1.8×10^{-5} (g/g) is too low, or that the turbidite has accumulated authigenic U and that the true $\delta^{234}U$ of the turbidite is <0‰ with the observed $\delta^{234}U$ representing a mix of lithogenic U with a $\delta^{234}U$ of <0‰ and authigenic U with a modern to recent marine $\delta^{234}U$ signature of 147‰ (Andersen *et al.*, 2010). Importantly, changing the fixed lithogenic U/Al ratio has only a minor impact on the estimated authigenic U fraction in anoxic Black Sea sediments that are rich in authigenic U. The rest of the core is characterized by an average $\delta^{234}U$ of 131 ± 6‰ (1SD) indicating that most of the sedimentary U is primarily authigenic in origin and derived from seawater, in agreement with the U/Al correction.

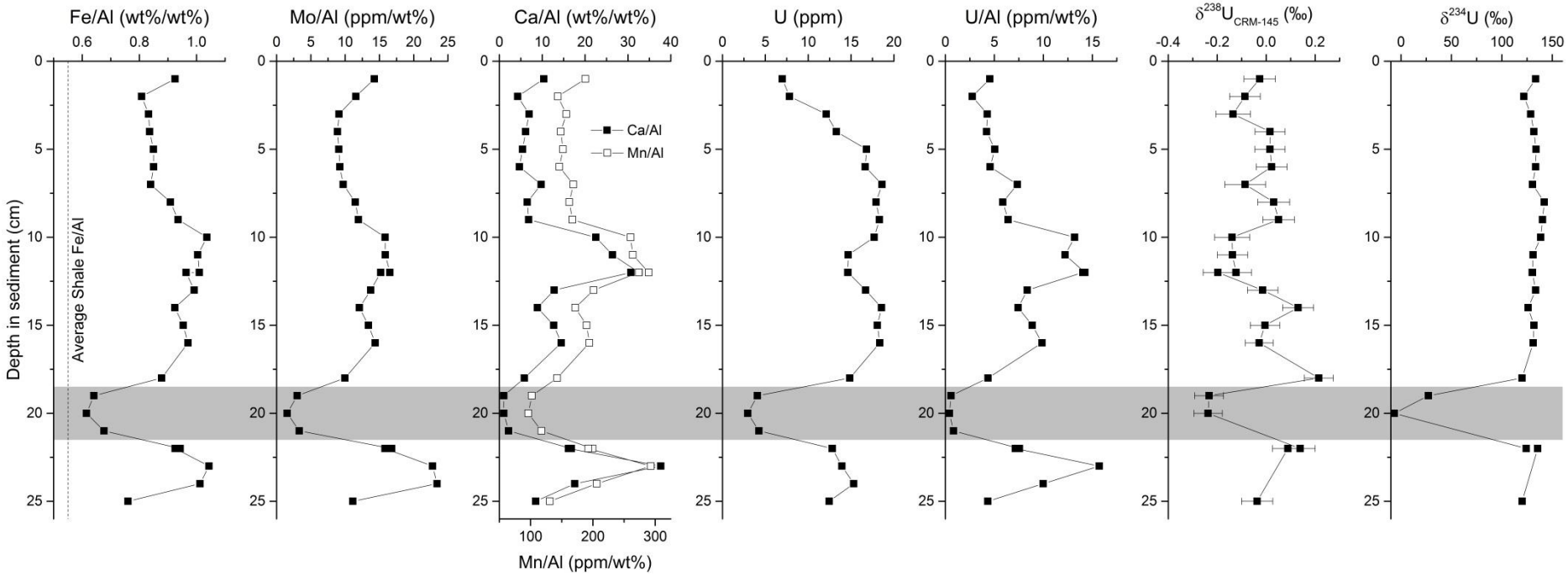

Fig. 6.5. Sedimentary depth profiles of Fe/Al, Mo/Al, Ca/Al, Mn/Al, U, U/Al, $\delta^{238}U$ and $\delta^{234}U$ in the station 2 sediment core collected in the Black Sea during the Dutch GEOTRACES expedition in 2013 (cruise 64PE373). The dashed vertical line in the Fe/Al plot corresponds to an average shale Fe/Al ratio of 0.55 wt%/wt% (Wedepohl, 1991). The horizontal grey band denotes the turbidite layer. The $\delta^{238}U$ data represent the estimated isotope composition of authigenic U and is calculated by correcting the bulk $\delta^{238}U$ for detrital and biogenic carbonate fractions. Error bars on $\delta^{238}U$ are the analytical uncertainty (2SE). See text for details.

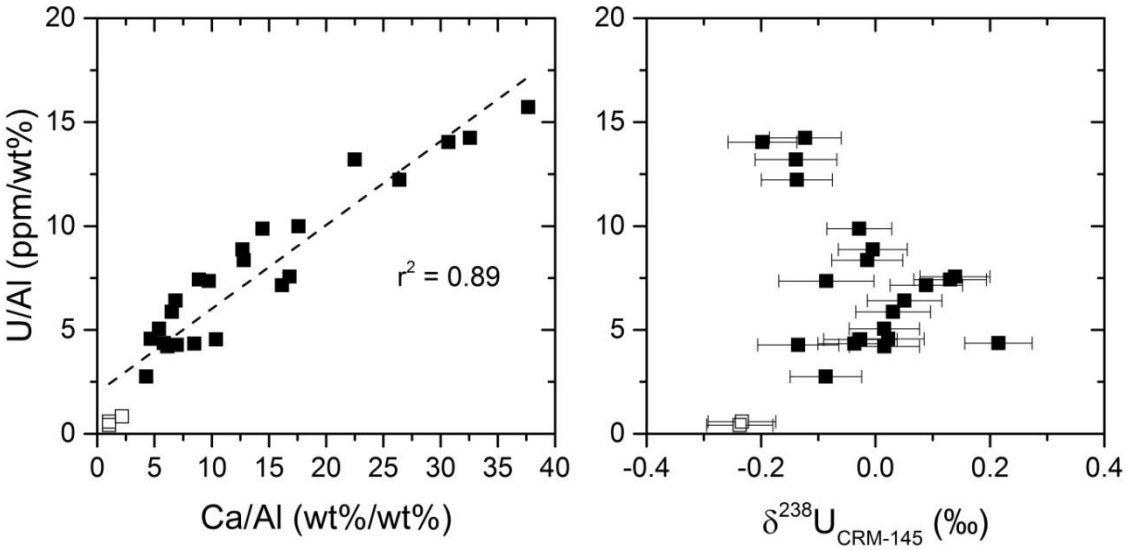

Fig. 6.6. Plot of Ca/Al vs. U/Al and $\delta^{238}U$ vs. U/Al in the sediment core collected at station 2 in the Black Sea during the Dutch GEOTRACES expedition in 2013 (cruise 64PE373). A strong correlation between Ca/Al and U/Al is present in the data, while the relationship between $\delta^{238}U$ and U/Al is not as clear. The open symbols are from the turbidite layer and are representative of the detrital background signature. The $\delta^{238}U$ data represent the estimated isotope composition of authigenic U and is calculated by correcting the bulk $\delta^{238}U$ for detrital and biogenic carbonate fractions. Error bars on $\delta^{238}U$ are the analytical uncertainty (2SE). See text for details.

6.5 Discussion

The use of $\delta^{238}U$ as a quantitative tracer of the extent of anoxic conditions present during oceanic anoxic events requires knowledge of the direction and magnitude of isotope fractionation during reduction of soluble U(VI) to insoluble U(IV) (Brennecka *et al.*, 2011a; Montoya-Pino *et al.*, 2010). Since marine sediments are our primary archive for reconstructing paleoredox conditions, accurately describing how the features observed in the water column are translated into a sedimentary signature is paramount to successfully using U isotopes as a paleoredox proxy. It is therefore important to understand the processes controlling the removal of U from the water column under anoxic conditions and how these processes fractionate U isotopes. The Black Sea is an ideal natural laboratory to observe the behavior of the ^{238}U-^{235}U isotope system under oxic to euxinic water column conditions and may potentially serve as an important analogue of past oceanic anoxic events. Owing to its unique ideal characteristics, previous calibrations of the U isotope paleoredox proxy are primarily from the Black Sea, but have been based on a limited number of observation and have

not included observation within the water column. This highlights the need for robust examination the U isotope systematics in both the water column and sediments in this important marine basin. The euxinic conditions found in deep waters of the modern Black Sea clearly impact the distribution and isotopic composition of U, not only in the water column itself, but also in the underlying sediments, and most likely also in porewaters near the sediment-water interface.

6.5.1 Behavior of U and $\delta^{238}U$ in the Black Sea

The decreasing concentration of U with depth in the Black Sea (Fig. 6.3) is readily explained by a removal of U due to the reduction of soluble U(VI) to insoluble U(IV) at a rate that is faster than the rate U renewal in the deep water column. The reduction of U(VI) to U(IV) by hydrogen sulfide (H_2S) is thermodynamically favourable under the euxinic conditions present in the water column of the Black Sea. Yet contrary to thermodynamic predictions, U is not present in substantial quantities as reduced U(IV) in the dissolved phase or adsorbed to particulate phases in the Black Sea water column (Anderson *et al.*, 1989). This conundrum is supported by the laboratory-controlled experiments of Hua *et al.* (2006) which demonstrate that the abiotic chemical reduction of U(VI) to U(IV) by H_2S is kinetically inhibited due to the formation of uranium-carbonate species. However, the U concentration in the Black Sea water column is strongly inversely correlated with H_2S (Fig. 6.7), indicating that the processes controlling their distributions are related. Sulfate-reducing bacteria can mediate the reduction of U(VI) to U(IV) (Lovely *et al.*, 1993), and may therefore be the common link between the distributions of H_2S and U in the Black Sea water column.

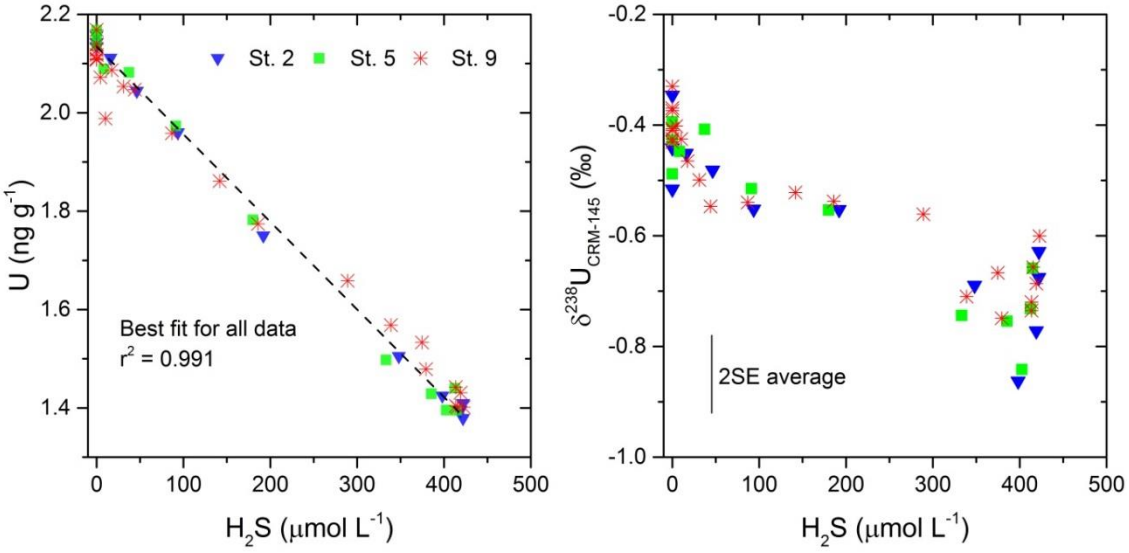

Fig. 6.7. Relationship between H_2S and dissolved U concentration and $\delta^{238}U$ in the Black Sea water column at stations 2, 5, and 9. The vertical bar represents the average analytical uncertainty of $\delta^{238}U$ (2SE).

Pore-water profiles in Black Sea sediments show significant removal of U in the uppermost ~5 cm of sediment and corresponding enrichment of U in the solid phase (Anderson *et al.*, 1991; Barnes and Cochran 1991; Fig. 6.5, this study). These observations support the hypothesis that the process of chemical reduction and subsequent removal of dissolved U from the Black Sea occurs primarily within the upper sediment pore waters (Anderson *et al.*, 1989; Barnes and Cochran, 1991). Accordingly, the U concentration gradient observed in the Black Sea water column has been widely attributed to diffusion of U across the sediment-water interface where it is subsequently reduced to U(IV) and sequestered, as opposed to reduction and removal of U in the overlying water column itself. This inference is also supported by the apparent lack of U(IV) in both the dissolved and particulate phases of the Black Sea water column (Anderson et a., 1989), as discussed previously. Contrarily, sulfate reduction in Black Sea sediments produces H_2S which then diffuses out of the sediment porewater in to the overlying water column, or is produced in the water column itself (Konovalov *et al.*, 2006, 2007). Thus, for this scenario to hold, the strong relationship between U and H_2S in the water column would likely be a result of diffusion acting as the common primary control on the distributions of both U and H_2S. Relative diffusion rates of U and H_2S must be related to a common removal/production process, such as sulfate reduction, and must have remained constant over the renewal time of the deep (>500 m) Black Sea in order for the water column relationship between U and H_2S to develop

across the entire deep basin. The renewal time of the deep (>500 m) Black Sea is estimated to be more than 500 y (Lee *et al.*, 2002), which implies that the relative removal/production rates of U and H_2S have remained constant for at least 500 y.

The upper water column (<100 m) of the Black Sea does not appear to be strongly affected by the removal of U and is relatively homogenous with respect to the dissolved U concentration and $\delta^{238}U$. Furthermore, the average $\delta^{238}U$ of surface waters is indistinguishable from open ocean seawater ($\delta^{238}U$ = -0.39‰). There are, however, some minor shifts in $\delta^{238}U$ to more negative values at depths <100 m which is possibly due to greater influence of rivers, although input from the Danube River, representing a major source of riverine U, has a more positive $\delta^{238}U$ signature of -0.22‰ (Stirling *et al.*, 2007) and would act to shift the U isotope compositions of the upper water column to heavier, rather than lighter values.

Decreasing values of $\delta^{238}U$ in the deeper (>100 m) water column is consistent with the preferential reduction of U(VI) to U(IV) and subsequent removal of ^{238}U from the water column which ultimately leaves modern unit I Black Sea sediments enriched in ^{238}U relative to the overlying water column (Table 6.1, 6.2; Fig. 6.4, 6.5). This pattern of dissolved $\delta^{238}U$ behavior under euxinic water column conditions has been observed previously in the Baltic Sea and Kyllaren fjord (Noordmann *et al.*, 2015) and inferred from sediments enriched in ^{238}U from the Black Sea (Andersen *et al.*, 2014; Montoya-Pino *et al.*, 2010; Weyer *et al.*, 2008). Since U reduction and removal is primarily occurring in porewaters in the Black Sea, the $\delta^{238}U$ of porewaters will shift to more negative values during the progressive removal of U (Andersen *et al.*, 2012; Clark and Johnson, 2008). Therefore, the overall negative shift in $\delta^{238}U$ with depth in the Black Sea likely reflects back-diffusion of U from porewaters into the overlying water column. The rate of U back-diffusion from porewaters, and the time interval over which Black Sea bottom waters have been permanently euxinic will therefore exert a strong control on the $\delta^{238}U$ of the overlying water column. The weak correlation between $\delta^{238}U$ and H_2S may indicate that the relative rates of U back-diffusion and H_2S diffusion from pore waters has not remained constant over the >500 y renewal time of the deep (>500 m) Black Sea or that variable H_2S concentrations in pore waters may result in changes in the stability of reduced U in sediments such that lower H_2S concentrations would lead to the release of sediment-bound U back to pore waters.

Interestingly, samples from below ~2000 m depth at station 2, and station 5 albeit less obvious, are characterized by higher $\delta^{238}U$ values relative to overlying

samples at depths between 1500-1750 m (Table 6.1; Fig. 6.4), resulting in a slight 'kink' in the vertical profiles of $\delta^{238}U$. There is also a very slight increase in the U concentration in the deepest samples at stations 2 and 5, relative to the overlying samples. As Black Sea sediments are enriched in ^{238}U relative to the water column, it is possible that minor sediment dissolution occurring at the sediment-water interface is responsible for this observed pattern, perhaps due to lower local H_2S concentrations. Release of U during respiration of organic matter may also be a possible mechanism for increasing $\delta^{238}U$ in bottom waters, but the $\delta^{238}U$ of organic matter in the Black Sea is currently unknown. Porewaters in Black Sea sediments are expected to be depleted in the ^{238}U isotope relative to overlying bottom waters due to preferential sequestration of ^{238}U in the sediments during reduction of U(VI) to U(IV) (Andersen *et al.*, 2014; Clark and Johnson, 2008). Therefore, U back-diffusion from porewater into overlying bottom waters is not a probable mechanism for producing the observed increase in $\delta^{238}U$ in Black Sea bottom waters at stations 2 and 5, unless the $\delta^{238}U$ of porewaters varies on time scales shorter than the >500 y renewal time of deep water (>500 m) in the Black Sea through, for example, time-dependent variations in the kinetics of U(VI)-U(IV) reduction as environmental conditions change.

The observation of a decreasing trend in authigenic $\delta^{238}U$, from -0.03‰ to -0.14‰, in the upper ~3 cm of the station 2 sediment core (Fig. 6.5) may be related to reactive-diffusive transport processes of U in porewaters. The $\delta^{238}U$ of authigenic U accumulating in reducing sediments will reflect the $\delta^{238}U$ of the associated porewaters, but will differ by the U isotope fractionation factor during reduction of U(VI) to U(IV). If the rate of U diffusing into sediments from the overlying water column is slower than the rate of U reduction and removal in the porewaters, then a vertical gradient in the U concentration and $\delta^{238}U$ in porewaters is expected to develop, with lower U concentrations and more negative $\delta^{238}U$ values developing deeper in the sediment (Andersen *et al.*, 2014; Clark and Johnson, 2008). As sediments are buried, they will move through the full porewater gradient and the accumulating authigenic $\delta^{238}U$ at a given depth is therefore expected to reflect changes in porewater $\delta^{238}U$ across the zone of U accumulation. The zone of U accumulation is estimated to be the upper ~5 cm of anoxic sediments in the Black Sea based on pore water U profiles and the gradient in U concentration in sediments themselves (Fig. 6.5). Thus, the decreasing trend in $\delta^{238}U$ in the upper ~3 cm of the station 2 sediment core may reflect the changing $\delta^{238}U$ of porewaters. This implies that the authigenic $\delta^{238}U$ of sediments from in the upper ~2

cm is still evolving and can be expected to become more negative during further burial until they exit the zone of U accumulation. Furthermore, changes to the idealized steady-state condition U accumulation, such as changes in the sedimentation rate or changes in the reactive-diffusive transport of U in porewaters can influence the authigenic $\delta^{238}U$ ofsediments which are still within the zone of U accumulation. Therefore, changes in the authigenic $\delta^{238}U$ signature in ancient sediments may not simply reflect changes in contemporaneous seawater $\delta^{238}U$.

The relationship between U/Al and authigenic $\delta^{238}U$ in Black Sea sediments (Fig. 6.6) may also be a result of the reactive-diffusive transport of U in porewaters. Black Sea sediments are expected to initially have a lithogenic $\delta^{238}U$ signature, close to that of the turbidite for example (-0.27‰). The $\delta^{238}U$ of authigenic U accumulating at the sediment-water interface will not be affected by reactive-diffusive transport and will therefore be higher than authigenic U accumulating deeper in the sediment, which is affected by reactive-diffusive transport. Burial of sediments that have not moved through the full porewater gradient of U and $\delta^{238}U$ would preserve the initial authigenic $\delta^{238}U$ incorporated at the sediment-water interface, which would result in an apparent mixing between lithogenic U with a $\delta^{238}U$ value around -0.27‰ and authigenic U with a $\delta^{238}U$ offset from bottom water by the U isotope fractionation factor. This would result in a linear relationship between U/Al and $\delta^{238}U$. Sediments that contain the highest concentrations of authigenic U are likely influenced by reactive-diffusive transport of U in porewaters and therefore the authigenic $\delta^{238}U$ of sediments with the highest U/Al ratios will show a shift to more negative $\delta^{238}U$ values, reflecting the change in porewater $\delta^{238}U$ across the zone of U accumulation. Such a shift in the authigenic $\delta^{238}U$ signature is observed at a U/Al of ~7 ppm/wt% in the station 2 sediment core (Fig. 6.6).

6.5.2 Salinity-normalized U concentrations

The measured U(VI) concentrations in the Black Sea water column are compiled for all three studied stations (St. 2, 5 and 9) in Fig. 6.8. The amount of U removed from the water column can be estimated by comparing the observed U concentrations to initial U concentration in the Black Sea water column prior to removal determined by a simple conservative mixing model. Specifically, in oxygenated marine waters, U displays conservative behavior and its concentration is linearly correlated with salinity (Ku *et al.*, 1977; Owens *et al.*, 2011). Thus, the initial

concentration of U ($[U]_{initial}$) in the Black Sea water column prior to removal can be predicted from the measured water column salinity if the U concentrations and salinities of the end member water masses which mix to form Black Sea water are known (Anderson *et al.*, 1989). In this study, the two end member water masses are assumed to be Bosporus Overflow water (S ~34.9; [U] = 3.16 ng g^{-1}) and river water, the latter of which is dominated by the Danube River (S = 0; [U] = 1.08 ng g^{-1}) (Palmer and Edmond, 1993). The U concentration in the Bosporus Overflow water is estimated from the average salinity of present day Bosporus Overflow water reported by Murray *et al.* (2006) and the salinity-U relationship reported by Owens *et al.* (2011). Once the initial U concentration is established, the fraction of U removed from the aqueous phase is calculated as 1-*f* where $f = [U]_{measured}/[U]_{initial}$ (Fig. 6.8). The initial U concentration in surface waters is calculated to be ~2.2 ng g^{-1}, while in deep waters it is ~2.4 ng g^{-1}. Therefore, a maximum of ~43% of the initial dissolved U has been removed from solution in the euxinic bottom waters of the Black Sea, while oxic surface waters contain >97% of the predicted U. The removal of U(VI) from the water column results in significant isotopic fractionation of the remaining dissolved U pool (Fig. 6.4).

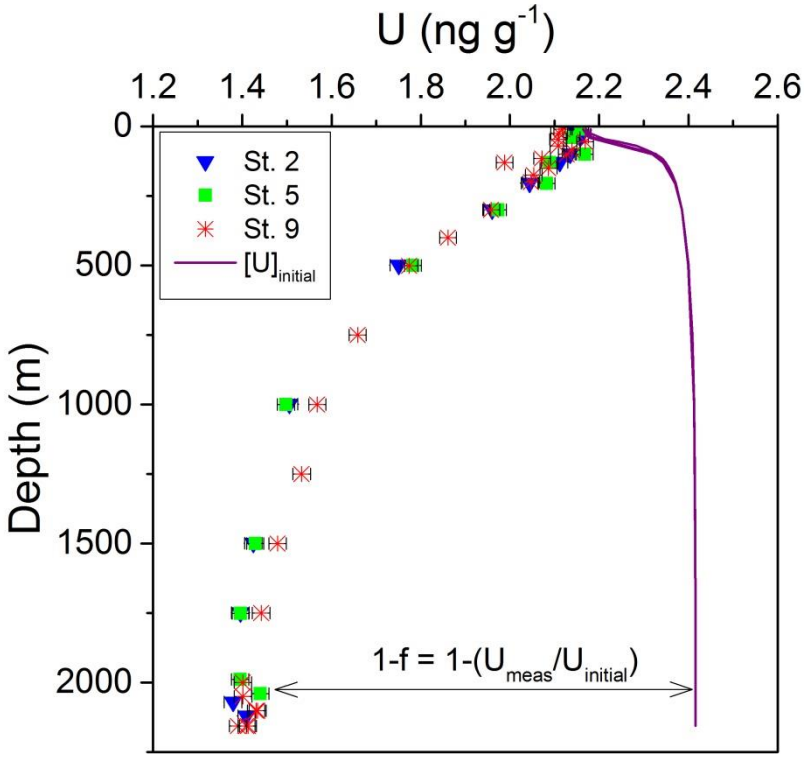

Fig. 6.8. Uranium concentration in the Black Sea water column at stations 2, 5 and 9. The solid line indicates the initial U concentration ($[U]_{initial}$) prior to removal and is predicted using the measured salinity and a simple two end member mixing model

between Bosporus Overflow water and Danube river water (see text for details). The fraction of uranium removed is calculated as 1-*f* where $f = [U]_{measured}/[U]_{initial}$.

6.5.3 Models for predicting the U isotope fractionation factor in the Black Sea

In the Black Sea, the magnitude and direction of the $\delta^{238}U$ fractionation after the partial reduction and removal of U from the aqueous phase, can, by convention, be described by the fractionation factor (α), which is independent of reaction progress. In the present study, α is defined as R_a/R_b where R_b denotes the $^{238}U/^{235}U$ value of the product (*i.e.* U(IV)) and R_a represents the $^{238}U/^{235}U$ composition of the reactant (*i.e.* U(VI)). Values for α can be derived by applying a fractionation model to the observational dataset, as discussed further below. Once isotopic fractionation factors have been established for the processes removing U from the water column under anoxic/euxinic conditions, it then becomes possible to interpret sedimentary archives of U isotopes as a record of the contemporaneous water column conditions during the time of sediment deposition. It is, however, important to bear in mind that modelled values of α should be regarded as 'apparent' values, which may differ from the intrinsic 'true' α value describing a particular reaction if the model does not adequately describe all of the relevant fractionation processes occurring within the system.

The Rayleigh fractionation model describes the change in the isotopic composition of the reactant as it is consumed during the progression of a reaction which induces isotope fractionation as shown in Eq. 4.

$$\delta^{238}U_{reactant} = \delta^{238}U_{initial} + (1/\alpha - 1) \times 10^3 \times ln(f) \quad (4)$$

Isotopic fractionation factors can be calculated from the slope of the best fit line in a linearized plot of $\delta^{238}U$ vs. ln(*f*) with the uncertainty in the slope serving as the uncertainty in the derived fractionation factor (Scott *et al.*, 2004). The model assumes the initial pool of U is finite and that U removed from the dissolved phase is irreversibly sequestered in to an insoluble phase after removal, so that the reactant (*i.e.* U(VI)) and product (*i.e.* U(IV)) do not interact once the process has occurred. These conditions are most likely not strictly met in the Black Sea due to the small but non-negligible continuous sources of dissolved U (*e.g.* Bosporus Overflow water and the Danube river water). Also, the water column profiles of $\delta^{238}U$ in Fig. 6.4 show signs of potential remobilization of authigenic U due to sediment dissolution at the sediment-

water interface. Despite these concerns, it is likely that Rayleigh fractionation type behavior of U is a valid assumption, to a first order, and there exists a strong relationship between $\delta^{238}U$ and U concentrations in the Black Sea water column (Fig. 6.9). Combining the U concentration and $\delta^{238}U$ datasets for all three stations yields a value for α of 0.99937 ± 0.00008 (2 SE), which, expressed in terms of the isotopic enrichment factor ($\varepsilon = (\alpha-1)\times10^3$), yields ε = -0.63 ± 0.08‰ (2 SE).

The Rayleigh fractionation model is also useful for predicting the isotopic composition of the product from a process resulting in isotopic fractionation. Assuming the removal of U from the Black Sea water column follows a single step uni-directional reaction (*i.e.* Rayleigh fractionation), the $\delta^{238}U$ composition of the instantaneously produced product ($\delta^{238}U_{inst}$) and the accumulated product ($\delta^{238}U_{accum}$) can be predicted following Eq. 5 and Eq. 6, respectively:

$$\delta^{238}\mathrm{U}_{\mathrm{inst}} = \delta^{238}\mathrm{U}_{\mathrm{initial}} + (1/\alpha - 1) \times 10^3 \times \ln(f) + (1/\alpha - 1) \times 10^3 \quad (5)$$

$$\delta^{238}\mathrm{U}_{\mathrm{accum}} = \delta^{238}\mathrm{U}_{\mathrm{initial}} + (1/\alpha - 1) \times 10^3 \times \left(\ln(f) - \frac{\ln(f)}{1-f}\right) \quad (6)$$

The observed $\delta^{238}U$ of authigenic U in Black Sea sediments can then be compared with the predicted $\delta^{238}U$ derived from the instantaneous and accumulative product models to assess if the sedimentary $\delta^{238}U$ record is easily interpreted by these simple models (Fig. 6.9).

The behavior of $\delta^{238}U$ in the water column of the Black Sea can also be modelled as closed system equilibrium isotope fractionation, where the product and reactant are allowed to remain in isotopic equilibrium as the reaction progresses and can be expressed by Eq. 7:

$$\delta^{238}\mathrm{U}_{\mathrm{reactant}} = \delta^{238}\mathrm{U}_{\mathrm{initial}} + (1/\alpha - 1) \times 10^3 \times (1 - f) \quad (7)$$

In this case, α values can be calculated from the slope of the best fit line in a plot of $\delta^{238}U$ vs. (1-*f*). Combing the U concentration and $\delta^{238}U$ datasets for all three stations yields a value for α of 0.99916 ± 0.00011 (2 SE) or ε = -0.84 ± 0.11‰ (2 SE). During equilibrium isotope fractionation, the product at all points during the reaction progression will always be offset from the reactant by the value of ε (Fig. 6.9).

The two models, defined by Rayleigh and equilibrium fractionation, do not diverge appreciably from one another until a high percentage of U has been removed from the dissolved phase, making it difficult to differentiate between these two scenarios with the available data in the Black Sea where the fractionation of U removed is <50%. Therefore, to a first order, both a Rayleigh fractionation model and a closed system equilibrium fractionation model are considered to adequately describe U removal from the Black Sea water column. If we consider the formation of reduced U(IV) minerals, such as uraninite, to be a unidirectional process with no isotope exchange after formation, then we would expect U isotope fractionation to follow a Rayleigh fractionation model.

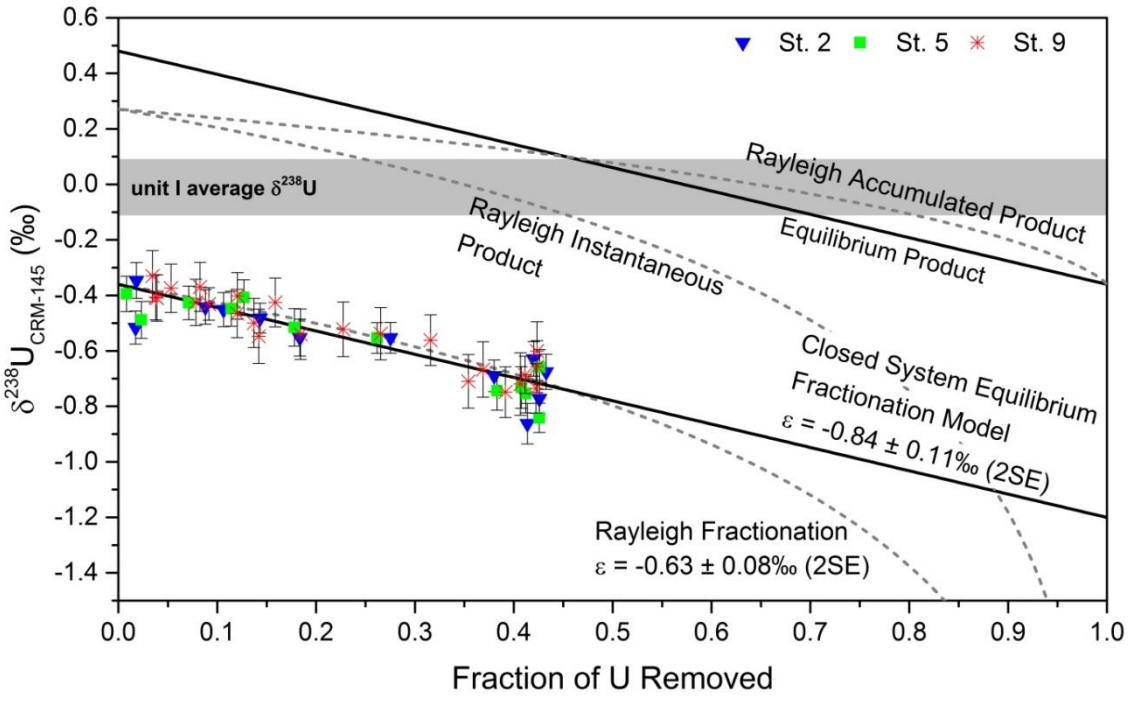

Fig. 6.9. Fraction of U removed versus $\delta^{238}U$ for all Black Sea water column data presented in this study. A Rayleigh fractionation model (dashed lines) and a closed system equilibrium model (solid lines) are used to calculate the isotopic fractionation factor, yielding a value of ε = -0.63 ± 0.08‰ (2 S.E) and ε = -0.84 ± 0.11‰ (2 S.E), respectively. The grey horizontal bar denotes the average authigenic $\delta^{238}U$ of recent unit I Black Sea sediments (-0.01 ± 0.10‰ (1SD)). Additional lines represent the $\delta^{238}U$ of products predicted by the two fractionation models.

6.5.4 Uranium isotope composition of Black Sea sediments

The observed $\delta^{238}U$ of authigenic U in unit I of the Black Sea sediments recovered from station 2 in the deep euxinic basin ranges between -0.2‰ and 0.2‰, which is in very good agreement with the $\delta^{238}U$ values of authigenic U reported in an

independent study of Black Sea sediments by Andersen *et al.* (2014). These $\delta^{238}U$ values correspond to ~13-53% removal of U based on the instantaneous product model and ~26-91% removal of U based on the accumulated product model (Fig. 6.10). In the context of present day accumulation, surface sediments are characterized by an average $\delta^{238}U$ value of -0.01 ± 0.10‰ (1SD) which is in good agreement with the $\delta^{238}U_{inst}$ signature of -0.07‰ that is predicted using the instantaneous product model, adopting the ~43% maximum removal of U inferred from the U distribution of modern Black Sea bottom waters, as discussed above (Fig. 6.9). Contrarily, the accumulative product model predicts $\delta^{238}U_{accum}$ values of <0‰ only when at least >67% of the U has been removed from bottom waters. Therefore, the average $\delta^{238}U$ composition of the most recent "unit I" Black Sea sediments is best explained by the instantaneous product model. However, substantial scatter in the $\delta^{238}U$ signatures acquired for the station 2 sediment core (Fig. 6.5) likely indicates that additional processes, each with differing fractionation factors, are influencing the $\delta^{238}U$ of sediments deposited under euxinic water conditions rather than being influenced by just a single water column reduction and removal processes or variability in the U reduction rate which would affect mass transport across the sediment water interface and the $\delta^{238}U$ signature of the sediment (Anderson *et al.*, 2014).

6.5.5 Mechanism for reduction of U(VI) to U(IV) in the Black Sea

The magnitude of the uranium isotope fractionation determined for the Black Sea water column (ε = -0.63 ± 0.09‰ to -0.84 ± 0.11‰) and the difference between the average $\delta^{238}U$ of sediment (-0.01 ± 0.10‰) and the average $\delta^{238}U$ of the three bottom water samples (-0.7 ± 0.1‰) is approximately -0.7‰. Thus, the magnitude of uranium isotope fractionation observed in the Black Sea falls within the range of uranium isotope fractionation determined experimentally during anoxic incubation studies of various sulfate and metal reducing bacterial isolates (ε = -0.64 to -1.02‰; Basu *et al.*, 2014, Stirling *et al.*, 2015; Stylo *et al.*, 2015). Although laboratory conditions will be considerably different than the conditions in the Black Sea, the agreement between the U isotopic fractionation factors is intriguing and potentially provides direct evidence of microbial mediated reduction of U(VI) to U(IV) in the Black Sea. This possibility is further reinforced by the striking positive correlation between U and H_2S concentrations in the Black Sea water column.

6.5.6 Implications for the $\delta^{238}U$ paleoredox proxy

Recent studies of $\delta^{238}U$ in marine sediments have attributed shifts in $\delta^{238}U$ recorded in sequential sedimentary layers as evidence of shifts in the $\delta^{238}U$ of contemporaneous seawater caused by increased oceanic anoxia (Brennecka *et al.*, 2011a; Montoya-Pino *et al.*, 2010). These authors propose simplified models of the U isotope mass balance of the oceans and consider anoxic and euxinic settings, due to the large U isotope fractionation associated with reduction, as the primary depositional setting that significantly influences the $\delta^{238}U$ of seawater. Oxic and hypoxic sedimentary U fluxes are associated with only minor (~0.1‰) isotope fractionation and are considered negligible. Thus, an increase in the spatial coverage of ocean anoxia will act to drive the $\delta^{238}U$ of seawater to more negative values due to the preferential removal of ^{238}U from seawater to sediments. The value of ~0.5‰ was assigned as the U isotope fractionation factor associated with the anoxic sink of U in both studies. Using a simple mass balance Montoya-Pino *et al.* (2010) suggest that the negative shift in $\delta^{238}U$ across Oceanic Anoxic Event 2 (OAE2) resulted from at least a threefold increase in the spatial converge of oceanic anoxia compared to the modern ocean. Similarly, Brennecka *et al.* (2011a) argue a sixfold increase in the anoxic flux of U is required to explain the negative shift in $\delta^{238}U$ across the end-Permian extinction horizon. Applying the U isotope fractionation factor determined in this study (*i.e.* $\varepsilon = -0.63 \pm 0.08$‰ to -0.84 ± 0.11‰) would decrease the required expansion of oceanic anoxia by ~25 to 50% in the models of Montoya-Pino *et al.* (2010) and Brennecka *et al.* (2011a). Furthermore, the apparent U isotope fractionation factors reported in this study potentially underestimate the true fractionation factor due to effects of diffusion within the sedimentary porewaters (Andersen *et al.*, 2014). Clearly, the magnitude of the U isotope fractionation factor is a necessary prerequisite before sedimentary records of $\delta^{238}U$ can be interpreted with confidence. Holmden *et al.* (2015) determined an apparent U isotope fractionation factor of 0.62 ± 0.17‰ in Saanich Inlet, an anoxic fjord, which is nearly identical to the fractionation factor calculated in this study with the Rayleigh fractionation model, while Andersen et al. (2016) have observed an ~0.51‰ offset between the authigenic U endmember in hypoxic sediments from off the coast of Washington, USA and seawater. The similarity between the results obtained indifferent settings indicate that a single U isotope fractionation factor may be generally applicable to anoxic depositional settings, although this still requires further scrutiny.

6.6 Conclusions

The successful use of $^{238}U/^{235}U$ as a paleoredox proxy is dependent on our ability to accurately describe and quantify the processes which fractionate U isotopes during the transfer of U from seawater to underlying sediments under anoxic conditions. In the Black Sea, the concentration of dissolved U and $\delta^{238}U$ decrease systematically with depth. An apparent fractionation factor (α) of 0.99937 ± 0.00008‰ (2 SE) is calculated from a Rayleigh fractionation model, while an apparent fractionation factor (α) of 0.99916 ± 0.00011‰ (2 SE) is calculated from a closed system equilibrium fractionation model. These α values are within the range of α values reported for microbially-mediated reduction of U(VI) to U(IV), indicating a biologic control on U isotope fractionation in the Black Sea. Further evidence of a biologic control on the U biogeochemistry in the Black Sea is the strong inverse correlation between the concentration of U and H_2S in the water column indicates a common process which produces H_2S and removes U, such as sulfate reduction. The $\delta^{238}U$ of sediments deposited under anoxic waters can be related back to the water column conditions via the calculated fractionation factors but not all variations in the sedimentary $\delta^{238}U$ are related to changes in the $\delta^{238}U$ of the water column. Variations in sedimentary $\delta^{238}U$ can also be related to changes in the depositional environment or changes in the fractionation factor associated with different environmental conditions.

CHAPTER 7

SUMMARY AND RECOMMENDATIONS FOR FUTURE WORK

7.1 Summary and conclusions

The marine biogeochemistry of trace metals and their isotopes is a rapidly expanding field that has applications in many areas of the Earth sciences. The distributions of trace metals in the ocean are controlled by their sources and sinks, the physical circulation of water masses with the ocean, and an array biogeochemical cycles occurring within the interior of the ocean. These processes are important to understand as they determine the availability of biologically essential trace metals to photosynthetic organisms in the euphotic zone of the oceans and thus impart a strong control on the magnitude of primary productivity in the surface ocean. As marine primary productivity represents a major source of O_2 to the atmosphere through photosynthesis and a major sink of CO_2 from the atmosphere through the ultimate burial of organic matter, the marine biogeochemistry of trace metals play an important role in determining the composition of Earth's atmosphere and therefore climate.

Sources of trace metals to the oceans are widely variable, but one very important source is atmospheric deposition of dust. In the open ocean, far removed from continental land masses, atmospheric deposition is the primary source of many biologically important trace metals, such as iron, to the surface ocean. As the Mediterranean Sea is one of the most heavily dust impacted marine water bodies in the world, it is an important location to investigate the impact of atmospheric deposition on the distributions of trace metals. The Mediterranean Sea is also an ideal location to investigate the effects of physical circulation of water masses on the distribution of trace metals. Overturning circulation occurs within the Mediterranean Sea on time scales of decades, allowing researchers to trace the evolution of water masses within the time frame of human lifetimes, which is not possible in the open ocean since deep water in the global ocean is renewed on ~1000 y time scales. Furthermore, the effects of anthropogenic activity are very strong in the Mediterranean Sea due to the relatively small size and confined nature of the basin and the abundance of large population centers bordering its shores. These factors, along with the accessibility of the important

sampling locations, make the Mediterranean Sea a very unique marine basin and an important natural laboratory for investigating the marine biogeochemistry of trace metals.

Sedimentary records of trace metals, both their abundances and isotopic compositions, are important tools for investigating the redox evolution of the ocean-atmosphere system during Earth's history. Under sulfidic conditions, many trace metals (e.g. Fe, Zn, Cu, Cd) form insoluble metals-sulfides that are transferred from the water column to the underlying sediments. Thus, enrichments of redox sensitive trace metals over background lithogenic concentrations in marine sediments indicate the presence of anoxic and sulfidic conditions. Trace metal enrichments may also be due to other processes though, such as increased biological production in surface waters which would supply more trace metals to the sediment. Recent advances in analytical techniques have led to the rapid development and application of redox sensitive trace metal isotope systems as additional paleoredox proxies. Many trace metal records indicate global scale changes in the redox state of the ocean-atmosphere system throughout Earth's history. As such, the fundamental processes and mechanisms that control the abundance and isotope composition of trace metals in sediments need to be thoroughly investigated in modern marine systems in order to ascertain how trace metal enrichments and isotope signatures recorded in marine sediments relate to the prevailing redox state of the ocean-atmosphere system at the time of sediment deposition. Anoxic marine basins, such as the Black Sea, represent modern marine environments that are analogous to the dominantly anoxic Precambrian oceans and during oceanic anoxic events during the Mesozoic and provide a natural laboratory to calibrate trace metal paleoredox proxies.

The Black Sea is the world's largest anoxic marine basin. The water column is permanently stratified, giving rise to a redoxcline that separates oxygenated surface waters from anoxic and sulfidic (euxinic) deep waters. The progression of prevailing microbial respiration pathways occurs through the redoxcline across a depth of range of up to tens of meters thick. Similar redox gradients occur in modern marine sediments but are generally on the order of centimetres think. Thus, the Black Sea water column represents an ideal location to investigate the redox chemistry of trace metals, including isotope fractionation induced by different redox processes. Understanding the aqueous chemistry of trace metals under variable redox conditions is a vital prerequisite to the successful interpretation of variations in trace metal abundances and isotopic

compositions recorded in marine sediments deposited throughout Earth's history during times of drastically different prevailing environmental redox conditions, such as during the initial rise of atmospheric O_2 in the Precambrian.

The primary objective of this thesis was to exploit the unique oceanographic conditions of the Mediterranean and Black Seas to gain a better understanding of important processes controlling the distributions of trace elements and their isotopes in the marine environment. Summaries and conclusions for each chapter are described below.

Chapter 1 provided an introduction to the field of trace metal marine biogeochemistry and to the use of sedimentary records of trace metals and their isotopes as tracers paleoredox proxies. New and improved methods now allow for the large scale sampling and analysis of trace metals and their isotopes in the world's oceans, which is exemplified through the GEOTRACES program. Larger datasets from more regions of the worlds' oceans will provide more information about the controls on the distributions of trace metals. Unique locations like the Mediterranean and Black Seas are useful for investigating how specific processes, such as dust deposition, circulation, anthropogenic contamination, and changes in redox state, control the distributions of trace elements and their isotopes.

Chapter 2 reported the zonal distribution of dissolved Al in the Mediterranean Sea. The concentrations of dissolved Al in the Mediterranean Sea are higher than in any other marine system, presumably due to the high amount of atmospheric deposition. However, dissolved Al is strongly correlated with salinity in the Mediterranean Sea, which strongly suggests that the distribution of dissolved Al primarily controlled by physical mixing. Furthermore, the nutrient-like distribution of dissolved Al and similarity with the distribution of Si in the Mediterranean Sea is also a result of physical mixing rather than biological utilization. Maintaining the current distribution of dissolved in the Al requires a large source of Al to the Mediterranean Sea, such as atmospheric deposition, and subsequent vertical transport of Al from surface to deep waters.

Chapter 3 described the zonal distributions of dissolved Fe, Cd, Zn and Pb in the Mediterranean Sea. The source of Fe to the Mediterranean Sea is dominated by

atmospheric deposition of lithogenic particles sourced from the Saharan desert. The highest concentrations of dissolved Fe are observed in surface waters of the eastern Mediterranean. The source of Cd, Zn, and Pb to the Mediterranean Sea appears to be primarily anthropogenic in origin, either from atmospheric deposition of metal laden anthropogenic particles or from continental run such as polluted rivers. Furthermore, the western Mediterranean basin displays concentrations of dissolved Cd, Zn, and Pb that are significantly elevated to the eastern Mediterranean basin, suggesting that the impact of anthropogenic activities is strongest in the eastern Mediterranean. Although leaded gasoline has been phased out in most of the world, countries in North Africa continue to use leaded gasoline and may be contributing the elevated concentrations of dissolved Pb observed in Mediterranean surface waters. These results highlight the impact of anthropogenic activity on the distributions of trace metals which could potentially in turn modulate the community structure of marine phytoplankton by alleviating the growth limiting effects of low trace metal concentrations thereby allowing different species to flourish or by promoting toxicity due to elevated concentrations of trace metals.

Chapter 4 explored the behavior of trace metals (Al, Ti, Mn, Fe, Cu, Zn, Ga, Y, Zr, Cd, and La) under variable redox conditions in the Black Sea. The behaviors of Mn, Fe, Cd, Cu, Zn, and La in the Black Sea have been previously investigated and the results presented here confirm the conclusions of the previous studies, while this study represents the first data on the distribution of dissolved Al, Ga, Ti, Zr, and Y in the Black Sea. The vertical profiles of Mn and Fe are strongly influenced by redox cycling between particulate oxidized phases and dissolved reduced phases in the redoxcline. Within the sulfidic deep basin, both Mn and Fe are deposited as insoluble metal-sulfides. Metal-sulfide forming elements such as Cd, Zn, and Cu tend to exhibit elevated concentrations in the oxidized surface waters and very low concentrations in the deep sulfidic zone due to precipitation of metal-sulfides and scavenging of soluble metal-sulfides on the surfaces of sinking particles. The behavior of Al, Ga, Ti, Zr, Y, and La all show slight surface maximum due to atmospheric deposition, removal due to scavenging onto the surfaces of Mn and Fe oxides in the redoxcline, and regeneration due to the dissolution of the oxide particles as they sink into the anoxic deep basin. In the deep basin, Al, Ga, Zr, Y, and La are all scavenged to varying degrees by sinking sulfide particles. The distribution of dissolved Ti in the deep anoxic basin is anomalous

though in that its concentration increases by nearly three orders of magnitude relative to surface waters, suggesting that Ti is more soluble under euxinic condtions or the existence of a large source of Ti to the deep Black Sea.

Chapter 5 utilizes the unique conditions in the Black Sea to investigate the fractionation of Fe isotopes during pyrite precipitation and oxidation. This study represents on the very first efforts to investigate these processes in a natural setting. The large Fe isotope fractionation observed during pyrite formation in the Black Sea, $\varepsilon_{\mathrm{Fe(II)-pyrite}}$ = +2.75 ± 0.22‰ (2SE), supports the results of the controversial experimental study Guilbaud *et al.* (2011), while the small Fe isotope fractionation during oxidation, $\varepsilon_{\mathrm{Fe(II)-Fe(III)}}$ =-0.19 ± 0.07‰ to -0.40 ± 0.12‰ (2SE) is contradictory to the current understanding of oxidation reactions. These results call for a re-examination of the Fe isotope record preserved in Precambrian sedimentary pyrite which has been previously interpreted as reflecting large scale changes in the oxidation state of the oceans associated with the oxidation of Earth's atmosphere. This study exemplifies the need to test assumptions about the behavior of redox sensitive trace metals and their isotopes under variable redox conditions in modern environments that can act as analogues to paleoceanographic conditions.

Chapter 6 examines the behavior of U isotopes in the Black Sea. The reduction of soluble U(VI) to insoluble U(IV) in marine sediments induces significant isotope fractionation. The U isotope fractionation factor during reduction of U(VI) to U(IV) was determined as α = 0.99937 ± 0.00008‰ to 0.99916 ± 0.00011‰ (2 SE). This value was derived from the U isotopic composition of the water column of the Black Sea. The calculated isotopic fractionation factor can be used to interpret records of U isotopic compositions recorded in marine sediments. The magnitude of the U isotope fractionation factor is similar to experiments using sulfate reducing bacteria to mediate the reduction of U(VI) and U(IV) and a strong inverse relationship between U and H2S concentrations in the Black Sea water column was observed. These observations indicate that sulfate reducing bacteria are possibly mediating the reduction of U(VI) to U(IV) in the Black Sea.

7.2 Synthesis of findings

The distributions of dissolved Al, Fe, Zn, Cd, and Pb in the Mediterranean Sea were presented in Chapters 2 and 3. All of these elements display unique distributions in the Mediterranean Sea compared with the global ocean, owing to the unique conditions present in the Mediterranean region. That is, the physical circulation of the Mediterranean Sea is similar to the global ocean overturning circulation, but is occurring on a much shorter time scale (<100 y versus ~1000 y, respectively). The atmospheric deposition of aerosols from natural sources, such as the Saharan desert, and from anthropogenic sources, such as European industry, supplies a vast amount of trace metals to the Mediterranean Sea, in additional to more point-sources, such as river runoff. High input of trace metals result in the elevated concentrations of dissolved Al, Fe, Zn, Cd, and Pb in the Mediterranean Sea versus the Atlantic Ocean, while the three-dimensional distributions of these metals are strongly modulated by the strong Mediterranean thermohaline circulation, biological cycling, and differences in the geochemistry of each metal. These processes ultimately result in different Mediterranean water masses with significant gradients in their trace metal contents and the mixing between these different water masses results in many of the unique patterns that are observed in the trace metal distribution in the Mediterranean Sea.

In the Black Sea, the redox gradient in the water column is the primary control on the trace metal distributions. Unlike the Mediterranean Sea, water circulation in the Black Sea is slow and atmospheric deposition is likely not as significant. Thus the contrast between the two basins is ideal for examining different controls on the distributions of trace metals in the marine environment. Similarly, comparing the distributions of trace metals with differing geochemistry offers the chance to understand how different processes occurring within the same environment are effecting the trace metal distributions. The water column cycling of trace metals in the Black Sea results in vertical profiles that display pronounced gradients typically around the redoxcline. This implies that the trace metals are being either released to solution through dissolution of sinking particles such as iron and manganese oxides, or are being removed from solution due to formation of insoluble species or being scavenged by sinking particles such as iron-sulfides. Most elements display a gradient around the redoxcline, but U is unique in that the removal of U most likely occurs within the underlying sediments. In contrast, Fe is removed from the water column as iron-

sulfides. The vertical profiles of U and Fe in the Black Sea, both concentration and isotope composition, reflect this difference in their geochemistry. The Black Sea is a unique environment in the modern world and it is expected that the behavior of Fe and U in other anoxic basins will differ. In other anoxic settings, such as some continental margin sediments, Fe is being reductively cycled and precipitated as pyrite within the sediment before diffusing out in to the overlying water column and is thus behaving more like U in the Black Sea. While in other settings, U may be reduced in the water column and therefore behave more like Fe in the Black Sea. Thus, although the isotope geochemistry of Fe and U are certainly different in the Black Sea, these distributions of these elements in the Black Sea provide a useful reference for understanding the behavior of trace metals under anoxic marine conditions.

7.3 Recommendations for future work

The marine biogeochemistry of trace metals is a bourgeoning field and is being driven by advances in sampling and analytical technology. This thesis clearly demonstrates this fact with the application of the best available technology to reliable collect and analyse trace metal concentrations and their isotopic concentrations in seawater to answer basic questions about the primary controls on the distributions of trace metals in the Mediterranean and Black Seas. Future research will surely continue to apply the best available technology to outstanding questions in the field of marine biogeochemistry of trace metals. From the work present in this thesis there are many future potential applications.

- The distributions of many trace metals in the Mediterranean Sea presented in this study can be used to test the ability of marine biogeochemistry models to produce the distributions of trace metals observed in the Mediterranean Sea. The processes occurring in the Mediterranean Sea are similar to the global ocean; therefore biogeochemical models developed for the Mediterranean Sea system should also be applicable to the global ocean.

- The source of the elevated concentrations of Cd, Zn, and Pb in the western Mediterranean may possibly be revealed through isotope composition measurements of Zn, Cd, and Pb in these samples. Large volume samples were

collected for this purpose and methods are being developed to process and analyse these samples for their isotopic compositions.

- The vertical profiles of trace elements in the Black Sea are very well constrained. Although the major processes controlling the vertical distributions of trace metals are reasonable well known, simple reaction transport modelling of the trace metal vertical profiles could be used constrain these initial observations.

- The mechanism for Fe isotope fractionation during pyrite formation is not fully understood. Pyrite formation is a multistep process with dissolved Fe first reacting with H_2S to form FeS and then further reacting with H_2S to form FeS_2. Fractionation of Fe isotopes occurring during both steps but it is unclear which step dominates the overall reaction in the Black Sea. Analyzing the Fe isotopic composition of FeS in the Black Sea water column would be a worthwhile exercise to answer this question.

- The large Fe isotope fractionation associated with pyrite formation implies that individual pyrites deposited in the Black Sea should be characterized by $\delta^{56}Fe$ values between approximately -3.5 to -0.7‰. The only available data to date is from bulk pyrite, but new methods capable of determining the Fe isotope composition of individual pyrites would provide a useful test of the Fe isotope fractionation factor determined for pyrite formation in Chapter 5.

- Oxidation of Fe(II) to Fe(III) in the surface water of the Black Sea is possibly driven by the surface reactions on particles of Mn oxides. Therefore, it would be useful to conduct experiments that aim to determine the Fe isotope fractionation associated with oxidation by MnO_2, as this may be a potential reason for the disagreement between the results obtained in the study and previous experimental studies on the Fe isotope fractionation during oxidation.

- The reduction of U(VI) to U(IV) occurs within the pore space of marine sediments. It is thus imperative to obtain high quality U isotope data on pore

waters from marine sediments in order to validate the U isotope fractionation factor determine from the U isotopic composition of the water column in the Black Sea.

REFERENCES

Abbott, A.N., Haley, B.A., McManus, J. and Reimers, C.E., 2015. The sedimentary flux of dissolved rare earth elements to the ocean. Geochimica et Cosmochimica Acta, 154: 186-200.

Algeo, T.J. and Maynard, J.B., 2008. Trace-metal covariation as a guide to water-mass conditions in ancient anoxic marine environments. Geosphere, 4(5): 872-887.

Alibo, D.S. and Nozaki, Y., 1999. Rare earth elements in seawater: particle association, shale-normalization, and Ce oxidation. Geochimica et Cosmochimica Acta, 63(3–4): 363-372.

Anbar, A.D. and Knoll, A., 2002. Proterozoic ocean chemistry and evolution: a bioinorganic bridge? Science, 297(5584): 1137-1142.

Anderson, R. and Fleisher, M., 1991. Uranium precipitation in Black Sea sediments, Black Sea Oceanography. Springer, pp. 443-458.

Anderson, R.F., Fleisher, M.Q. and LeHuray, A.P., 1989. Concentration, oxidation state, and particulate flux of uranium in the Black Sea. Geochimica et Cosmochimica Acta, 53(9): 2215-2224.

Anderson, T.F. and Raiswell, R., 2004. Sources and mechanisms for the enrichment of highly reactive iron in euxinic Black Sea sediments. American Journal of Science, 304(3): 203-233.

Archer, C. and Vance, D., 2006. Coupled Fe and S isotope evidence for Archean microbial Fe (III) and sulfate reduction. Geology, 34(3): 153-156.

Azoury, S., Tronczynski, J., Chiffoleau, J.-F., Cossa, D., Nakhle, K., Schmidt, S. and Khalaf, G., 2013. Historical records of mercury, lead, and polycyclic aromatic hydrocarbons depositions in a dated sediment core from the Eastern Mediterranean. Environmental Science & Technology, 47(13): 7101-7109.

Barnes, C.E. and Cochran, J.K., 1991. Geochemistry of uranium in Black Sea sediments. Deep Sea Research Part A. Oceanographic Research Papers, 38: S1237-S1254.

Basu, A., Sanford, R.A., Johnson, T.M., Lundstrom, C.C. and Löffler, F.E., 2014. Uranium isotopic fractionation factors during U (VI) reduction by bacterial isolates. Geochimica et Cosmochimica Acta, 136: 100-113.

Beard, B.L. and Johnson, C.M., 2004. Fe isotope variations in the modern and ancient earth and other planetary bodies. Reviews in Mineralogy and Geochemistry, 55(1): 319-357.

Beard, B.L., Johnson, C.M., Cox, L., Sun, H., Nealson, K.H. and Aguilar, C., 1999. Iron isotope biosignatures. Science, 285(5435): 1889-1892.

Bekker, A., Holland, H.D., Wang, P.L., Rumble, D., Stein, H.J., Hannah, J.L., Coetzee, L.L. and Beukes, N.J., 2004. Dating the rise of atmospheric oxygen. Nature, 427(6970): 117-120.

Benedicto, J., Andral, B., Martínez-Gómez, C., Guitart, C., Deudero, S., Cento, A., Scarpato, A., Caixach, J., Benbrahim, S. and Chouba, L., 2011. A large scale survey of trace metal levels in coastal waters of the Western Mediterranean basin using caged mussels (Mytilus galloprovincialis). Journal of Environmental Monitoring, 13(5): 1495-1505.

Bergamasco, A. and Malanotte-Rizzoli, P., 2010. The circulation of the Mediterranean Sea: a historical review of experimental investigations. Advances in Oceanography and Limnology., 1(1): 11-28.

Beşiktepe, Ş.T., Sur, H.I., Özsoy, E., Latif, M.A., Oğuz, T. and Ünlüata, Ü., 1994. The circulation and hydrography of the Marmara Sea. Progress in Oceanography, 34(4): 285-334.

Bigeleisen, J., 1996. Nuclear size and shape effects in chemical reactions. Isotope chemistry of the heavy elements. Journal of the American Chemical Society, 118(15): 3676-3680.

Biller, D.V. and Bruland, K.W., 2012. Analysis of Mn, Fe, Co, Ni, Cu, Zn, Cd, and Pb in seawater using the Nobias-chelate PA1 resin and magnetic sector inductively coupled plasma mass spectrometry (ICP-MS). Marine Chemistry, 130: 12-20.

Bopp IV, C.J., Lundstrom, C.C., Johnson, T.M., Sanford, R.A., Long, P.E. and Williams, K.H., 2010. Uranium $^{238}U/^{235}U$ isotope ratios as indicators of reduction: results from an in situ biostimulation experiment at Rifle, Colorado, USA. Environmental Science & Technology, 44(15): 5927-5933.

Boyd, P.W., Jickells, T., Law, C.S., Blain, S., Boyle, E.A., Buesseler, K.O., Coale, K.H., Cullen, J.J., de Baar, H.J.W., Follows, M., Harvey, M., Lancelot, C., Levasseur, M., Owens, N.P.J., Pollard, R., Rivkin, R.B., Sarmiento, J., Schoemann, V., Smetacek, V., Takeda, S., Tsuda, A., Turner, S. and Watson, A.J., 2007. Mesoscale iron enrichment experiments 1993-2005: Synthesis and future directions. Science, 315(5812): 612-617.

Boyle, E., Chapnick, S., Bai, X. and Spivack, A., 1985. Trace metal enrichments in the Mediterranean Sea. Earth and Planetary Science Letters, 74(4): 405-419.

Boyle, E. and Edmond, J.M., 1975. Copper in surface waters south of New Zealand. Nature, 253(5487): 107-109.

Boyle, E.A., Sclater, F. and Edmond, J.M., 1976. On the marine geochemistry of cadmium. Nature, 263(5572): 42-44.

Brand, L.E., Sunda, W.G. and Guillard, R.R.L., 1983. Limitation of Marine-Phytoplankton Reproductive Rates by Zinc, Manganese, and Iron. Limnology and Oceanography, 28(6): 1182-1198.

Brennecka, G.A., Herrmann, A.D., Algeo, T.J. and Anbar, A.D., 2011a. Rapid expansion of oceanic anoxia immediately before the end-Permian mass

extinction. Proceedings of the National Academy of Sciences, 108(43): 17631-17634.

Brennecka, G.A., Wasylenki, L.E., Bargar, J.R., Weyer, S. and Anbar, A.D., 2011b. Uranium isotope fractionation during adsorption to Mn-oxyhydroxides. Environmental Science & Technology, 45(4): 1370-1375.

Brewer, P.G. and Spencer, D., 1974. Distribution of some trace elements in Black Sea and their flux between dissolved and particulate phases. Am. Assoc. Pet. Geol. Bull.;(United States), 20.

Brown, M.T. and Bruland, K.W., 2008. An improved flow-injection analysis method for the determination of dissolved aluminum in seawater. Limnology and Oceanography-Methods, 6: 87-95.

Bruland, K.W., 1980. Oceanographic distributions of cadmium, zinc, nickel, and copper in the North Pacific. Earth and Planetary Science Letters, 47(2): 176-198.

Bruland, K.W., Knauer, G.A. and Martin, J.H., 1978. Zinc in north-east Pacific water. Nature, 271(5647): 741-743.

Bruland, K.W. and Lohan, M.C., 2003. 6.02 - Controls of Trace Metals in Seawater. In: D.H. Editors-in-Chief: Heinrich and K.T. Karl (Editors), Treatise on Geochemistry. Pergamon, Oxford, pp. 23-47.

Bruland, K.W., Middag, R. and Lohan, M.C., 2014. 8.2 - Controls of Trace Metals in Seawater. In: H.D.H.K. Turekian (Editor), Treatise on Geochemistry (Second Edition). Elsevier, Oxford, pp. 19-51.

Butler, I.B., Archer, C., Vance, D., Oldroyd, A. and Rickard, D., 2005. Fe isotope fractionation on FeS formation in ambient aqueous solution. Earth and Planetary Science Letters, 236(1): 430-442.

Canfield, D., 1998. A new model for Proterozoic ocean chemistry. Nature, 396(6710): 450-453.

Canfield, D. and Thamdrup, B., 2009. Towards a consistent classification scheme for geochemical environments, or, why we wish the term ‘suboxic’would go away. Geobiology, 7(4): 385-392.

Caschetto, S. and Wollast, R., 1979. Vertical distribution of dissolved aluminium in the mediterranean sea. Marine Chemistry, 7(2): 141-155.

Caspers, H. and Schmidt, K.P., 1957. Black sea and sea of Azov. Geological Society of America Memoirs, 67: 801-890.

Castillo, M.A., Trujillo, I.S., Alonso, E.V., de Torres, A.G. and Pavón, J.C., 2013. Bioavailability of heavy metals in water and sediments from a typical Mediterranean Bay (Málaga Bay, Region of Andalucía, Southern Spain). Marine pollution bulletin, 76(1): 427-434.

Chisholm, S.W., 2000. Oceanography: stirring times in the Southern Ocean. Nature, 407(6805): 685-687.

Chou, L. and Wollast, R., 1997. Biogeochemical behavior and mass balance of dissolved aluminum in the western Mediterranean Sea. Deep Sea Research Part II: Topical Studies in Oceanography, 44(3): 741-768.

Clark, S.K. and Johnson, T.M., 2008. Effective isotopic fractionation factors for solute removal by reactive sediments: A laboratory microcosm and slurry study. Environmental Science & Technology, 42(21): 7850-7855.

Conway, T.M. and John, S.G., 2014. Quantification of dissolved iron sources to the North Atlantic Ocean. Nature, 511(7508): 212-215.

Conway, T.M., Rosenberg, A.D., Adkins, J.F. and John, S.G., 2013. A new method for precise determination of iron, zinc and cadmium stable isotope ratios in seawater by double-spike mass spectrometry. Analytica Chimica Acta, 793: 44-52.

Copat, C., Bella, F., Castaing, M., Fallico, R., Sciacca, S. and Ferrante, M., 2012. Heavy metals concentrations in fish from Sicily (Mediterranean Sea) and evaluation of possible health risks to consumers. Bulletin of Environmental Contamination and Toxicology, 88(1): 78-83.

Cossa, D., Buscail, R., Puig, P., Chiffoleau, J.-F., Radakovitch, O., Jeanty, G. and Heussner, S., 2014. Origin and accumulation of trace elements in sediments of the northwestern Mediterranean margin. Chemical Geology, 380: 61-73.

Craddock, P.R. and Dauphas, N., 2011. Iron isotopic compositions of geological reference materials and chondrites. Geostandards and Geoanalytical Research, 35(1): 101-123.

Croot, P.L., Streu, P. and Baker, A.R., 2004. Short residence time for iron in surface seawater impacted by atmospheric dry deposition from Saharan dust events. Geophysical Research Letters, 31(23).

Czaja, A.D., Johnson, C.M., Yamaguchi, K.E. and Beard, B.L., 2012. Comment on "Abiotic pyrite formation produces a large Fe isotope fractionation". Science, 335(6068): 538-538.

Dahl, T.W., Boyle, R.A., Canfield, D.E., Connelly, J.N., Gill, B.C., Lenton, T.M. and Bizzarro, M., 2014. Uranium isotopes distinguish two geochemically distinct stages during the later Cambrian SPICE event. Earth and Planetary Science Letters, 401: 313-326.

de Baar, H., Buma, A., Nolting, R.F., Cadee, G.C., Jacques, G. and Treguer, P.J., 1990. On iron limitation of the Southern Ocean: experimental observations in the Weddell and Scotia Seas. Marine Ecology Progress Series, 65: 105-122.

de Baar, H.J.W., Boyd, P.W., Coale, K.H., Landry, M.R., Tsuda, A., Assmy, P., Bakker, D.C.E., Bozec, Y., Barber, R.T., Brzezinski, M.A., Buesseler, K.O., Boye, M., Croot, P.L., Gervais, F., Gorbunov, M.Y., Harrison, P.J., Hiscock, W.T., Laan, P., Lancelot, C., Law, C.S., Levasseur, M., Marchetti, A., Millero, F.J., Nishioka, J., Nojiri, Y., van Oijen, T., Riebesell, U., Rijkenberg, M.J.A., Saito, H., Takeda, S., Timmermans, K.R., Veldhuis, M.J.W., Waite, A.M. and

Wong, C.S., 2005. Synthesis of iron fertilization experiments: From the iron age in the age of enlightenment. Journal of Geophysical Research-Oceans, 110(C9).

de Baar, H.J.W., Timmermans, K.R., Laan, P., De Porto, H.H., Ober, S., Blom, J.J., Bakker, M.C., Schilling, J., Sarthou, G., Smit, M.G. and Klunder, M., 2008. Titan: A new facility for ultraclean sampling of trace elements and isotopes in the deep oceans in the international Geotraces program. Marine Chemistry, 111(1–2): 4-21.

Demaison, G. and Moore, G.T., 1980. Anoxic environments and oil source bed genesis. AApG Bulletin, 64(8): 1179-1209.

Dideriksen, K., Baker, J. and Stipp, S., 2006. Iron isotopes in natural carbonate minerals determined by MC-ICP-MS with a 58 Fe–54 Fe double spike. Geochimica et Cosmochimica Acta, 70(1): 118-132.

Duce, R.A., Liss, P.S., Merrill, J.T., Atlas, E.L., Buat-Menard, P., Hicks, B.B., Miller, J.M., Prospero, J.M., Arimoto, R., Church, T.M., Ellis, W., Galloway, J.N., Hansen, L., Jickells, T.D., Knap, A.H., Reinhardt, K.H., Schneider, B., Soudine, A., Tokos, J.J., Tsunogai, S., Wollast, R. and Zhou, M., 1991. The atmospheric input of trace species to the world ocean. Global Biogeochemical Cycles, 5(3): 193-259.

Dumas, C., Ludwig, W., Aubert, D., Eyrolle, F., Raimbault, P., Gueneugues, A. and Sotin, C., 2015. Riverine transfer of anthropogenic and natural trace metals to the Gulf of Lions (NW Mediterranean Sea). Applied Geochemistry, 58: 14-25.

Dunk, R., Mills, R. and Jenkins, W., 2002. A reevaluation of the oceanic uranium budget for the Holocene. Chemical Geology, 190(1): 45-67.

Dymond, J., Collier, R., McManus, J., Honjo, S. and Manganini, S., 1997. Can the aluminum and titanium contents of ocean sediments be used to determine the paleoproductivity of the oceans? Paleoceanography, 12(4): 586-593.

Eckert, S., Brumsack, H.-J., Severmann, S., Schnetger, B., März, C. and Fröllje, H., 2013. Establishment of euxinic conditions in the Holocene Black Sea. Geology, 41(4): 431-434.

Elbaz-Poulichet, F., 2005. River inputs of metals and Arsenic, The Mediterranean Sea. Springer, pp. 211-235.

Elbaz-Poulichet, F., Dezileau, L., Freydier, R., Cossa, D. and Sabatier, P., 2011. A 3500-year record of Hg and Pb contamination in a Mediterranean sedimentary archive (The Pierre Blanche Lagoon, France). Environmental Science & Technology, 45(20): 8642-8647.

Farquhar, J., Bao, H. and Thiemens, M., 2000. Atmospheric influence of Earth's earliest sulfur cycle. Science, 289(5480): 756-758.

Font, J., García-Ladona, E., Malanotte-Rizzoli, P., Pascual, A., Tintoré, J. and Triantafyllou, G., 2013. Physical forcing and physical/biochemical variability of the Mediterranean Sea: a review of unresolved issues and directions for future research. Ocean Science Discussions, 1280: 1205-1280.

Froelich, P.N., Klinkhammer, G., Bender, M.a.a., Luedtke, N., Heath, G.R., Cullen, D., Dauphin, P., Hammond, D., Hartman, B. and Maynard, V., 1979. Early oxidation of organic matter in pelagic sediments of the eastern equatorial Atlantic: suboxic diagenesis. Geochimica et Cosmochimica Acta, 43(7): 1075-1090.

Gehlen, M., Beck, L., Calas, G., Flank, A.-M., Van Bennekom, A. and Van Beusekom, J., 2002. Unraveling the atomic structure of biogenic silica: evidence of the structural association of Al and Si in diatom frustules. Geochimica et Cosmochimica Acta, 66(9): 1601-1609.

Gehlen, M., Heinze, C. and Maier-Reimer, E., 2003. Coupled Al-Si geochemistry in an ocean general circulation model: A tool for the validation of oceanic dust deposition fields? Global Biogeochemical Cycles, 17(1).

German, C.R., Holliday, B.P. and Elderfield, H., 1991. Redox cycling of rare earth elements in the suboxic zone of the Black Sea. Geochimica et Cosmochimica Acta, 55(12): 3553-3558.

Group, S.W., 2007. GEOTRACES–An international study of the global marine biogeochemical cycles of trace elements and their isotopes. Chemie der Erde-Geochemistry, 67(2): 85-131.

Guerzoni, S., Chester, R., Dulac, F., Herut, B., Loye-Pilot, M.D., Measures, C., Migon, C., Molinaroli, E., Moulin, C., Rossini, P., Saydam, C., Soudine, A. and Ziveri, P., 1999. The role of atmospheric deposition in the biogeochemistry of the Mediterranean Sea. Progress in Oceanography, 44(1-3): 147-190.

Guieu, C., Chester, R., Nimmo, M., Martin, J.-M., Guerzoni, S., Nicolas, E., Mateu, J. and Keyse, S., 1997. Atmospheric input of dissolved and particulate metals to the northwestern Mediterranean. Deep Sea Research Part II: Topical Studies in Oceanography, 44(3): 655-674.

Guieu, C., Loÿe-Pilot, M.D., Benyahya, L. and Dufour, A., 2010. Spatial variability of atmospheric fluxes of metals (Al, Fe, Cd, Zn and Pb) and phosphorus over the whole Mediterranean from a one-year monitoring experiment: Biogeochemical implications. Marine Chemistry, 120(1–4): 164-178.

Guieu, C., Loÿe-Pilot, M.D., Ridame, C. and Thomas, C., 2002. Chemical characterization of the Saharan dust end-member: Some biogeochemical implications for the western Mediterranean Sea. Journal of Geophysical Research: Atmospheres (1984–2012), 107(D15): ACH 5-1-ACH 5-11.

Guieu, C., Martin, J.-M., Tankere, S., Mousty, F., Trincherini, P., Bazot, M. and Dai, M., 1998. On trace metal geochemistry in the Danube River and western Black Sea. Estuarine, Coastal and Shelf Science, 47(4): 471-485.

Guilbaud, R., Butler, I.B. and Ellam, R.M., 2011. Abiotic pyrite formation produces a large Fe isotope fractionation. Science, 332(6037): 1548-1551.

Guilbaud, R., Butler, I.B. and Ellam, R.M., 2012. Response to Comment on "Abiotic Pyrite Formation Produces a Large Fe Isotope Fractionation". Science, 335(6068): 538-538.

Habfast, K., 1998. Fractionation correction and multiple collectors in thermal ionization isotope ratio mass spectrometry. International Journal of Mass Spectrometry, 176(1): 133-148.

Han, Q., Moore, J.K., Zender, C., Measures, C. and Hydes, D., 2008. Constraining oceanic dust deposition using surface ocean dissolved Al. Global Biogeochemical Cycles, 22(2).

Haraldsson, C. and Westerlund, S., 1988. Trace metals in the water columns of the Black Sea and Framvaren Fjord. Marine Chemistry, 23(3): 417-424.

Hart, S.R. and Zindler, A., 1989. Isotope fractionation laws: a test using calcium. International Journal of Mass Spectrometry and Ion Processes, 89(2): 287-301.

Hay, B.J., 1988. Sediment accumulation in the central western Black Sea over the past 5100 years. Paleoceanography, 3(4): 491-508.

He, Y., Ke, S., Teng, F.Z., Wang, T., Wu, H., Lu, Y. and Li, S., 2015. High-Precision Iron Isotope Analysis of Geological Reference Materials by High-Resolution MC-ICP-MS. Geostandards and Geoanalytical Research.

Heimbürger, L.-E., Migon, C., Dufour, A., Chiffoleau, J.-F. and Cossa, D., 2010. Trace metal concentrations in the North-western Mediterranean atmospheric aerosol between 1986 and 2008: Seasonal patterns and decadal trends. Science of The Total Environment, 408(13): 2629-2638.

Hiess, J., Condon, D.J., McLean, N. and Noble, S.R., 2012. $^{238}U/^{235}U$ systematics in terrestrial uranium-bearing minerals. Science, 335(6076): 1610-1614.

Holland, H.D., 2002. Volcanic gases, black smokers, and the Great Oxidation Event. Geochimica et Cosmochimica Acta, 66(21): 3811-3826.

Holland, H.D., 2005. 100th anniversary special paper: sedimentary mineral deposits and the evolution of earth's near-surface environments. Economic Geology, 100(8): 1489-1509.

Holmden, C., Amini, M. and Francois, R., 2015. Uranium isotope fractionation in Saanich Inlet: A modern analog study of a paleoredox tracer. Geochimica et Cosmochimica Acta, 153(0): 202-215.

Horner, T.J., Williams, H.M., Hein, J.R., Saito, M.A., Burton, K.W., Halliday, A.N. and Nielsen, S.G., 2015. Persistence of deeply sourced iron in the Pacific Ocean. Proceedings of the National Academy of Sciences, 112(5): 1292-1297.

Hua, B., Xu, H., Terry, J. and Deng, B., 2006. Kinetics of uranium (VI) reduction by hydrogen sulfide in anoxic aqueous systems. Environmental Science & Technology, 40(15): 4666-4671.

Hydes, D., 1983. Distribution of aluminium in waters of the North East Atlantic 25 N to 35 N. Geochimica et Cosmochimica Acta, 47(5): 967-973.

Hydes, D., De Lange, G. and De Baar, H., 1988. Dissolved aluminium in the Mediterranean. Geochimica et Cosmochimica Acta, 52(8): 2107-2114.

Hydes, D., Statham, P. and Burton, J., 1986. A vertical profile of dissolved trace metals (Al, Cd, Cu, Mn, Ni) over the median valley of the Mid Atlantic Ridge, 43 N: implications for hydrothermal activity. Science of the Total Environment, 49: 133-145.

Hydes, D.J., 1979. Aluminum in seawater: Control by inorganic processes. Science, 205(4412): 1260-1262.

Icopini, G., Anbar, A., Ruebush, S., Tien, M. and Brantley, S., 2004. Iron isotope fractionation during microbial reduction of iron: the importance of adsorption. Geology, 32(3): 205-208.

Jacobs, L., Emerson, S. and Skei, J., 1985. Partitioning and transport of metals across the O2H2S interface in a permanently anoxic basin: Framvaren Fjord, Norway. Geochimica et Cosmochimica Acta, 49(6): 1433-1444.

Jenkyns, H.C., 2010. Geochemistry of oceanic anoxic events. Geochemistry, Geophysics, Geosystems, 11(3).

John, S.G., 2012. Optimizing sample and spike concentrations for isotopic analysis by double-spike ICPMS. Journal of Analytical Atomic Spectrometry, 27(12): 2123-2131.

Johnson, C.M., Beard, B.L. and Roden, E.E., 2008. The iron isotope fingerprints of redox and biogeochemical cycling in modern and ancient Earth. Annual Reviews in Earth and Planetary Science, 36: 457-493.

Johnson, K.S., Gordon, R.M. and Coale, K.H., 1997. What controls dissolved iron concentrations in the world ocean? Marine Chemistry, 57(3–4): 137-161.

Jordi, A., Basterretxea, G., Tovar-Sánchez, A., Alastuey, A. and Querol, X., 2012. Copper aerosols inhibit phytoplankton growth in the Mediterranean Sea. Proceedings of the National Academy of Sciences, 109(52): 21246-21249.

Kelly, A.E., Reuer, M.K., Goodkin, N.F. and Boyle, E.A., 2009. Lead concentrations and isotopes in corals and water near Bermuda, 1780–2000. Earth and Planetary Science Letters, 283(1): 93-100.

Kendall, B., Brennecka, G.A., Weyer, S. and Anbar, A.D., 2013. Uranium isotope fractionation suggests oxidative uranium mobilization at 2.50 Ga. Chemical Geology, 362: 105-114.

Kendall, B., Komiya, T., Lyons, T.W., Bates, S.M., Gordon, G.W., Romaniello, S.J., Jiang, G., Creaser, R.A., Xiao, S. and McFadden, K., 2015. Uranium and molybdenum isotope evidence for an episode of widespread ocean oxygenation during the late Ediacaran Period. Geochimica et Cosmochimica Acta, 156: 173-193.

Klein, B., Roether, W., Manca, B.B., Bregant, D., Beitzel, V., Kovacevic, V. and Luchetta, A., 1999. The large deep water transient in the Eastern Mediterranean. Deep Sea Research Part I: Oceanographic Research Papers, 46(3): 371-414.

Koning, E., Gehlen, M., Flank, A.-M., Calas, G. and Epping, E., 2007. Rapid post-mortem incorporation of aluminum in diatom frustules: Evidence from chemical and structural analyses. Marine Chemistry, 106(1): 208-222.

Konovalov, S., Murray, J., Luther, G. and Tebo, B., 2006. Processes controlling the redox budget for the oxic/anoxic water column of the Black Sea. Deep Sea Research Part II: Topical Studies in Oceanography, 53(17): 1817-1841.

Konovalov, S., Samodurov, A., Oguz, T. and Ivanov, L., 2004. Parameterization of iron and manganese cycling in the Black Sea suboxic and anoxic environment. Deep Sea Research Part I: Oceanographic Research Papers, 51(12): 2027-2045.

Konovalov, S.K., Luther, G.W. and Yücel, M., 2007. Porewater redox species and processes in the Black Sea sediments. Chemical Geology, 245(3): 254-274.

Kramer, J., Laan, P., Sarthou, G., Timmermans, K.R. and de Baar, H.J.W., 2004. Distribution of dissolved aluminium in the high atmospheric input region of the subtropical waters of the North Atlantic Ocean. Marine Chemistry, 88(3–4): 85-101.

Ku, T.-L., Knauss, K.G. and Mathieu, G.G., 1977. Uranium in open ocean: concentration and isotopic composition. Deep Sea Research, 24(11): 1005-1017.

Landing, W.M. and Lewis, B.L., 1991. Thermodynamic modeling of trace metal speciation in the Black Sea, Black Sea Oceanography. Springer, pp. 125-160.

Lascaratos, A., 1993. Estimation of deep and intermediate water mass formation rates in the Mediterranean Sea. Deep Sea Research Part II: Topical Studies in Oceanography, 40(6): 1327-1332.

Lascaratos, A., Roether, W., Nittis, K. and Klein, B., 1999. Recent changes in deep water formation and spreading in the eastern Mediterranean Sea: a review. Progress in Oceanography, 44(1–3): 5-36.

Lee, B.-S., Bullister, J.L., Murray, J.W. and Sonnerup, R.E., 2002. Anthropogenic chlorofluorocarbons in the Black Sea and the Sea of Marmara. Deep Sea Research Part I: Oceanographic Research Papers, 49(5): 895-913.

Lewis, B. and Landing, W., 1991. The biogeochemistry of manganese and iron in the Black Sea. Deep Sea Research Part A. Oceanographic Research Papers, 38: S773-S803.

Lewis, B.L. and Landing, W.M., 1992. The investigation of dissolved and suspended-particulate trace metal fractionation in the Black Sea. Marine Chemistry, 40(1): 105-141.

Li, F., Ren, J., Yan, L., Liu, S., Liu, C., Zhou, F. and Zhang, J., 2013. The biogeochemical behavior of dissolved aluminum in the southern Yellow Sea: Influence of the spring phytoplankton bloom. Chinese Science Bulletin, 58(2): 238-248.

Li, Y.H. and Schoonmaker, J.E., 2003. 7.01 - Chemical Composition and Mineralogy of Marine Sediments. In: H.D.H.K. Turekian (Editor), Treatise on Geochemistry. Pergamon, Oxford, pp. 1-35.

Little, S.H., Vance, D., Lyons, T.W. and McManus, J., 2015. Controls on trace metal authigenic enrichment in reducing sediments: Insights from modern oxygen-deficient settings. American Journal of Science, 315(2): 77-119.

Luo, C., Mahowald, N.M. and del Corral, J., 2003. Sensitivity study of meteorological parameters on mineral aerosol mobilization, transport, and distribution. Journal of Geophysical Research: Atmospheres, 108(D15): 4447.

Lyons, T.W., Anbar, A.D., Severmann, S., Scott, C. and Gill, B.C., 2009. Tracking euxinia in the ancient ocean: a multiproxy perspective and Proterozoic case study. Annual Review of Earth and Planetary Sciences, 37: 507-534.

Lyons, T.W., Reinhard, C.T. and Planavsky, N.J., 2014. The rise of oxygen in Earth/'s early ocean and atmosphere. Nature, 506(7488): 307-315.

Lyons, T.W. and Severmann, S., 2006. A critical look at iron paleoredox proxies: new insights from modern euxinic marine basins. Geochimica et Cosmochimica Acta, 70(23): 5698-5722.

Mackenzie, F.T., Stoffyn, M. and Wollast, R., 1978. Aluminum in Seawater: Control by Biological Activity. Science, 199(4329): 680-682.

Mackin, J.E. and Aller, R.C., 1984. Processes Affecting the Behavior of Dissolved Aluminum in Estuarine Waters. Marine Chemistry, 14(3): 213-232.

Maring, H.B. and Duce, R.A., 1987a. The Impact of Atmospheric Aerosols on Trace-Metal Chemistry in Open Ocean Surface Seawater .1. Aluminum. Earth and Planetary Science Letters, 84(4): 381-392.

Maring, H.B. and Duce, R.A., 1987b. The impact of atmospheric aerosols on trace metal chemistry in open ocean surface seawater, 1. Aluminum. Earth and Planetary Science Letters, 84(4): 381-392.

Martín, J., Sanchez-Cabeza, J., Eriksson, M., Levy, I. and Miquel, J., 2009. Recent accumulation of trace metals in sediments at the DYFAMED site (Northwestern Mediterranean Sea). Marine Pollution Bulletin, 59(4): 146-153.

Martin, J.H. and Fitzwater, S.E., 1988. Iron-Deficiency Limits Phytoplankton Growth in the Northeast Pacific Subarctic. Nature, 331(6154): 341-343.

Measures, C. and Vink, S., 2000. On the use of dissolved aluminum in surface waters to estimate dust deposition to the ocean. Global Biogeochemical Cycles, 14(1): 317-327.

Measures, C.I., Brown, M.T. and Vink, S., 2005. Dust deposition to the surface waters of the western and central North Pacific inferred from surface water dissolved aluminum concentrations. Geochemistry, Geophysics, Geosystems, 6(9): Q09M03.

Measures, C.I., Sato, T., Vink, S., Howell, S. and Li, Y.H., 2010. The fractional solubility of aluminium from mineral aerosols collected in Hawaii and implications for atmospheric deposition of biogeochemically important trace elements. Marine Chemistry, 120(1–4): 144-153.

Middag, R., de Baar, H.J.W., Laan, P. and Bakker, K., 2009. Dissolved aluminium and the silicon cycle in the Arctic Ocean. Marine Chemistry, 115(3-4): 176-195.

Middag, R., de Baar, H.J.W., Laan, P., Cai, P.H. and van Ooijen, J.C., 2011a. Dissolved manganese in the Atlantic sector of the Southern Ocean. Deep-Sea Research Part Ii-Topical Studies in Oceanography, 58(25-26): 2661-2677.

Middag, R., Séférian, R., Conway, T.M., John, S.G., Bruland, K.W. and de Baar, H.J.W., 2015b. Intercomparison of dissolved trace elements at the Bermuda Atlantic Time Series station. Marine Chemistry, 177, Part 3: 476-489.

Middag, R., van Slooten, C., de Baar, H.J.W. and Laan, P., 2011b. Dissolved aluminium in the Southern Ocean. Deep-Sea Research Part Ii-Topical Studies in Oceanography, 58(25-26): 2647-2660.

Migon, C., 2005. Trace metals in the Mediterranean Sea, The Mediterranean Sea. Springer, pp. 151-176.

Migon, C. and Caccia, J.-L., 1990. Separation of anthropogenic and natural emissions of particulate heavy metals in the western Mediterranean atmosphere. Atmospheric Environment. Part A. General Topics, 24(2): 399-405.

Migon, C. and Nicolas, E., 1998. Effects of antipollution policy on anthropogenic lead transfers in the Ligurian Sea. Marine Pollution Bulletin, 36(10): 775-779.

Migon, C., Robin, T., Dufour, A. and Gentili, B., 2008. Decrease of lead concentrations in the Western Mediterranean atmosphere during the last 20 years. Atmospheric Environment, 42(4): 815-821.

Millet, M.-A., Baker, J.A. and Payne, C.E., 2012. Ultra-precise stable Fe isotope measurements by high resolution multiple-collector inductively coupled plasma mass spectrometry with a 57 Fe–58 Fe double spike. Chemical Geology, 304: 18-25.

Millot, C., 2013. Levantine Intermediate Water characteristics: an astounding general misunderstanding! Scientia Marina, 77(2): 217-232.

Millot, C., Candela, J., Fuda, J.-L. and Tber, Y., 2006. Large warming and salinification of the Mediterranean outflow due to changes in its composition. Deep Sea Research Part I: Oceanographic Research Papers, 53(4): 656-666.

Millot, C. and Taupier-Letage, I., 2005. Circulation in the Mediterranean Sea. In: A. Saliot (Editor), The Mediterranean Sea. Handbook of Environmental Chemistry. Springer Berlin Heidelberg, pp. 29-66.

Miralles, J., Véron, A., Radakovitch, O., Deschamps, P., Tremblay, T. and Hamelin, B., 2006. Atmospheric lead fallout over the last century recorded in Gulf of Lions sediments (Mediterranean Sea). Marine Pollution Bulletin, 52(11): 1364-1371.

Montoya-Pino, C., Weyer, S., Anbar, A.D., Pross, J., Oschmann, W., van de Schootbrugge, B. and Arz, H.W., 2010. Global enhancement of ocean anoxia during Oceanic Anoxic Event 2: A quantitative approach using U isotopes. Geology, 38(4): 315-318.

Moore, C.M., Mills, M.M., Arrigo, K.R., Berman-Frank, I., Bopp, L., Boyd, P.W., Galbraith, E.D., Geider, R.J., Guieu, C., Jaccard, S.L., Jickells, T.D., La Roche, J., Lenton, T.M., Mahowald, N.M., Maranon, E., Marinov, I., Moore, J.K., Nakatsuka, T., Oschlies, A., Saito, M.A., Thingstad, T.F., Tsuda, A. and Ulloa, O., 2013. Processes and patterns of oceanic nutrient limitation. Nature Geoscience, 6(9): 701-710.

Moran, S.B. and Moore, R.M., 1988. Evidence from mesocosm studies for biological removal of dissolved aluminium from sea water. Nature, 335(6192): 706-708.

Moran, S.B. and Moore, R.M., 1991. The potential source of dissolved aluminum from resuspended sediments to the North Atlantic Deep Water. Geochimica et Cosmochimica Acta, 55(10): 2745-2751.

Moran, S.B. and Moore, R.M., 1992. Kinetics of the removal of dissolved aluminum by diatoms in seawater: A comparison with thorium. Geochimica et Cosmochimica Acta, 56(9): 3365-3374.

Morley, N., Burton, J., Tankere, S. and Martin, J.-M., 1997. Distribution and behaviour of some dissolved trace metals in the western Mediterranean Sea. Deep Sea Research Part II: Topical Studies in Oceanography, 44(3): 675-691.

Murphy, M.J., Stirling, C.H., Kaltenbach, A., Turner, S.P. and Schaefer, B.F., 2014. Fractionation of $^{238}U/^{235}U$ by reduction during low temperature uranium mineralisation processes. Earth and Planetary Science Letters, 388(0): 306-317.

Murray, J.W., Top, Z. and Özsoy, E., 1991. Hydrographic properties and ventilation of the Black Sea. Deep Sea Research Part A. Oceanographic Research Papers, 38: S663-S689.

Murray, J.W. and Yakushev, E., 2006. The suboxic transition zone in the Black Sea, Past and Present Water Column Anoxia. Springer, pp. 105-138.

Nicolau, R., Lucas, Y., Merdy, P. and Raynaud, M., 2012. Base flow and stormwater net fluxes of carbon and trace metals to the Mediterranean sea by an urbanized small river. Water Research, 46(20): 6625-6637.

Nieto, J.M., Sarmiento, A.M., Olías, M., Canovas, C.R., Riba, I., Kalman, J. and Delvalls, T.A., 2007. Acid mine drainage pollution in the Tinto and Odiel rivers (Iberian Pyrite Belt, SW Spain) and bioavailability of the transported metals to the Huelva Estuary. Environment International, 33(4): 445-455.

Noordmann, J., Weyer, S., Montoya-Pino, C., Dellwig, O., Neubert, N., Eckert, S., Paetzel, M. and Böttcher, M.E., 2015. Uranium and molybdenum isotope systematics in modern euxinic basins: Case studies from the central Baltic Sea and the Kyllaren fjord (Norway). Chemical Geology, 396(0): 182-195.

Nozaki, Y., Thomson, J. and Turekian, K., 1976. The distribution of 210 Pb and 210 Po in the surface waters of the Pacific Ocean. Earth and Planetary Science Letters, 32(2): 304-312.

Orians, K.J. and Bruland, K.W., 1985. Dissolved aluminium in the central North Pacific. Nature, 316(6027): 427-429.

Orians, K.J. and Bruland, K.W., 1986. The biogeochemistry of aluminum in the Pacific Ocean. Earth and Planetary Science Letters, 78(4): 397-410.

Oursel, B., Garnier, C., Durrieu, G., Mounier, S., Omanović, D. and Lucas, Y., 2013. Dynamics and fates of trace metals chronically input in a Mediterranean coastal zone impacted by a large urban area. Marine Pollution Bulletin, 69(1): 137-149.

Owens, S., Buesseler, K. and Sims, K., 2011. Re-evaluating the 238 U-salinity relationship in seawater: Implications for the 238 U–234 Th disequilibrium method. Marine Chemistry, 127(1): 31-39.

Palmer, M. and Edmond, J., 1993. Uranium in river water. Geochimica et Cosmochimica Acta, 57(20): 4947-4955.

Patterson, C., 1974. Lead in Seawater. Science, 183(4124): 553-554.

Polat, S.Ç. and Tugrul, S., 1995. Nutrient and organic carbon exchanges between the Black and Marmara Seas through the Bosphorus Strait. Continental Shelf Research, 15(9): 1115-1132.

Potter, E.-K., Stirling, C.H., Andersen, M.B. and Halliday, A.N., 2005. High precision Faraday collector MC-ICPMS thorium isotope ratio determination. International Journal of Mass Spectrometry, 247(1): 10-17.

Poulton, S.W., Fralick, P.W. and Canfield, D.E., 2010. Spatial variability in oceanic redox structure 1.8 billion years ago. Nature Geoscience, 3(7): 486-490.

Puig, P., Palanques, A. and Martín, J., 2014. Contemporary Sediment-Transport Processes in Submarine Canyons. Annual Review of Marine Science, 6(1): 53-77.

Rademacher, L.K., Lundstrom, C.C., Johnson, T.M., Sanford, R.A., Zhao, J. and Zhang, Z., 2006. Experimentally determined uranium isotope fractionation during reduction of hexavalent U by bacteria and zero valent iron. Environmental Science & Technology, 40(22): 6943-6948.

Raiswell, R. and Canfield, D.E., 1998. Sources of iron for pyrite formation in marine sediments. American Journal of Science, 298(3): 219-245.

Resing, J.A. and Measures, C., 1994. Fluorometric determination of Al in seawater by flow injection analysis with in-line preconcentration. Analytical Chemistry, 66(22): 4105-4111.

Richter, S., Eykens, R., Kühn, H., Aregbe, Y., Verbruggen, A. and Weyer, S., 2010. New average values for the n (238 U)/n (235 U) isotope ratios of natural uranium standards. International Journal of Mass Spectrometry, 295(1): 94-97.

Rijkenberg, M.J., de Baar, H.J., Bakker, K., Gerringa, L.J., Keijzer, E., Laan, M., Laan, P., Middag, R., Ober, S. and van Ooijen, J., 2015. "PRISTINE", a new high volume sampler for ultraclean sampling of trace metals and isotopes. Marine Chemistry, 177: 501-509.

Robinson, A.R., Leslie, W.G., Theocharis, A. and Lascaratos, A., 2001. Mediterranean Sea Circulation. In: J.H. Steele (Editor), Encyclopedia of Ocean Sciences. Academic Press, Oxford, pp. 1689-1705.

Roether, W., Klein, B., Manca, B.B., Theocharis, A. and Kioroglou, S., 2007. Transient Eastern Mediterranean deep waters in response to the massive dense-water output of the Aegean Sea in the 1990s. Progress in Oceanography, 74(4): 540-571.

Rolison, J., Middag, R., Stirling, C., Rijkenberg, M. and de Baar, H., 2015. Zonal distribution of dissolved aluminium in the Mediterranean Sea. Marine Chemistry, 177: 87-100.

Romaniello, S.J., Herrmann, A.D. and Anbar, A.D., 2013. Uranium concentrations and $^{238}U/^{235}U$ isotope ratios in modern carbonates from the Bahamas: Assessing a novel paleoredox proxy. Chemical Geology, 362: 305-316.

Rouxel, O.J., Bekker, A. and Edwards, K.J., 2005. Iron isotope constraints on the Archean and Paleoproterozoic ocean redox state. Science, 307(5712): 1088-1091.

Rudge, J.F., Reynolds, B.C. and Bourdon, B., 2009. The double spike toolbox. Chemical Geology, 265(3): 420-431.

Rudnick, R.L. and Gao, S., 2003. 3.01 - Composition of the Continental Crust. In: H.D. Holland and K.K. Turekian (Editors), Treatise on Geochemistry. Pergamon, Oxford, pp. 1-64.

Ruiz-Pino, D., Nicolas, E., Bethoux, J. and Lambert, C., 1991. Zinc budget in the Mediterranean Sea: a hypothesis for non-steady-state behavior. Marine Chemistry, 33(1): 145-169.

Saito, M.A., Goepfert, T.J. and Ritt, J.T., 2008. Some thoughts on the concept of colimitation: three definitions and the importance of bioavailability. Limnology and Oceanography, 53(1): 276.

Sarthou, G., Baker, A.R., Blain, S., Achterberg, E.P., Boye, M., Bowie, A.R., Croot, P., Laan, P., de Baar, H.J. and Jickells, T.D., 2003. Atmospheric iron deposition and sea-surface dissolved iron concentrations in the eastern Atlantic Ocean. Deep Sea Research Part I: Oceanographic Research Papers, 50(10): 1339-1352.

Schauble, E.A., 2007. Role of nuclear volume in driving equilibrium stable isotope fractionation of mercury, thallium, and other very heavy elements. Geochimica et Cosmochimica Acta, 71(9): 2170-2189.

Schijf, J., de Baar, H.J., Wijbrans, J.R. and Landing, W.M., 1991. Dissolved rare earth elements in the Black Sea. Deep Sea Research Part A. Oceanographic Research Papers, 38: S805-S823.

Schlitzer, R., 2011. Ocean Data View, h ttp. odv. awi. de.

Schröder, K., Gasparini, G.P., Tangherlini, M. and Astraldi, M., 2006. Deep and intermediate water in the western Mediterranean under the influence of the

Eastern Mediterranean Transient. Geophysical Research Letters, 33(21): L21607.

Scott, K., Lu, X., Cavanaugh, C. and Liu, J., 2004. Optimal methods for estimating kinetic isotope effects from different forms of the Rayleigh distillation equation. Geochimica et Cosmochimica Acta, 68(3): 433-442.

Severmann, S., Lyons, T.W., Anbar, A., McManus, J. and Gordon, G., 2008. Modern iron isotope perspective on the benthic iron shuttle and the redox evolution of ancient oceans. Geology, 36(6): 487-490.

Shen, G.T. and Boyle, E.A., 1988. Thermocline ventilation of anthropogenic lead in the western North Atlantic. Journal of Geophysical Research: Oceans (1978–2012), 93(C12): 15715-15732.

Siebert, C., Nägler, T.F. and Kramers, J.D., 2001. Determination of molybdenum isotope fractionation by double-spike multicollector inductively coupled plasma mass spectrometry. Geochemistry, Geophysics, Geosystems, 2(7).

Skliris, N., 2014. Past, Present and Future Patterns of the Thermohaline Circulation and Characteristic Water Masses of the Mediterranean Sea. In: S. Goffredo and Z. Dubinsky (Editors), The Mediterranean Sea. Springer Netherlands, pp. 29-48.

Skliris, N. and Lascaratos, A., 2004. Impacts of the Nile River damming on the thermohaline circulation and water mass characteristics of the Mediterranean Sea. Journal of Marine Systems, 52(1–4): 121-143.

Skrabal, S.A., 2006. Dissolved titanium distributions in the Mid-Atlantic Bight. Marine Chemistry, 102(3): 218-229.

Skrabal, S.A. and Terry, C.M., 2002. Distributions of dissolved titanium in porewaters of estuarine and coastal marine sediments. Marine Chemistry, 77(2): 109-122.

Sohrin, Y., Urushihara, S., Nakatsuka, S., Kono, T., Higo, E., Minami, T., Norisuye, K. and Umetani, S., 2008. Multielemental determination of GEOTRACES key trace metals in seawater by ICPMS after preconcentration using an ethylenediaminetriacetic acid chelating resin. Analytical Chemistry, 80(16): 6267-6273.

Sorokin, Y., 1983. The Black Sea. In: B. Ketchum (Editor), Ecosystems of the World: Estuaries and Enclosed Seas. Elsevier, Amsterdam.

Soto-Navarro, J., Criado-Aldeanueva, F., García-Lafuente, J. and Sánchez-Román, A., 2010. Estimation of the Atlantic inflow through the Strait of Gibraltar from climatological and in situ data. Journal of Geophysical Research: Oceans (1978–2012), 115(C10).

Statham, P., Burton, J. and Hydes, D., 1985. Cd and Mn in the Alboran Sea and adjacent North Atlantic: geochemical implications for the Mediterranean. Nature, 313: 565-567.

Stewart, K., Kassakian, S., Krynytzky, M., DiJulio, D. and Murray, J.W., 2007. Oxic, suboxic, and anoxic conditions in the Black Sea, The Black Sea Flood Question: Changes in Coastline, Climate, and Human Settlement. Springer, pp. 1-21.

Stirling, C.H., Andersen, M.B., Potter, E.-K. and Halliday, A.N., 2007. Low-temperature isotopic fractionation of uranium. Earth and Planetary Science Letters, 264(1–2): 208-225.

Stoffyn, M., 1979. Biological Control of Dissolved Aluminum in Seawater: Experimental Evidence. Science, 203(4381): 651-653.

Suess, E. and Thiede, J., 1983. Coastal upwelling: Its sediment record, Part A: Responses of the sedimnentary regime to present coastal upwelling. NATO Conference Series, 10B. Plenum Press, New York.

Tanhua, T., Hainbucher, D., Schroeder, K., Cardin, V., Alvarez, M. and Civitarese, G., 2013. The Mediterranean Sea system: a review and an introduction to the special issue. Ocean Science, 9(5): 789-803.

Tankere, S., Muller, F., Burton, J., Statham, P., Guieu, C. and Martin, J.-M., 2001. Trace metal distributions in shelf waters of the northwestern Black Sea. Continental Shelf Research, 21(13): 1501-1532.

Tissot, F.L. and Dauphas, N., 2015. Uranium isotopic compositions of the crust and ocean: age corrections, U budget and global extent of modern anoxia. Geochimica et Cosmochimica Acta, 167: 113-143.

Tria, J., Butler, E.C.V., Haddad, P.R. and Bowie, A.R., 2007. Determination of aluminium in natural water samples. Analytica Chimica Acta, 588(2): 153-165.

Tsimplis, M.N., Zervakis, V., Josey, S.A., Peneva, E.L., Struglia, M.V., Stanev, E.V., Theocharis, A., Lionello, P., Malanotte-Rizzoli, P. and Artale, V., 2006. Changes in the oceanography of the Mediterranean Sea and their link to climate variability. Developments in Earth and Environmental Sciences, 4: 227-282.

Turner, D.R., Whitfield, M. and Dickson, A.G., 1981. The equilibrium speciation of dissolved components in freshwater and sea water at 25°C and 1 atm pressure. Geochimica et Cosmochimica Acta, 45(6): 855-881.

Twining, B.S., Rauschenberg, S., Morton, P.L. and Vogt, S., 2015. Metal contents of phytoplankton and labile particulate material in the North Atlantic Ocean. Progress in Oceanography, 137, Part A: 261-283.

UNEP, 2005. United Nations Environment Programme, Mediterranean Action Plan MED POL Transboundary diagnostic analysis (TDA) for the Mediterranean Sea. UNEP MAP Publication, Athens.

UNEP, 2015. United Nations Environment Programme, Partnership for Clean Fuels and Vehicles. Leaded Petrol Phase-Out: Global Status. http://www.unep.org/Transport/new/PCFV/pdf/Maps_Matrices/world/lead/MapWorldLead_January2015.pdf

Van Cappellen, P., Powley, H.R., Emeis, K.C. and Krom, M.D., 2014. A biogeochemical model for phosphorus and nitrogen cycling in the Eastern Mediterranean Sea: Part 1. Model development, initialization and sensitivity. Journal of Marine Systems, 139(0): 460-471.

Van Geen, A., Boyle, E.A. and Moore, W.S., 1991. Trace metal enrichments in waters of the Gulf of Cadiz, Spain. Geochimica et Cosmochimica Acta, 55(8): 2173-2191.

van Geen, A., Rosener, P. and Boyle, E., 1988. Entraînaient of trace-metal-enriched Atlantic-shelf water in the inflow to the Mediterranean Sea. Nature, 331: 4.

van Hulten, M.M.P., Sterl, A., Tagliabue, A., Dutay, J.C., Gehlen, M., de Baar, H.J.W. and Middag, R., 2013. Aluminium in an ocean general circulation model compared with the West Atlantic Geotraces cruises. Journal of Marine Systems, 126(0): 3-23.

Velaoras, D., Krokos, G., Nittis, K. and Theocharis, A., 2014. Dense intermediate water outflow from the Cretan Sea: A salinity driven, recurrent phenomenon, connected to thermohaline circulation changes. Journal of Geophysical Research: Oceans, 119(8): 4797-4820.

Wedepohl, K., 1991. Chemical composition and fractionation of the continental crust. Geologische Rundschau, 80(2): 207-223.

Wei, C.-L. and Murray, J.W., 1991. 234 Th/238 U disequilibria in the Black Sea. Deep Sea Research Part A. Oceanographic Research Papers, 38: S855-S873.

Welch, S., Beard, B., Johnson, C. and Braterman, P., 2003. Kinetic and equilibrium Fe isotope fractionation between aqueous Fe (II) and Fe (III). Geochimica et Cosmochimica Acta, 67(22): 4231-4250.

Weyer, S., Anbar, A.D., Gerdes, A., Gordon, G.W., Algeo, T.J. and Boyle, E.A., 2008. Natural fractionation of $^{238}U/^{235}U$. Geochimica et Cosmochimica Acta, 72(2): 345-359.

Wiederhold, J.G., 2015. Metal stable isotope signatures as tracers in environmental geochemistry. Environmental Science & Technology, 49(5): 2606-2624.

Wijsman, J.W., Middelburg, J.J. and Heip, C.H., 2001. Reactive iron in Black Sea sediments: implications for iron cycling. Marine Geology, 172(3): 167-180.

Wilkin, R.T. and Arthur, M.A., 2001. Variations in pyrite texture, sulfur isotope composition, and iron systematics in the Black Sea: Evidence for late Pleistocene to Holocene excursions of the O 2-H 2 S redox transition. Geochimica et Cosmochimica Acta, 65(9): 1399-1416.

Wu, L., Percak-Dennett, E.M., Beard, B.L., Roden, E.E. and Johnson, C.M., 2012. Stable iron isotope fractionation between aqueous Fe (II) and model Archean ocean Fe–Si coprecipitates and implications for iron isotope variations in the ancient rock record. Geochimica et Cosmochimica Acta, 84: 14-28.

Yamaguchi, K.E., Johnson, C.M., Beard, B.L. and Ohmoto, H., 2005. Biogeochemical cycling of iron in the Archean–Paleoproterozoic Earth: constraints from iron isotope variations in sedimentary rocks from the Kaapvaal and Pilbara Cratons. Chemical Geology, 218(1): 135-169.

Yiğiterhan, O., Murray, J.W. and Tuğrul, S., 2011. Trace metal composition of suspended particulate matter in the water column of the Black Sea. Marine Chemistry, 126(1): 207-228.

Yilmaz, A.B., 2003. Levels of heavy metals (Fe, Cu, Ni, Cr, Pb, and Zn) in tissue of Mugil cephalus and Trachurus mediterraneus from Iskenderun Bay, Turkey. Environmental Research, 92(3): 277-281.

Yoshiya, K., Sawaki, Y., Shibuya, T., Yamamoto, S., Komiya, T., Hirata, T. and Maruyama, S., 2015. In-situ iron isotope analyses of pyrites from 3.5 to 3.2 Ga sedimentary rocks of the Barberton Greenstone Belt, Kaapvaal Craton. Chemical Geology, 403: 58-73.

Yuan-Hui, L., 1991. Distribution patterns of the elements in the ocean: A synthesis. Geochimica et Cosmochimica Acta, 55(11): 3223-3240.

Zhang, J., Amakawa, H. and Nozaki, Y., 1994. The comparative behaviors of yttrium and lanthanides in the seawater of the North Pacific. Geophysical Research Letters, 21(24): 2677-2680.